Hydrological Modeling and Management Practices to Augment Reservoir Capacity in Wadi Shueib Catchment Area – Jordan: Geo-Informatics Approach

A Thesis submitted in partial fulfilment of the requirement

for the award of a degree of

Doctor of Philosophy

in

Civil Engineering

Submitted by

Odai Ibrahim Mohammed Al Balasmeh

Reg. No: 901702004

Under the Guidance of:

Dr. Tapas Karmaker

Associate Professor

Department of Civil Engineering

Dr. Richa Babbar

Associate Professor

Department of Civil Engineering

Civil Engineering Department

Thapar Institute of Engineering and Technology

(Deemed to be University)

December 2020

CERTIFICATE

I hereby certify that the work in this thesis,"**Hydrological Modeling and Management Practices to Augment Reservoir Capacity in Wadi Shueib Catchment Area – Jordan: Geo-Informatics Approach",** submitted in the partial fulfilment of the requirement for the award of the degree of Doctor of Philosophy (Ph.D.) in Civil Engineering Department, Thapar Institute of Engineering and Technology (TIET), Patiala is an authentic record of my work carried out under the supervision of **Dr. Tapas Karmaker** and **Dr. Richa Babbar**. The work embodied in this thesis has not been submitted in part or whole to any other institute/university to award any degree.

Odai Ibrahim Mohammed Al Balasmeh

This is to certify that the above statement made by the candidate is accurate to the best of my knowledge.

Date: 11 Dec 2020

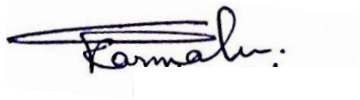

Dr. Tapas Karmaker

Associate Professor

Department of Civil Engineering

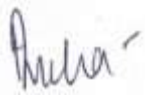

Dr. Richa Babbar

Associate Professor

Department of Civil Engineering

ACKNOWLEDGMENT

Most of all, I am grateful to God, who was a source of inspiration and blessing to me all through my PhD. Undertaking this Ph.D. has been a truly life-changing experience for me. It would not have been possible without the support and encouragement of numerous people, including my family, supervisors, colleagues, friends and various institutions.

I want to say a huge thank you to my supervisors Dr. Tapas Karmaker and Dr, Richa Babbar for all the support and encouragement they both gave me during the long months I spent undertaking my work. Without their guidance and constant feedback, this Ph.D. would not have been achievable.

This thesis has been kept on track and been seen through to completion with numerous people's support and encouragement, including my family, supervisors, colleagues, and friends. I have had great luck working and collaborating with many inspiring, competent, and friendly people who contributed in many ways to the success of this study. It is a pleasant task to use this space to thank them.

PREFACE

This Ph.D. thesis is the outcome of my study Civil Engineering, specialization Water Resources at Thapar Institute of Engineering and Technology. It will not only be the last research, but it is also a milestone that emphasizes the end of a full-time educational career that took not less than twenty years. Although twenty years sounds like quite a long time in which many lessons are learnt, I got convinced that learning does not stop after achieving a certificate.

During my studies, I became more aware that there are too many subjects I do not know much about them. I found out that multidisciplinary work suits me more than thoroughgoing research. However, a reasonable fundamental knowledge basis is essential to contribute to multidisciplinary projects. I am grateful that I was able to acquire this knowledge at TIET, Patiala.

Regarding collaboration, I feel it is always not required. There are often other interests that impede collaboration, e.g., concerns about data. Many data were not available in this research despite my utmost endeavour. Despite this, I want to thank the few data suppliers who made my research possible.

I also want to thank my Ph.D. committee, Dr. Tapas Karmaker, Dr. Richa Babbar, Dr. Prem Pal Bansal, Dr. Sarbjit Singh, Dr. Dwarika Nath Ratha, Dr. Harish Garg, and Dr. Danie Roy A. B for finding the time to assess my thesis.

Last but not least, I like to thank my parents and brother for their unconditional support and trust during those times when I needed it the most.

I hope you enjoy reading my thesis!

Table of Contents

List of Figures

List of Tables

List of Abbreviations

Abbreviation	Stand For
a.m.s.l.	above mean sea level
ACF	Auto-Correlation Function
AGNPS	Agricultural Non-Point Source Pollution Model
AHP	Analytical Hierarchy Processes
ANN	Artificial Neural Network
ANSWERS	Watershed Environmental Response Simulation
AR	Autoregressive
ARIMA	Autoregressive Integrated Moving Average
ASTER	Advanced Spaceborne Thermal Emission and Reflection Radiometer
b.m.s.l.	below mean sea level
BR	Bayesian regularization
CN	Curve number
CoI	Cone of influence
CREAMS	Agricultural Management Systems
CREAMS	Chemicals, Runoff, and Erosion from Agricultural Management Systems
DEM	Digital Elevation Model
DSM	Digital Surface Model
DTM	Digital Terrain Model
ENN	Ensemble Neural Network
ENVISAT	Environmental Satellite
EPIC	Environmental Impact Policy Climate
EPIC	Erosion Productivity Impact Calculator
ESA	European Space Agency
EUROSEM	European Soil Erosion Model
F-AHP	Fuzzy Analytical Hierarchy Processes
FAO	Food and Agriculture Organization
FNN	Feedforward Neural Network
GCP	Ground Control point
GIS	Geographical Information System
GLEAMS	Groundwater Loading Effects on Agricultural Management Systems
GLUE	Generalized Likelihood Uncertainty Estimation
GPS	Global Positioning System
Green	Green band in satellite image
H	Hurst index
HDI	Hybrid Drought Index
HSPF	Hydrologic Simulation Program-Fortran
I	Integrating
IDI	Integrated Drought Index
ITA	Innovative Trend Analysis
KE	Kinetic energy
Landsat ETM+	Landsat Enhanced Thematic Mapper Plus
Landsat TM	Landsat Thematic Mapper
LiDAR	Light Detection and Ranging

LULC	Land Use and Land Cover
MA	Moving average
MCM	Million Cube Meter
MK	Mann-Kendall
MMK	Modified Mann-Kendall
MSDI	Multivariate Standardized Drought Index
MUSLE	Modified Universal Soil Loss Equation
N	North
NASA	National Aeronautics and Space Administration
NDVI	Normalized Difference Vegetation Index
NDWI	Normalized Difference Water Index
NIR	Near Infrared band
NIR	Near infrared band in satellite image
NOAA	National Oceanic and Atmospheric Administration
NSE	Nash-Sutcliffe efficiency
OLI/TIRS	Operational Land Imager and Thermal Infrared Sensor
PACF	Partial Auto-Correlation Function
PCC	Pearson Correlation Coefficient
PDSI	Palmer's Drought Severity Index
PHDI	Palmer's Hydrological Drought Index
PN	Point density
Radar	RAdio Detection and Ranging
RBF	Radial Basis Function network
RED	Red band in satellite image
RJGC	Royal Jordanian Geographical center
RMSE	Root mean Square Error
RNN	recurrent neural network
RS	Remote Sensing
RUSLE	Revers Universal Soil Loss Equation
S	South
SPI	Standardized Precipitation Index
SPI	Standardized Precipitation Index
SRTM	Shuttle Radar Topography Mission
SSFI	Standardized Streamflow Index
SSFI	Standardized Streamflow Index
SSMI	Standardized Soil Moisture Index
SSMI	Standardized Soil Moisture Index
Std	Standard deviation error
SUIF-2	Sequential Uncertainty Fitting 2
SWAT	Soil Water Assessment Tools
SWAT-CUP	Soil Water Assessment Tools - Calibration and Uncertainty Procedures
SWI	standardized water level index
SWRRB	Simulator for Water Resources in Rural Basins
TIN	Triangulated Irregular Networks
TIN	Triangulated Irregular Networks
TOPO	Topographic Map

USGS	United State Geological Survey
USLE	Universal Soil Loss Equation
VCI	Vegetation Cover Index
W	West
WEPP	Water Erosion Prediction Project
WRI	World Resources Institute

List of Symbols

Symbol	Stand For
E_a	Amount of evapotranspiration on day
R_{day}	Amount of precipitation on day
Q_{surf}	Amount of surface runoff on day
Q_{gw}	Amount of water returning to the groundwater on day
A_b	Area of a drainage basin
$U\vartheta(p)$	Assurance level connected with the likelihood p
ϕ	Autoregressive model parameter
$W_x(m,n)$	Continuous wavelet transform of $x(t)$
$W_y(m,n)$	Continuous wavelet transform of $y(t)$
f_c	Cumulative infiltration rate
h_i	Distance (m) of the underwater triangle vertices
$\text{Elev}_{\text{Reference}}$	Elevation of a checked point from DSM
$\text{Elev}_{\text{examined}}$	Elevation of an examined point from DEM
f_c	Final or equilibrium infiltration capacity
f_o	Initial infiltration capacity
SW_0	Initial Soil water content at the time t
L_s	length of stream channels
σ_e^2	Likelihood function
θ	Moving average model parameter
S_i	Projected water surface area
ε	Random error
S_R	Retention parameter (mm)
SW_t	Soil water content at time t
ΔV_{a-b}	The change in capacity between water level
$\text{Elev}_{\text{Error}}$	The difference in elevation
$\bar{x}_1$	The mean of the first sample
$\bar{x}_2$	The mean of the second sample
S_1	The variance of the first sample
S_2	The variance of the second sample
t	t-test value
$\mathbb{R}$	Universal set of the real number
W_{seep}	Water percolation to the bottom of the soil profile on day
W_{seep}	Water percolation to the bottom of the soil profile on day
C	Cover-management factor (dimensionless)

C_u	Christiansen coefficient
D_d	Drainage Density
f	Focal length
g	Number of estimated coefficients
H	Hurst index
H_1	Alternative hypothesis
H_o	Null hypothesis
I	Integrating
k	Rate of decline of infiltration capacity
K	Soil erodibility factor ($t \cdot h \cdot MJ^{-1} \cdot mm^{-1}$)
K_s	Saturated hydraulic conductivity
L	Slope length factor (dimensionless)
P	Support practice factor (dimensionless).
q	Flow rate in m^3s^{-1}
Q	Runoff volume (m^3)
R	Average annual rainfall-runoff erosivity factor ($MJ \cdot mm \cdot ha^{-1} \cdot h^{-1} \cdot year^{-1}$)
$\boldsymbol{R_o}$	Orthogonal rotation matrix
S	Projected water surface area (m^2)
V	*S*torage capacity (m^3)
V_R	Raindrop velocity
V_T	Terminal velocity
x_a	Element point on the image in the x-direction
X_A	Element shifting in east direction
X_L	Center of an image in east direction
x_o	The principal point of the image in the x-direction
y_a	Element point on the image in the y-direction
Y_A	Element shifting in North direction
Y_L	Center of the image in North direction
y_o	The principal point of the image in the y-direction
Z_A	Element elevation
Z_L	Center point elevation
θ_f	Field moisture capacity
θ_s	Saturated water content
θ_w,	Wilting coefficient
κ_o	Rotation angle around z-direction
σ^2	Sample Variance
σZ	Surface roughness
φ_o	Rotation angle around y-direction
ω_o	Rotation angle around x-direction

SUMMARY

The available water resources information must be quantitatively considered with detailed hydrological processes for efficient water resources planning and management of a catchment. Although the primary source is surface water, most of the studies in the Middle-East region focus on groundwater. So, modelling the water cycle (e.g. rainfall-runoff modelling processes) in a catchment was not attentively in these studies. The changes in the hydrological cycle due to climate change could worsen the availability of water resources. The global projections regarding climate change have predicted an increase in drought and flood events. This investigation presents hydrological modelling and integrated water resources management in the Wadi Shueib catchment area, Jordon. One of the issues related to the catchment study is the periodic occurrence of drought, besides soil erosion and its deposition into the dam, coupled with increased water demands due to increased population and decreased irrigation capacity of the agricultural area. A total of six main components are addressed in this research: (i) The hydrological parameters and streamflow have been studied using four digital elevation models extracted through numerous platforms. (ii) Coupled Remote sensing data and water level observations for reservoir sustainability. (iii) Investigated the historical and future trend of precipitation data from five gauge stations using the Mann-Kendall (MK) test and Innovation Trend Analysis (ITA) and predicted the future using the ARIMA model. (iv) The hydrological model has been developed using SWAT to model and develop the area's streamflow. (v) Sl. No. (ii) and (iii) were used as inputs to determine the impact on drought conditions in the area. (vi) Experimental investigation by utilizing various vegetative covers under laboratory conditions to model the soil and water conservation

processes. Various techniques such as trend analysis, wavelet analysis, and cross wavelet analysis are applied to evaluate the effects, with the ensemble, and fuzzy models are developed. In hydrological parameters and streamflow modelling, the ASTER GeoDEM shows the closest match to other DEMs in both the study areas. So this data was used as input for the streamflow modelling in the Wadi Shueib watershed. The precipitation trend using ITA detects a better trend than the MK test. Later, the SWAT model was parameterized, calibrated, and validated using observed streamflow data in the study area. The future streamflow was predicted up to 2030 using the calibrated model. The analysis of the historical data shows a decreasing trend in the Wadi Shueib catchment as there is a decreasing trend in inflow, causing water deficiency and increasing water stress. It was observed that maximum water defect is expected to occur ~ -0.7 m^3/s from 2020 onwards. The water management practices using wheat straw cover gave interesting results to protect the land by reducing soil erosion and increasing infiltration. This technique can be used on the high soil erodible area in the watershed, reducing the sediment transport into the reservoir. Utilization of agricultural refuse is also another benefit from the practices.

Chapter 1: Introduction

1.1 Background

The present century has witnessed rapid expansion in human society and competition for water, quantitatively and qualitatively. Due to this, there is a rapid increase in the demand for natural water resources worldwide. Currently, water security is the main challenge, which takes various aspects of water supply, and environmental conservation. Usually, developing countries are the most affected by water stress and scarcity due to already limited freshwater availability in these countries and the lack of infrastructure to utilize these available resources.

The United Nations have defined water stress and water scarcity terms based on freshwater availability for different uses, where the portion capacity per person per year lies under 1700 m^3 and 1000 m^3, respectively (Falkenmark, 1989). Most of the countries located in arid to semi-arid regions suffer critically due to water scarcity. The water availability under 500 m^3/capita/yr is defined as absolute water scarcity. United Nation's Development Programme (UNDP, 2006) estimated that approximately one billion people worldwide suffer from water stress caused by a deficiency in water resources. Besides, more than 500 million people live in the threatened zone, as their surface-water resources have been exploited beyond sustainable limits (CAWMA, 2007). Fig. 1.1 illustrates the regions and freshwater availability and indicates that the Middle East and North African countries are the most affected due to water scarcity.

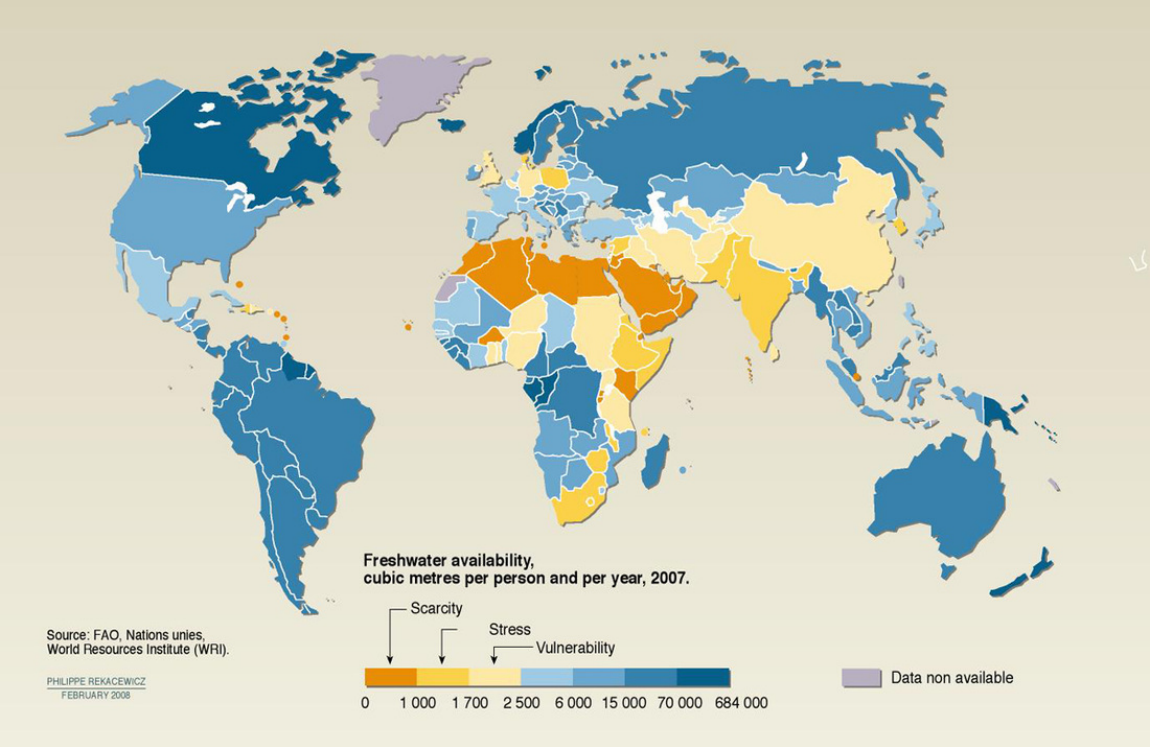

Fig. 1.1 Areas with freshwater scarcity worldwide

Climate change is an important phenomenon that has been taking place slowly but consistently over the years. It causes variation in hydrological, climatological, and meteorological parameters across the globe (IPCC 2007). As per the Intergovernmental Panel on Climatic Change (IPCC), the global mean surface temperature has increased by 0.6 ± 0.2 ^{o}C since 1861. A further increase of 2 to 4 ^{o}C is expected over the next 100 years, increasing the incidences of drought and its trend (Griggs and Noguer 2002; Alexander et al., 2006; IPCC 2007). Drought is one of the most critical global issues countries face, especially in arid to semi-arid regions.

Besides, precipitation is an important meteorological parameter, which is considered the principal source of water in many places on the earth, thus being utilized for various human activities such as agriculture, industry (Sun et al., 2018). The

precipitation is a crucial parameter in several hydrologic and flood risk models (e.g., Bellu et al., 2016; Terêncio et al., 2018), making it an essential parameter of interest. Precipitation is characterized by two aspects, namely, duration and intensity. Alteration in any of these two aspects can cause a severe natural hazard (Gong and Wang, 2006; Sun and Kim, 2016), such as floods and droughts. One of the powerful implications of climate change on precipitation is altering precipitation's time, quantity, and intensity in any area. Hence, there is a need to analyze its changing pattern over time, based on historical data and forecast it for early preparedness especially, in water-stressed areas.

Jordan is considered the second poorest country globally regarding freshwater availability and its resources, as it is facing severe issues due to water stress and scarcity. The population of Jordon is also rapidly increasing, mainly due to political conflicts and the influx of refugees. This increase in the population decreased annual water portions per capita from 3600 m^3 in 1946 to only 145 m^3 in recent years (RWC, 2009). Jordan has a unique topographic and climatic condition, where the rainfall is distributed according to land topography. The high altitude lands of Jordan receive a considerable amount of rain that varies between 200 to more than 600 mm/year and is considered the principal source of surface and groundwater recharge. The rest of the areas lie below 200 mm/year, and the long term average rainfall in Jordan is ~95 mm/year (1963-2002).

These fluctuations in precipitation amount over time results in drought or drought-like conditions in some areas of Jordan (Al-Masaeid, 2010). Riepl (2013) concluded a decrease in precipitation in 67% of data recorded in Jordan valley, and the annual rainfall was below 200 mm. Wadi Shueib region in Jordan urgently needs water management due to the simultaneous intersection of increasing municipal, industrial, and

agricultural demand. In contrast, springs, a source of water supply, are already water deficit and also polluted. These conditions are only expected to worsen with a rapid increase in population (Riepl, 2013).

The Wadi Shueib catchment area is located in North-western Jordan, with an approximate drainage area of 180 km^2; The Wadi Shueib dam is the most crucial for irrigating the agriculture fields in Jordan valley. Besides, the behaviour of hydrological processes of the catchment produces periodic water scarcity and drought events. This work quantifies future precipitation scenarios based on the different frameworks for an overview of water resource conditions in the area. However, as precipitation is the lifeblood of the whole mechanism in the catchment (e.g., overland flow, groundwater recharge, erosion, and drought), this research will answer further water management and decision making.

1.2 Motivation for Research

Due to the critical situation of Jordan's water resources, some surface water modelling and surface water management studies have been conducted to improve freshwater yield while reducing the impact of overland flow and reservoir sedimentation. Earlier studies have given more attention to groundwater and a few on surface-water and runoff processes modelling. The present research is an output of an analysis of the hydrological processes of the Wadi Shueib catchment area. The study's main objective is to draw general conclusions on the factors of streamflow generation and management practices in arid to semi-arid regions. Usually, region-scale models under different cases and situations are helpful for water management strategies.

1.3 Thesis Outline

The thesis is organized as follows:

Chapter 1: This chapter gives a brief description and background of the current situation of water availability in the world. Besides, it also discusses the research motivations to address the water stress in Jordan.

Chapter 2: This chapter discusses previous studies on the impact of spatial resolution on hydrological parameters. A more comprehensive technique to monitor water capacity in the reservoir and the trend analysis and climatic forecast are also discussed. Moreover, previous studies related to hydrological modelling and drought management are summarized here. Finally, the studies related to soil erosion mechanism and its management are also discussed.

Chapter 3: This chapter represents a brief description and overview of the Wadi Shueib catchment. The climatic, meteorological, and hydrological conditions of the study sites are discussed. Besides that, the data collection for this research and a brief description of the methodology are also discussed.

Chapter 4: This chapter analyzes, compares, and models the various digital elevation models (DEM). Simple statistical analyses have been applied to compare DEM sources with high-resolution DTM from aerial photography. Later, the ensemble neural network model was used to carry out DEM corrections with minimum error compared with the available DEM.

Chapter 5: This chapter contains the integration of the remote sensing data with reservoir operations for its monitoring. The satellite images were used along with

reservoir water level to produce bathymetry of Wadi Shuieb dam, and sediment deposition over the time was estimated by validating using two different reservoirs.

Chapter 6: In this chapter, the trend analysis and forecasting methods were carried out using time series records of precipitation data. Two trend analysis methods, Mann-Kendall and innovative trend analysis methods, were carried out and compared to find the best way to detect the trend. The Autoregressive Integrated Moving Average (ARIMA) model was used to predict future precipitation.

Chapter 7: This chapter describes watershed modelling using the SWAT model. The procedure for SWAT model calibration and validation is described for simulating streamflow at the watershed outlet. A forecasting technique is also illustrated to predict the trend of water deficit in the area.

Chapter 8: This chapter proposes a hybrid drought index by integrating meteorological, hydrological, and soil moisture derived drought indices. The application of fuzzy-AHP and entropy weight methods have been described to work out the weightage for the three variables chosen. The purpose of developing the hybrid drought index is to capture the drought trend in the area

Chapter 9: This chapter describes building an experimental laboratory-scale model for analyzing the interactions between rainfall, overland flow, soil erosion, infiltration, and its behaviour with different land use. An efficient soil cover is proposed to reduce soil erosion and thus improve the dam's useful life and efficiency.

Chapter 10: This chapter draws a general conclusion concerning watershed management and practices in the Wadi Shueib. It also provides an overview of the potential applicability of the developed model and any further investigations possible.

Chapter 2: Literature Review

2.1 Introduction

This chapter summarizes the previous studies related to different methods and techniques to achieve the objectives. It was described in the last chapter that this work is composed of various aspects, for example, topographic analysis, hydrological parameters, reservoir operations, and soil erosion management for the most effective utilization of the water resources.

This chapter is divided into six sections as follows:

1. Hydrological and topographic analysis based on digital elevation models
2. Reservoir sediment deposition based on remote sensing platforms
3. Trend analysis
4. Hydrological modelling based on SWAT model
5. Drought analysis based on meteorological, hydrological, and agricultural information
6. Soil erosion analysis based on experimental studies

2.2 Hydrological and topographic analysis based on digital elevation models

The availability of remote sensing techniques to compute the digital elevation models (DEMs) makes the spatial terrain easy to extract and calculate. Numerous studies have documented the impact of errors in topographic data collection using different techniques.

There are different methods to generate DEM; e.g., interferometry (Kervyn, 2001), the photogrammetric method using stereo pairs aerial photographs (Schenk, 1996; Hohle, 2009), land survey and contour maps (Wilson and Gallant, 2000; Taud et al.,

1999), and laser scanned imagery (Favey et al., 2003). DEM is subject to various distortion, for example, gross error while gathering the data (Rodgriguez et al., 2006), lack of stereo photos orientation (Mukherjee et al., 2011), and a combination of human, instrument, and climatic errors which neither can be estimated nor neglected. In contrast, these geographical errors depend on topographical characteristics (Holmes et al., 2000). Moreover, the spatial resolution of DEM and interpolation methods play an essential role in the accuracy of DEM.

Aerial photos have been used in the studies for more than half a century due to high accuracy in DTM resolution and ortho-photo when the sky is clear, or cloud cover is minimum (Lucas et al., 2002). The aerial photographs are available in the multi-spectral format as panchromatic, true colour, and infrared (Avery and Berlin, 1992). The Global Positioning System (GPS) with aerial photos was used in many cases to improve the accuracy and reduce the time for field surveys (Eugene, 2005).

Most hydrological parameters, such as slope, flow-direction, drainage network, watershed, can be extracted using DEM (Garbrecht. and Martz, 1999). Many factors affect DEM accuracy, which also affects its derivatives, such as the spatial resolution, vertical precision, and DEM source are the most important among these factors (Thompson et al., 2001). The DEM has been used in different fields, such as modelling and predicting environmental, geomorphological, and hydrological areas, where accuracy plays a significant role in spatial distribution (Thompson et al., 2001). Vaze et al., 2010 studied the accuracy of DEM, and they found that the DEM from different sources generates absolute errors in hydrological parameters within the watershed area. The DEM and other topography parameters such as slope gradients, slope aspects, and drainage

density affect the hydrological modelling output and applications (Vaze et al., 2010). Some researchers reported that the DEM quality and resolution affect the derived hydrological parameters (features) (e.g., Kenward et al., 2000).

Generating a quality DEM that covers a vast area is difficult due to the difficulty in the generation process. There are many open-source DEMs available with various spatial resolution, e.g., SRTM (1-arc second, and 3-arc second with global cover), ASTER GDEM (30 meters), GTOPO 30 (30 arc second), and others with low resolution (Di Luzio et al., 2005; Kiamehr and Sjoberg, 2005; Frey and Paul, 2012). The global and regional studies can be studied and represented using low-resolution DEM, while the main factor for these applications depends on the vertical accuracy (Dragut and Eisank, 2011). Numerous studies have been carried out to evaluate the vertical accuracy of DEM (Hirano et al., 2003; Bourgine and Baghdadi, 2005; Frey and Paul, 2012; Zhou et al., 2012).

Due to DEM uncertainties, different studies have estimated these errors (Thompson et al., 2001; Heritage et al., 2009; Spaete et al., 2011). The earlier studies assessed that the DEM error is uniformly distributed on the entire DEM. For that, basic statistics (root mean square error (RMSE) or standard deviation) were used to estimate the DEM error using truth ground points (Brasington et al., 2000, 2003). Lane et al. (2003) used two different terrain lands (wet and dry lands) to improve the basic statistical methods by applying non-uniform error. Due to the uneven topographical shape of the earth, the uniform error calculation methods outcomes over and under-estimated in flat and sloped areas, respectively (Bangen et al., 2016). The DEM errors and uncertainties estimation are recently focused on using machine learning techniques and modelling

empirical, morphometric, regression, and fuzzy theory (Erdogan, 2010; Sofia et al., 2013).

2.3 Reservoir sediment deposition based on remote sensing data

The estimation of reservoir sediment deposition was carried out by researchers based on empirical and remote sensing methods. This task cannot be achieved using soil erosion models due to sediment transport and surface flow complexities. The increasing demand for freshwater has opened the gate to scientists. They have started to monitor the available water at the spatial and temporal scale of reservoirs through hydrological observations (Alsdorf, 2007). Water resources management and planning are essential for countries with water scarcity to secure water to meet various demands (e.g., drinking, irrigation, domestic use, livestock watering). To monitor the water levels of rivers, oceans, many satellites data are available presently, e.g., National reference point of water level, SARAL-AltiKa, radar altimetry, Hydrologie par altimétrie spatiale, Global Monitoring for Environment and Security (GMES), Envisat/RA-2. Several studies were conducted to find the water level using different satellite images (Maillard et al., 2015; Jiang et al., 2017).

Space born radar altimetry is widely used to study and monitor surface water levels (Song et al., 2015; Crétaux et al., 2016). It has become a helpful tool as a data source for monitoring the variations of surface water, which otherwise cannot be accessed.

The storage of water bodies is derived by water budgeting of various parameters (precipitation, transpiration, evaporation) and studying the interaction between surface water and groundwater (Medina et al., 2010). The reservoir capacity can also be

estimated based on morphometric and aerial data (Shanlong et al., 2013). The Geoinformatics approach is widely used as a new technique to monitor and assess the water level, surface area, and capacity of the water bodies. Gleason et al. (2007) developed a model from surface area-capacity relationship using field survey (GPS) data. Lane and D'Amico (2010) calculated the water storage capacity of wetlands. Landsat, Sentinel-2 among other satellite images, were used in different studies to determine the NDVI or NDWI for wetland detection (e.g., Behera et al., 2018; Valderrama-Landeros et al., 2018).

The area (*A*), depth (*H*), and volume (*V*) of the reservoir were estimated in many studies by different methods and techniques. Vegetation indices and mathematical shape models are the main methods (Minke and Westbrook, 2010; Jiang et al., 2015). Jiang et al. (2015) investigated the water depth through the *A*-*H* relationship using multi-spectral satellite images from the ETM+ sensor from Landsat 7 satellite. Based on the characteristics of visible and infrared spectra, models were developed to estimate the depth of the water body. The relation between water storage and the surface area of the reservoir was determined from the synchronized observations. Minke and Westbrook (2010) carried out a study to assess the *A*-*V*-*H* relations for a reservoir. However, the accuracy of this method to estimate the area and water storage depends on the availability of the detailed survey data (Waiser, 2006).

In recent decades, multispectral remote sensing study has become a priority application technique for estimating the capacity and sedimentation of reservoirs. Changes in sediment transportation focus due to sediment trapping at various points (Kummu and Varis, 2007). Human activities play a significant role in natural

sedimentation, while reservoir construction can change the sediment flow and river morphology (Kummu and Varis, 2007). About 0.5 - 1% of reservoir capacity is lost every year because of incoming sediment (Walling, 2006) generated through soil erosion (Keller et al., 2000).

Vegetation indices are a combination of two or more bands that can be used to detect the surface water boundaries (Qiao et al., 2012). Image classification of remote sensing datasets usually depends on human knowledge and interpretation and is generally hard to produce or extract land surface water information (Ouma and Tateishi, 2006). But, vegetation indices can easily extract quick and accurate land surface water than image classification (Li et al., 2013). The NDVI and NDWI are the standard indices used for this purpose (McFeeters, 1996). Moreover, the modified NDWI shows its ability to extract highly accurate surface water boundaries (Xu, 2006; Li et al., 2013; Feyisa et al., 2014).

McFeeters (1996) introduced normalized difference water index (NDWI) for extracting the boundary between water bodies and soil using multi-spectral images (near-infrared and green bands interaction). Later, Xu (2006) had enhanced the NDWI using short-wave infrared (SWIR) instead of using near-infrared (NIR) band and renamed the index to be modified NDWI. Ouma and Tateishi (2006) proposed a new index to delineate the water bodies by incorporating NDVI with Tasseled Cap Wetness (TCW) index. Water boundaries were extracted using these indices from Landsat, Moderate Resolution Imaging Spectroradiometer (MODIS), Système Pour l'Observation de la Terre (SPOT), Advanced Spaceborne Thermal Emission and Reflection Radiometer

(ASTER), and HJ-1A/B data (Rogers and Kearney 2004; Xiao et al. 2005; Sivanpillai and Miller 2010; Lu et al. 2011; and Zhang et al. 2011).

2.4 Trend analysis

Trend Analysis is commonly used to detect the changes or variations in climatic, meteorological, and hydrological observations (McCabe and Wolock, 2002; Miller and Piechota, 2008). Numerous studies have been discussed detecting the trend of climatic, meteorological, and hydrological variables by using various methods (Mann, 1945; Yevjevich 1972; Kendall, 1975; Kottegoda 1980; Hirsch et al., 1982; Lettenmaier et al., 1982; Schertz et al., 1991; Reckhow et al., 1993; von Storch, 1995; Gauthier, 2001; Zhang et al. 2001; Burn and Elnur, 2002; Libiseller and Grimvall 2002; Onoz and Bayazit 2003; Huth and Pokorn, 2004; Kahya and Kalaycı 2004; UN 2004, 2012; Pujol et al. 2007; IPCC 2007, 2008; Kumar et al. 2010). For example, the trends of precipitation, temperature, runoff, streamflow, and water quality parameters (e.g., pH, chemical oxygen demand (COD), dissolved oxygen (DO), and nitrate) were detected using parametric and non-parametric methods (Burn and Elnur 2002; Hrynkiw et al., 2003; Ravichandran, 2003; Sun et al., 2013).

Several researchers have performed the trend analysis of climatic and hydrological data using different methods such as Mann–Kendall (M-K) trend analysis (Chattopadhyay et al., 2012; Kisi and Ay, 2014; Kisi, 2015; Ay and Kisi, 2015), Innovative Trend Analysis (ITA) (Sen, 2012; and Sanikhani et al., 2018), and linear regression (Atilgan et al., 2017). In all these methods, the historical data are collected and studied sequentially at regular intervals, such as hourly runoff readings, daily temperature and weekly rainfall volume (Peña et al., 2001). The trend analysis can further be

classified as parametric and non-parametric methods such as linear regression, Mann-Kendall test, Sen's Slope estimator, Spearman's Rho test, and Artificial Neural Network (ANN) (e.g. Mann, 1945; Kendall, 1975; Plessis, 1999; Maragatham, 2012; Borges et al., 2014; Palizdan et al., 2014; Ay and Kisi, 2015; Amiratae et al., 2016; Hu et al., 2016; Chowdhury and Sen, 2017; and Meshram et al., 2017).

The forecasting in hydrological time series data has excellent relevance due to its applications in water-resources management and other fields such as environment, water-planning projects (Mohan and Vedula, 1995; Wang et al., 2009; Zhang et al., 2011; Eni and Adeyeye, 2015; Wang et al., 2015; Narasimha Murthy et al., 2018 and Rizeei et al., 2018). Moreover, precipitation forecasting prioritises other climatic and hydrological parameters directly affecting water use (Sun et al., 2018).

2.5 Hydrological modelling based on SWAT model

Soil and Water Assessment Tool (SWAT) was used to model the rainfall-runoff of the watershed. The SWAT model is a result of experiments over the years carried out by USDA Agricultural Research Services by integrating earlier models for Runoff, Erosion, and Chemicals from the Groundwater Loading Effects on Agricultural Management Systems (GLEAMS) model, the Environmental Impact Policy Climate (EPIC) model, and Agricultural Management Systems (CREAMS) model (Knisel, 1980; Leonard et al., 1987; Izaurralde et al., 2006). However, this model is closely related to the Simulator for Water Resources in Rural Basins (SWRRB). SWRRB model was explicitly used to simulate sediment and water movement for different soil management practices.

2.5.1 Hydrologic modelling studies

SWAT model can be used as a hydrologic balance. There are several reports on the hydrologic calibration and validation in streamflow and other components of hydrologic balance. Earlier reports contained many applications of the SWAT model. Arnold et al. (1996) validated the SWAT model in Illions for surface flow, groundwater flow, and evapotranspiration of the water component in three watersheds. In a similar study by Santhi et al. (2001), this model was validated successfully for a larger watershed in Texas for different water balance components, e.g., surface flow and baseflow. Arnold et al. (1999) validated streamflow in watersheds in Texas using a large number of stream monitoring gauges.

Further, in northern Mississippi reports this model was validated for streams from multiple sub-basins based on daily and annual observations by Bingner (1996). In Texas, Srinivasan et al. (1998) validated this model successfully for a watershed with a limited period of data.

2.5.2 Sediment modelling studies

SWAT is also a helpful tool for simulating sediment deposition and has been widely used to model many watersheds worldwide. In a study in the North Bosque River in north Texas, Saleh et al. (2000) applied this model to evaluate sediment load. They found that the simulated results were similar to observed sediment load based on monthly data. On the other hand, the results obtained by the SWAT model on a daily scale were not so satisfactory. Another study by Santhi et al. (2001) successfully simulated sediment deposits at different time scales in two sub-watersheds in Bosque River, Texas.

2.5.3 Uncertainties methods

Based on the Bayesian approach, numerous uncertainty analysis methods are established to be used in hydrological modelling. These methods can be categorized into three major groups. According to Yang et al. (2008), these methods are classified as a) all uncertainties given by uncertainty parameter [Sequential Uncertainty Fitting Version-2 (SUFI-2); Generalized Likelihood Uncertainty Estimation (GLUE)]; b) the input and model structural uncertainty considered implicitly by introducing an additive error model (Beven and Binley, 1992; Abbaspour et al., 2007; Ajami et al., 2007; Huard and Mailhot, 2008; Reichert and Mieleitner, 2009; Laloy et al., 2010; Schopus and Vrugt, 2010) c) the input and model structural uncertainty considered explicitly by using the time-dependent stochastic parameters; multiplicative input error model; additive input error model; Sequential Data Assimilation (SDA) method. This section briefly discusses SWAT-CUP application and different types of uncertainty analysis in hydrological modelling combined with the SWAT model (Arnold et al., 1998).

Many researchers used the SWAT model in their studies (e.g. Duru et al. 2017; Liu et al. 2019; Wang et al. 2019). Different investigations were concluded with different results. Some researchers concluded that the SWAT model gives good results for simulating the streamflow and estimating sediment yield (e.g. Duru et al., 2017; Ezz-Aldeen et al., 2018; Liu et al., 2019); other researchers (e.g. Uzeika et al. 2012) concluded unsatisfactory results.

2.6 Drought analysis

Drought is an unavoidable and periodic event of the water cycle, affecting different sectors, e.g., societal, economic, and ecologic (Hielkema et al. 1986; Marengo et al.

2011). For drought analysis, the essential step is to define the underlying parameters (Dracup et al., 1980). The drought affects hydrological, meteorological, and agricultural balance. Numerous drought indicators were developed and modelled to state the drought condition at a particular place. In the following section, some of the studies have been discussed.

Thus, researchers often restore to several approaches and techniques to gain insight into the drought phenomenon in an attempt to characterise drought. These approaches can be as simple as using one or more variables that may have caused drought. Either way, the drought indicator obtained is a better way of communicating drought characteristics in an area (Mishra and Singh 2010; Oertel et al. 2018). McKee et al. (1993) established a standardized precipitation index (SPI) to determine the drought based on precipitation time series data. Nury and Hasan (2016) discussed the drought conditions based on the only SPI, and they tried to analyze the trend and pattern of rainfall in northwestern Bangladesh.

However, drought is a multivariate phenomenon, and its effects exhibit multi-dimensional characteristics. Droughts, as a phenomenon, are found to be influenced by local geography, soil parameter and vegetation, and these factors affect its development and localized severity. The simple indices that depend on one variable to define the drought in an area are usually difficult to capture the drought onset and terminus (Hao and AghaKouchak 2013; Zhu et al. 2018). Recently, several studies have proposed various techniques to combine different drought variables (e.g., precipitation, streamflow, soil moisture). In these studies, the method to integrate the variables is different so that drought is decomposed into the predominant variable. Each selected procedure also has

its limitations in its application and gives a further scope of improvement in the methodology. Huang et al. (2015) proposed an integrated method using a nonparametric multivariate drought index and combined meteorological and hydrological drought information. Rajsekhar et al. (2015) combined meteorological, hydrological, and soil moisture to develop a multivariate drought index. Kwon et al. (2019) studied the drought characteristics in South Korea by combining the meteorological and agriculture drought using the cupola family. They grouped the HDI by using the hierarchical agglomerative clustering approach for classifying regional patterns. This study used the copula probability family to build an integrated drought index to assess drought and flood extremes. Drought and floods as two weather extremes have often been studied with similar techniques. Numerous studies have used multivariate concepts, including a couple of approaches for flood analysis in an area (e.g., Favre et al., 2004; Zhang and Singh, 2006; Jongman et al., 2014). The atmospheric blocking was one of the most important parameters associated with extreme weather events such as drought and flood, as studied by researchers (Scherrer et al., 2006; Sillmann and Croci-Maspoli 2009). Lonita (2014) has studied the flood in Europe, combining different variables such as precipitation, soil moisture, and water lever using multiple linear regression models to predict the streamflow of the Elbe River.

Copula probability family has been observed to have specific limitations, such as the data is required to follow a probability density function to use this technique (Huang et al., 2014). A model structure lacks flexibility where more than three variables are integrated (Rajsekhar et al., 2015). There is a possibility of negative values of the integrated index to occur (Erhardt and Czado, 2018). According to Real-Rangel et al.

(2020), using the copula family to build an integrated drought index shows severe deficits. When variables are more than one, then it can marginally detect drought conditions.

Zhu et al. (2018) proposed an integrated hybrid drought index based on the entropy weight method and a fuzzy set theory combining metrological, hydrological, and agriculture information. The entropy method under normal conditions is used to determine the subjective and objective weight while exploiting the entire original data. Now, since it cannot reflect experts and decision-makers knowledge, it has the disadvantage of causing large fake weights (Roodposhti et al. 2016). Zhao et al. (2017) proposed the F-AHP method to determine the objective weight, reflecting the knowledge of experts and decision-makers. A fuzzy approach has several other advantages: the boundaries that separate the index categories are fuzzy by integrating the variables as an index (Wilhite and Glantz, 1985). The variable fuzzy set theory can characterize vague phenomena and capture their dynamics to better arrive at a hybrid drought index. Huang et al. (2015) and Zhu et al. (2018) successfully applied fuzzy set theory combining meteorological, hydrological, and agriculture factors and proposed an integrated drought index (IDI). However, in these studies, the results of IDI were compared only with SPI and Standardized Streamflow Index (SSFI), regardless of any information about soil moisture or its related drought indicator.

Different studies have reported the water supply and drought conditions in Jordan. Tarawneh (2011) discussed the water supply in Jordan under drought conditions and showed that Jordan is under water stress even during rainy seasons (October to May). Törnros and Menzel (2014) addressed the drought based on precipitation,

evapotranspiration, and NDVI and found that the drought will increase the irrigation water demand for the agriculture sector in Jordan valley. Recently, Rajsekhar and Gorelick (2017) investigated the drought conditions in the Jordan valley under current and future climate change conditions. In their study, precipitation, streamflow, and soil moisture were used. Based on the historical data, they concluded that the drought condition would be more severe in the future. Mohammad et al. (2018) discussed the impact of natural conditions on drought events in the Yarmuk Basin on the northern side of Jordan. The study compared the SPI and standardized water level index (SWI). Gilbert (2017) found that the drought frequency in Jordan is increasing; almost double winter droughts were observed from 1961-2010 compared to 1901-1960. The future prediction says that there will be an increase in temperature and a decrease in precipitation trends during the winter season (Shakhatreh, 2010, Al Balasmeh et al., 2019).

2.7 Soil erosion and management based on experimental studies

Land use and land cover (including vegetative covers) have a significant role in soil and water conservation management, as it directly affects the hydrological cycle (surface runoff, evaporation, filtration), water quantity (Wang et al. 2014), and groundwater recharge (Kader et al., 2017). Soil and water conservation have been studied by many researchers in the field and at a laboratory scale. However, in situ soil erosion requires 20-25 years of observation to achieve reliable data on land changing due to different intensities of natural rainfall (Wischmeier and Smith, 1978). Scanlon et al. (2005) studied the effect of the natural vegetation on soil conservation, groundwater recharge and water quality in the southwestern part of the USA. Apart from this, the waste disposal from agriculture, e.g., straw, dry leaves, is a severe issue of the water deficit regions as people

typically burn these materials causing air pollution. These materials can be effectively used for bare soil covers solving both: disposal and air pollution issues. In addition, it also conserves soil nutrients. Adekhlu et al. (2007) reported that covering soil using waste agriculture material is an effective method of conserving water as it reduces surface runoff and increases infiltration rate.

The studies of overland flow in arid to semi-arid regions are vast due to several variables (e.g. rain, natural rain and its intensity, raindrop size and energy, and spatio-temporal distribution). Due to this, the rainfall simulator provides good information in less time at laboratory and field scales. Marston (1952) found that vegetation cover had reduced more than 65% of surface runoff and increased the infiltration into the soil as groundwater recharge in the experimental setup at the laboratory. Wang et al. (2014) used rainfall simulators to study the impact of different parameters on soil moisture after the storm. They found that the moisture yield in soil with vegetation cover is more significant than bare soil. This moisture yield is considered an essential factor for determining the recharge coefficient.

Further, recent studies reported that the laboratory's small-scale plots could be used to estimate the large-scale plots under similar rainfall conditions (Schindewolf and Schmidt, 2012). This information allows us to compare various soil conditions, rainfall, and environments (Martínez-Murillo et al., 2013). Nevertheless, rainfall simulator requires calibration to estimate the accurate runoff as natural raindrop sizes and its energies.

In simulated rainfall experiments, the overland flow and sediment play a significant role in analyzing the soil erosion mechanism, where it is used to monitor the

hydrological processes (Helming et al., 1998; Römkens et al., 2002). The overland flow curve depicts a rising inflow at the starting of the experiment; after a time, the curve will be steady. In contrast, the sediment curve begins to drop up to some extent and then remain constant. These curves are mainly affected by natural and human factors, like soil type and properties, rainfall, and vegetation cover (Huang and Lee, 2009; Pappas et al., 2008; Rai et al., 2010).

Irrespective of geographic location, the arid to semi-arid regions are characterized by particular vegetative cover and climatic conditions. In these regions with a water shortage, some plants can face a shortage of water, e.g., cactus, mesquites, bushes. (Valles-Septién et al., 1998; Nobel, 1998). Normally these vegetations are spatially distributed and recognized as strips of shrubs and grasses (Aguiar et al., 1992; Aguiar and Sala 1994; Facelli and Temby, 2002).

All these methods are controlled by the landscape and vegetation cover (Ridolfi et al., 2008). These lands are easily breakable and usually subjected to desert areas (UNCCD, 2004). In most fertile lands, the erosion and overland flow sealing decreases compared to barren land due to the vegetation-covered regions that protect the land from eroding and improve the soil's physical, chemical and biological properties (Casermeiro et al., 2004). Many studies gave importance to semiarid patches of vegetation that impact soil's physical, chemical and biological properties (Puigdefábregas, 2005; Bautista et al., 2007). Limited research has been carried out on the interaction between soil mechanism, land-use, and overland flow at arid to semi-arid regions (Chen et al., 2007; Bautista et al., 2007).

The literature studies show that researchers have addressed different methods and techniques for studying various watershed issues concerning water availability. There are no general recommendations on a technique, which will be most suitable for a location.

2.8 Research Gaps

The gaps in the research found from the studies as mentioned earlier are thus summarized as:

- Several studies were carried out to evaluate the derived hydrological parameters and streamflow simulation using available digital elevation models (DEMs). For example, Zhou et al. (2012), Frey and Paul (2012), Vaze et al. (2010), Bourgine and Baghdadi (2005), Hirano et al. 2003, Kenward et al. (2000) studied the hydrological parameters and DEM accuracy in a catchment. However, these accuracies are site-specific and need to be accessed locally. In Jordan, no study was carried out to assess the accuracy of the low-resolution open-source and high-resolution paid DTM/DEM data and methods to improve the accuracy of the open sources DEM data and validate it based on hydrological parameters and streamflow.
- The parametric analysis (as regression) was used in few studies in Jordan; mainly (Ghanem 2011 and 2013) discussed trends in mean seasonal and annual rainfall with its prediction using fundamental statistical analysis. Al-Taani (2014) studied the trend analysis of water quality and found a correlation among these parameters in the Al-Wahda dam of north Jordan, while Abu Sada et al. (2015) addressed the effect of climate change on the temperature and annual precipitation. While other studies by Smadi and Zghoul (2014), the change in

rainfall in the Amman (capital of Jordan) was addressed using parametric and non-parametric analysis (as a Mann Kendall (MK) rank test) during 1938-2002. These studies used either a parametric test (linear correlation) for trend analysis and forecasting process or a non-parametric test (MK rank test) in a large study area with stations distributed only in the vicinity of the study area. So in the previous studies, the scale of the trend through long-term data analysis was not addressed in the water-stressed area of Jordan valley.

- Many researchers have studied soil erosion in the field or at a laboratory scale. Kertesz et al. (2004) studied the effect of the *K* factor on soil erosion. Olivares et al. (2011) used a physical soil erosion experiment. Sobol et al. (2017) studied the effect of rainfall intensity and slopes steeply on soil erosion. A few experimental studies on soil erosion have been conducted in Jordan, such as Al Qaeda et al. (2015) studied the recharge rates in arid areas using a field experiment. However, there is a lack of study investigating the effects of organic soil cover on overland flow, soil erosion, infiltration, and groundwater recharge. Moreover, there is no equation available that can be used to quantify the reduction of soil loss using organic cover

2.9 Research Objectives

This study aims to perform hydrological modelling to propose management intervention for augmenting reservoir capacity in the study area. This study will be fulfilled by archiving the following objectives:

1- To generate Ortho-photo and derive high accuracy digital terrain model using aerial photos by photogrammetry techniques and compare the hydrological parameters from DTM with available DEM using visual and statistical methods,

2- To perform trend analysis for hydrological and rainfall-runoff modelling for the watershed by properly calibrating and validating the model.

3- To propose land cover management practices to reduce the soil erosion from the catchment.

Chapter 3: Study Area and Data Collection

3.1 Introduction

This chapter discusses the details of the study area of the present work. The study area includes the space for the dam site under consideration, i.e., the Wadi Shueib dam and its catchment and the locations for DEM data validation and reservoir bathymetry model validation. This chapter also summarizes the various data collected during the study and analyses those data for a detailed understanding of the hydrological behaviour of the catchment and its management for reservoir augmentation. It includes the climatic data (e.g. precipitation, temperature) and remote sensing data (satellite images and aerial photography).

Due to the scarcity of qualitative and quantitative data and the topography, Wadi Shueib has a challenging research environment. Wadi Shueib is located between high attitude lands in the east and Jordan valley in the west. This catchment area is close to Amman and Salt city (East part), making the catchment an exciting area to many researchers and academic campaigns. The climate in the catchment varies from the Mediterranean climate on the Upper East Side to the arid to semi-arid climate on the western side. The arid to semi-arid climate covers most of the catchment area, including the Wadi Shueib Dam area (for details, see section 3.2). The Wadi word is originally an Arabic word meaning valley and describes a dry river bed. This valley gets water only during the rainy season. Wadi Shueib is also crucial for agricultural land downstream of the Jordan valley of the Wadi Shueib Dam. Hence comes the need to maintain the capacity of the dam for its agricultural activity.

The Wadi Shueib catchment is chosen for two major reasons. As discussed, the Wadi Shuieb dam faces a sediment deposition issue from the eroded soil from its catchment area. Secondly, rapid urbanization is leading to an increase in water needs shortly. Due to these reasons, the water situation in Wadi Shueib can be considered an issue to be addressed by the Jordanian Water Strategy.

3.2 Geographic Overview of Wadi Shueib Catchment

The study site is located in the eastern part of Jordan Valley and west of the salt city in Jordan (Fig. 3.1). Wadi Shueib (also: Shu'aib, Shoeib) is a sub-basin area of the Lower Jordan River Basin in the Balqa governorate (west of the capital Amman) (LJRB) and lies between 31° 50' - 32° 02'N and 35° 35'- 35° 50' E, covering an area of ~180 km^2. The outlet of the sub-basin is the Shueib dam, which is used to cater to the needs of water for irrigating the agriculture fields in Jordan valley. The area has a steep slope with an elevation ranging from 200 m below mean sea level (b.m.s.l) at Jordan valley to 1200 m above mean sea level (a.m.s.l.) near Salt City.

3.2.1 Climate

In the Wadi Shueib catchment, the climate conditions vary with topographic variations from arid at Jordan valley to the Mediterranean climate in the Northside at high attitude lands (orographic effect). The Mediterranean circulation significantly impacts the region, i.e., hot with no rainfall events during summer months. The climate during the winter months is affected by the eastern Mediterranean climate, in which rainfall occurs with low pressure and southwest wind. The upper catchment area of Wadi Shueib has a dry Mediterranean climate, while the lower catchment (near the Dead Sea) is an arid region (Werz 2006). Precipitation as rainfall generally occurs from October to March in

this catchment. The maximum annual rainfall exceeds 500 mm (44 % of the recorded years) at the northern high altitude lands. At the same time, it decreases towards the Jordan valley, where annual precipitation is below 450 mm (67 % of the recorded years). This analysis is carried out based on spatial interpolation of long term annual average precipitation.

The average temperature in the catchment is ~12 °C in January and ~30 °C in July and August. The variations were observed in average monthly precipitation and temperature using long-term datasets from two high altitude gauging stations situated at Jordan valley of Wadi Shueib (Fig. 3.1). Please refer to Appendix-A for more details.

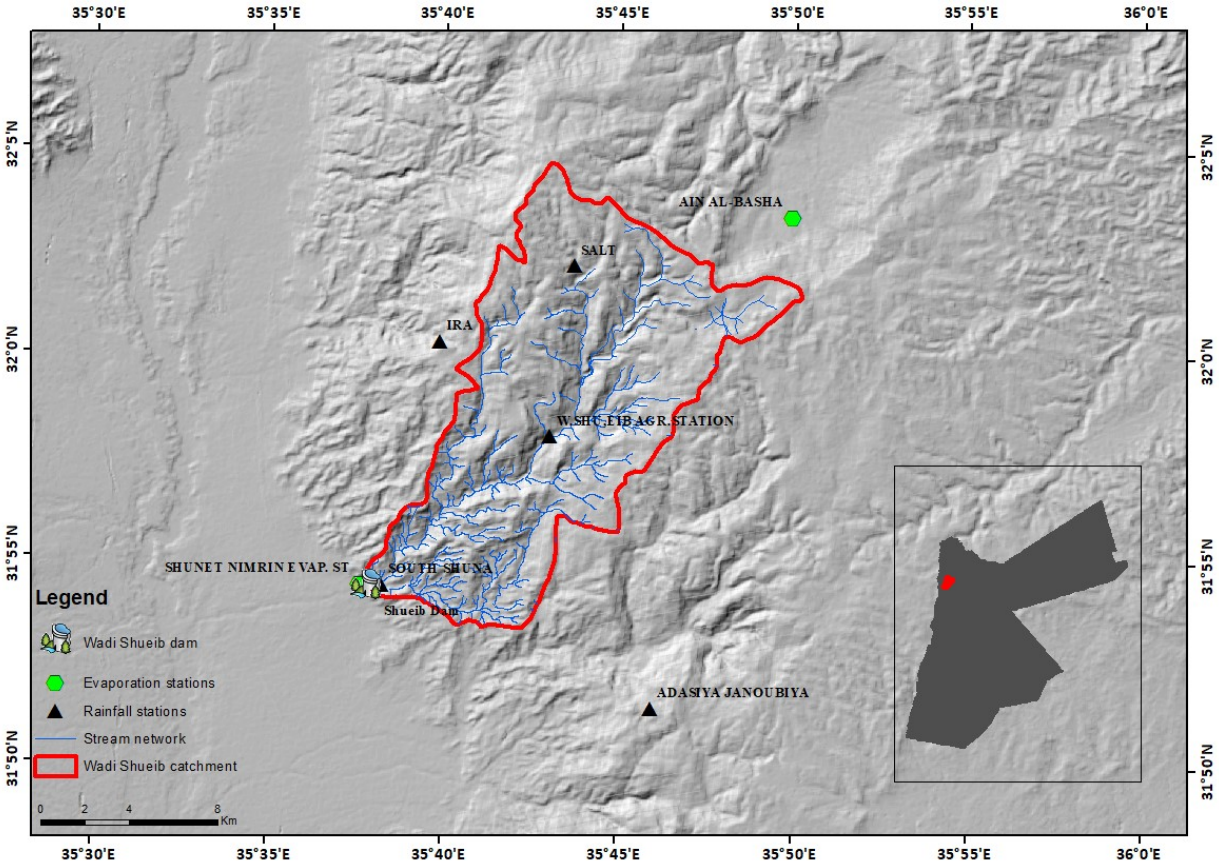

Fig. 3.1 Location map of the Study Area

3.2.2 Soil and Vegetation

A variety of soil can be found in this catchment. However, the majority of the area is covered with sandy soil. Although some natural vegetation grows during the spring season, the site has mainly bare soil characteristics. The upstream region contains a high percentage of clay (Clayey Loam), making this soil suitable for agricultural activities. Usually, clayey loam includes a good quantity of plant nutrients and supports most plants and crops. The area is endowed with trees, bushes, and vegetation. The most common plants/trees found in the catchment are almond, oleander, and Retama. Vegetation (grass) usually grows on the drainage banks, and these areas are not suitable for agriculture.

3.2.3 Geology

3.2.3.1 Geological Setting

Geological characteristics of the Wadi Shueib catchment area were studied in detail by various researchers, e.g., Werz (2006), Hahne et al. (2008), and Sahawneh (2011) (Fig. 3.2). The following geological maps (1:50,000) and reports were collected from the National Resources Authority of Jordan covering the study area:

i. As Salt – 3154-III (Kahlil, 1993)
ii. Karama – 3153-IV (Shawabkeh, 2004)
iii. Suwaylih – 3154-II (Barjous, 1993)
iv. Amman – 3153-II (Diabat, 2004)

Various taxonomies and classifications describe stratigraphic units of the areas (e.g. (Masri, 1963; Parker, 1970; Bender, 1974; Andrews, 1992).

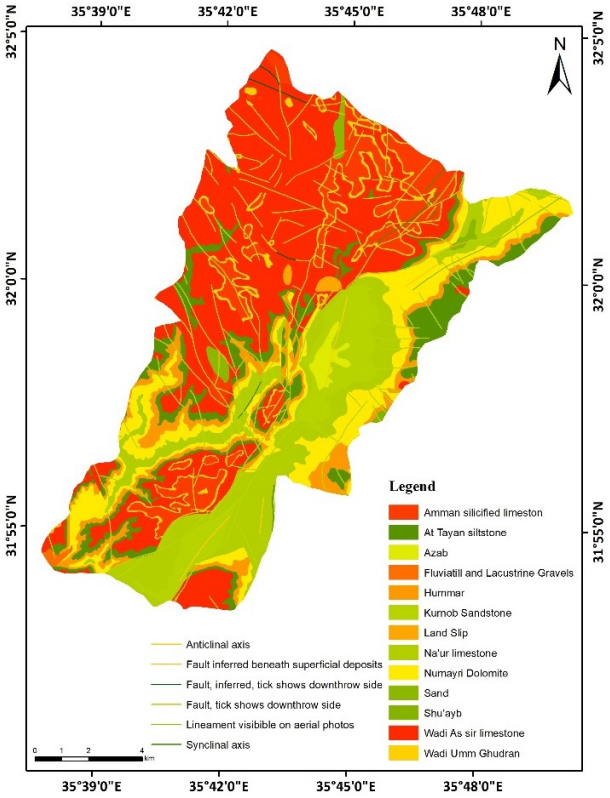

Fig. 3.2 Geological map of the Wadi Shueib catchment Stratigraphy of the Study Area

The Wadi Shueib catchment is mainly composed of sedimentary rocks according to the stratigraphical taxonomy of the National Resources Authority (NRA) of Jordan (Upper Cretaceous Age Albian to Maastrichtian). This sedimentary rock is based on each era and group of a specific rock type exposed. For example, marls, dolomites, and limestones were exposed at Ajloun and Belqa Groups from Late Cretaceous Subperiod, whereas the sandstones were exposed at the Kurnub Group from the Lower Cretaceous age (Mikbel & Zacher, 1981; Salameh, 1980; Bender, 1968a). Fig. 3.2 shows the stratigraphic units in the Wadi Shueib catchment. The thickness of limestones, marly limestones, and dolomitic limestones in the Ajloun Group varies between 350 to 400 m.

3.2.4 Hydrology

3.2.4.1 Drainage and Streamflow

The drainage density is usually connected with rainfall, lithological infiltration capabilities, and topographic characteristics, which gives a specific and preliminary indication of the precipitation. In turn, the rain is converted into the overland flow (Gregory & Walling, 1976; Schumm, 1977). The drainage density (D_d) can be expressed using the following equation (Eq. 3.1) as proposed by Horton (1932):

$$D_d = \frac{L_s}{A_b} \tag{3.1}$$

where A_b represents the drainage basin, and L_s is the length of stream channels.

High drainage density can indicate high overland flow, high flood peaks, and increased sediment transport, while low density indicates high infiltration rates (Singh, 1989).

In semi-arid regions, the drainage density can be found to vary from ~1 to more than 600 km/km² (Gregory & Walling, 1976). In the Wadi Shueib catchment, the drainage density was 1.13 km/km², considered moderate compared to other carbonate drainage areas (Segura et al., 2007). Major streams in the Wadi Shueib catchment are connected to the mainstream. During the rainy season, these stream networks collect the overland flow and feed the main channel, thus ultimately reaching the dam (Fig. 3.3).

Table 3.1 Stratigraphy of Wadi Shueib catchment area

Late Cretaceous	Campanian	Balqa(*or:Belqa*)	B2b	Al Hisa Phosphorite	Phosphorite beds, with layers of chert, limestone and silicate limestone	10-15 m
			B2a	Amman Silicified Limestone	Silicified limestone and massive cherts	40-60 m
	Santonian		B1	Wadi Um Ghudran	Chalk and marlstone, (some marly limestone)	40 m
	Coniacian	Ajlun	A7	Wadi Es Sir Limestone	Massive limestone banks and dolomite limestone, (Chert), marly limestone	80-150 m
	Turonian		A5/6	Shueib	Marly limestone, Chalky limestone, nodular limestone, marls	80 m
			A4	Hummar	limestone, dolomitic limestone, dolomite, (merly interbeds)	40-65 m
	Cenomanian		A3	Fuheis	Mari, calcareous siltstone, nodular limestone, marly limestone	50-80 m
			A2	Na'ur	Limestone and marl overlain by marly limestone. Dolomitic nodular limestones towards the top.	90-200 m
					Limestone and dolomite with interbedded marly, sandy facies towards the base.	
			A1			
Early Cretaceous	Albian	Kurnub	K2	Subeihi	Massive, cross-bedded varicoloured sandstone, siltstone layers towards the top.	150-350 m
	Berriasian		K1	Aardo	Cross-bedded medium to coarse-grained white, pale, yellow and pink sandstone.	
Jurassic	Oxfordian	Zarqa Group	Zarqa Group Z2	[Mughanniya],[Hammam], [Ramla], [Dhahab], [Silal], [Nimr], [Hihi]	Sandstone, limestone, dolomite, marl and clayey siltstone	50-400 m
	Hettangian					
Triassic	Norian		Z1	[Umm Tina], [Iraq el Amir], [Mukheiris], [Hisban], [Suwayma]	Shales, siltstone, sandstones, marl, limestone, dolomite, oolithic limestone and evaporites. No outcrops in Wadi Shueib area	250-500 m

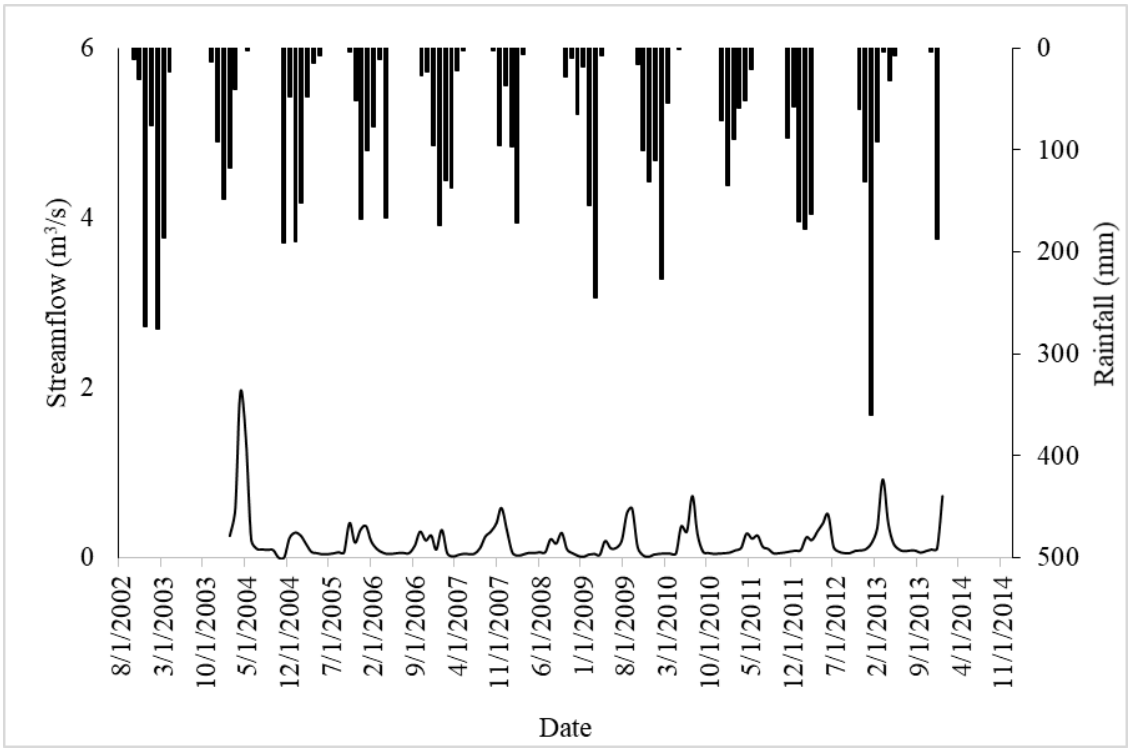

Fig. 3.3 Recorded rainfall and inflow at the Wadi Shueib reservoir

3.2.5 Reservoir

Excess rainfall (direct runoff) is mainly stored in the Wadi Shueib catchment area outlet at the Wadi Shueib Reservoir outlet's outlet. The dam was constructed and prepared to hold 2.4 Mm^3 water but presently has only 1.4 Mm^3 storage capacity due to deposited soil at the dam base. The water stored in the reservoir is also used for groundwater recharge; the water pumped through wells is later used for agriculture purposes for Jordan valley lands. Thus, the Wadi Shueib dam is used as a runoff surface storage and an artificial groundwater recharge.

Fig. 3.4 shows the variations in water storage of the Wadi Shueib dam. During the rainy season (October-May), the dam reaches the peak storage, while during summer (June-September), the dam usually remains empty. The outflow from the dam is utilized

for agriculture purposes using a channel and serves ~ 250 ha downstream of Jordan valley. With regards to the water rights, each farm gets this water free of charge

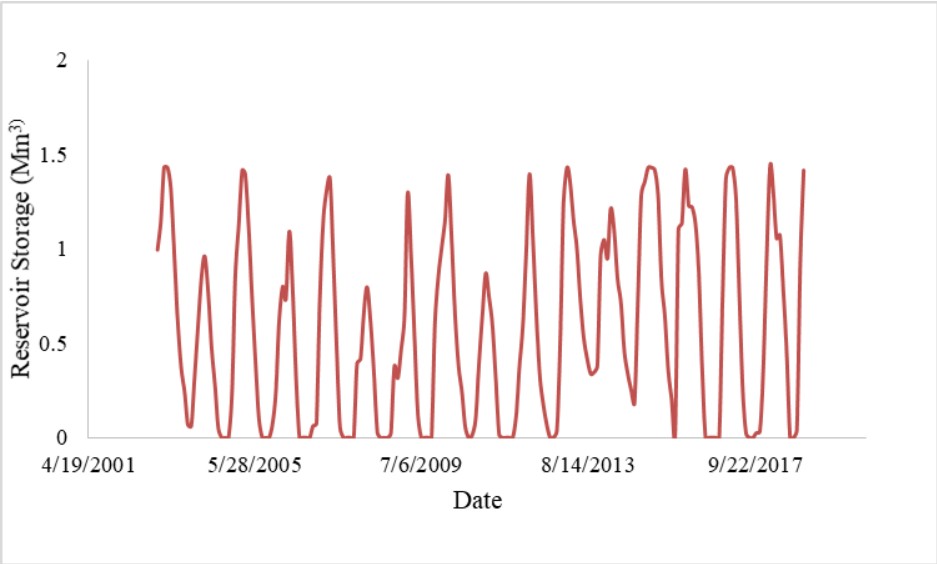

Fig. 3.4 Observed water storage at Wadi Shueib reservoir

3.2.6 Land Use and Land Cover

Wadi Shueib catchment has variable land use land cover. Rain-fed and irrigated agriculture dominate the high-altitude lands on the north-eastern part, while along the mainstream, the pastures are growing during spring months (Fig. 3.5). At the upper part (north-eastern), forest land use dominates a small area of the catchment. The remaining area is dominated by high population density at As-Salt city (Fig. 3.5). Towards the downstream near the dam (southern part), there are less population density and almost no vegetation, as bare rocks with or without a thin soil layer are present in this part (Fig. 3.5).


(a)


(b)


(c)

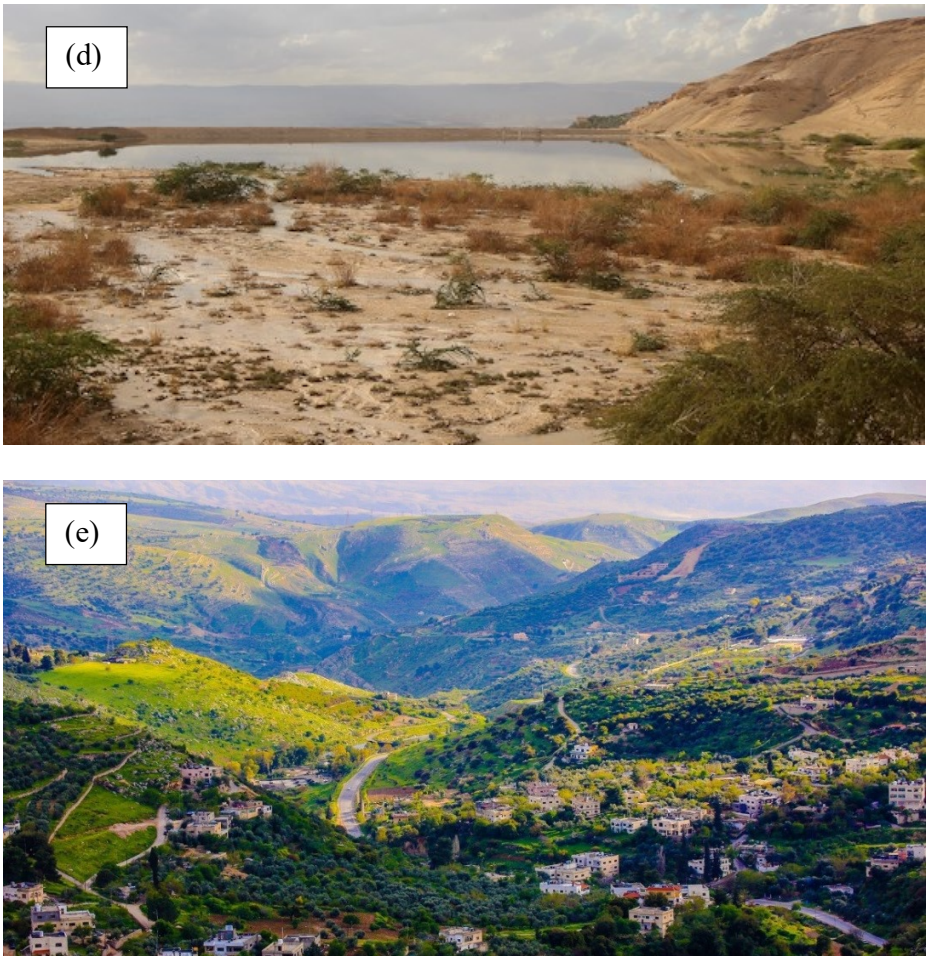

Fig. 3.5 **(a)** Agricultural area at the high elevation lands, **(b)** low vegetation cover in the middle of the catchment, **(c), (d)** bare rocks and thin soil cover onwards to the Dam, and **(e)** high population density at the upper part

The significant population and industrial activities are concentrated at the catchment's high attitude lands (north-eastern part). Wadi Shueib catchment is mainly divided into five municipalities. Table 3.2 Demographic development in Wadi Shueib catchment areashows the total population in these municipalities in 1994, 2004, and 2018, with an annual average increase rate found to vary between 2.33 and 3.22%. The rate of population growth is due to a local cement factory in Fuheis city.

Table 3.2 Demographic development in Wadi Shueib catchment area

Year	As-Salt (Sub-District)	Mahis	Fuheis	Ira & Yarqa	Wadi Shueib total
1994	56458	8000	10098	6319	80875
2004	77441	10649	11641	8654	108385
2018	114350	19173	20427	12030	165980

3.2.7 Water Supply

The primary water demand in the Wadi Shueib area is for municipal drinking water. It is provided through groundwater (springs and wells). The municipalities receive the pumped water, which is then stored in underground reservoirs. According to the Ministry of Water and Irrigation, Jordan (2004), the average water consumption per person in the Balqa Governorate was estimated from the volume unit provided by the Water Authority of Jordan as 86 l/d for domestic uses and 24 l/d for non-domestic municipal uses. Thus an increase in population contributes to a supply deficit in the catchment, which has forced households to buy additional water from private sectors.

3.2.8 Site for Digital Elevation Model Analysis

The digital elevation model analysis was conducted in the eastern part of Jordan valley near As-Salt city in Jordan (locally known as Humrat Es-Sahen). The site was chosen based on the availability of aerial photography data. The high-resolution aerial data is very costly and was not available readily at the reservoir site, so the DEM assessment was done in this location. Humrat Es-Sahen lies between 35˚36.8' to 35˚42.2' *E* and 32˚04.7' to 32˚07.5' *N*. This area has an elevation range from 1300 m (a.m.s.l) near of As-Salt city, to 200 meters (b.m.s.l) in Jordan valley. The slope in the area is steep and sharp, which makes the field survey very difficult. When rainfall and snowfall occur in the

winter season, the water starts flowing into the streams from east to west due to its topography (Fig. 3.6). Another site was selected north of this site to verify the results and is locally known as Jabal Ajlun. Jabal Ajlun lies between 35˚ 43.1' to 35˚ 44.1' *E* and 32˚ 19.4' to 32˚ 20.0' *N*.

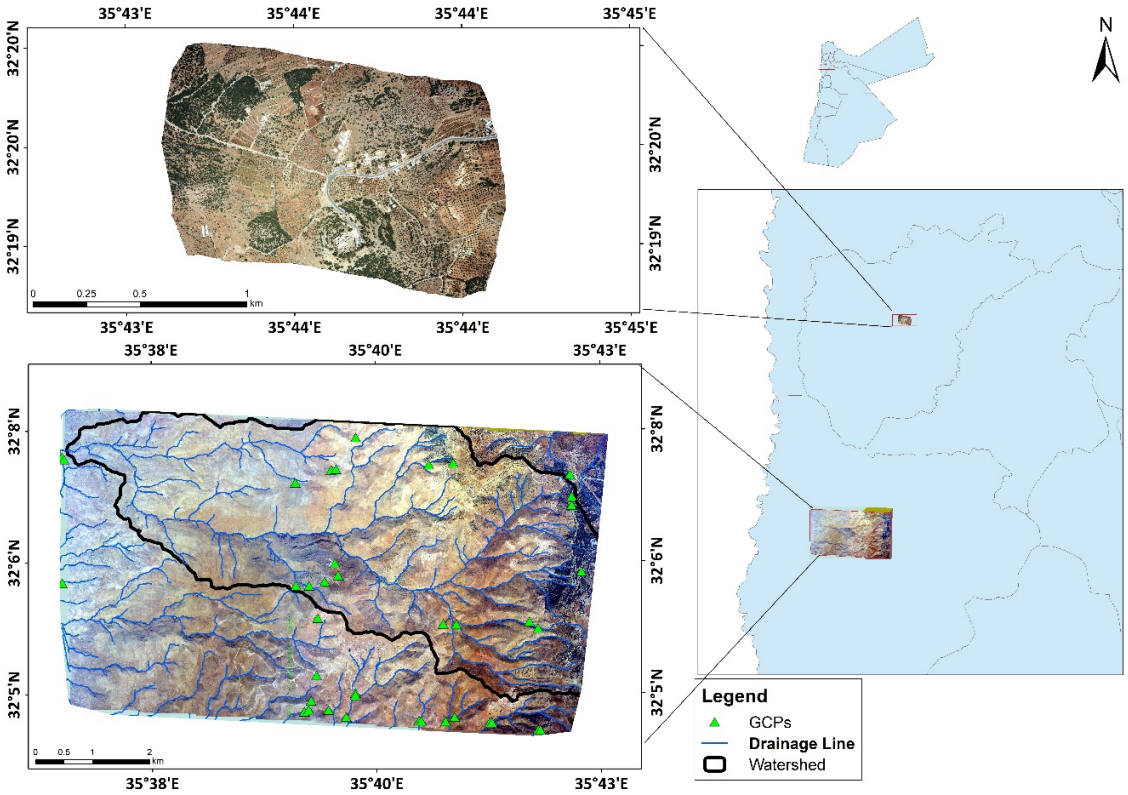

Fig. 3.6 Study Area for DEM data analysis

3.2.9 Site for Reservoir sedimentation Analysis and Validation

The following two reservoirs were chosen to analyse the sedimentation, whose detailed data are used to validate the process.

Anderson Ranch Dam is an earth rock-fill dam on the South Fork of the Boise River, lies at 43˚21' N, 115˚26' W. The dam is located in an arid to a semi-arid region (Fig. 3.7). It is a multi-purpose dam that provides irrigation and hydro-power benefits

and operates in conjunction with Arrowrock and Lucky Peak Reservoirs to provide downstream flood control. Due to sediment accumulation, the dam was closed in 1945. The reservoir capacity survey has been carried out since 1945 (Ferrari, 1999).

The Elephant Butte dam is located in Sierra County on the Rio Grande River (33˚09' N 107˚11' W) in a semi-arid region (Ferrari, 2008). Elephant Butte Dam was one of the first major structures built by reclamation after its formation in 1902 (Fig. 3.7). The total drainage area above Elephant Butte Dam is 67140.26 km^2. Sediment from the remaining regions is trapped by upstream dams, including Jemez Canyon, Galisteo, and Cochiti (Ferrari, 2008).

The rainfall intensities at these two locations vary between 50.8 and 114.3 mm/hr, while the average daily rainfall varies between 127 and 762 mm (USGS, 2017).

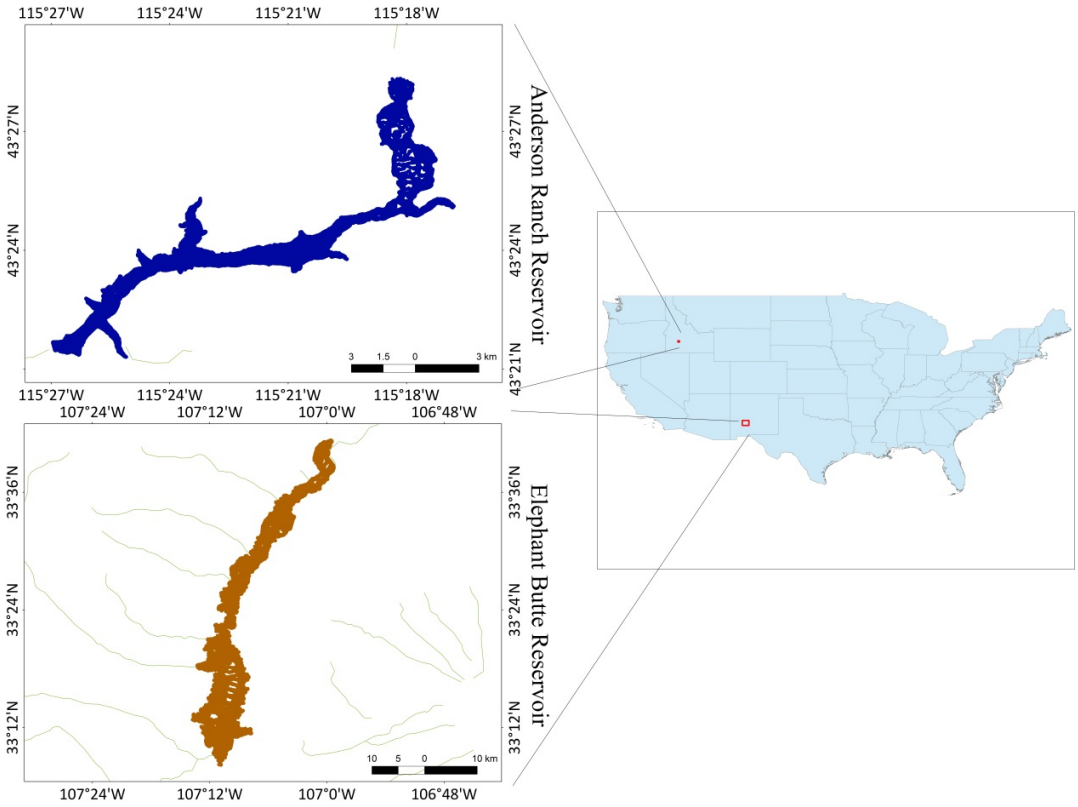

Fig. 3.7 Location of Anderson Ranch and Elephant Butte reservoirs in the USA

3.3 Data Collection and Analysis

3.3.1 Data Source

As water plays a significant role in the development process in arid to semi-arid areas, understanding local hydrology is vital for maximizing sustainable water usage. The hydrological model analysis is the most suitable technique to help understand the interactions between natural and anthropogenic environments. Nevertheless, the hydrological models require good quality input data, besides an up-to-date database for getting good quality results. For example, in rainfall-runoff modelling, the inputs are watershed properties (e.g. watershed boundary, stream network, topography, soil data and properties, land use land cover for the watershed, and time series of meteorological and hydrological data). At the same time, the output is streamflow time series at the outlet (Tarboton, 2003).

In the hydrological model, the following data are required:

- **Watershed structural data** represents the surface boundary of the catchment, stream network, and sub-watersheds.
- **Time-series input data** includes precipitation from rainfall stations in or around the catchment, temperature, humidity, and evaporation data.
- **Observed data** includes streamflow and runoff data for calibration and validation purposes.

3.3.2 Wadi Shueib Dam Data

Daily water level records and water storage data were collected from the Ministry of Water and Irrigation Jordan from 2003 till 2018 (Fig. 3.8).

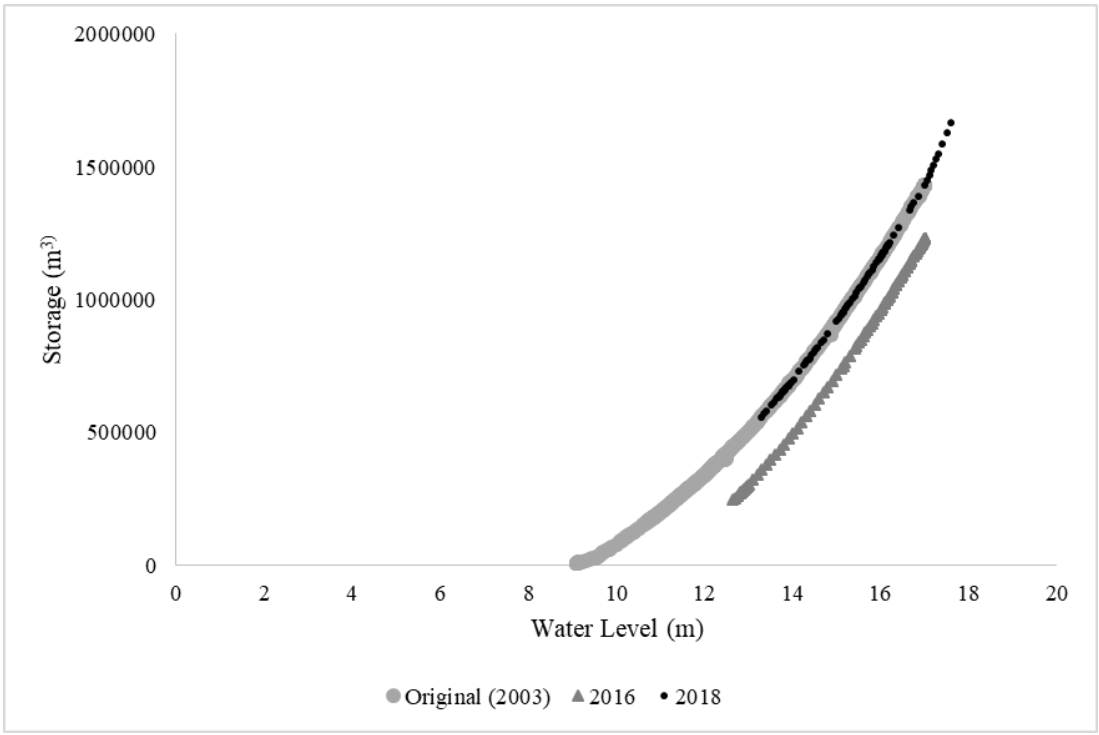

Fig. 3.8 Elevation–capacity curves of Wadi Shueib dam in 2003, 2016, and 2018

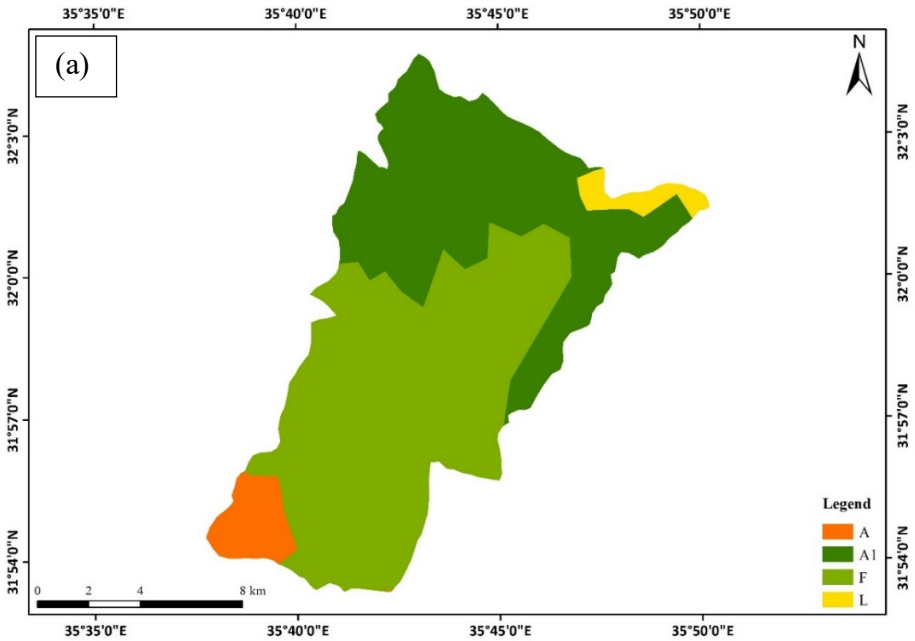

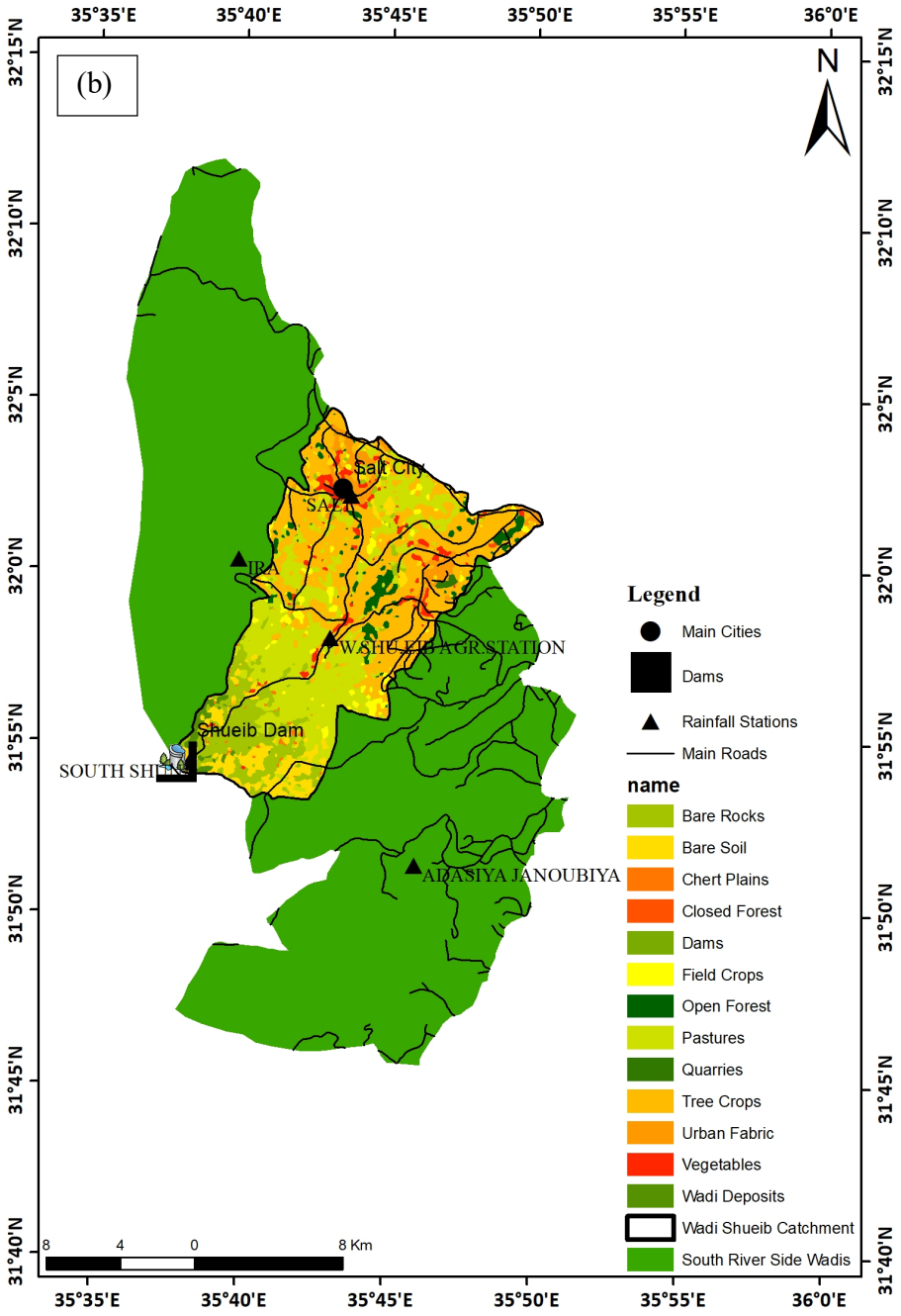

Fig. 3.9 (a) Soil map, (b) Land use and Land cover map, Road networks, important locations, and rain-gauge stations map

The soil type and properties for the study area were extracted from the Jordan level-1 soil map. The level-1 soil map for Jordan, based on a survey between 1989 and

1995, was collected from the Ministry of Agriculture with a scale of 1:2,50,000. The analysis of soil type consists mainly of four types of soil. Fig. 3.9**a** shows the soil types configured in the SWAT model for the Wadi Shueib catchment.

The detailed map of Land use and land cover was collected from Royal Jordanian Geographic Center (RJGC) for 2011. The map indicates that a significant part of the catchment is represented by bare soil. At the same time, other land uses indicate agricultural and urban areas, as shown in Fig. 3.9b. Rainfall is the main form of dam recharge, which is the sole water supply to the agricultural lands.

3.3.3 Weather Data

The precipitation data from five rain-gauge stations in and around the study area was obtained from the Jordan Ministry of Water and Irrigation. The duration of these daily precipitation data was 81, 50, 45, and 44 years at Salt, Adasy, South Shuna, IRA and EIB-AGR stations, respectively.

Statistical analysis of these data was carried out and is shown in the form of boxplots. The total annual mean rainfall was found to vary from 97 mm (std. dev. 58 mm) at South Shuna station to 387 mm (std. dev. 201 mm) at Salt station, while the mean rainfall during the rainy season varies from 48 mm (std. dev. 38 mm) to 161 mm (std. dev. 109 mm). The record also shows maximum precipitation of 870 mm in 1992 and 472 mm in 1953 at Salt station during the rainy and non-rainy season.

Wind speed, relative humidity, maximum and minimum temperature, and solar radiation data were obtained from the Ministry of Water and Irrigation, Jordan, for one EIB-AGR station in the study area. The summary of the statistical analysis of the rainfall and climatology data is shown as boxplots (Fig. 3.10 and Fig. 3.11).

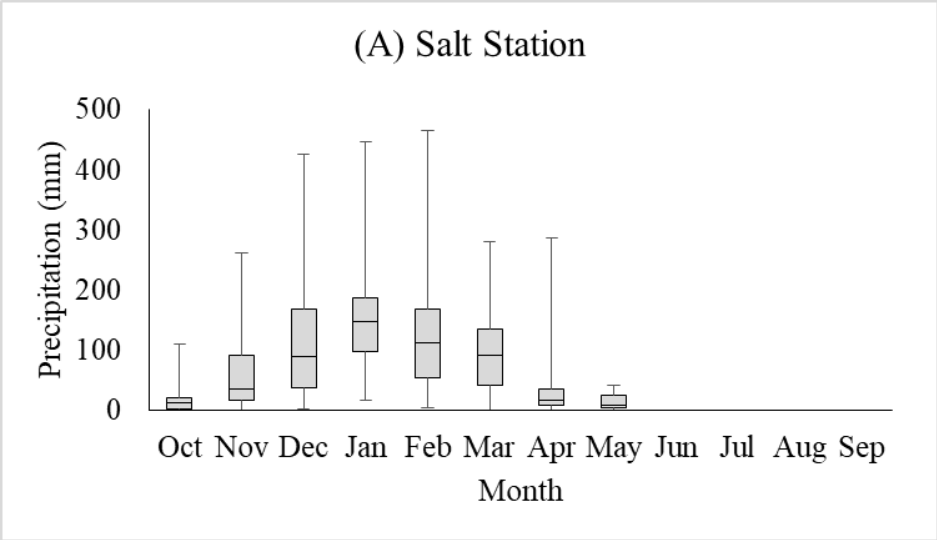
(A) Salt Station
Precipitation (mm)
500
400
300
200
100
0
Oct Nov Dec Jan Feb Mar Apr May Jun Jul Aug Sep
Month

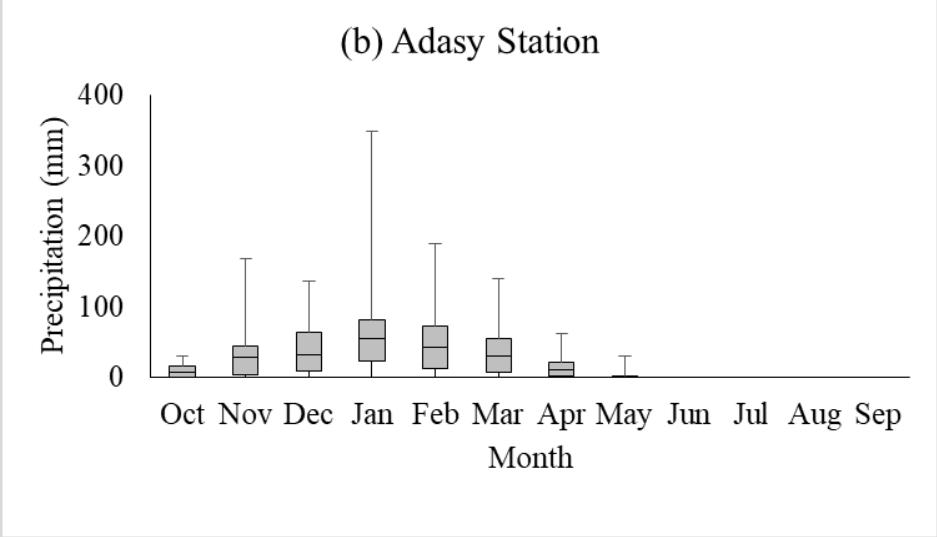
(b) Adasy Station
Precipitation (mm)
400
300
200
100
0
Oct Nov Dec Jan Feb Mar Apr May Jun Jul Aug Sep
Month

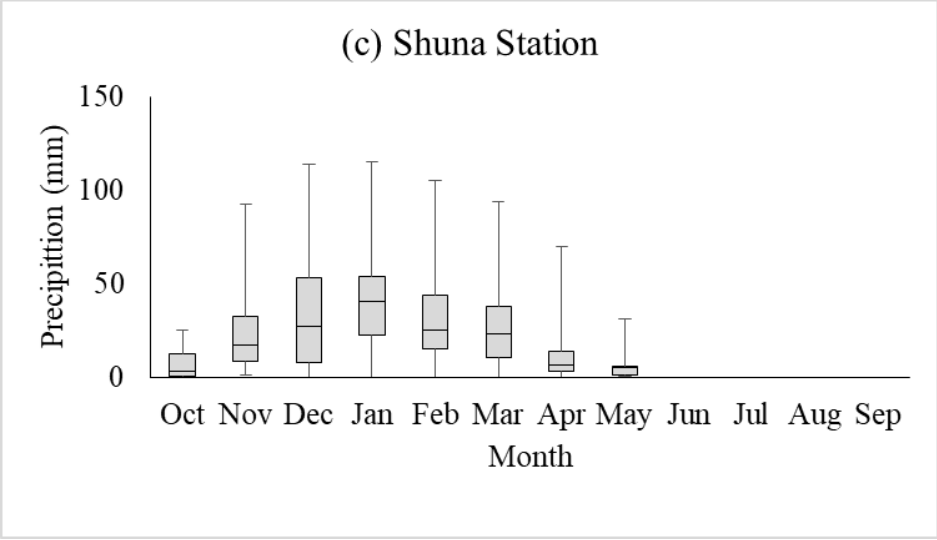
(c) Shuna Station
Precipittion (mm)
150
100
50
0
Oct Nov Dec Jan Feb Mar Apr May Jun Jul Aug Sep
Month

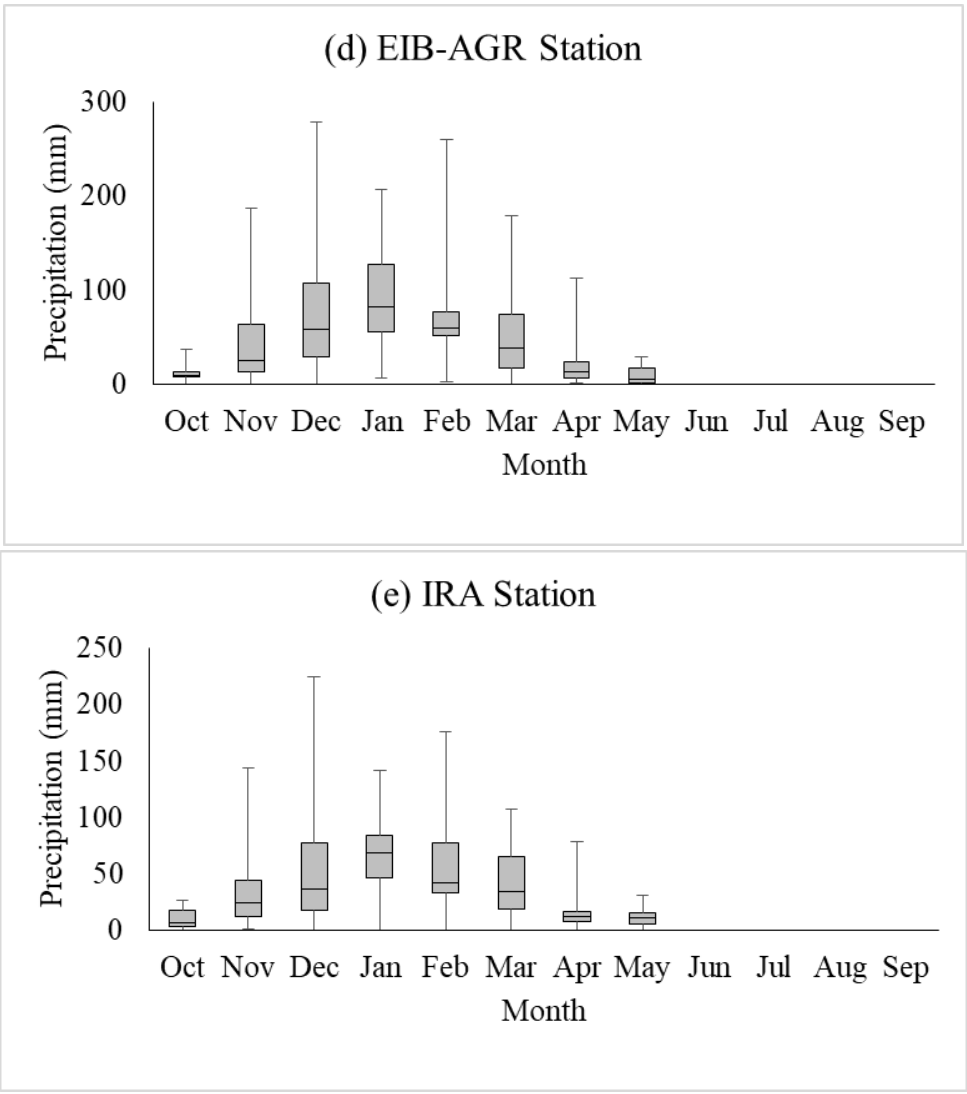

Fig. 3.10 Monthly Precipitation boxplots of (a) Salt station, (b) Adasy station, (c) Shuna station, (d) EIB-AGR station, and (e) IRA station, all units are in mm.

3.3.4 Topographic maps and Aerial Photographs, and DEM data

Topographic map (scale 1:50,000), four aerial photos (two pair photos, scale 1:25,000), and two aerial photos (scale 1:10,000) were collected from the Royal Jordanian Geographical Centre (RJGC) (Fig. 3.12). The topographic map has a 20 m interval with an additional 10 m contour interval to show the more minor details of the earth surface. The map also shows the main roads between the cities, urbanization density, and places

of interest such as dams and agricultural lands. Most importantly, the map illustrates the upstream and downstream portions of the mainstream for each catchment. On the other hand, the aerial photos represent the earth's surface topography, and the stream network in the area is clearly shown.

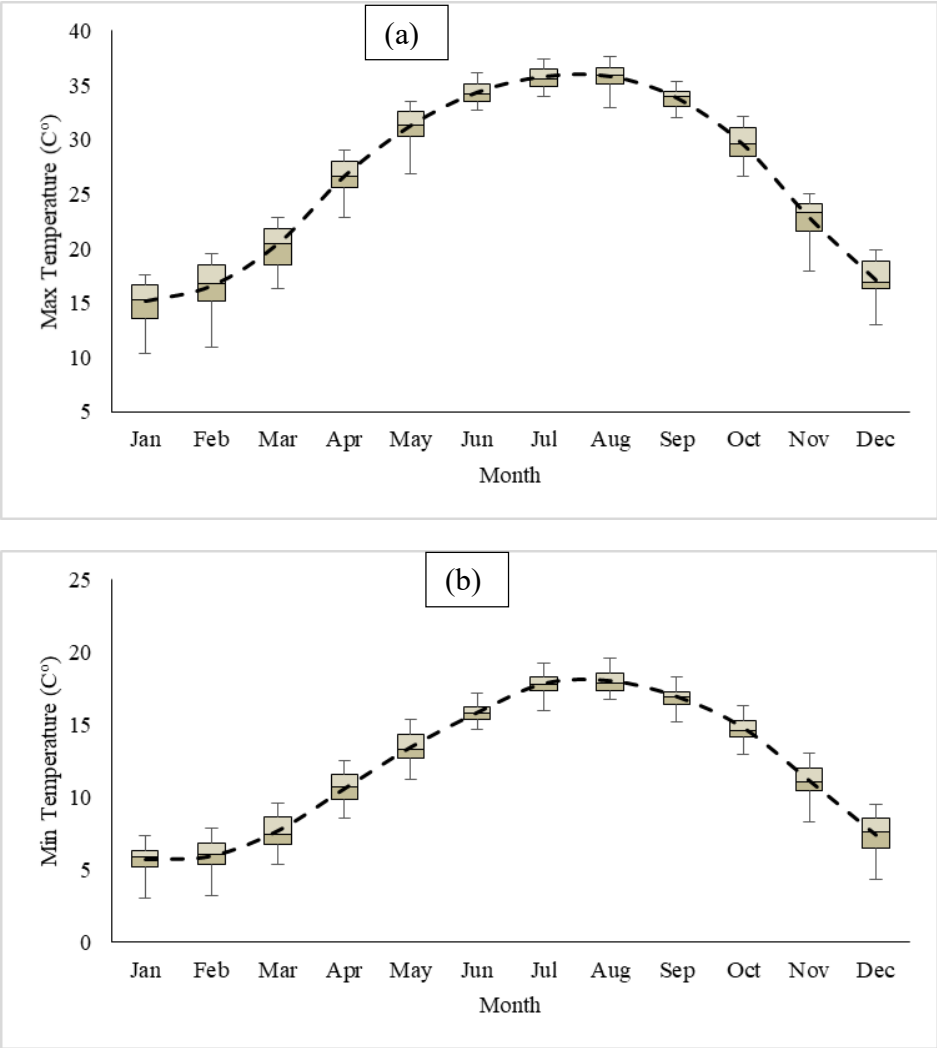

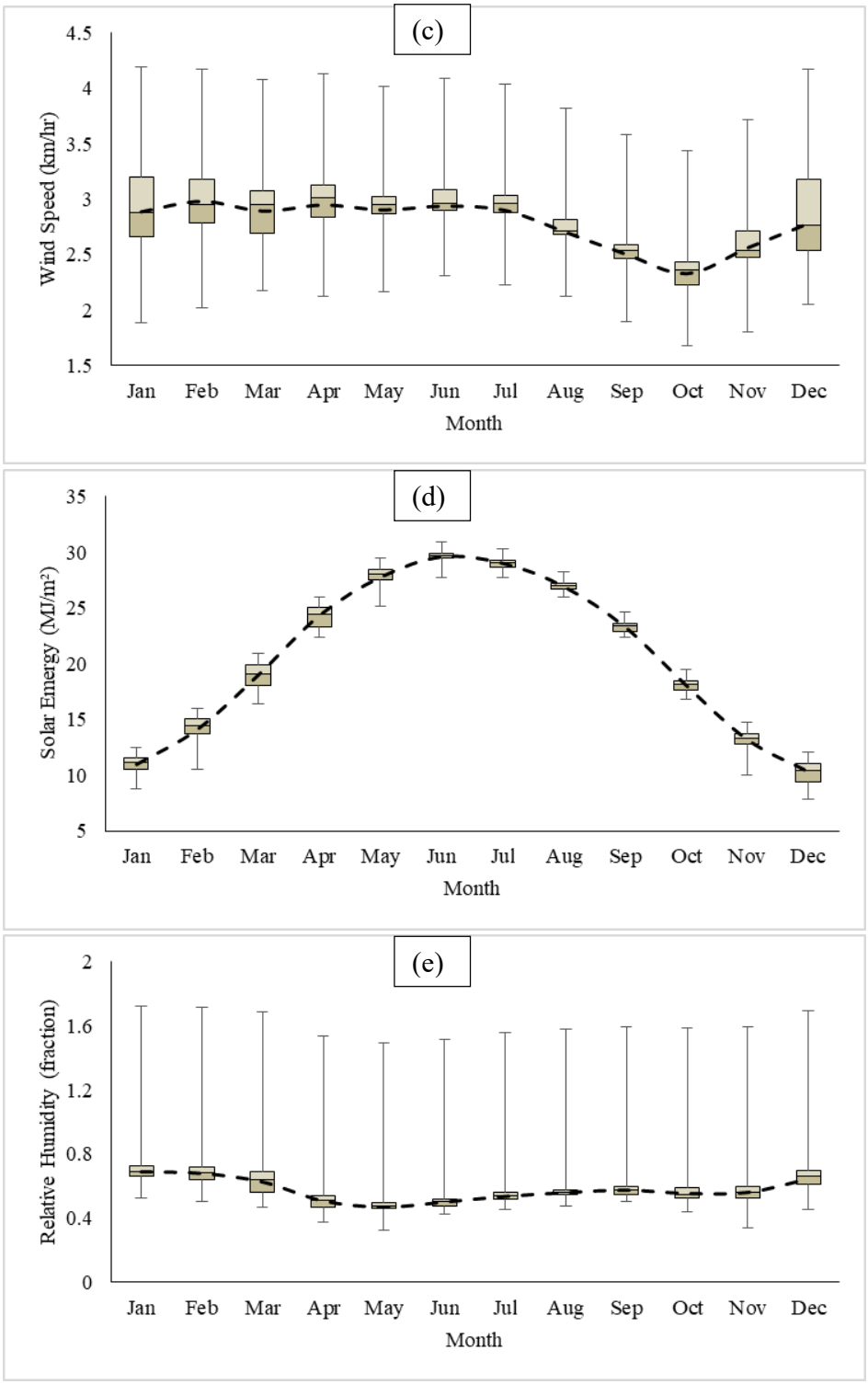

Fig. 3.11 Monthly climatic parameters in the study area(a) Max. Temperature, (b) Minimum Temperature, (c) Wind Speed, (d) Solar Energy, and (e) Relative Humidity.

Four different sources of elevation data have been used to evaluate the most suitable DEM, which will give the most accurate result in hydrological studies. The datasets were collected from two sources: paid and open source. The SRTM and ASTER GDEM were used to compare as open-source DEM. The SRTM DEM is freely available as a 3-arc second (~ 90 m resolution) and 1-arc second (~30 m resolution) (Deilami et al., 2013). Each dataset has an area coverage of approximately $5^{o} \times 5^{o}$. The ASTER GDEM has a dataset that covers $1^{o} \times 1^{o}$ with a 30-meter spatial resolution (Garbrecht and Martz, 1999).

(a)

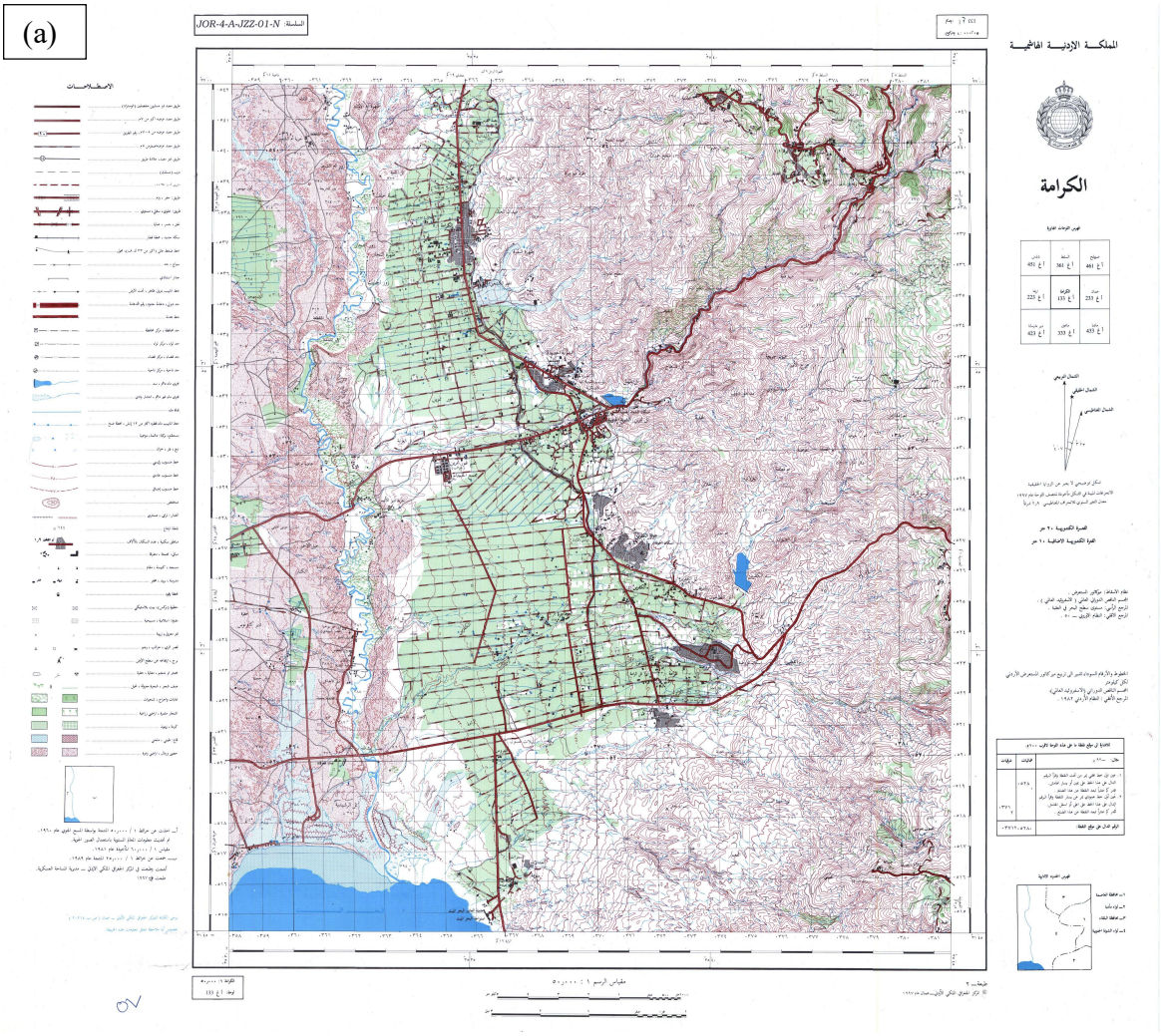

(b)

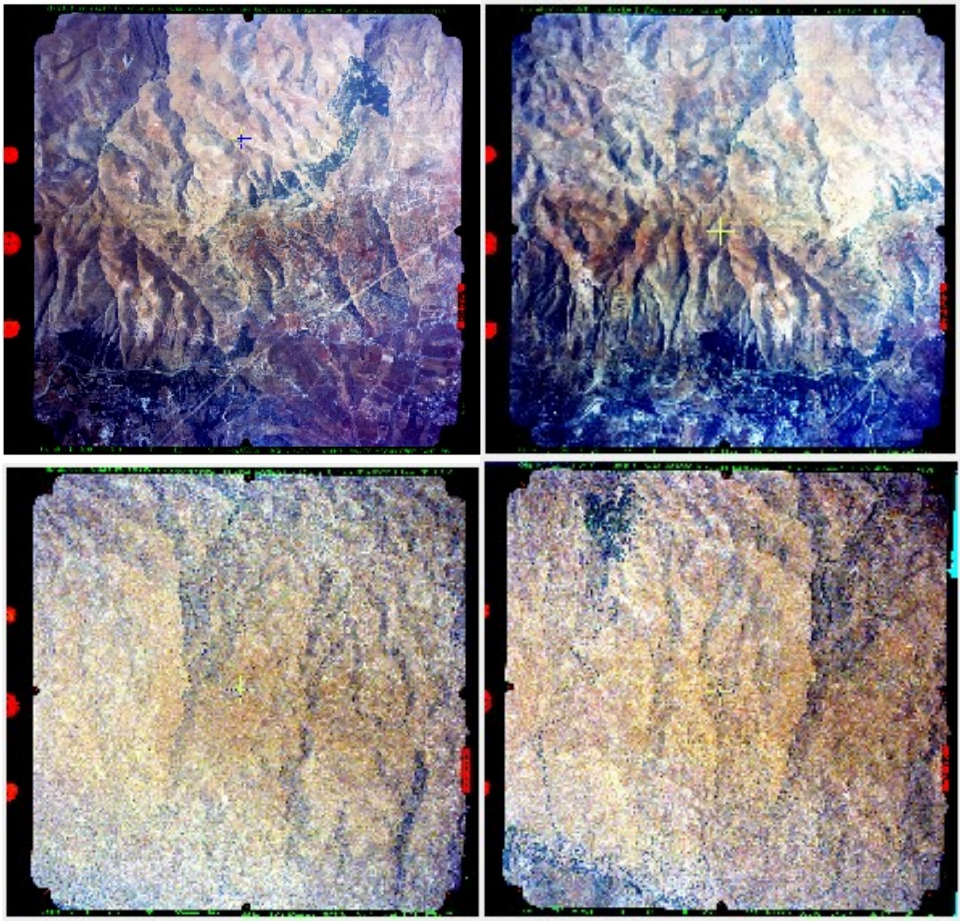

(c)

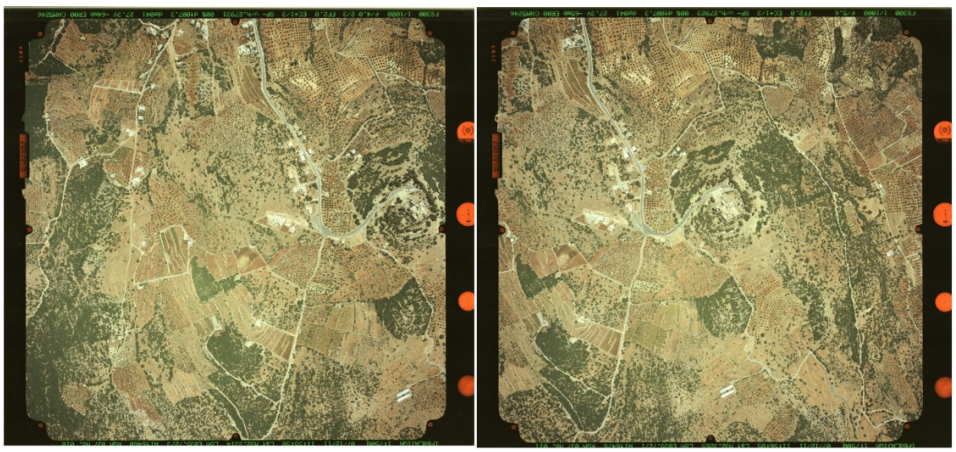

Fig. 3.12 (a) Topographic map, (b) Aerial Photos scale 1:25000, and (c) Aerial Photos scale 1:10000

3.3.5 Satellite images and Soil Moisture Data

The satellite images were downloaded from United States Geographical Surveying (USGS) website https://earthexplorer.usgs.gov from 2003 through 2018. Three generations of Landsat images Thematic Mapper (TM), Enhanced Thematic Mapper Plus (ETM+), and Operational Land Imager and Thermal Infrared Sensor (OLI/TIRS) satellite images, were used to extract the water spread area at different water levels. All these images have differences in spatial, spectral, and also radiometry resolutions. Table 3.3 shows the details of these satellite imagery.

Table 3.3 Comparison of spatial and spectral resolution between the satellite images

Band	Landsat 8			Landsat 7 &5		
	Description	Wavelength (μm)	Resolution (m)	Description	Wavelength (μm)	Resolution (m)
1	Coastal / Aerosol	0.433 - 0.453	30	Blue	0.458 - 0.523	30
2	Blue	0.458 - 0.523	30	Green	0.543 - 0.578	30
3	Green	0.543 - 0.578	30	Red	0.650 - 0.680	30
4	Red	0.650 - 0.680	30	NIR	0.785 - 0.900	30
5	NIR	0.785 - 0.900	30	SWIR-1	1.565 - 1.655	30
6	SWIR-1	1.565 - 1.655	30	TIR	11.5 - 12.5	60
7	SWIR-2	2.100 - 2.280	30	SWIR-2	2.100 - 2.280	30
8	Pan.	0.50 - 0.68	15	Pan (Landsat 7)	0.50 - 0.68	15
9	Cirrus	1.36 - 1.39	30	NA	NA	NA
10	TIR-1	10.3 - 11.3	100	NA	NA	NA
11	TIR-2	11.5 - 12.5	100	NA	NA	NA

(USGS & NASA), NIR, SWIR, and TIR represent near-infrared, short wave infrared, and thermal infrared, respectively.

The soil moisture was obtained from the European Space Agency (ESA) Climate Change Initiative soil moisture version 3.3. The available data covered 0.25^{o} x 0.25^{o} resolution daily data from 1978 onwards. The soil moisture was found based on average values of square cells in and around the watershed.

3.4 Methodology for handling various research work components

The following flowchart (**Fig. 3.13**) describes the methodology adopted to fulfil the research components. As shown, the present work uses precipitation, temperature, wind speed, humidity, and solar radiation, streamflow, soil moisture, aerial photography, topographic map, digital elevation data (DEM), satellite images, and observed experimental data as various inputs. The analysis of these raw data based on the different objectives was carried out to utilize the output of each stage and will be discussed in the respective chapters.

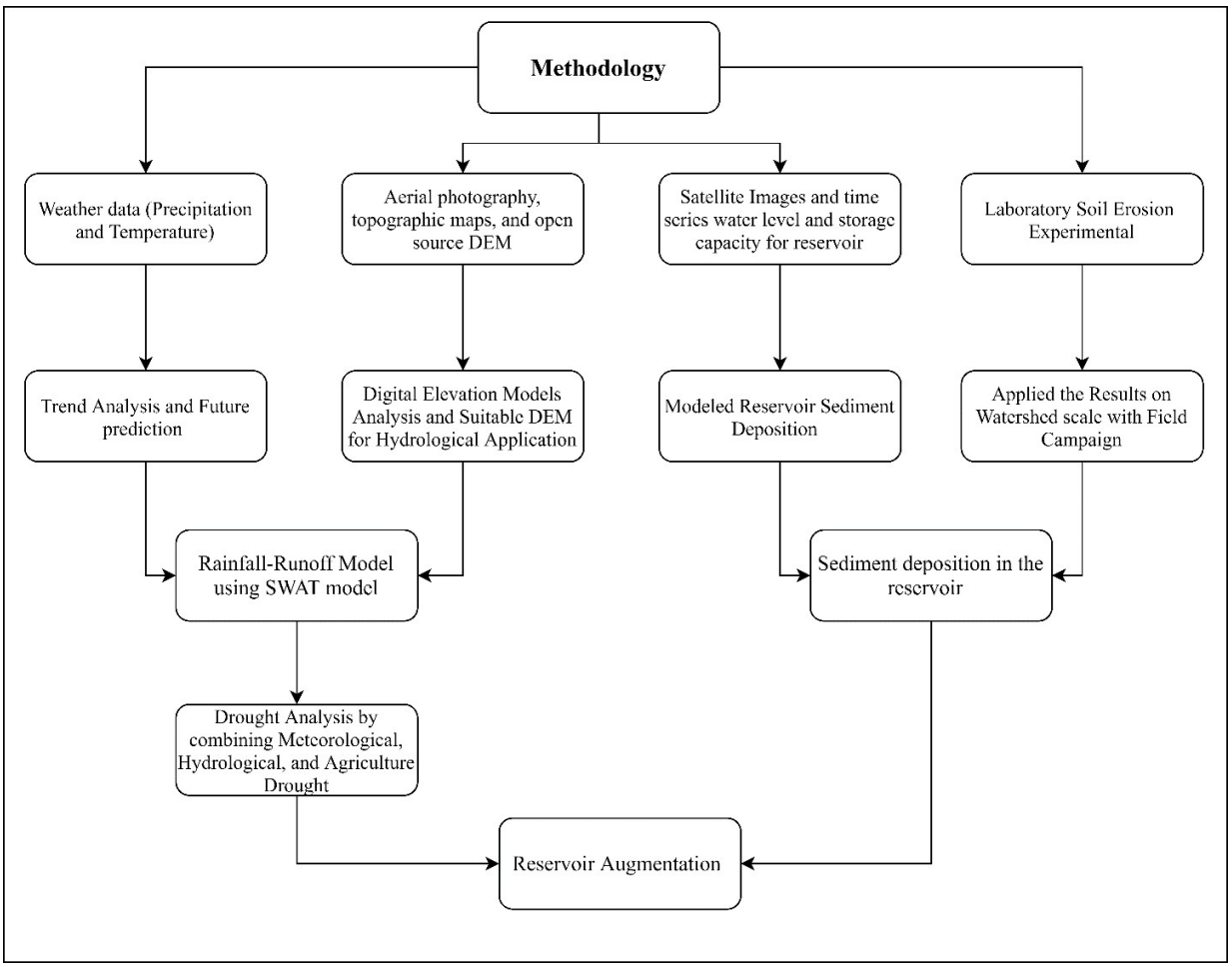

Fig. 3.13 Flowchart of the proposed research

3.5 Conclusions

This chapter primarily discusses the details of the study area of the Wadi Shueib catchment. The other sites used for the validation of models were also discussed. Besides that, this chapter also discussed the data collection and their sources and their utilization. Finally, a process-based flow chart is prepared to understand the methods applied to fulfil the research components using these datasets.

Chapter 4: Evaluation of Digital Terrain Models

4.1 Introduction

Very low and high altitudes in Jordan valley (elevation ranges between 1400 and -400 m under sea level) are primary concerns for water resources management. Applications of hydrological modelling require high-quality digital elevation models (DEMs) with acceptable spatial resolution. This requirement is due to the hydrological parameters are affected by DEM accuracy (Vaze et al., 2010). In this chapter, several elevation models from different sources were tested and evaluated for their relative accuracies. Those elevation models were used to derive hydrological parameters and stream flow modelling. Further, those hydrological parameters were also assessed, and based on that, elevation models were evaluated. Besides that, a technique is proposed to improve the accuracy of existing DEM compared with the digital terrain model (DTM) using the bootstrap technique in Ensemble Neural Network (ENN).

4.2 Data Analysis

The details of the study area are described in section 3.8. The methodology followed here can be summarized into five stages: (i) digitizing the raw topographic map (contour map), (ii) generate DTM and orthophoto using stereo pairs aerial photography, (iii) extract sample data as point (x,y) locations and altitude (z) from DTM, examining these points with the corresponding points from a topographic DEM, SRTM, and ASTER GDEM data, (iv) calculate hydrological parameters from different DEM and verify them for the best suitability of the DEM data, and (v) correction of the raw DEM data using ENN model and verify the improvement. Refer to sections 4.1.3 and 4.2.1 for the raw data used

in this chapter. The analysis is discussed in the following sections. Fifty ground control points (GCPs) were used to improve the vertical and horizontal accuracy of the ortho-photo and DTM. The aerial photos with ground control points (GCPs) were used to derive high-resolution ortho-photo with spatial-resolution 0.6 m and high accuracy DTM with resolution 10 m. Besides that, the topographic maps were converting to DEM with a 25 m spatial resolution.

4.2.1 Digitization

Digitization is the process of converting the information into a digital format using manual or digital techniques. Most researchers used different digitization techniques due to the lack of data (Xin et al., 2006; Samet et al., 2010; Samet and Hancer, 2012). The feature can be generated in the GIS environment through digitization, converting analogue information into a digital representation. After digitizing the topographic map, spatial techniques have been used to derive DEM from the contour map (Fig. 4.1).

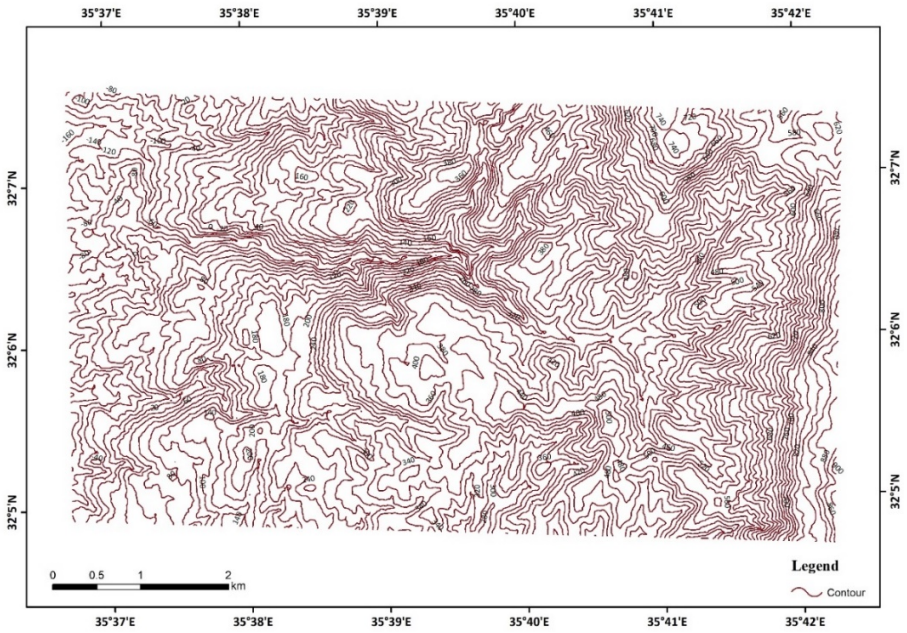

Fig. 4.1 Contour map with 20 m interval

4.2.2 Photogrammetry

There are several mathematical models available to extract the elevation and geometry correction of aerial photography. The Toutin's Model (Toutin, 1995), Orun and Natarajan Model (Orun and Natarajan, 1994), Collinearity equations model (El-Beik and Masaad 1993), among other techniques as Rigorous Geometric Models, and (2D Polynomial Models, 3D Polynomial Models, Projective Transformation) were used as Simple Geometric Models. (**Section 4.1.3**)

4.2.2.1 Collinearity Equations Model

The Collinearity Equations Model (El-Beik and Masaad, 1993) is used to find the relation between the aerial photos among stereo pairs and between the aerial photos coordinate system and an actual coordinate system (Kim, 2000).

The following equations (Eq. 4.1-4.3) can be summarized using the following relations:

$$x_a = x_o - f\left[\frac{r_{11}(X_A - X_L) + r_{12}(Y_A - Y_L) + r_{13}(Z_A - Z_L)}{r_{31}(X_A - X_L) + r_{32}(Y_A - Y_L) + r_{33}(Z_A - Z_L)}\right] \quad 4.1$$

$$y_a = y_o - f\left[\frac{r_{21}(X_A - X_L) + r_{22}(Y_A - Y_L) + r_{23}(Z_A - Z_L)}{r_{31}(X_A - X_L) + r_{32}(Y_A - Y_L) + r_{33}(Z_A - Z_L)}\right] \quad 4.2$$

R an orthogonal rotation matrix with the three angles ω, φ and κ expressed by:

$$R = \begin{bmatrix} \cos\varphi\cos\kappa & -\cos\varphi\sin\kappa & \sin\varphi \\ \cos\omega\sin\kappa + \sin\omega\sin\varphi\cos\kappa & \cos\omega\cos\kappa + \sin\omega\sin\varphi\sin\kappa & -\sin\omega\cos\varphi \\ \sin\omega\sin\kappa + \sin\omega\sin\varphi\cos\kappa & \sin\omega\cos\kappa + \cos\omega\sin\varphi\sin\kappa & \cos\omega\cos\varphi \end{bmatrix} 4.3$$

The six parameters, namely, X_L, Y_L, Z_L, ω, φ, and κ, are the unknown exterior orientation elements. The image coordinates x_o, y_o and x_a, y_a are usually known (i.e., measured), and the calibrated focal length f is constant. Every measured point leads to two equations and adds three other unknowns, namely the object point coordinates (X_A,

Y_A, Z_A). Unless the object points are known using GPS as ground control points (GCPs), a pair of aerial photos needs to be solved (Schenk, 2005).

The data used for photogrammetry was scanned from aerial images with 20 μm resolution. Camera calibration was carried out for focal length and interior points. DGPS with sub-centimetre level accuracy in both horizontal and vertical directions was used to collect GCPs data. These data were used to determine (X, Y, Z, ω, φ, κ) for each photo.

The accuracy of geometric rectification depends on the selection of ground control points (GCPs), the number of GCPs, and the distribution of GCPs (Wu et al., 2008). As per Goncalves et al. (2009), a total of 30 control points may be considered as the most common number of control points used for manual geometric correction. Therefore, uniform distribution of control points provides better accuracy with considering overall deformation rates at the entire image for rectification (Liewa et al., 2012).

4.2.2.2 Ortho-photo and DSM

The PCI Geomatica® software was used to derive high-resolution ortho-photo with spatial-resolution 0.6 m and high accuracy DTM with a resolution of 10 m. The GCPs were used to improve the vertical and horizontal accuracy of the ortho-photo and DTM. Fig. 4.2 shows the ortho-photo and DTM, where the terrain features can be interpreted easily.

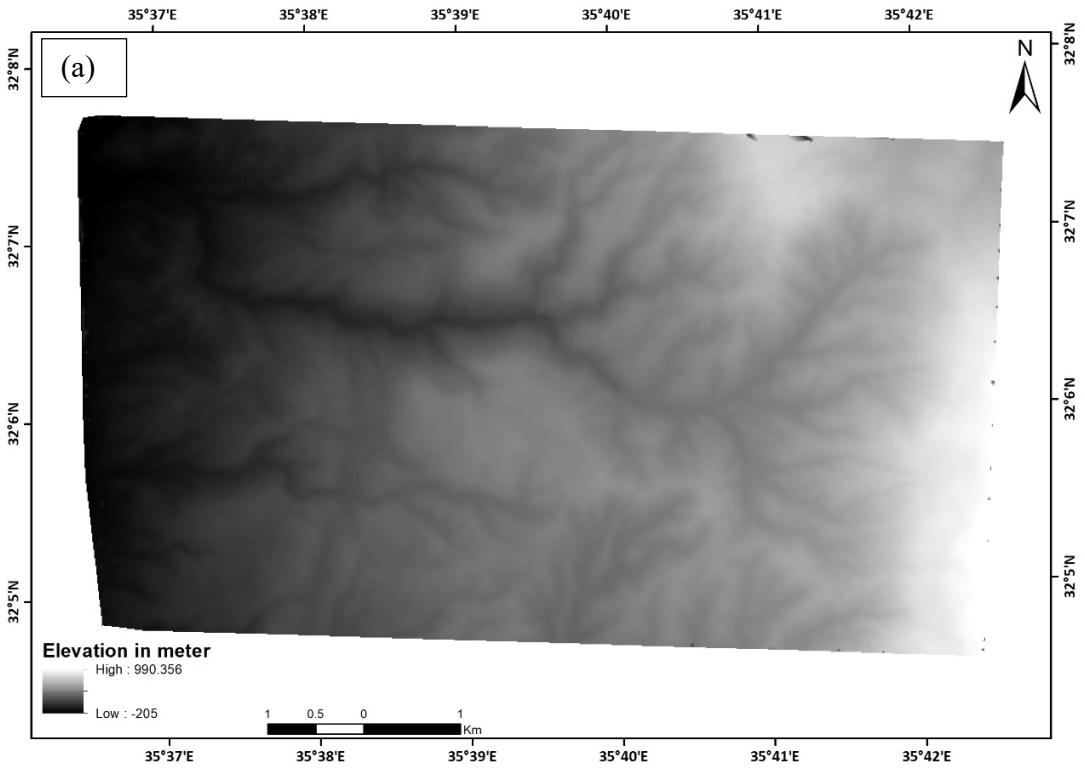
(a)
35°37'E
35°38'E
35°39'E
35°40'E
35°41'E
35°42'E
32°8'N
32°7'N
32°6'N
32°5'N
N
Elevation in meter
High : 990.356
Low : -205
1 0.5 0 1
Km

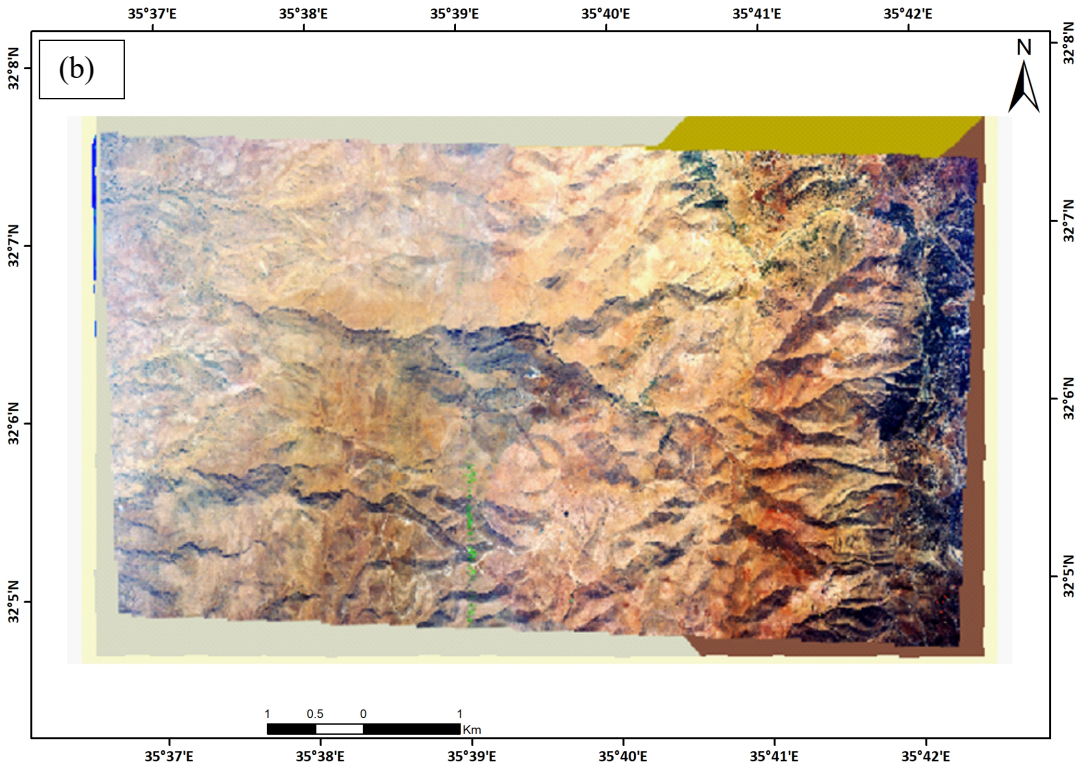
(b)
35°37'E
35°38'E
35°39'E
35°40'E
35°41'E
35°42'E
32°8'N
32°7'N
32°6'N
32°5'N
N
1 0.5 0 1
Km

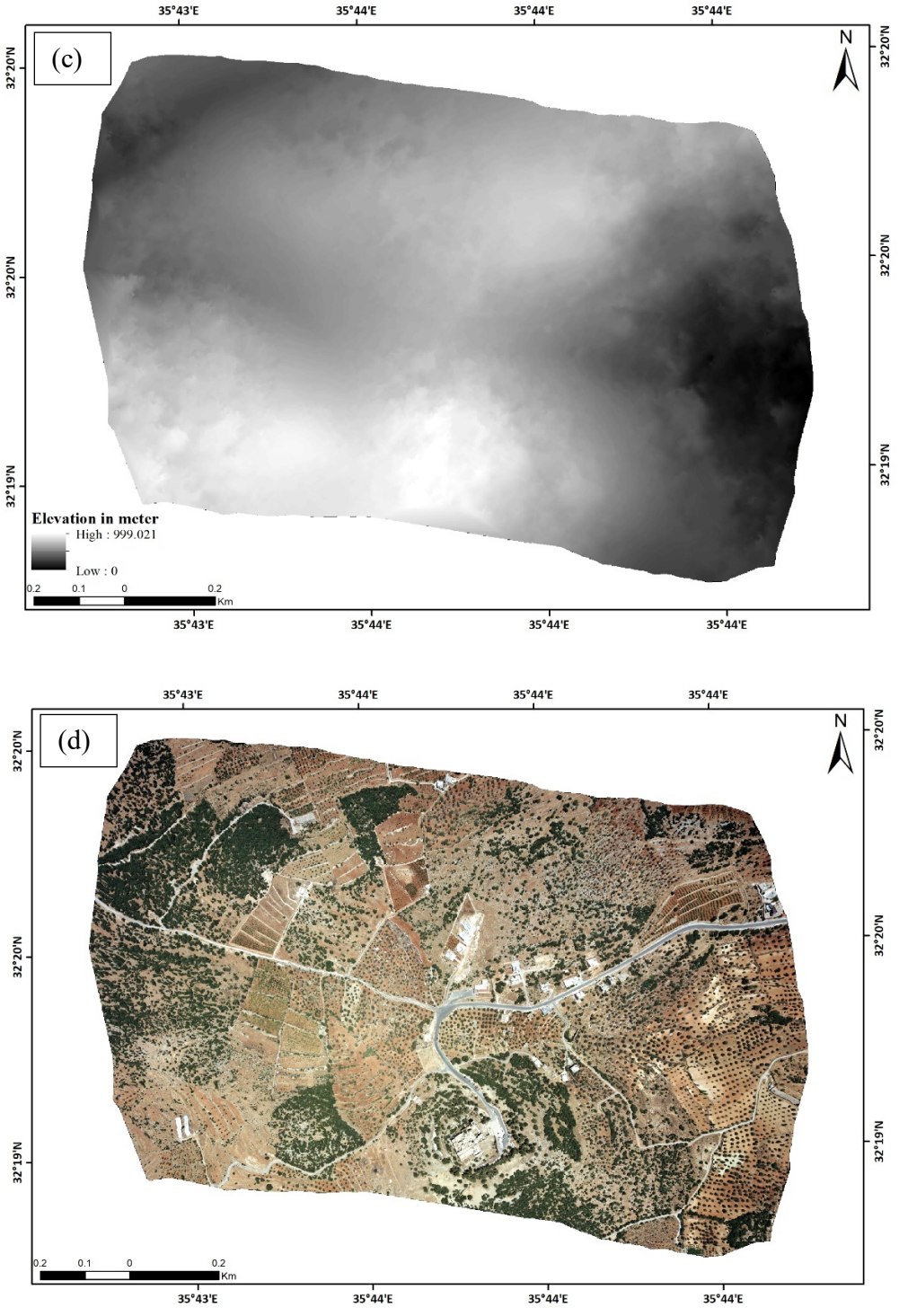

Fig. 4.2 (a) Digital Terrain Model (DTM) of the study area-1 and **(b)** Ortho-photo represent the study area-1, and **(c)** Digital Terrain Model (DTM) of the study area-2 and **(d)** Ortho-photo represent the study area-2

4.2.3 Statistical Methods

The statistical analysis was carried out to analyze the dataset; for example, fundamental analysis (mean, minimum, maximum, standard deviation) and higher-level analysis using hypothesis tests (Normal distribution, *f* distribution, correlation) (Reva and Saunders, 2007).

4.2.3.1 Point to Point Comparison

The primary comparison process is a point-to-point comparison to find the minimum dataset error with reference data. The following equation (Eq. 4.4) was used to calculate the error:

$$\mathrm{Elev}_{\mathrm{Error}} = \mathrm{Elev}_{\mathrm{examined}} - \mathrm{Elev}_{\mathrm{Reference}} \quad 4.4$$

The examined point from DEM, $\mathrm{Elev}_{\mathrm{Reference}}$ is the checked point from DSM and $\mathrm{Elev}_{\mathrm{Error}}$ is the difference in elevation or error.

The mean error and RMSE can be computed by:

$$\mathrm{Mean}_{\mathrm{Error}} = \frac{\sum_{i=1}^{n} \mathrm{Elev}_{\mathrm{Error_i}}}{n} \quad 4.5$$

$$\mathrm{RMSE} = \sqrt{\frac{\sum_{i=1}^{n} (\mathrm{Elev}_{\mathrm{Error_i}})^2}{n}} \quad 4.6$$

Each error may be any of the three cases: a positive value representing the DEM elevation above the reference DSM. The negative value indicates that the DEM is below the reference DSM. Zero error indicates the same elevation in both DEM and DSM. The

statistical parameters such as mean, standard deviation (*Std*), Sample Variance (σ^2), and *RMSE* values were calculated for vertical accuracy.

4.2.3.2 t-*Test Distribution*

The *t*-test is one of the most common methods to compare the mean of two or more samples. The hypothesis has been built as:

H_o: the difference between the mean of DTM and DEM = 10.

H_1: the difference between the mean of DTM and DEM ≠ 10.

$$t = \frac{\overline{x}_1 - \overline{x}_2}{\sqrt{\frac{S_1^{\,2}}{N_1} + \frac{S_2^{\,2}}{N_2}}} \qquad 4.7$$

Where t is the t -test value, $\overline{x}_1$ and $\overline{x}_2$ are the mean of DTM and DEM, S_1 and S_2 are the variance of DTM and DEM, and N_1 N_2 are the size of the sample.

4.2.4 Hydrological Parameter

The DEM is a vital source of topographic information, which provides essential information about terrain characteristics (Wu et al., 2008). Most hydrological parameters can be determined using DEM, such as slope, aspect, curvature, flow direction, slope-length and steepness (LS) factor, streams, and watershed delineation.

4.2.4.1 Slope, Aspect and Flow Direction

The terms slope, aspect, and flow direction have a significant link to each other, where the slope has a role in both aspects and flow directions. From the definition, the slope is a change of the elevation over the distance. The slope influences surface and subsurface water flow velocity, soil erosion potential, and many earth surface processes (Wu et al., 2008).

Aspect and flow direction are nearly similar terms. While the aspect is calculated based on the orientation or the azimuth slope, flow-direction is the parameter, which estimates the flow direction at any particular point based on the elevation of its neighbour. The aspect and flow direction are essential for hydrological studies. The aspect can estimate the amount of solar radiation available that can be used in various environmental factors, such as estimating potential evapotranspiration (Pakoksung and Takagi, 2016). The aspect is classified into nine directions (N, NE, E, SE, S, SW, W, NW, and flat), and the flow can be towards any of the eight directions using the 2^n numbering system (where n = 1, 2…, 8). In ArcGIS, the flow direction output values refer to the direction of the steepest gradient (Fig. 4.3). In the case of aspect, the direction indicates the slope face of that cell.

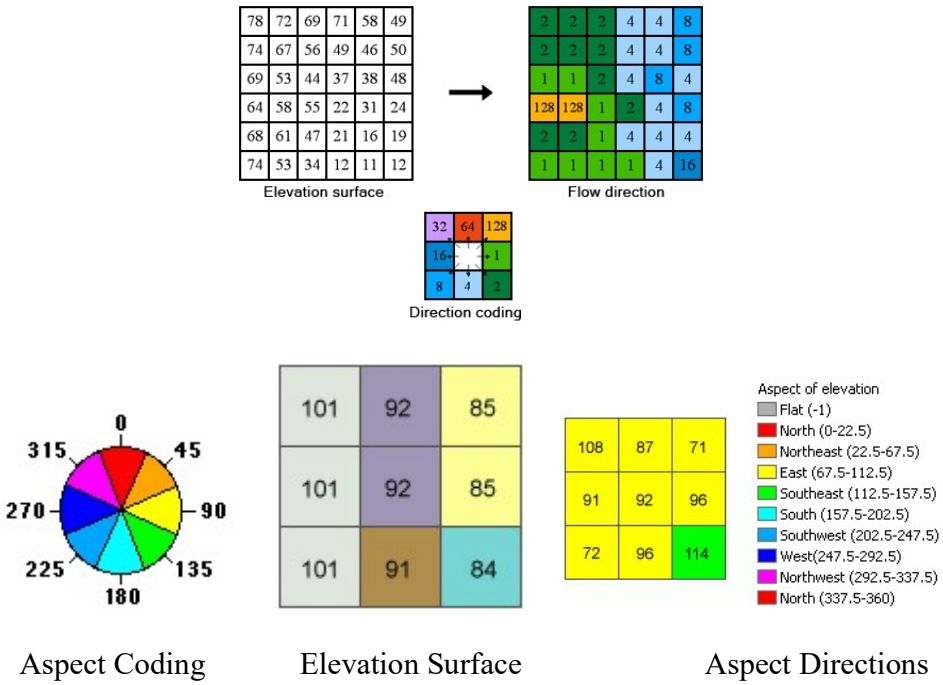

Fig. 4.3 Aspect and flow direction digitization (Source: ArcGIS Pro documentation)

4.2.4.2 Curvature and LS Factor

The curvature is the parameter that is directly related to slope and aspect. Two common curvatures were used: (1) profile, computed using the change of slope down a flow line, and (2) plane, computed using the change of aspect and contour. Profile curvature indicates the flow acceleration, zones of enhanced erosion and deposition, and sediment transport processes. In contrast, plan curvature has significant implications on flow convergence and divergence and soil water properties (Vaze et al., 2010) .

The LS factor is one of the Universal Soil Loss Equation (USLE) factors. LS factor indicating the length (L) and steepness (S) of terrain (Pakoksung and Takagi, 2016). The LS factor estimates the spatial distribution of sediment transport (Jarvis et al., 2004).

4.2.4.3 Stream and Watershed Delineation

The stream network and watershed delineation are two terms related to each other, where the streams show the flow path of surface water, estimated based on the slope at each point regarding its neighbour. The watershed delineation uses the stream network to produce the watershed's boundary from high altitude to the watershed outlet.

4.2.5 Ensemble Neural Network (ENN) Constructions

The ENN method aims to provide reasonable predictions of DEM through constructing a model. For the training process, there are three different algorithms typically used: Gradient descent with momentum and adaptive learning rate back-propagation (GDX), Levenberg Marquardt (LM), and Bayesian regularization (BR) (Daliakopoulos et al. 2005). The combination of any ANN architecture with a training process is known as the ENN ensemble. Combining FNNs with LM based training gives better estimations for non-linear relations than other methods and is used widely in environmental research.

Due to this reason, the FNNs with LM training were chosen for estimating the DEM corrections in this chapter.

Fig. 4.4 shows the inputs parameters which will be used in ENN. These parameters can be calculated from any DEM (Nguyen et al., 2018; Nguyen et al., 2019). Fig. 4.4 represent the workflow process,

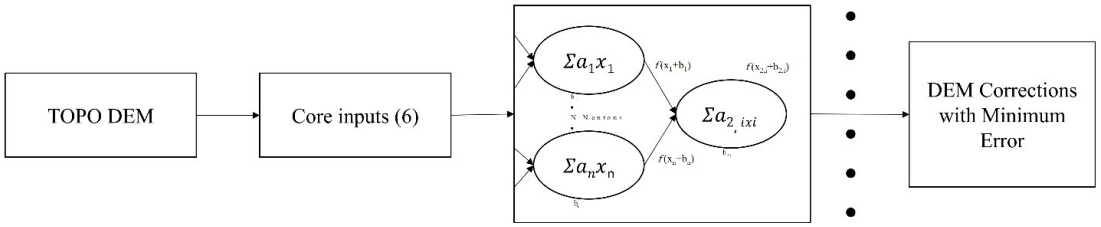

Fig. 4.4 Ensemble Neural Network Model

For model evaluation, the results were compared as per respective accuracy using evaluation measures as correlation (r), coefficient of determination (R^2), and RMSE measured by Eqs. 4.8-4.11.

$$r = \frac{\sum_{i=1}^{n}(p_i - \overline{p})(a_i - \overline{a})}{\sqrt{\sum_{i=1}^{n}(p_i - \overline{p})^2 \sum_{i=1}^{n}(a_i - \overline{a})^2}} \tag{4.8}$$

$$R^2 = r \times r \tag{4.9}$$

$$RMSE = \sqrt{\frac{\sum_{i=1}^{n}(p_i - a_i)^2}{n}} \tag{4.10}$$

$$Acc = \frac{100}{n}\sum_{i=1}^{n} c_i$$
$$c_i = \begin{cases} 1, & \text{if } |p_i - a_i| \le e \\ 0, & \text{otherwise} \end{cases} \tag{4.11}$$

where p and a are predicted and actual values, respectively; e is the acceptable error.

Table 4.1 Input parameters for ENN model

Id	Core
1	Point density (PN)
2	Surface roughness (σZ)
3	Principal component analysis eigenvalue 1st dimension (λ1)
4	Principal component analysis eigenvalue 2nd dimension (λ1)
5	Principal component analysis eigenvalue 3rd dimension (λ1)
6	Normalized height (NZ)

4.3 Results and Discussion Accuracy Assessment of DEMs

4.3.1 Accuracy Assessment of DEMs

The outputs of the accuracy assessment for each DEM to the DTM (as reference) are shown in Table 4.2. Fig. 4.5 shows different datasets, where the elevation variation in each DEM can be recognized clearly with the difference in cell size. There are several methods to measure the DEM error, where the RMSE was introduced by Nikolakopoulos et al. (2006) and became widely used to analyze the vertical accuracy of DEMs. The distribution of the residuals or errors for each DEM (as a point to point evaluation) shows a linear relation (Fig. 4.6). This result supports the previous study conducted by Mukherjee et al. (2013) in the western part of the Himalayas. They also proposed that the ASTER has higher vertical accuracy (due to higher spatial resolution) than SRTM. However, Thomas et al. (2015) disagree with the observations mentioned above and suggest that SRTM is better than ASTER DEM. There is a contradiction between the two studies by Mukherjee et al. (2013) and Thomas et al. (2015). Mukherjee et al. (2013) have conducted their study on the hilly area (elevation range between 0 and >900 m above the sea level), whereas Thomas et al. (2015) have conducted the study on moderate elevation area only (elevation between 0 and 450 m above the sea level). The elevation ranges in the present study are between <-100 and >700 m above the sea level results

have agreed with Mukherjee et al. (2013). So, these studies conclude that the ASTER data accuracy is higher for moderate elevations than SRTM data.

Table 4.2 Accuracy Assessment of DEMs to DTM

Analysis	Topo - DTM	SRTM - DTM	ASTER - DTM
Max	367.87	101.49	67.56
Min	-62.67	-60.68	-152.89
Mean	0.36	20.85	25.85
RMSE	5.40	15.07	7.10

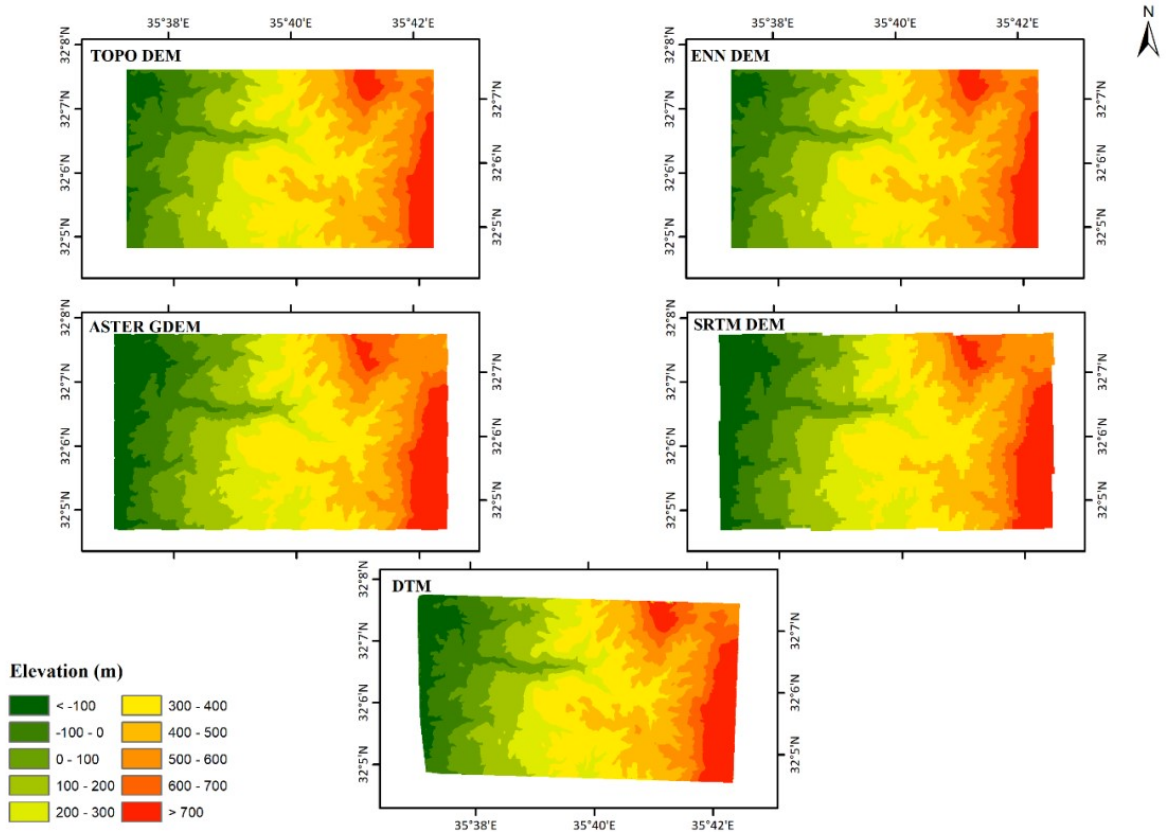

Fig. 4.5 DEM derived from Aerial photo, TOPO DEM, ASTER GDEM, and SRTM DEM

Table 4.3 Correlation relation between DTM and other DEMs

	DTM	Contour	SRTM	ASTER
DTM	1			
Contour	0.9998	1		
SRTM	0.9987	0.9989	1	
ASTER	0.9996	0.9996	0.9988	1

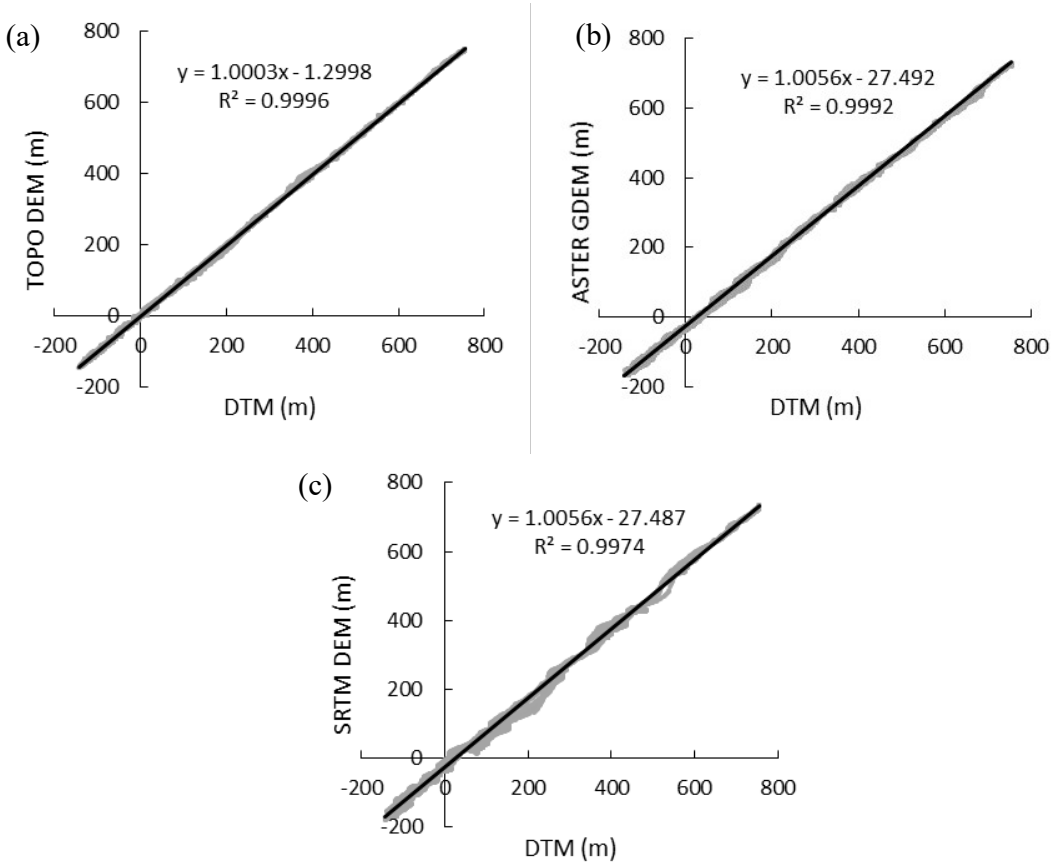

Fig. 4.6 Point to Point elevation relation

In Fig. 4.6, the linear correlation between the DTM and others DEMs are shown. The DEMs from a topographic map and ASTER closely match (R^2 of the TOPO DEM > 0.99 and ASTER DEM > 0.99). The SRTM DEM gives better fitting with correlation (> 0.99). The *t*-test was used to find out how much the other DEM sources were close to DTM data. The p-values found for 95% confidence level in the DEM from a topographic map gave a minimum *p*-value (0.003). The ASTER and SRTM DEMs were close in terms of *p*-values (ASTER = 0.021 and SRTM = 0.022). The results indicate that the ASTER GDEM is the best suited for DEM data used in the absence of aerial photos (Table 4.4). The p-value is very small (significantly close) between the mean of two DEMs, as the ASTER GDEM has a smaller p-value than SRTM, so ASTER data indicate

better accuracy than SRTM data. The variations of global DEMs examined results in the previous studies with different study areas, return to the surface properties, reference points, terrain characteristics, and location (Mokarram and Hojati, 2016).

Table 4.4 *t*-Test Distribution

Statistical	DTM	Contour	DTM	SRTM	DTM	ASTER
Mean	142.24	140.98	142.24	115.55	142.24	115.54
Variance	54236.76	54286.00	54236.76	54989.11	54236.76	54883.78
t Stat	-2.65		2.02		2.03	
P(T<=t) one-tail	0.003		0.0215		0.0213	
t Critical one-tail	1.64		1.64		1.64	
P(T<=t) two-tail	0.010		0.0430		0.0425	
t Critical two-tail	1.96		1.96		1.96	

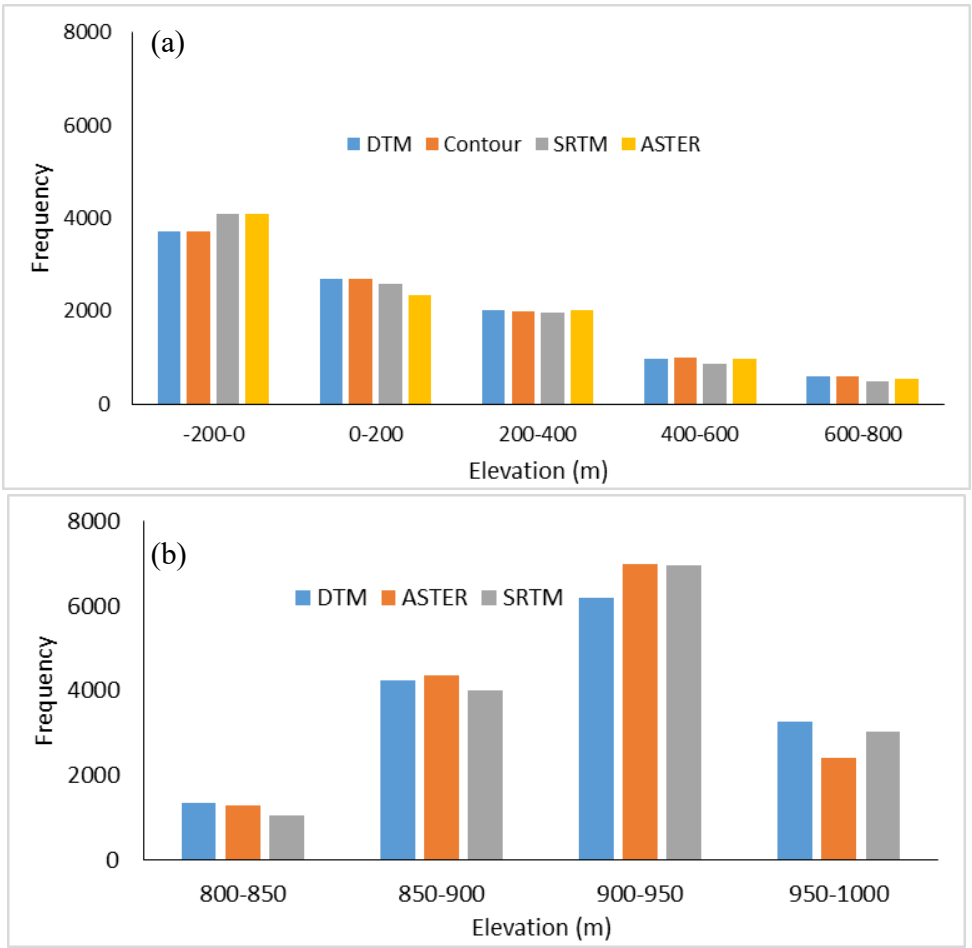

Fig. 4.7 Elevation distribution for each DEM

Elevation data of site-1 was divided into five equal ranges starting from -200 m to 800 m with a 200 m increment (Fig. 4.7a). On the other hand, elevation data of site-2 was divided into four equal ranges from 800 to 1000 m with 50 m increments (Fig. 4.7b). It was found that, for all ranges at site-1, DTM and contour provide equal absolute elevations while SRTM provides poor results in 400-600 m range than ASTER within 2 %. In site 2, ASTER provides low absolute elevations than SRTM in the range of 950-1000 within 6%; otherwise, both are almost similar, although higher elevation differences are present than the DTM.

4.3.2 DEM accuracy using ENN model

The ENN model was developed based on the minimum error to rectify DEM. The results of the accuracy assessment of corrected DEM using ENN were compared with DTM. The elevation variation with corrected DEM is in agreement with that of DTMs. The model's accuracy was found to be 94.69% using Eq. (11), while the RMSE was 0.58 m. This result is acceptable, as the pixel size was 30 m (< 2% of pixel size). The distribution of the corrected DEM to DTM (as a point to point evaluation) shows a linear relation (R^2> 0.99) (Fig. 4.8). This method was applied earlier in a study conducted by Nguyen et al. (2019). They corrected Terrestrial Laser Scanner (TLS) points based on Real-Time Kinematic (RTK) points.

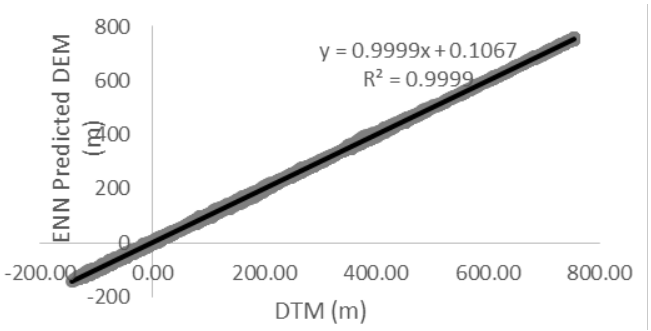

Fig. 4.8 Point to Point elevation relation between DTM and predicted DEM

4.3.3 Hydrological Parameters

The estimated hydrological parameters were assessed to evaluate the ability and the impact of spatial resolution using different DEM sources compared to the DTM. Fig. 4.9 and Fig. 4.10 shows the difference between the profile sections for various DEMs utilised in the DSM. Additional sections cover all the directions to examine different DEMs. It was found that the DTM and TOPO profile has been well fitted among all the profiles with minimum error, and the topographic terrain gave almost similar results presented in DTM and TOPO DEM and the error related to the difference in cell size. The ASTER DEM follows the similar DTM and TOPO DEM pattern in all the profiles directions better than SRTM DEM, shown in sections A-A and B-B.

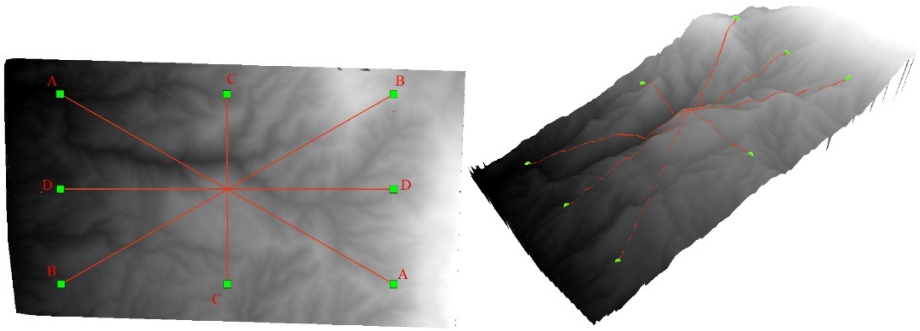

Fig. 4.9 Perspective view of the study area from digital elevation model. (Red lines show transects for profiles)

The slope degree was estimated for each DEM (Fig. 4.11), the cell size and the middle of the main-stream has the maximum slope value at each DEM. The slope from DTM (as reference DEM) ranges 0-88.56, and slope TOPO DEM ranges 0 - 42.21. The ASTER GDEM and SRTM DEM slope range 0-50.49 and 0.12-33.55, respectively. The slope gradient is shown for different DEM datasets in Fig. 4.12a, indicating that the slope from TOPO DEM and ASTER were within 3 % close to the slope from DTM and

is better than the SRTM slope. It can be found that after 45 degrees, the TOPO slope behaves differently due to the range of slope TOPO DEM and ASTER GDEM

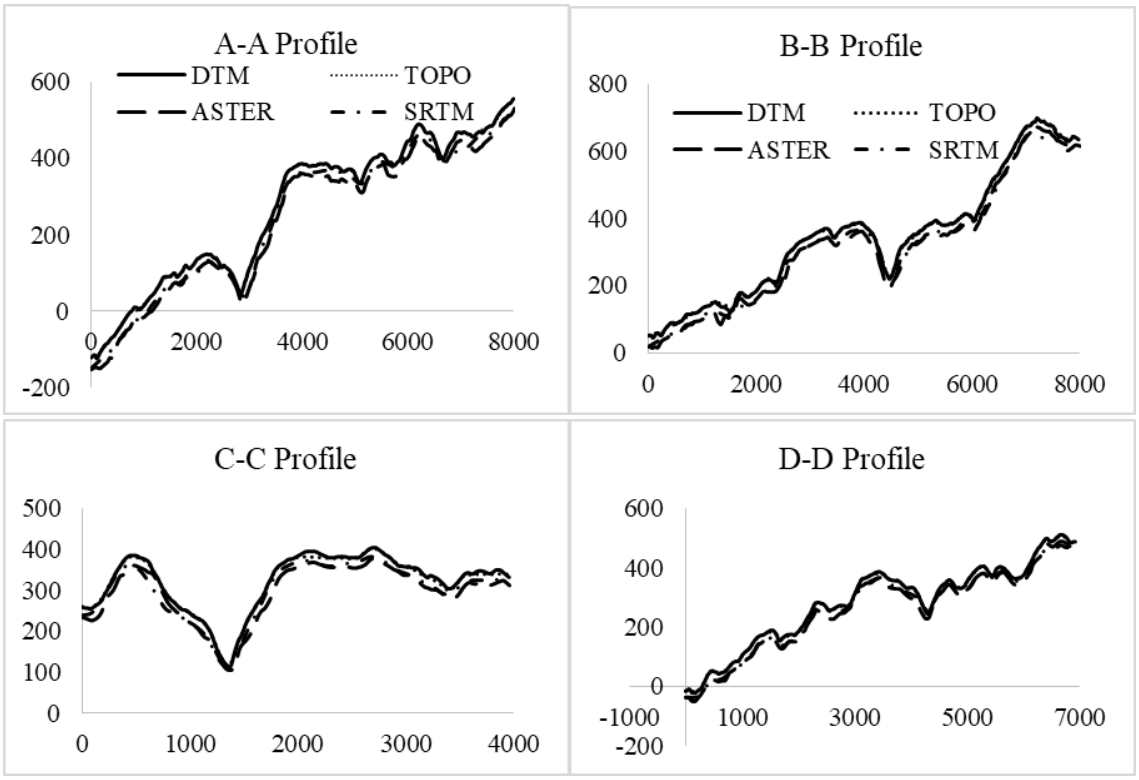

Fig. 4.10 Profiles of the three DEMs with DTM

LS factor (Fig. 4.12b) shows a close match between TOPO and DTM (absolute error = 0.61 m), where ASTER follows the similar path with DTM (absolute error = 3.49 m) with gaps slightly different than that of SRTM (absolute error = 5.55 m). The comparison between all DEMs is shown in the range 0.9-1.2 and, in some cases, more than 1.2. The profile and plane curvature in Fig. 4.12c and d, respectively, shows that the ASTER GDEM was within a 2 % close match to DTM more than TOPO and SRTM DEM. The TOPO and SRTM DEMs have well fitted to each other plane and profile curvature. The high resolution DEM captures comprehensive topography changes, leading to a more accurate estimation of soil loss. In the LS factor (one of the soil loss

parameters), the figure shows a close match between DTM, TOPO, and ENN DEM than that of SRTM and ASTER (as global datasets). Also, the curve of the *LS* factor derived from various DEMs show comparability among ASTER and SRTM with DTM (Fig. 4.12). However, the majority trend of ASTER shows a similar and close trend with DTM compared with SRTM. TOPO DEM's behaviour differs from DTM and ENN DEM and matches ASTER DEM in the slope case.

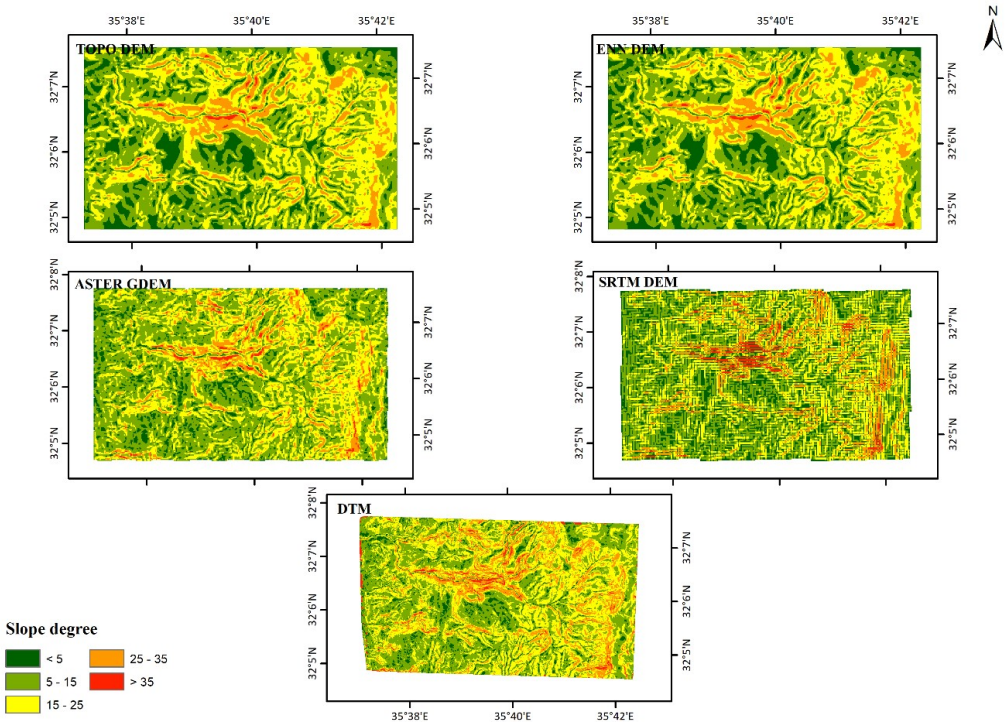

Fig. 4.11 Slope map derived from Aerial photo, TOPO DEM, ASTER GDEM, and SRTM DEM

Similarly, the analysis of DEM according to terrain aspects and flow direction was carried out. Each DEM shows a similar pattern of aspect (Fig. 4.13). Regarding the aspect error, the SRTM has a higher elevation error than other DEMs, especially ASTER, which matches with DTM. The ASTER GDEM closely matches the DTM aspect in all the directions (absolute error = 0.63), the TOPO DEM differs the most in the W direction

(absolute error = 0.84). The SRTM DEM behaves differently between S and W and has followed the same shape and direction (absolute error = 2.23 m). On the other hand, the flow directions have differently behaved. The TOPO fitted well with DTM (absolute error = 0.68 m) in all the directions better than ASTER, which behaves differently in ranges 64 and 1 (absolute error = 3.33 m). However, SRTM follows a different path between 32 and 1 (absolute error = 4.10 m). Hence, some cells have an undefined aspect due to the slope value being less than the threshold value (Mitasova and Hofierka 1993).

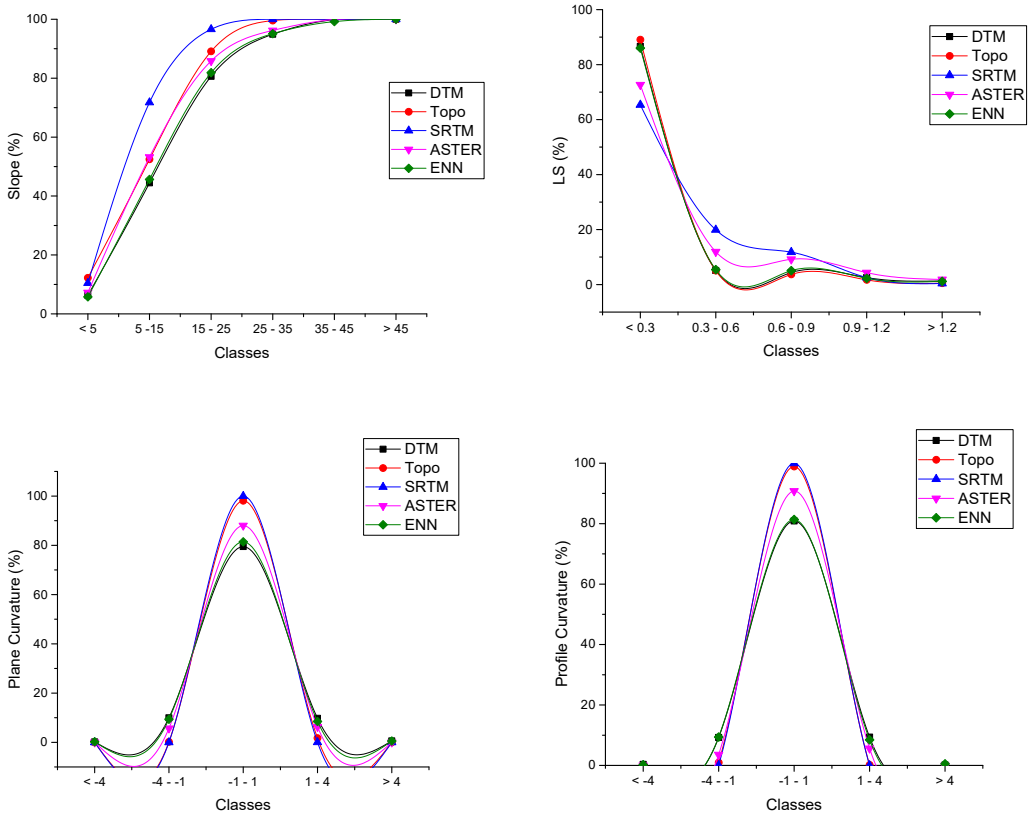

Fig. 4.12 (a) Slope gradient, **(b)** LS Factor, **(c)** Profile Curvature and **(d)** plan Curvature of various DEMs/DTM

A similar analysis was carried out with the rectified DEM (through ENN). Fig. 4.12 and 4.13 show the results of the slope, LS factor, plan curvature, profile curvature,

aspect, and flow direction prepared with the rectified DEM. The results from rectified DEM show good agreement with that of DTM than the original DEMs.

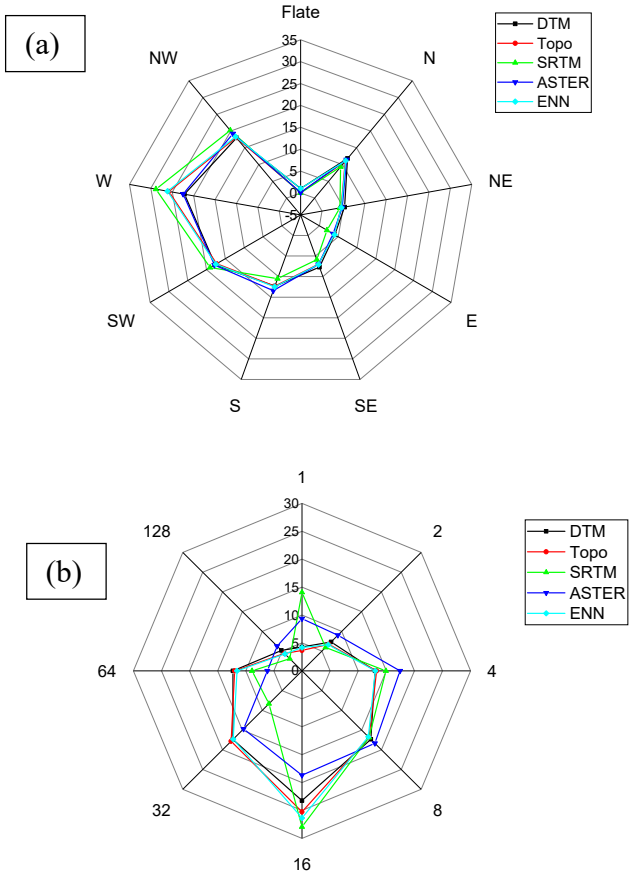

Fig. 4.13 (a) Aspect and (b) Flow Direction of various DEMs/DTM

4.3.4 Stream network and watershed

The assessment of the derived stream network and watershed and the visual comparison was finally done. The stream network derived from DEMs represents the pattern of streams networks. The drainage network (flow path) generated from this DTM is shown in Fig. 4.14a with other drainage paths. It is observed that the developed streams network was in close agreement with DEM from the contour map more than DEM from SRTM

and ASTER. The watershed was also derived from each DEM and compared with the DTM watershed, as shown in Fig. 4.14b. The statistical analysis results of both, based on DTM and GCPs, gives similarity for ranking in the available DEMs (Table 4.5). The DTM from an aerial photo and DEM derived from the topographic map shows a minor error after ASTER, and the SRTM DEM ranks last in this test.

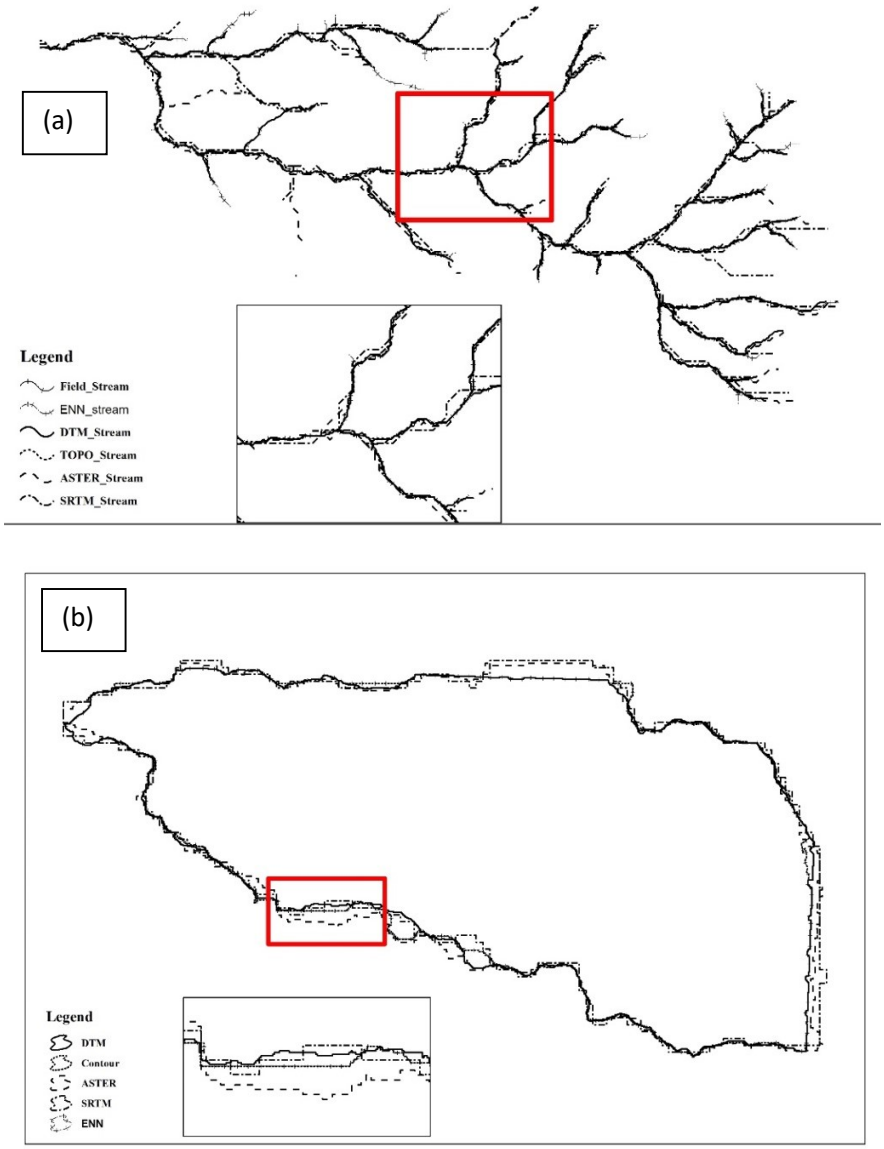

Fig. 4.14 (a) Streams network and (b) Watersheds extracted from various DEMs

Frey and Paul (2012) and Shafique et al. (2011) found that ASTER GDEM depends on three main factors: terrain complexity, quality of the image pair, and image acquisition angle. In the case of TOPO DEM, for some cases, the TOPO DEM has low accuracy compared to others DEM that was generated by other methods, whereas the TOPO DEM generated by using contour lines suffered from overlapping at steep areas and generalizations in flat terrain (Vaze et al., 2010; Wise, 2007). Results from rectified DEM shows better agreement with the DTM. Therefore, this ENN technique can improve the original DEM data and can be used for hydrological estimation.

Table 4.5 Summary of stream Network for each DEM

	DTM	ENN	TOPO	ASTER	SRTM	Field
Network Length (m)	41572.63	43315.12	41037.85	43754.66	40032.21	55565.65
Main Stream (m)	8780.66	8387.68	8462.11	8586.59	8441.27	7975.86
Watershed Area (m^2)	28390800	28419721	28509811.16	29290557.86	29142257.02	--------
Stream Order	4	4	4	4	4	4
First-order streams	29	29	29	28	27	40

4.3.5 Validation

According to National Geospatial Program (NGP) standards and specifications, the minimum number required for verifying the accuracy of DEM is 28 points distributed as 20 interiors and eight edge points (USGS 1998). The 47 GCPs, used for validation was distributed randomly in the study area and was used to calculate the RMSE for each DEM. Results indicate that the DTM has the most accurate DEM (RMSE = 1.11 m). Topo DEM shows better elevation data (RMSE = 4.21 m), and ASTER GDEM is found to give the closest match with GCPs. Table 4.6 shows the correlation between these DEMs and GCPs. The result agrees with Mokarram and Hojati (2016), who concluded that the DEM derived from the topographic map has a high correlation with GCPs with a correlation coefficient almost equal with paper results.

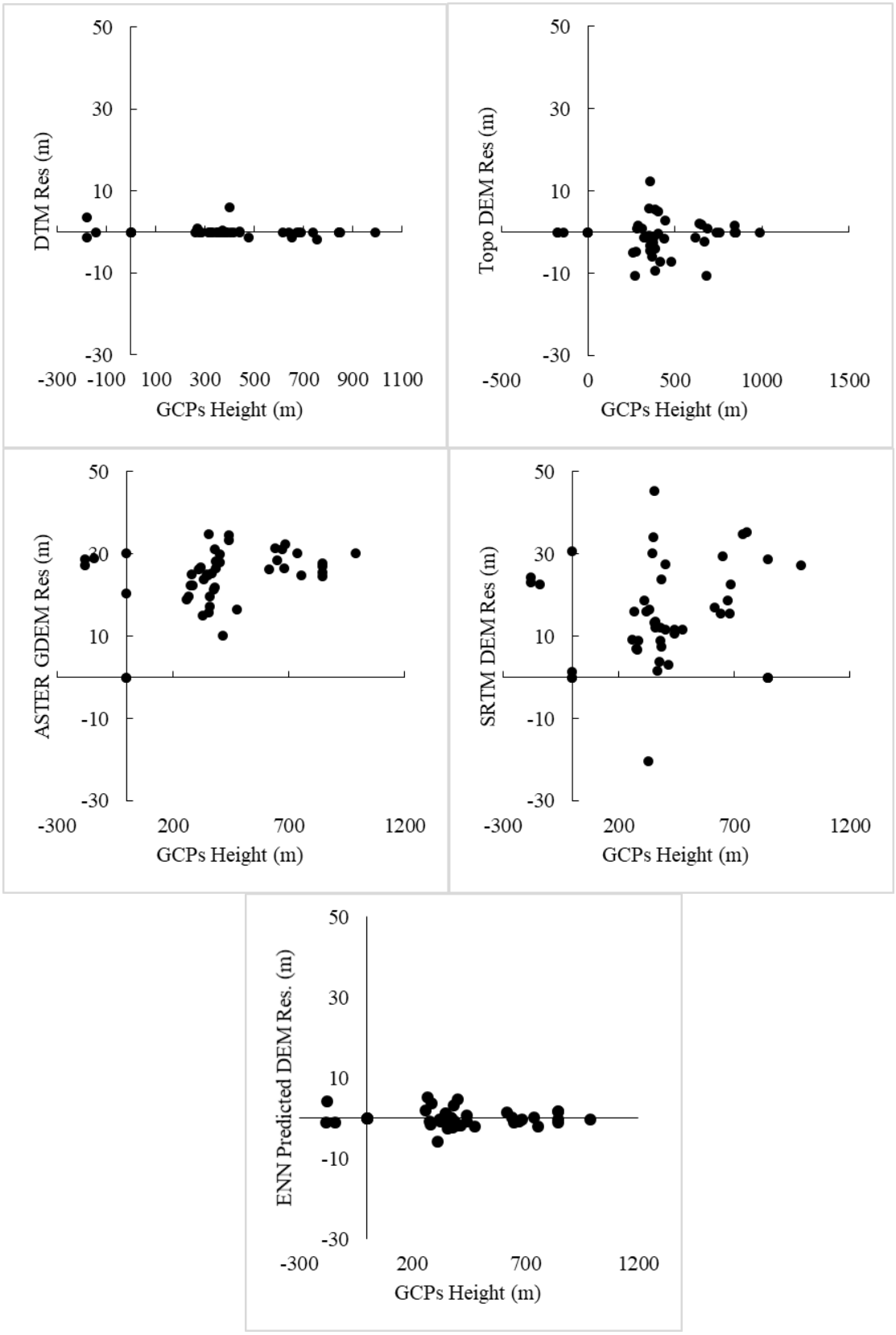

Fig. 4.15 Residuals distribution among the elevation data

The ENN predicted DEM was also compared with GCPs, where the RMSE was 1.97 m. Fig. 4.15 shows the distribution of the residuals with elevations among different DEMs. These results support the previous studies (Frey and Paul, 2012; Mukherjee et al., 2013; Thomas et al., 2015) and prove that one can use a topographic map as a paid source or ASTER GDEM open source in place of using aerial photos to derive DTM.

Table 4.6 Correlation between DEM and GCPs

	GCPs	DSM	TOPO	SRTM	ASTER	ENN Predicted
GCPs	1					
DSM	0.999989	1				
TOPO	0.999764	0.999783	1			
SRTM	0.998955	0.998982	0.99935	1		
ASTER	0.998978	0.99959	0.562814	0.706836	1	
ENN Predicted	0.999974	0.999982	0.566813	0.710354	0.999564	1

4.3.6 Streamflow estimation at the outlet

Streamflow was calculated for different DEMs using the SWAT model. **Fig. 4.16** shows the different periods of streamflow under three types of precipitation events (high, moderate, and low) to determine the impact of DEM source on hydrological modelling. During high precipitation events, the variations in streamflows between DEM sources were shallow, except ASTER DEM, which behaved differently during a sudden change in the precipitation. During a moderate rainfall, the SRTM DEM showed a different trend up to the peak. In low rainfall, the SRTM had another behaviour at peak in 2007. These hydrographs showed that the DTM simulation generally had a higher elevation than flows simulated with low-resolution DEM.

Table 4.7 provides the lengths of the channel networks extracted using a threshold value of 0.5 km^2 and the drainage density (Montgomery and Foufoula-Georgiou, 1993). The size of the DTM channel network is 8% longer than that extracted by contour maps,

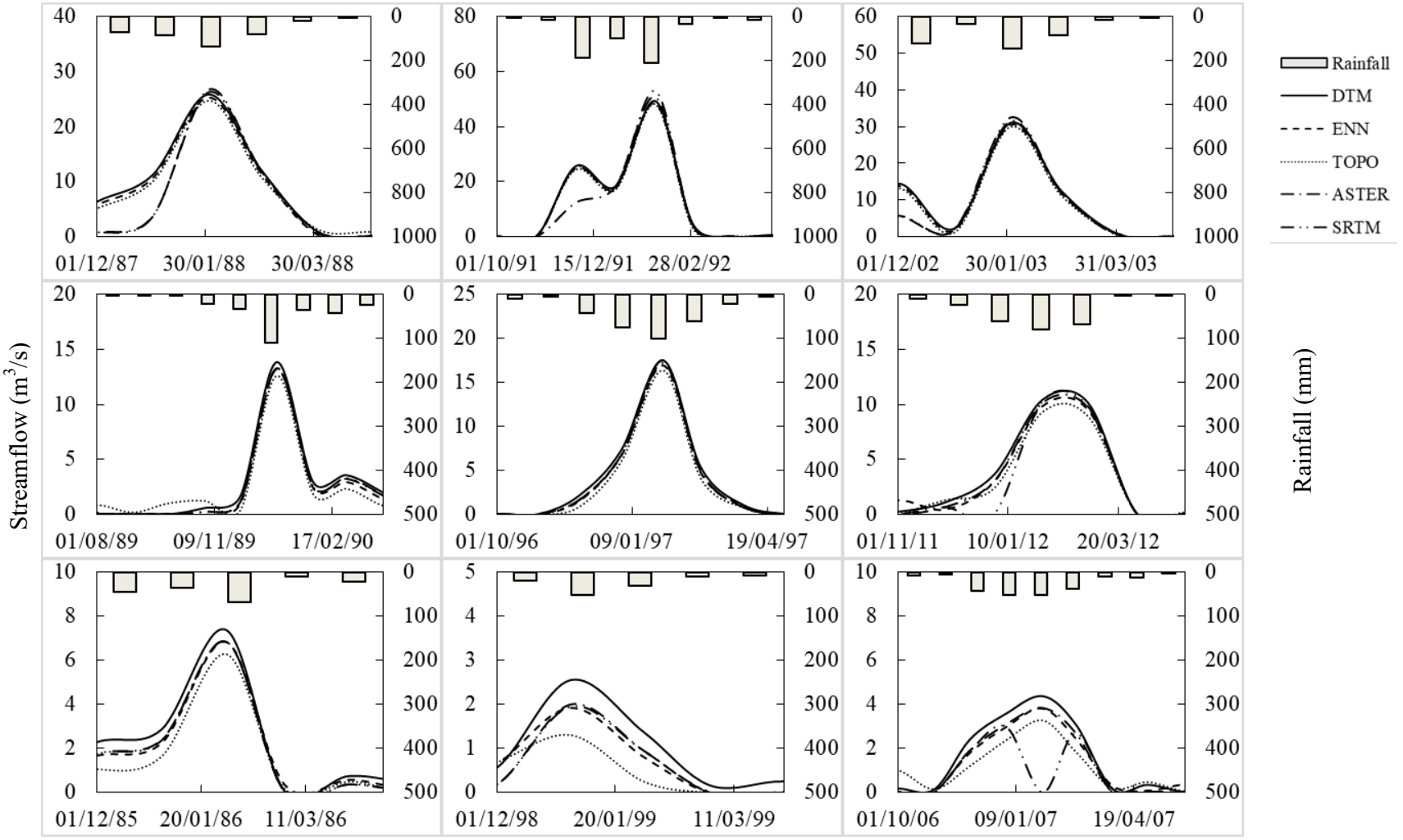

Fig. 4.16 Simulated streamflow during different precipitation events

25% and 26% longer than that extracted by ASTER GDEM and SRTM DEM, respectively. While that extracted from predicted DEM using ENN was 6.7% longer, suggesting its higher ramification and further extending upslope. The channel network's greater length and ramification indicate a faster transfer of excess rainfall to the outlet because the flow velocity through the channel is always greater than the velocity over the natural surface. This phenomenon leads to a higher peak flow and a shorter peak time. Degetto et al. (2015) applied similar techniques on two study areas using different DEMs. They found that when the basin area is equal, the corresponding DEM's peak flow, which has higher stream ramification and longest flow drainage path, is always higher than other DEMs.

Table 4.7 Summary of stream network for each DEM

	DTM	ENN	TOPO	ASTER	SRTM	Field
Network Length (m)	41572.63	43315.12	41037.85	40754.66	40032.21	55565.65
Main Stream (m)	8780.66	8387.68	8462.11	8586.59	8441.27	7975.86
Watershed Area (m^2)	28390800	28509811.32	28509811.16	29290557.86	29142257.02	--------
Stream Order	4	4	4	4	4	4
First-order streams	30	36	29	28	27	40
Drainage density (m/m^2)	0.00145	0.00152	0.00144	0.00139	0.00137	--------
Maximum flow path length (m)	15094.20	14073.17	13867.23	11326.47	11201.81	14055.48

4.4 Conclusion

This chapter is dedicated to analyzing various Elevation data (or models) available as an open repository or commercial platform. In many cases, the accuracies of the elevation data are reported based on their absolute accuracies. But, for hydrological studies, the relative accuracies are also essential to find out the slopes and aspects. This chapter discusses these studies and found that the ASTER GDEM gives acceptable results in

modelling the streamflow than DTM and DEM derived from topographic maps. Moreover, the analyses were carried out with the rectified DEM through ENN models for the above mentioned hydrological parameters. The results were found that the results were improved and agreed reasonably well with the DTM.

Chapter 5: Capacity Estimation and Sediment Deposition of Reservoir

5.1 Introduction

Wadi Shueib catchment has mild to steep slopes, which increases the possibility of soil erosion and its movement downstream because of the impact of rainfall and overland flow generation. As the Wadi Shueib dam is located at the catchment outlet, estimating the dam's capacity change is needed. Thus, the dam sustainability and monitoring using optical remote sensing technology will increase the efficiency by minimizing the risks during the surveying instead of traditional techniques (e.g. handicraft survey). This technique is also helpful in the time to time updating of reservoir capacity. In this chapter, a 3-dimensional model was developed to estimate the reservoir capacity using the dam's remotely sensed data and synchronized water levels. Subsequently, sediment deposition in the Wadi Shueib dam was calculated from the reservoir capacity for two different dates. The work involves modelling the reservoir's underwater topography using water levels and extracted surface area from Landsat imagery.

5.2 Data Analysis

The details of the study area are explained in chapter 3. Besides the Wadi Shueib catchment, two more dam sites were used in this study to develop the model and its validation (Refer section 3.2 and 3.9). Considering additional sites was due to the absence of detailed data regarding reservoir capacity at various times in the Wadi Shueib dam. However, two other dams were chosen so that the reservoir's capacity is available at different times. The method involved in this work can be summarized into three parts: (i) applying vegetation indices techniques to determine the extent of water surface through

image processing of satellite data, (ii) establishing the relationships between water level-area-capacity of a reservoir, and (iii) validating the model from reservoir data and finally applying in Wadi Shueib dam for its capacity.

Remote sensing data obtained from Landsat satellites and data recorded at the dam sites were used to develop a 3-Dimensional reservoir bathymetry model using Triangulated Irregular Networks (TIN) technique (Table 5.1). From the satellite data, the water spread area was obtained. From the observed record of water level and storage capacity, a mathematical model was developed. Thus, the reservoir storage volume was determined (Fig. 5.1). The TIN was used because it is considered superior amongst other split methods to assess the underwater topography (Mi et al., 2007; Lu et al., 2013). Details of the model will be discussed in the respective chapter.

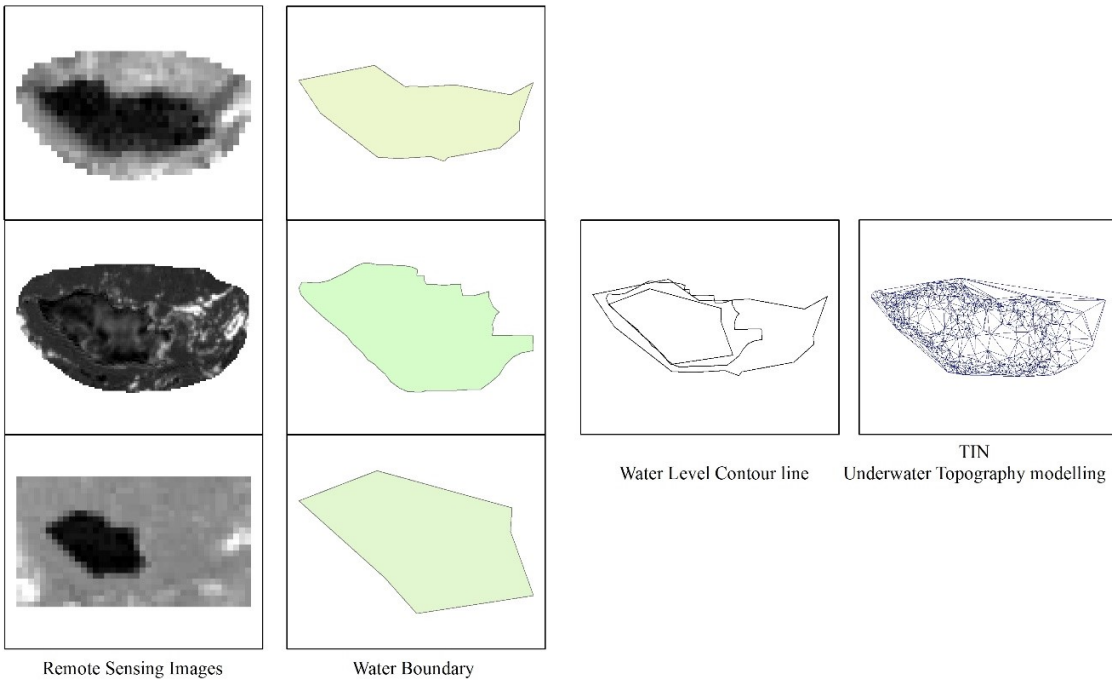

Fig. 5.1 Framework of reservoir capacity calculation method used

Table 5.1 Remote sensing data used

Sensor	Acquisition Date	Sensor	Acquisition Date
Landsat-5 / TM	4/12/2003	Landsat-7 / ETM+	5/22/2009
	6/23/2003		2/18/2010
	8/10/2003		7/12/2010
	10/13/2003		12/3/2010
	3/21/2004		1/20/2011
	5/24/2004		4/4/2012
	7/11/2004		8/26/2012
	12/2/2004		4/8/2013
	4/25/2005		2/13/2014
	11/19/2005		1/31/2015
	2/23/2006	Landsat-8 / OLI	8/27/2015
	12/24/2006		4/23/2016
Landsat-7 / ETM+	1/25/2007		2/5/2017
	5/1/2007		4/26/2017
	5/3/2008		5/2/2017
	12/13/2008		10/19/2017
	1/30/2009		4/13/2018

5.2.1 Image processing

Vegetation indices are the most common techniques used in remote sensing to determine wetlands' optical measurement of vegetation canopy greenness. The vegetation indices are based on chlorophyll presence (Huete, 2014). The essential elements of vegetation indices are red with the spectral region and near-infrared, while the chlorophyll is absorbed in the red area and reflected in the infrared region. The widely used vegetation index and water index are described below in brief.

5.2.1.1 Normalize Difference of Vegetation Index (NDVI)

Rouse et al. (1974) proposed a new approach for vegetation monitoring based on the spectral region using remote sensing data and NDVI. The NDVI can be calculated using the formula given in Eq. 5.1 below:

$$NDVI = \frac{NIR - RED}{NIR + RED} \quad 5.1$$

NIR are reflectance data from the near-infrared band, and RED are data from the visible red band of the electromagnetic spectrum. Mathematically, the NDVI can vary from -1 to +1, where negative values indicate water pixels.

5.2.1.2 Normalize Difference of Water Index (NDWI)

Ouma and Tateishi (2006) proposed NDWI as a water index based on a logical combination of the TCW index. As to water extraction, NDWI is adopted here, which is defined as

$$NDWI = \frac{Greeen - NIR}{Greeen + NIR} \quad 5.2$$

Where Green has a spectral region, and NIR represents the band in satellite images. This index is designed to exploit water reflectance by using the green band and minimizing the NIR band's low reflectance by water features (McFeeters, 1996). Values greater than 0.3 indicate water pixels.

5.2.2 Reservoir Capacity and Sediment Estimation

The analysis was divided into two major stages: first, vegetation indices were calculated to extract the surface water area of the dam using time-series satellite imagery. Water contours were created from the water level record corresponding to the satellite data using the Arc-GIS platform. A 3-D reservoir model was generated using Triangulated Irregular Networks (TIN) model from this water level and spread area. From this model, the storage volume can be estimated corresponding to any water level. The storage capacity of the reservoir was calculated using the following Eq. 5.3 as:

$$V = \sum_{i=1}^{n} \frac{S_i (h_i + h_{i+1} + h_{i+2})}{3} \quad 5.3$$

Where V is the storage capacity (m^3), S_i is the projected water surface area (m^2), h_i, h_{i+1}, and h_{i+2} are the distance (m) of the underwater triangle vertices to the water surface, and n is the number of triangular grids (Lai et al., 2009). The variable $h_{i,}$ can be estimated based on the observed water levels of the reservoir from a fixed datum.

The change in reservoir storage capacity between two water levels was calculated using the Prismoidal equation (Eq. 5.4) of water spread area at those levels:

$$\Delta V_{a-b} = \frac{\Delta h \left(A_a + A_b + \sqrt{A_a A_b} \right)}{3} \quad 5.4$$

Where, ΔV_{a-b} is the change in capacity between water level E_b and E_a ($E_b > E_a$), and A_b are the water spread at water level E_b and E_a, $\Delta h = E_b - E_a$.

The sediment deposition volume for the Wadi Shueib dam was calculated from the capacity difference between the base year curve (2003) and the satellite data. The overall capacity of the Wadi Shueib dam was observed to be 1.43 Mm^3, at a water level of 17.0 m. The sediment deposition rate was estimated from the loss in storage capacity of the reservoir. Hence, a storage capacity survey was carried out using remote sensing data from 2003-2018 in water levels between 9.3 and 17.0 m. The difference in the cumulative storage of water capacity between the initial (base year = 2003) and final (2016) remote sensing survey gives the loss in live reservoir storage. For example, the elevation-capacity curve was obtained from the dam site in the year 2003. However, the estimated elevation-capacity curve from satellite data in 2016 curve was estimated using remote sensing data. The cumulative (integrated) difference will be calculated to

determine the sediment deposited between 2003 and 2016. Sediment deposited volume (V_s) was estimated using the Eq. 5.5:

$$V_s = \left[\int_{L_1}^{L_2} V\right]_{\text{Initial}} - \left[\int_{L_1}^{L_2} V\right]_{\text{Final}} \quad 5.5$$

Where L_1 and L_2 represent the water level in the reservoir.

In the second part, another two reservoirs were considered to validate the capacity and sediment deposition estimation method. The method mentioned above was thus applied to the Anderson Ranch and Elephant Butte reservoirs to validate the results.

5.3 Results and Discussion

5.3.1 Validation of sediment estimation

The Wadi Shueib reservoir does not have a continuous sedimentation record. For this reason, it was not possible to directly assess the sediment estimation using this technique. Two separate reservoirs were chosen to overcome this deficiency with continuous capacity and sedimentation records (e.g., water level, water surface, water capacity, and sediment deposition). Fig. 5.2 and Fig. 5.3 shows the elevation-area-capacity curve of Elephant Butte and Anderson Ranch reservoir, respectively. Satellite images were used to extract the spread surface area when the capacity data were available. From the water spread area, the capacity of the reservoirs was calculated. Also shown are the estimated surface area and capacity based on satellite images with original data for Anderson Ranch and Elephant Butte reservoirs. Table 5.2 and Table 5.3 shows the significance of the results using *t*-test while comparing area and reservoir capacity. The test compares each sample based on a 95% confidence level. Based on these results, it was found that the

satellite images can be used to estimate the surface area and storage capacity with a reasonable error (RMSE < 0.04) for water bodies (e.g. lake, reservoir, wetland).

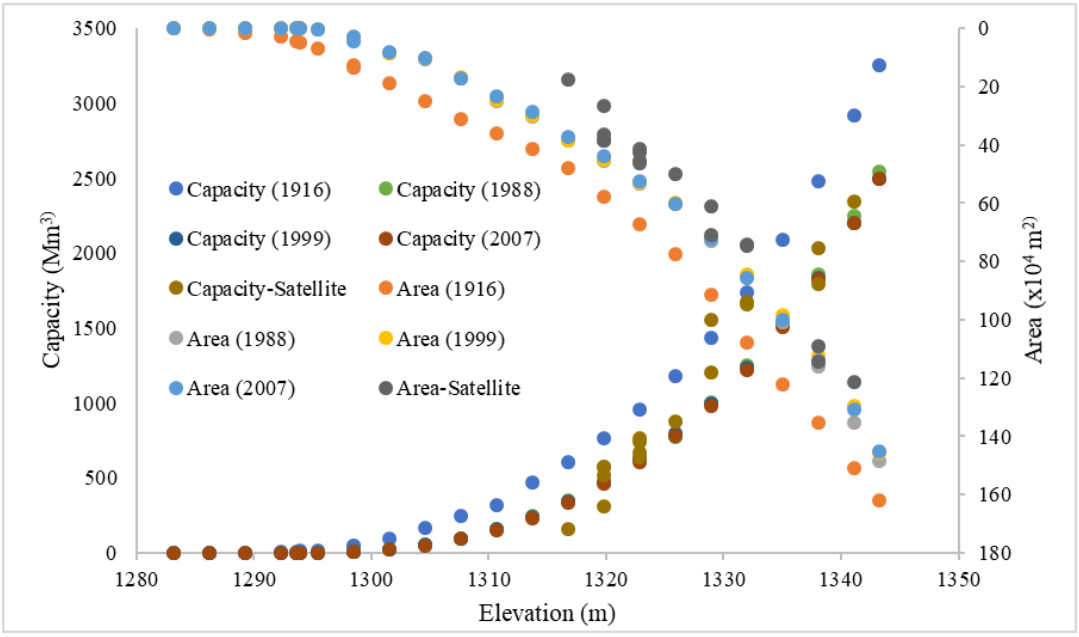

Fig. 5.2 Curve relation of calculated area and capacity with original data of Elephant Butte reservoir

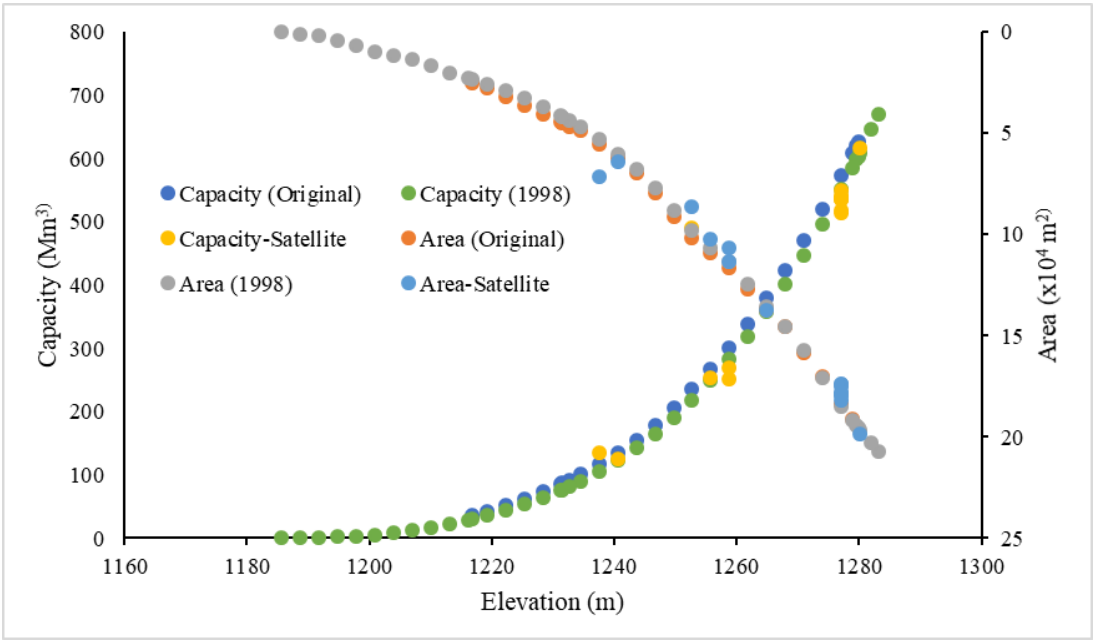

Fig. 5.3 Curve relation of calculated area and capacity with original data of Anderson Ranch reservoir

Table 5.2 *t*-test of comparison between calculated and original data of Elephant Butte reservoir (n= 17)

Parameter	Value Area 1999	Value Area 2007	Value Capacity 1999	Value Capacity 2007
t Stat	6.33	7.01	-1.76	-2.00
p(T<=t) one-tail	5.02E-06	1.48E-06	0.048	0.03
t Critical one-tail	1.75	1.75	1.75	1.75
p(T<=t) two-tail	1.01E-05	2.96E-06	0.097	0.063
t Critical two-tail	2.12	2.12	2.12	2.12

Table 5.3 *t*-test of comparison between calculated and original data of Anderson Ranch Reservoir (n= 16)

Parameter	Value Area 1998	Value Capacity 1998
t Stat	1.85	-3.89
p(T<=t) one-tail	0.0424	0.0007
t Critical one-tail	1.75	1.75
p(T<=t) two-tail	0.085	0.001
t Critical two-tail	2.13	2.13

Sediment deposition was estimated for Anderson Ranch and Elephant Butte reservoirs using Eq. (5.5), and significance tests were performed using *t*-test. Table 5.4 and Table 5.5 shows the *t*-test results of calculated and observed sediment deposition. The difference between computed sediment from satellite images and reported sediment deposited in the reservoir was within the acceptable error ($p < 0.05$).

Table 5.4 *t*-test of comparison between calculated and original sediment volume in Elephant Butte Reservoir (n=17)

Parameter	Value 1999	Value 2007
t Stat	2.31	2.60
p(T<=t) one-tail	0.017	0.0096
t Critical one-tail	1.76	1.76
p(T<=t) two-tail	0.035	0.019
t Critical two-tail	2.12	2.12

Table 5.5 *t*-test of comparison between calculated and original sediment volume in Anderson Ranch Reservoir (n=15)

Parameter	Value
t Stat	-1.81
p(T<=t) one-tail	0.046
t Critical one-tail	1.76
p(T<=t) two-tail	0.092
t Critical two-tail	2.15

The validation part shows that the models applied by Lu et al. (2013) and Pandey et al. (2016) are applicable, regardless of the environmental conditions of the basin. Both these studies used satellite images to estimate the reservoir sedimentation and storage capacity with the help of water level and storage capacity, where they applied different mathematical models for that. The results were acceptable, as they found the approximate sediment deposition in the reservoir to the environment. They also recommended the use of satellite images accompanied by field surveys to get more accurate results.

5.3.2 Estimation of Sediment volume in Wadi Shueib reservoir

The analyses were made based on remote sensing data, with a common data period between 2003 and 2018. The statistical analysis (*t*-test) of reservoir capacity was carried out using a standard spreadsheet program. The water level-capacity curve was obtained from the Ministry Water and Irrigation of Jordan. The water level varies from 8.98 to 17.0 m (maximum water level) in the reservoir. The satellite images were collected to cover the Wadi Shueib dam at different times as available within the study period.

5.3.2.1 Water level contour and underwater topographic map

Based on water surface area with various water levels, the contour map was generated. Fig. 5.4 shows the water level variation, water surface area, and reservoir capacity at a temporal scale.

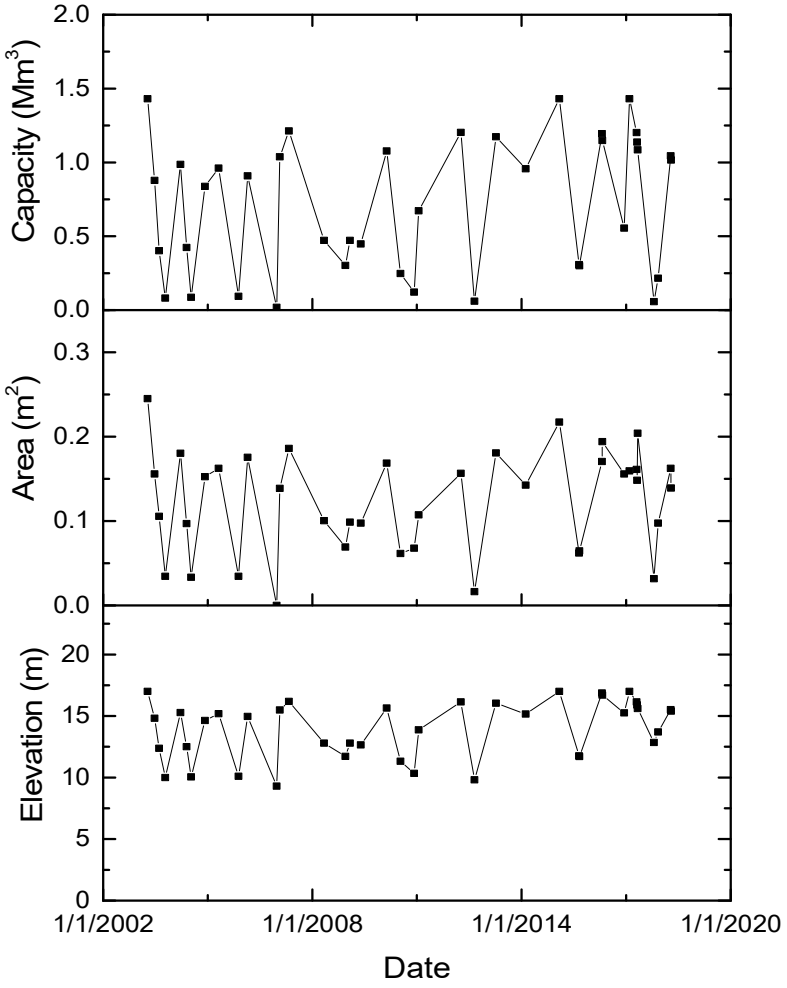

Fig. 5.4 The changing of water level-area-capacity of Wadi Shueib dam to time

5.3.2.2 Water level-area-capacity relations

The calculated storage capacity from satellite images of the Wadi Shueib dam using the TIN model varies from 0.01 to 1.24 Mm^3; however, the Ministry of Water and Irrigation of Jordan reported that the capacity ranged from 0.02 to 1.43 Mm^3. Fig. 5.5 and Fig. 5.6

shows the relation between calculated capacity and original capacity with water level and surface area. Table 5.6 shows the *t*-test results for comparing observed and computed capacity from satellite images for the Wadi Shueib dam. The results are within a 5% significance level. The second-order polynomial equation was fitted with R^2 ~0.90 and R^2 ~0.93 for calculated and reported capacity, respectively. Similar results were also reported by Lu et al. (2013) and Ferrari (1999, 2008). They found that the relation between water level and reservoir capacity lies with R^2 greater than 0.90.

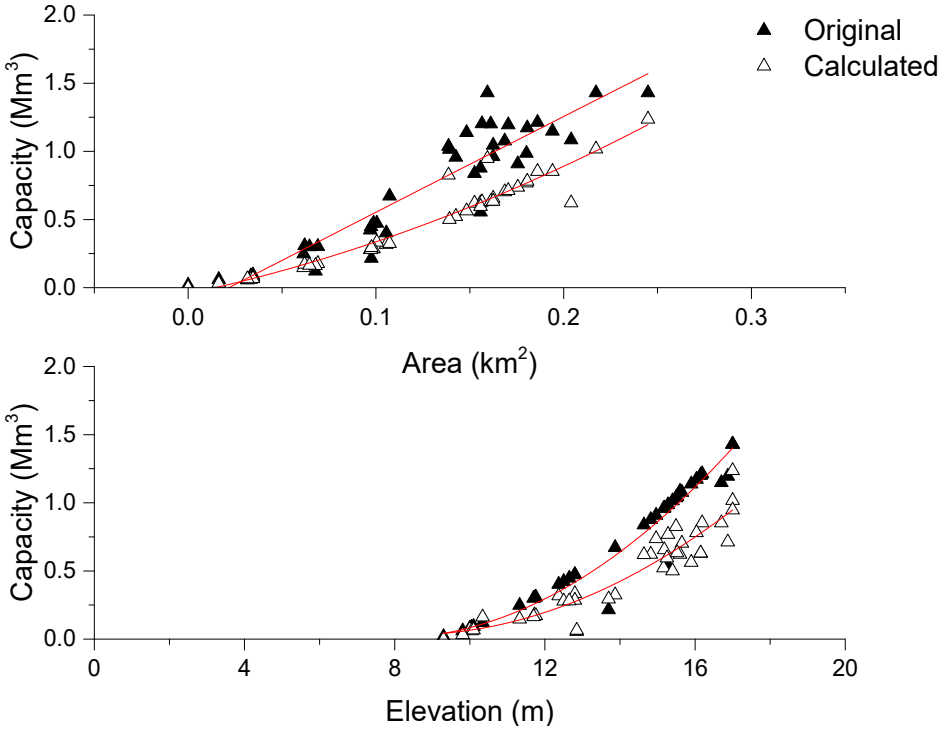

Fig. 5.5 Relationship between area-capacity and stage-capacity of Wadi Shueib dam

Table 5.6 *t*-test of calculated and observed capacity data (n=40) of Shueib dam

Parameter	Value
t Stat	7.81
p(T<=t) one-tail	8.42E-10
t Critical one-tail	1.68
p(T<=t) two-tail	1.68E-09
t Critical two-tail	2.02

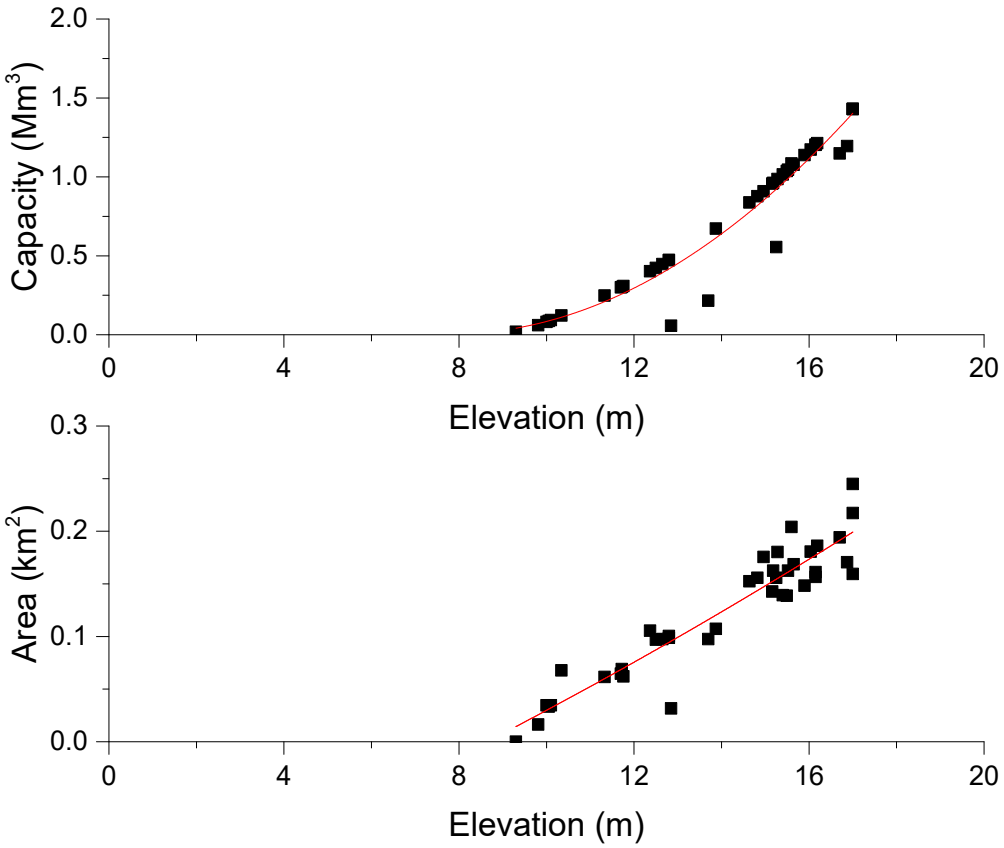

Fig. 5.6 Relationship between water level-calculated area and water level-capacity of Wadi Shueib dam

The linear regression analysis between calculated and reported capacity shows satisfactory fitting with R^2 ~0.90, with slope = 0.67 (Fig. 5.7). The RMSE between estimated and observed reservoir capacity was found as 0.09. The difference between calculated and reported capacity may be attributed to satellite imagery's quality and spatial resolution. The proposed method is widely used for calculating and monitoring the water capacity in lakes and reservoirs with variations in water level at Karaj Dam Reservoir, the Areal Sea, Urmia Lake, Lake Baiyangdian, Patratu Reservoir (India) (Destouni et al. (2010); Ding and Li (2011); Lu et al. (2013); Pandey et al. (2016); Mushtaq and Lala (2017)).

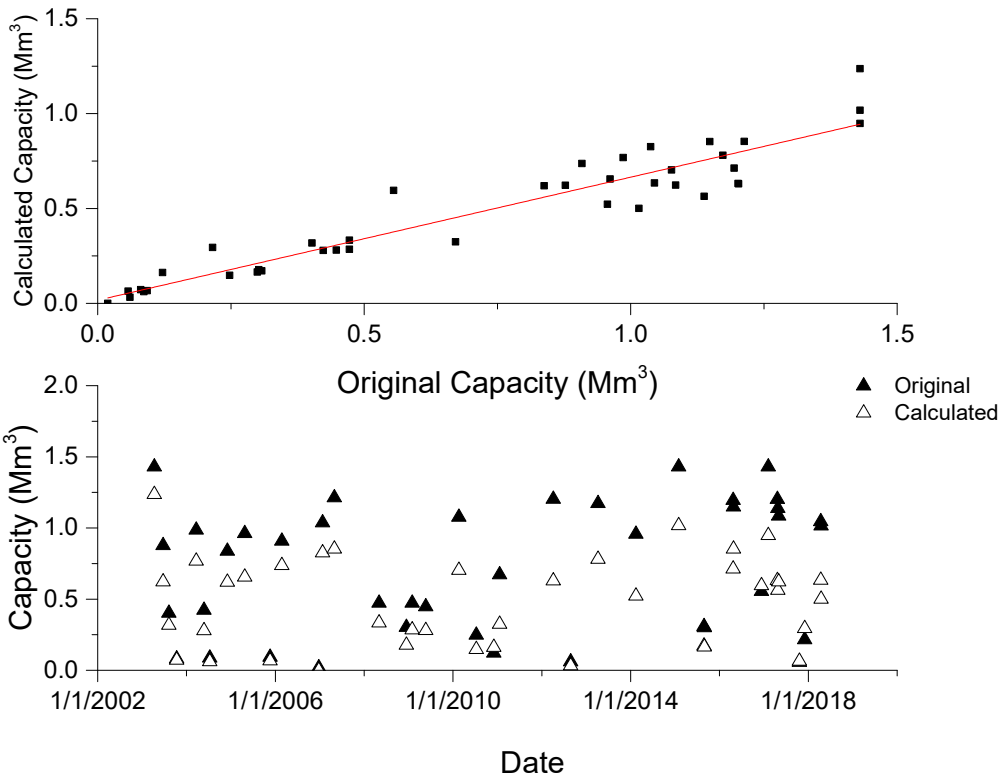

Fig. 5.7 Comparison between calculated and original reservoir capacity of Wadi Shueib dam

5.3.2.3 Estimation of reservoir sedimentation

The main objective of this chapter was to estimate the sediment deposited volume in the reservoir based on the remote sensing data in the data-scarce region. Through the satellite images, the spread surface area for the reservoir was calculated at a particular water level. Fig. 5.8 shows the difference between the original and calculated capacity using satellite images, where the sediment deposited was calculated within 9.3 and 17.0 m water level using Eq. 5.5. The sediment deposition volume was 0.66 Mm^3 during the study period. The increase of sediment deposition leads to a decrease in the storage capacity in the dam during the period, thus decreasing the water availability. Fig. **5.9** shows the relationship between water level and capacity at two different periods, 2003 and 2016. The figure also

shows a difference between these periods at the same water level, indicating sediment deposited in the dam during this period. The Jordan Valley Authority (JVA) reported ~0.56 Mm^3 sedimentation deposited based on the Wadi Shueib dam at the end of 2016.

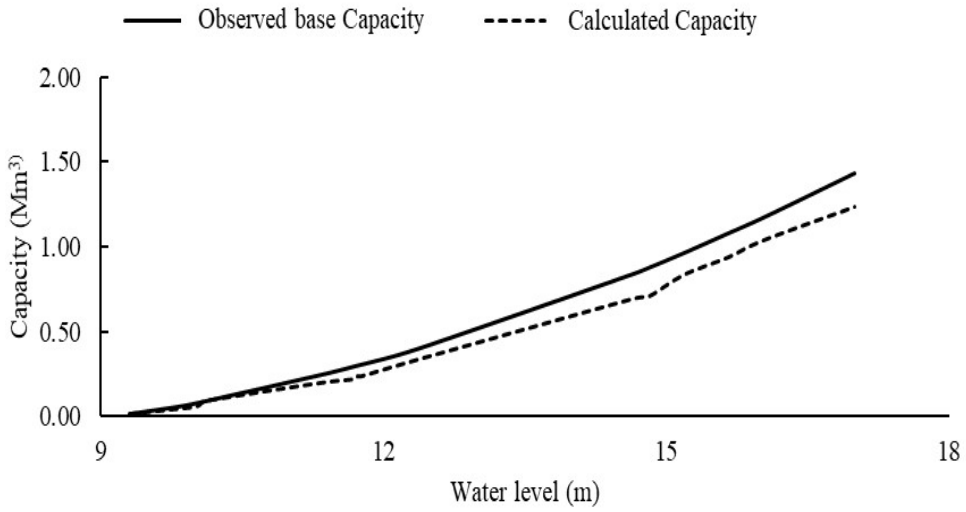

Fig. 5.8 Comparison of elevation–capacity curves of Wadi Shueib dam

Based on the present work, it is found that the future trend of precipitation in the Wadi Shueib area is increasing. It will directly affect the water availability in the Wadi Shueib dam. This problem can be managed by adopting different strategies to control soil erosion in the area, where the high variations in the slope lead to erosion. For this reason, the Ministry of Water and Irrigation of Jordan took initiatives to increase the storage capacity up to 2.3 Mm^3 for this dam and the work was finished in 2017. Fig. 5.9 represents water level vs capacity for periods 2003, 2016, and 2018. Interestingly, the water level-capacity curve in 2018 merged with the original curve of 2003. The increase of dam elevation does not solve the sediment problem, and hence, it is expected that this strategy may serve only for a short period.

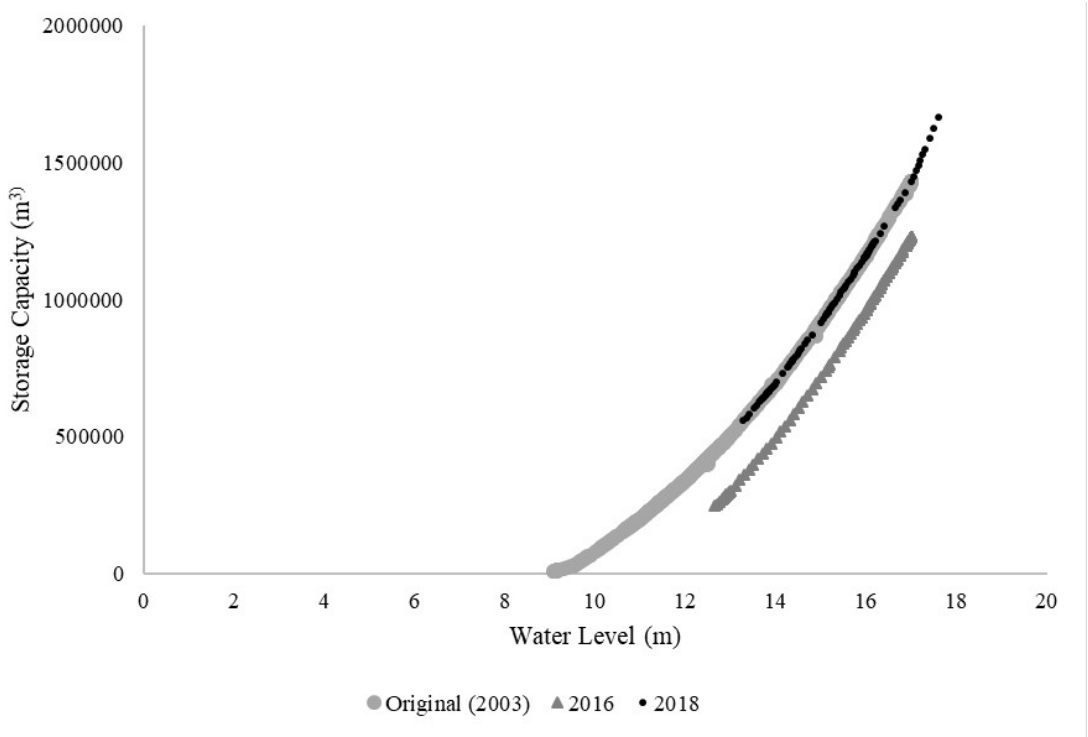

Fig. 5.9 Comparison of elevation–capacity curves of Wadi Shueib dam during 2003, 2016, and 2018

5.3.3 Field campaign

Based on field data, the topographic condition of the Wadi Shueib catchment area was a steep slope, where the slope ranges between 0 to ~45 degrees and analysed from digital elevation model (DEM) data. Fig. 5.10 shows the location map of the Wadi Shueib catchment along with soil samples locations. The soil sample was collected to find out the soil properties (hydraulic properties). Table 5.7 shows the hydraulic properties of soil samples in the field, similar to that of the experimental work. Fig. 5.10 represents the geographic location of soil samples. According to the Ministry of Water and Irrigation in Jordan, the rainfall intensity in Jordan varies between 30 to 250 mm/hr, while the average rainfall varies between 50 to 600 mm.

Table 5.7 Soil characterization and hydraulic properties for different sites in Jordan

Soil Mark	S-1	S-2	S-3	S-4	S-5
Sand (%)	70	67	55	50	30
Silt (%)	19	30	30	32	50
Clay (%)	11	3	15	18	20
θ_s (m^3/m^3)	0. 44	0. 29	0. 52	0. 58	0. 65
θ_f(m^3/m^3)	0.384	0.399	0.398	0.395	0.42
K_s (mm/s)	0.03	0.0504	0.015	0010	0.011

Notes: θ_s, θ_f, θ_w, and K_s refer to saturated water content, field moisture capacity, and saturated hydraulic conductivity, respectively.

National Soil Map and Soil Sample from Wadi Shueib Catchment

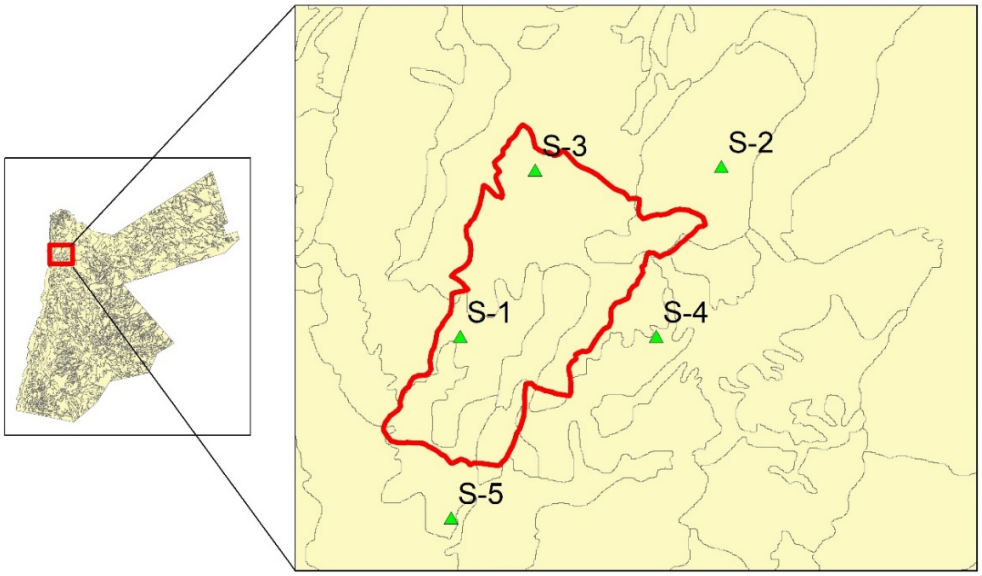

Fig. 5.10 S-1, S-2, S-3, S-4, and S-5 are soil samples from Wadi Shueib Catchment, and the grey lines represented the boundary of each sample (Source: Ministry of Agriculture)

5.3.4 Verification of field data

Due to the limitation in sediment deposition records in the Wadi Shueib catchment, the MUSLE model was chosen to estimate the sediment volume rate in the catchment area.

Jordan Valley Authority (JVA) reported sediment deposition of ~0.015 Mm^3 in the Wadi Shueib dam at the end of 2016. Fig. **5.11** shows the JVA machines removing the sediment from the Wadi Shueib dam. Karadsheh et al. (2013) reported that the annual soil loss due to water erosion amounts to 200 t/ha in the mountainous region of Jordan. The Ministry of Water and Irrigation of Jordan and JVA are putting an effort to utilize the dam for irrigation purposes by increasing the dam height.

Fig. 5.11 Jordan valley Authority removing sedimentation from Wadi Shueib dam using machines (in dry condition of the dam)

5.4 Conclusions

In this chapter, a 3-dimensional model is developed using satellite imagery synchronized with the water level and the reservoir capacity. The relationship was established among these three parameters. The model was validated in Anderson Ranch and Elephant Butte reservoirs located far away from the study site. However, the model worked well for both the reservoirs. Then based on the area-water level relationship of the Wadi Shueib dam, respective reservoir capacities were determined. It was found indirectly that the model

performed well in this dam which was also evident from the field verification. The calculated annual sediment volume deposition in the Wadi Shueib dam was close to the reported value by the Jordan Valley Authority. This sediment deposition quantity was used for the annual average sediment erosion from this catchment in further studies in chapter 9. Also, the reservoir status will be studied from a different view through estimation of the streamflow into the reservoir in chapter 8.

Chapter 6: Trend Analysis and Forecasting of Precipitation

6.1 Introduction

The study area has an arid to semi-arid climate with a high evaporation rate compared to precipitation events. This condition has implications for the availability of water for present and future use. Therefore, any management intervention to safeguard water availability is of utmost importance. Water resources management requires predicting and forecasting the future precipitation in the study area to realize the need to augment the water supply. This chapter describes a model to predict and forecast the monthly, average, and seasonal precipitation patterns in the study area. The specific work described in this chapter includes trend analysis using the MK test and ITA. Predicting the future precipitation pattern using the ARIMA model in the Box-Jenkins method is discussed here.

The chapter includes a brief introduction to time series, trend analysis and forecasting as techniques before applying these concepts to the precipitation data of the study area.

6.2 Time series

A time series is a set of observations (e.g., precipitation), where each observation is recorded at a specific time. The understanding of meteorological data (precipitation) leads to understanding the current and future situations. Data exploration is an essential part of analyzing the precipitation data. The data visualisation against the time shows the rainfall patterns during the time; in seasonal, monthly trend patterns, it is also possible to interpret the wet and the dry years (Brockwell et al., 1987; Peña et al., 2001).

6.2.1 Types of Time Series

There are two types of time series, (i) discrete: when the observations are recorded at a fixed time interval and (ii) continuous when the observations are recorded continuously at a specific time interval (Fig. 6.1a). The time series can be further classified into (i) stationary, where the mean value of the observations remain constant, and (ii) non-stationary, where the mean of observations changes with time. Non-stationary time series may be spurious in that they may indicate a relationship between two variables where one does not exist (Fig. 6.1b) (Chatfield, 2003; Cryer and Chan 2008). Also, the time series can be classified into seasonal and non-seasonal time series, where the time series is called a season when there is a repeating pattern at each specific time (e.g. year). In contrast, the non-seasonal time series happens when the series has an irregular pattern (not dependent on the time) (Fig. 6.1c) (Peña D. et al., 2001).

6.3 Trend Analysis

Trend analysis is a technique for understanding how and why patterns have changed or will change over time. The trend of time series has three possible results, decreasing, increasing, and no trend (Fig. 6.2), and these can be investigated using different techniques and methods. Usually, the decreasing trend shows falling in the time series data as it used to be, while the increasing trend shows a rising trend. The trendless or no trend term indicates no change in data (Cryer and Chan 2008).

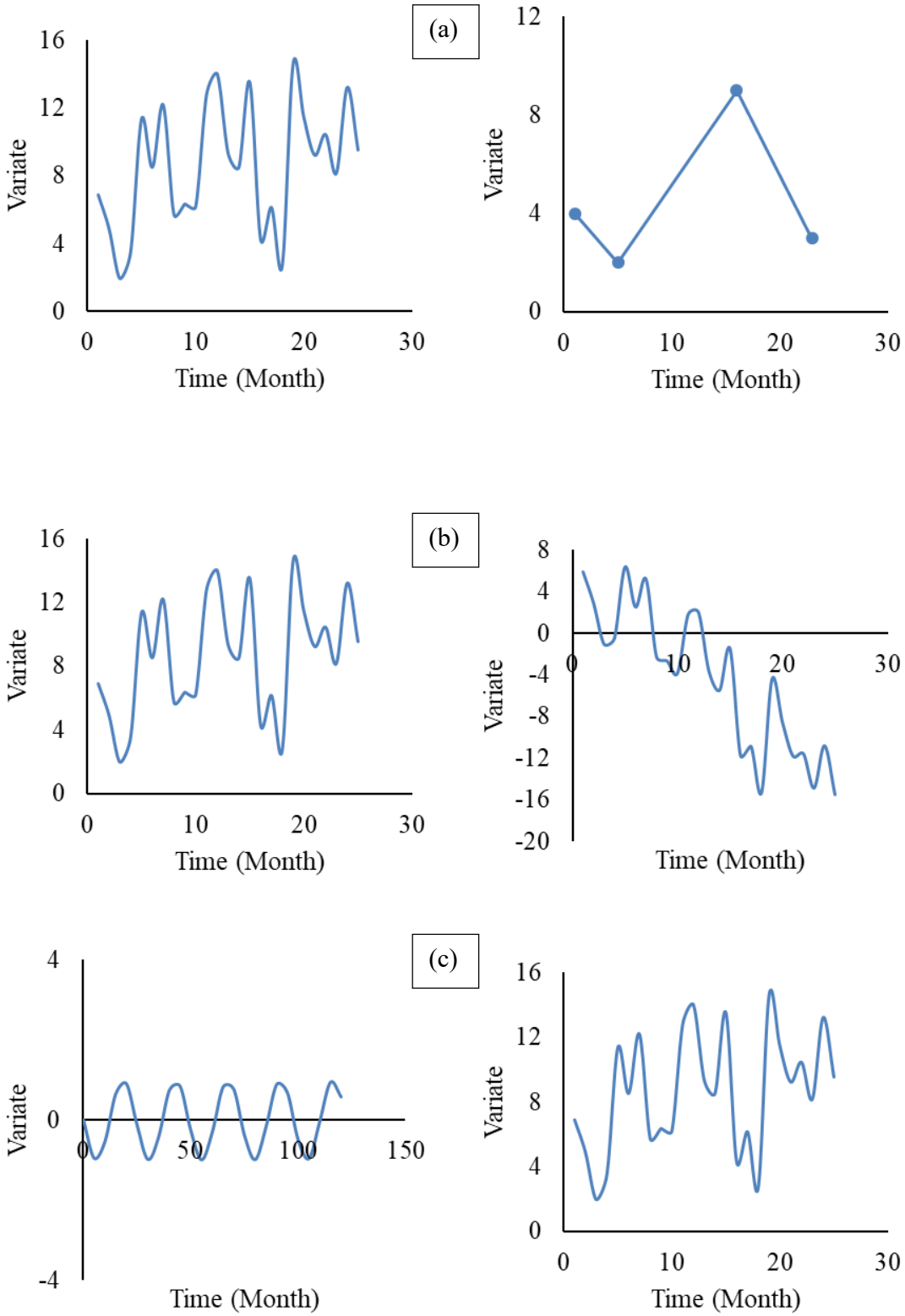

Fig. 6.1 Types of time series data

Several methods are used for detecting the trend in time series data, such as parametric, non-parametric, and machine learning techniques. These include Mann-Kendall (MK) test, Innovative trend analysis (ITA), Artificial Neural Network (ANN), Regression and more.

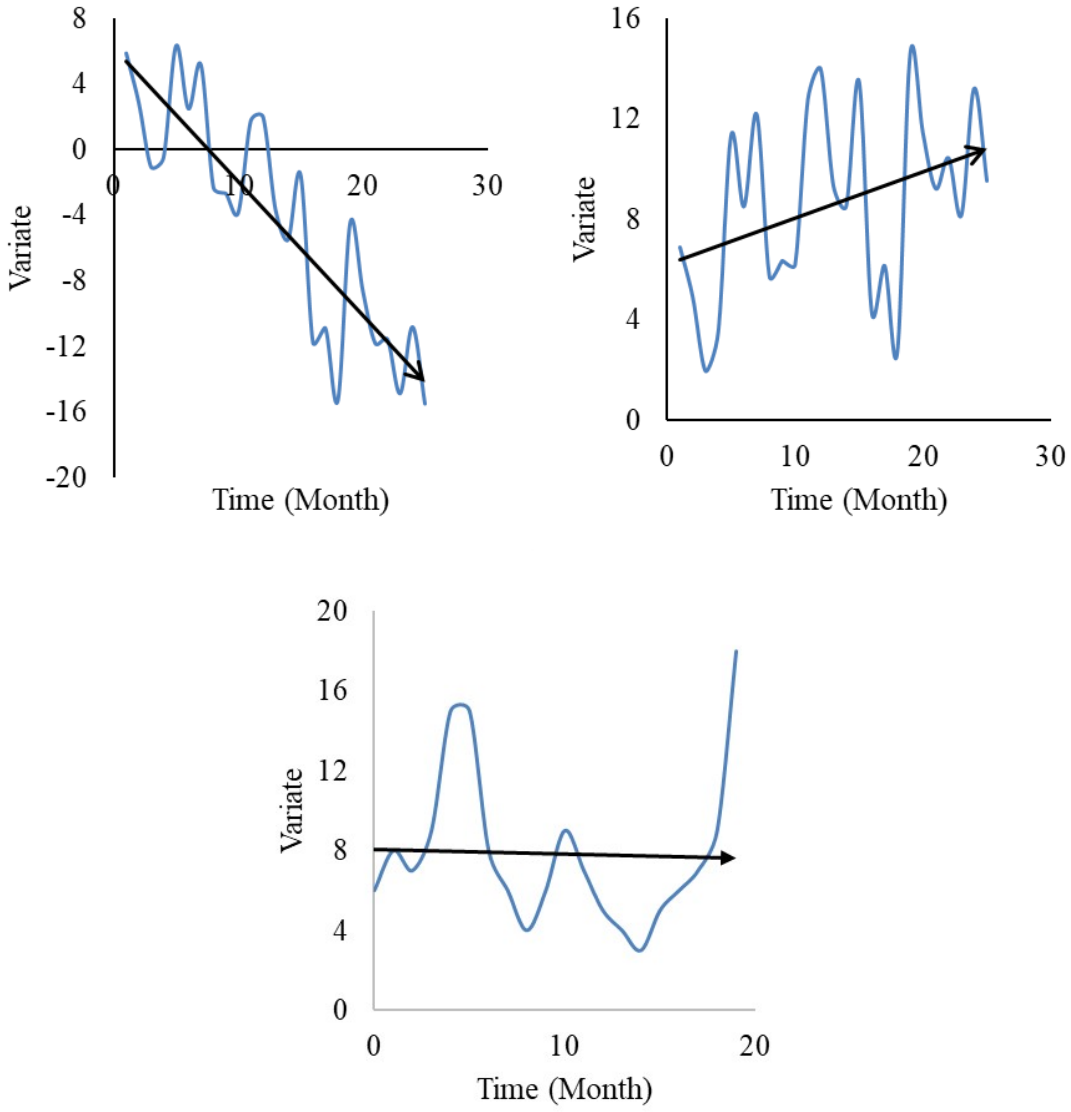

Fig. 6.2 Types of trend in time series data

6.4 Forecasting

Forecasting is a prediction of the future events of the time series. Forecasting can be (i) short term, (ii) medium term, or (iii) long term forecasting. Short-term forecasting involves predicting future events based on a short interval of time, e.g. days, weeks, and months; medium-term forecasts extend future events predicting up to 1-2 years. On the other hand, the long term may extend up to many years of future predicting. Short and medium-term forecasting is usually carried out for management and development purposes, while long term forecasts affect the issue like strategically planned (Montgomery et al., 2008; Peña D. et al., 2001; Kassambara, 2017; Hyndman and Athanasopoulos, 2018).

Auto-Regressive Integrated Moving Average (ARIMA) is one forecasting method used to predict data trends over time. The ARIMA model is based on a combination of three processes, Autoregressive (AR), Moving average (MA), and Integrating (I) between AR and MA. The AR (*p*) model uses the current value in time series, where ***p or d*** determines the number of the steps of past needed to forecast the present value (Brockwell and Davis, 2001; Peña D. et al., 2001; Kassambara, 2017; Hyndman and Athanasopoulos, 2018).

The principal difference between an AR and MA model is the correlation between time series objects at different time points. The covariance between x(t) and x(t-n) is zero for MA models. However, the correlation of x(t) and x(t-n) gradually declines, with *n* becoming more significant in the AR model. This result implies that the moving average (MA) model does not use the past forecasts to predict the future values, whereas it uses the errors from the past estimates. The autoregressive model uses past forecasts to predict future values.

6.4.1 Autoregressive Process

Most time series consists of serially dependent elements in the sense that one can estimate a coefficient or a set of coefficients that describe consecutive elements of the series from specific, time-lagged (previous) elements. This process can be summarized in equation 6.1:

$$x_t = \xi + \phi_1 x_{t-1} + ... + \phi_p x_{t-p} + \varepsilon \quad 6.1$$

Where ξ is a constant, ϕ is the autoregressive model parameter, and ε is random error.

An autoregressive process is stable if the parameters lie within a specific range. For example, if there is only one autoregressive parameter, it must fall within the interval of -1 $< \phi <$ 1. This condition is often referred to as stationarity. Otherwise, past effects would accumulate, and the values of successive x_t's would move towards infinity; i.e., the series would not be stationary. If more than one autoregressive parameter, similar (general) restrictions on the parameter values can be defined (Box and Jenkins, 1976; Kassambara, 2017; Hyndman and Athanasopoulos, 2018).

6.4.2 Moving Average Process

Each element in the series can be affected by the previous error (or random error) that cannot be accounted for by the autoregressive component, which can be given as (Eq. 6.2):

$$x_t = \mu + w_t + \theta_1 w_{t-1} + ... + \theta_q w_{t-q} \quad 6.2$$

Where μ is a constant, θ is the moving average model parameter, and w is random error.

There is always a duality between the moving average and autoregressive processes (Box and Jenkins 1976; Montgomery et al., 1990). The moving average equation above can be rewritten (inverted) into an autoregressive form of infinite order. This process is known as the Invertibility requirement. However, analogous to the stationarity conditions mentioned above, it can only be done if the moving average parameters are under certain constraints. For example, the invertibility of the model is required; otherwise, the series will not be stationary.

The summary is Pure AR Models depends on the lagged values of the data you are modelling to make forecasts. It depends on the errors (residuals) of the previous forecasts you made to make current forecasts.

6.4.3 **Auto-Correlation and Partial Auto-Correlation Function*s***

The Auto-Correlation Function (ACF) gives auto-correlation values of any series (time series) with its lagged values. These values are plotted with a confidence band, showing the relation of present values with its previous values. The ACF combines the time series trend, seasonality, cyclic, and residuals to determine the ACF plot. On the other hand, the partial auto-Correlation Function (PACF) finds the correlation of the residuals with the next lag value (Brockwell and Davis, 1991; Cromwell et al., 1994) .

In simple terms, the ACF describes how well the present value of the series is related to its past values; for that, the ACF is used in the moving average process because it shows a good correlation even with lags that are far in the past. A time series can have components like a trend, seasonality, cyclic and residual. So, the PACF is used to find any hidden information in the residual, which the subsequent lag can model, and later used in the autoregressive process (Montgomery et al., 2008; Kassambara, 2017). A

typical ACF and PACF are shown (Fig. 6.3). This indicates that either a trend should be removed or the series should be differenced (Fig. 6.3). In Figure 6, the autocorrelations seem to die down reasonably regularly after lag 1. The partial autocorrelations seem to be small after the first one, so it will be decided to fit an ARIMA (1,0,1) to these data.

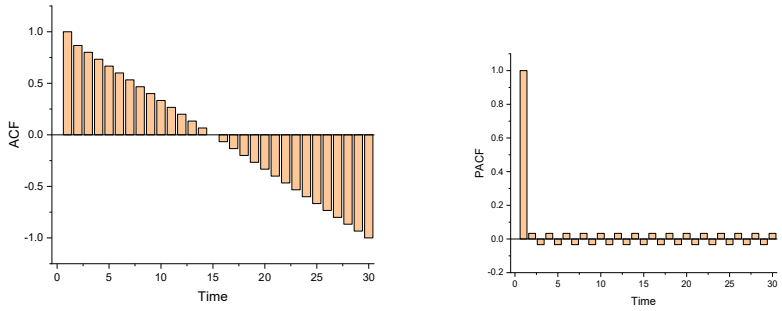

Fig. 6.3 ACF and PACF for time series

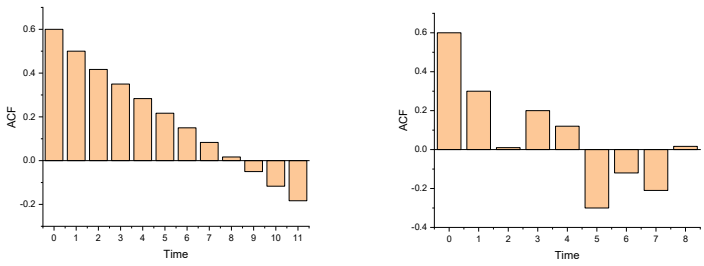

Fig. 6.4 ACF and PACF for time series for ARIMA (1,0,1)

6.5 Trend Analysis and Forecasting Model

In this section, trend analysis is performed, and a forecasting model is determined for the precipitation data in the area. Different methods used for evaluating the trend are mentioned, and conclusions are drawn on future precipitation trends. The section begins with a brief description of the procedures and their application to the given data set.

6.5.1 Techniques Used

6.5.1.1 Mann-Kendall Trend Analysis

This trend analysis method is one of the most common methods to detect hydrological, climatological, and metrological time series data trends. (Hu, et al., 2016; Meshram, et al., 2017). This study used the MK test to analyze the trend instead of Modified MK (MMK) because MMK is suitable for a large sample size (Hamed and Rao, 1998). The MK test uses two hypotheses: the null hypothesis (H_o) to describe no trend, and the alternative hypothesis (H_1) in which the null hypothesis is rejected, indicating an increasing or decreasing trend (Gajbhiye et al., 2016; Meshram et al., 2017; Hu et al., 2016). Each data in the series is compared with all subsequent data. There are three different values for *S* statistic, incremented (+1) which refers to the previous (X_i) value higher than the later value (X_{i+1}), decremented (-1) when the later value (X_{i+1}) is higher than the previous value (X_i), and constant (zero) when the earlier and later values are equal (Gajbhiye et al., 2016; Meshram et al., 2017; Hu et al., 2016). The *S* statistic in the Mann-Kendall trend can be calculated using Eq 6.3-6.4 given below:

$$S=\sum_{i=1}^{n-1}\sum_{j=i+1}^{n}\operatorname{sgn}(x_j - x_i) \tag{6.3}$$

where,

$$\operatorname{sgn}(x_j - x_i) = \begin{cases} +1 & , (x_j > x_i) \\ 0 & , (x_j = x_i) \\ -1 & , (x_j < x_i) \end{cases} \tag{6.4}$$

The mean and variance of *S* is given by Eq. 6.5 and 6.6:

$$E(S) = 0 \tag{6.5}$$

$$Var(S) = \frac{n(n-1)(2n+5) - \sum_{p=1}^{q} t_p (t_p - 1)(2t_p + 5)}{18} \quad 6.6$$

The standardized statistic (Z) of S, for one-tailed test is given by Eq. (6.7):

$$Z = \begin{cases} \frac{S-1}{\mathrm{Var}(S)} & , S > 0 \\ 0 & , S = 0 \\ \frac{S+1}{\mathrm{Var}(S)} & , S < 0 \end{cases} \quad 6.7$$

6.5.1.2 Sen's Slope Estimator Test

Sen's slope is a statistical test that estimates the magnitude of the trend as identified by the MK test (Sen 1968). In this test, a linear model is used to determine the slope of the trend, where the residual variances of data constant during a time can be calculated using Eq. 6.8 below:

$$T_i = \frac{x_j - x_k}{j - k} \quad 6.8$$

For i = 1, 2 … N,

Where x_j and x_k are the time series values at time j and k, where j is present, k is earlier, and N is total observations. The slope of trend (Q-value) of the time series is found using Eq. 6.9 below:

$$Q = \begin{cases} T_{\frac{N+1}{2}} & , N \text{ is odd} \\ \frac{1}{2}\left(T_{\frac{N}{2}} + T_{\frac{(N+2)}{2}} \right) & , N \text{ is even} \end{cases} \quad 6.9$$

The Q-value is positive if the trend increases and vice versa (Gajbhiye et al., 2016; Meshram et al., 2017).

6.5.1.3 Innovative Trend Analysis (ITA)

Sen (2012) suggested a new method for detecting trends based on historical time-series data. In this method, the time series data is divided into two halves with descending or ascending way for each half separately and scatter of the second half (y-axis) depend on the first half (x-axis) (Sen, 2012 and 2013). A line with slope 1:1 is used to show the trend among the variables of the scatter points along the line. In general, there are three possibilities for a trend in any dataset: trendless, increasing or decreasing. However, in this method, seven possible trends indicate whether a trend is rising, trendless, or falling, and the level of trend intensity as low, medium or high depending on the location of the points about the 1:1 line. This method has the advantage of being independent of any assumptions, serial correlation or number of the sample size used.

6.5.1.4 Box-Jenkins Forecasting (ARIMA)

The Box-Jenkins methodology is a sophisticated statistical way of examining and constructing a forecasting model that presents a time series better. The Box-Jenkins (1976) method has been used to forecast the precipitation in the present work. ARIMA modelling in Box and Jenkins refers to identifying, fitting, and checking univariate models for forecasting. This method applies to stationary time-series data, used for highly accurate forecasting or future prediction (Gaynor and Kirkpatrick 1994; Lu and AbouRizk, 2009; Hyndman and Athanasopoulos, 2018). Usually, the time series needs to be differenced to make it stationary to apply log transformation as d represents the number of times the series requires to reach stationary. The principle of the Box-Jenkins method is that it uses observed time series data and find the forecasting noise (error) for reasonable adjustment for prediction (Lu and AbouRizk, 2009). It is mainly used for dependent time series data that cannot be used with other methods. The Box-Jenkins

process contains three main steps: (i) Identification to find the stationary in time series and also Autoregressive (AR) and Moving Average (MR) parameters, (ii) estimation involving the error, and (iii) diagnostic checker. In general, for non-seasonal time series data, the ARIMA model can be modelled in the form of ARIMA (p,d,q), and the following expression is used:

$$x_t = \phi_1 x_{t-1} + ... + \phi_p x_{t-p} + w_t + \theta_1 w_{t-1} + ... + \theta_q w_{t-q} \qquad 6.10$$

Where, x_t and w_t are the actual time series with noise (error), ϕ θ are the model parameters, and p , q are model order autoregressive and moving average, distributed with mean zero and constant variance.

In the beginning, the type of ARIMA parameters has to be estimated. The ARMA (*p,q*) or ARIMA order can be identified throughout ACF and PACF. The ACF coefficient refers to the autoregressive parameter (*p*), and PACF refers to the moving average parameter (*q*). For example, the ARIMA model (1,1,2) has one autoregressive parameter, two moving average parameters, and one difference. Also, ACF and PACF coefficient can be described as ACF exponential decay starting at lag 1; PACF - exponential decay starting at lag 2.

The diagnostic checker is the last method where it used to select the best fit model among numbers of ARIMA order based on some of the criteria as (i) Residual portmanteau test, (ii) T-test for coefficient significance and (iii) AIC and BIC for model selection.

AIC is a metric developed by Hirotugu Akaike (1970). The concept of AIC is to penalize the inclusion of additional variables to a model. BIC is a variant of AIC with a more substantial penalty for including additional variables in the model (Kassambara,

2017). The AIC and BIC for model selection are the most common methods used for diagnostic checker where the Akaike's Information Criterion (AIC) and Schwarz's Bayesian Information Criterion (BIC) can be calculated using Eq. 6.11 - 6.13:

$$AIC(p,q) = \frac{-2\ln(\text{maximum likelihood}) + 2g}{N} \quad 6.11$$

$$AIC(p,q) = \ln(\sigma_e^2) + g\frac{2}{N} + \text{constant} \quad 6.12$$

where, σ_e^2 is the likelihood function value, g the number of estimated coefficients $g = p + q + 1$, and N number of observations.

$$BIC(p,q) = \ln(\hat{\sigma}_e^2) + g\frac{\ln(N)}{N} \quad 6.13$$

Where $\hat{\sigma}_e^2$ is the maximum likelihood of σ_e^2.

The BIC imposes a more significant penalty for the number of estimated model parameters than does AIC. For model selection, any model with minimum BIC/AIC is chosen. The *t*-test distribution is used to find out the best prediction model. The hypothesis that has been built is as follows:

H_o: the difference between the mean of original time series and projected time series = 10.

H_1: the difference between the mean of original time series and projected time series ≠ 10.

$$t = \frac{\bar{x}_1 - \bar{x}_2}{\sqrt{\frac{S_1^2}{N_1} + \frac{S_2^2}{N_2}}} \quad 6.14$$

where, t is the t -test value, $\bar{x}_1$ and $\bar{x}_2$ are the mean of original and projected time series, S_1 and S_2 the variance of original and projected time series and N_1 N_2 the sample size.

The last stage of the Box-Jenkins method is to forecast the chosen model; for example, the preferred model to fit a time series is as in Eq. 6.15:

$$Y_t = Y_{t-1} + \alpha_1 \left(Y_{t-1} - Y_{t-2} \right) + \mathrm{e_t} \qquad 6.15$$

And suppose that, N=99, α=0.2, Y_{99}=132.5, and Y_{98}=135.2, then, Y_{100}=131.96.

6.5.2 Application of techniques

6.5.2.1 Data and Data Processing

The precipitation data for trend analysis was obtained from the Ministry of Water and Irrigation, Jordan. The length of daily precipitation data available was 81, 50, 45, and 44 years at Salt, Adasy, South Shuna, IRA and EIB-AGR stations, respectively(As detailed in section 4.1.2). The raw data was processed for missing values and consistency check according to standard procedures and further analyzed for a pattern of event occurrence in other months. As was evident from Fig. 4.1, three different groups can be distinguished based on average rainfall, i.e., rainy season or winter season (Dec, Jan, and Feb), non-rainy season (Mar, Apr, May, Oct, and Nov), and zero rainfall season or summer season (Jun, July, Aug, and Sep). Therefore, based on exploratory data analysis (Fig. 4.4), the precipitation data was divided into the rainy season with an average of more than 280 mm, the non-rainy season with an average of ~50 mm, and the summer season having less than rainfall 10 mm.

Also, major precipitation events are obtained during the rainy season and are also a principal source of water supply in the area through storage in the dam; hence, the trend

analysis study is only confined to rainfall. This rainy season was further categorized as monthly (total rainfall for each month at each station), seasonal (total rain during the rainy season at each station), and catchment average value (for monthly and seasonal). The data shows non-stationary and non-seasonality as there was variation in mean, and the time series pattern did not repeat itself over time.

The analyses were made on monthly, seasonal, and average values, with a common data period between five stations from 1973 to 2016. The trend detection and precipitation forecast were carried out using R software and Xlstat software in Microsoft Excel.

6.5.2.2 Performing Trend analysis

6.5.2.2.1 Basin Average trend

Lowess smooth curve (Helsel and Hirsch 2002) was used to fit the time series data. Fig. **6.5** shows the historical data based on average values during January from 1973 to 2016.

The rainfall varied around the mean, and in the period 1973 to 1995 there is an increasing trend, after that decreasing till 2004, and again the trend is positive from 2004 to 2016. The average monthly precipitation data from each rain gauge station did not show any trend using the MK test described in section 6.5.1 (Table 6.1). However, the ITA showed increasing trends at a low level during January, February, and December, increasing in medium and high levels during January. However, data was trendless at a medium level in February and December, decreasing to a high level in February and December. While in the rainy season, the data showed decreasing in low and high trend levels and increasing in medium levels (Fig. 6.5).

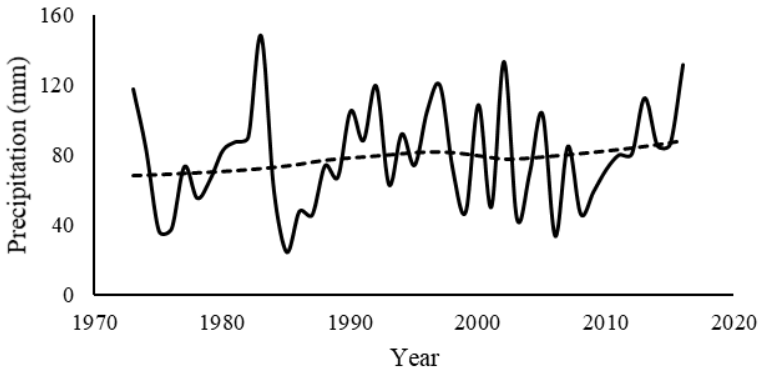

Fig. 6.5 Time series data and LOWESS curve trend (dashed) in average values during January 1974 to 2014

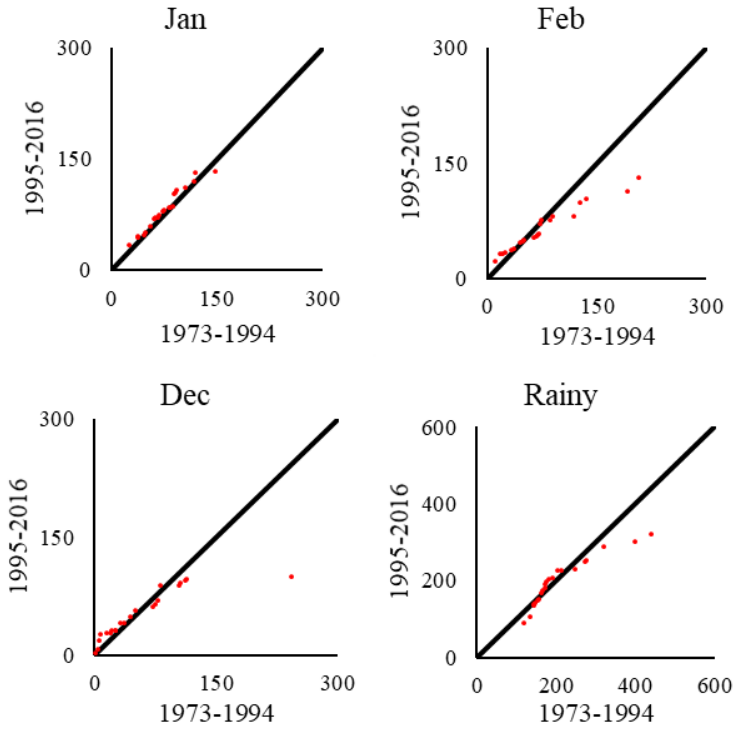

Fig. 6.6 Monthly precipitation trend using average values in the catchment

Table 6.1 Comparison of MK and ITA

Station		ITA			MK and Sen's slope			
		low	Medium	High	Z-value	Q-value	p-value	Trend
Salt	Jan	Y+	Y+	Y+	**1.52**[a]	**1.52**	0.04	Y
	Feb	Y+	N	Y-	0.11	0.11	0.95	N
	Dec	Y+	Y+	Y-	-0.12	-0.12	0.92	N
Adasy	Jan	Y+	Y+	Y+	**0.71**[b]	**0.71**	0.07	Y
	Feb	Y+	Y-	Y-	0.40	0.40	0.37	N
	Dec	Y+	N	Y-	0.10	0.10	0.82	N
Shuna	Jan	N	N	N	0.18	0.18	0.52	N
	Feb	Y+	Y-	Y-	0.02	0.02	0.97	N
	Dec	Y+	N	Y-	0.10	0.10	0.63	N
EIB-AGR	Jan	Y+	N	Y+	0.69	0.69	0.12	N
	Feb	Y+	Y-	Y-	0.03	0.03	0.97	N
	Dec	Y+	Y-	Y-	-0.07	-0.07	0.77	N
IRA	Jan	No	No	No	0.43	0.43	0.23	N
	Feb	No	No	Y+	0.23	0.23	0.60	N
	Dec	No	No	No	0.01	0.01	1.00	N
Average Value	Jan	Y+	Y+	Y+	0.01	0.46	0.22	N
	Feb	Y+	No	No	0.01	0.32	0.41	N
	Dec	Y+	No	Y-	0.00	0.21	0.68	N
Salt	Seasonal	Y-	Y+	Y-	**0.23**[a]	**1.38**	**< 0.0001**	Y
Adasy	Seasonal	Y-	Y+	N	**0.02**[b]	**0.87**	**0.06**	Y
Shuna	Seasonal	N	N	Y-	0.00	0.20	0.66	N
EIB-AGR	Seasonal	Y-	Y+	Y-	0.01	0.55	0.35	N
IRA	Seasonal	Y-	Y+	Y-	0.02	0.53	0.20	N
Average Value	Seasonal	Y-	Y+	Y-	0.01	0.62	0.26	N

Numbers in bold indicate to p-value less than (a) 5% and (b) 10% confidence level. Y refers to existing trends, N refers to no trend or trendless. "+" and "–" refer to a positive and negative trend, respectively

6.5.2.2.2 Monthly trend

Fig. **6.7** shows the observed trend at each station based on 5 and 10 % significance levels. Table 6.1indicates a trend at only two stations, Salt and Adasy, during January based on monthly precipitation data. A significant positive trend was observed based on Sen's slope estimator, at confidence level 95% and 90% at Salt and Adasy station, respectively, and precipitation was increased by 1.52 mm and 0.71 mm

during January month at Salt and Adasy station, respectively. ITA detected a trend in precipitation based on monthly data, while Fig. **6.7** shows the change in trend during the monthly data at all stations. The low, medium, high trend, and trendless has been detected for all stations during the monthly data.

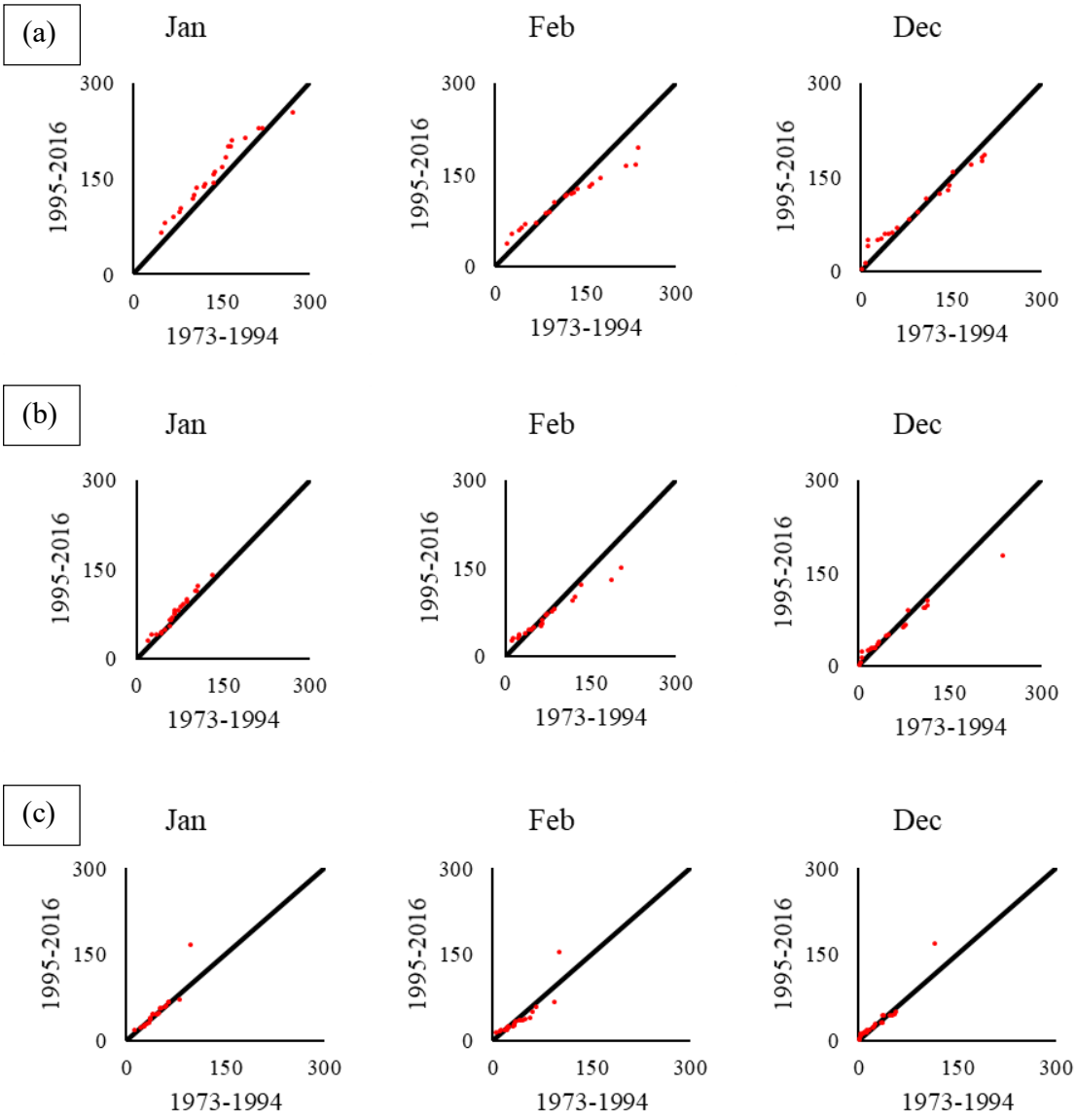

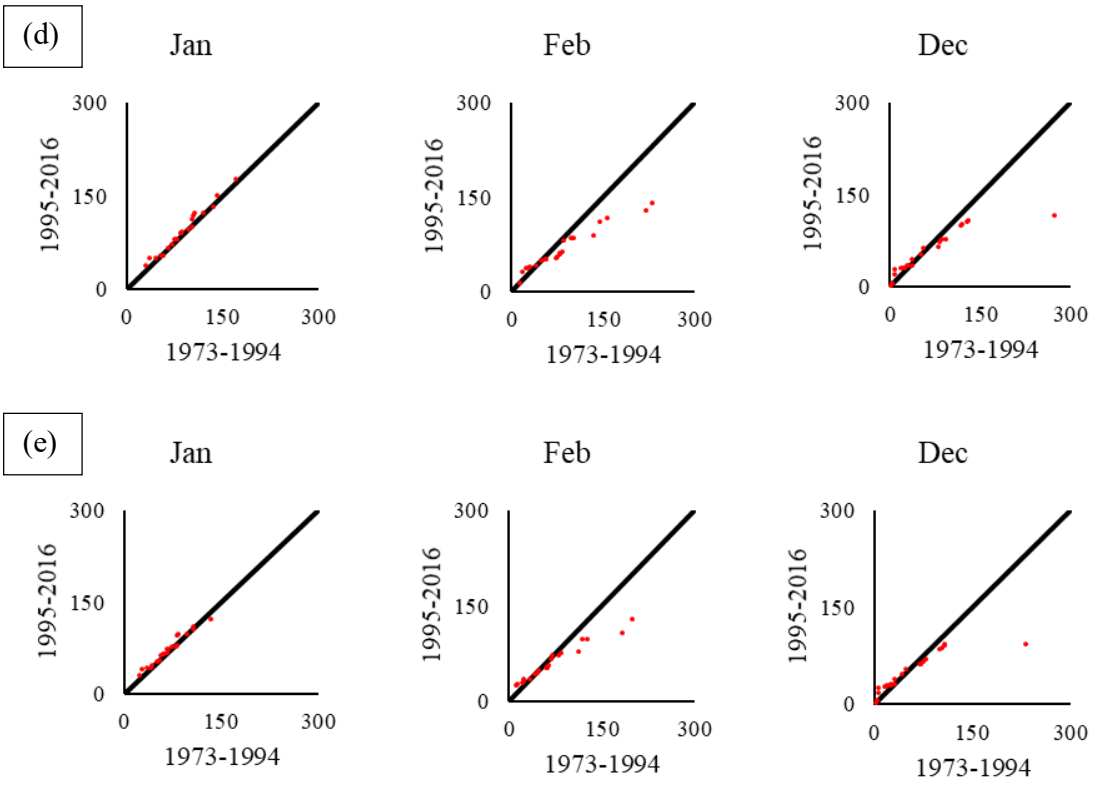

Fig. 6.7 Monthly precipitation trend at (a) Salt station, (b) Adasy station, (c) Shuna station, (d) EIB-AGR station, and (e) IRA station.

The high-level trend increased during January at all stations except in South Shuna, and IRA stations were trendless in the same month while decreasing trends during February and December. Most stations had an increasing trend in low-level trends, whereas trendless were detected in South Shuna during January and in the IRA station during monthly data. The medium trend level was seen as an increasing, decreasing and trendless trend at all stations.

6.5.2.2.3 Seasonal trend

The MK confirmed the trend at Salt and Adasy station (Table in the seasonal (6.1 precipitation data, while Sen's slope estimator detected a positive trend at these stations. An increase of 1.38 mm and 0.87 mm precipitation was found at Salt and Adasy station

during the rainy season, respectively. Moreover, ITA based on seasonal data showed a decreasing trend at a medium level at all stations except South Shuna, where it was trendless. It showed a decreasing trend in low and high-level, except in low level in South Shuna and high level in Adasy station it was trendless (Fig. 6.8).

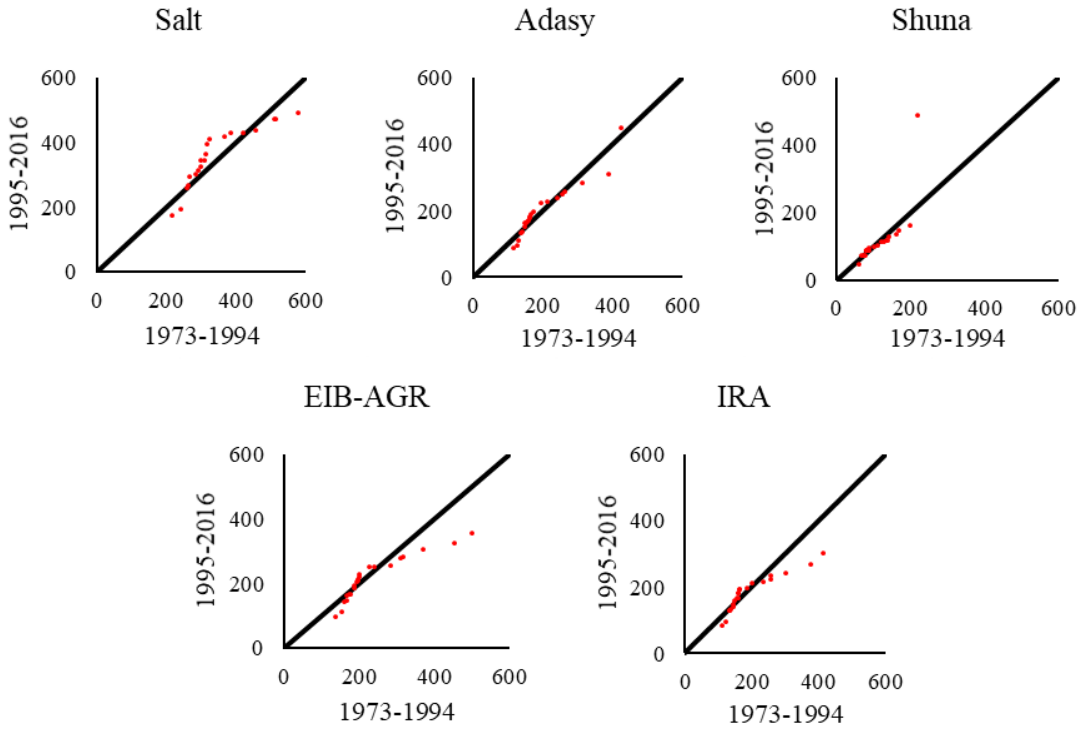

Fig. 6.8 Trend analysis of Seasonal precipitation at each station

The trend analysis is similar to a recent study conducted by Tarawneh and Chowdhury (2018) in Saudi Arabia. They concluded that the rainfall decreased in most areas and forecasted the precipitation might be variable in the future. However, the ITA and MK trend comparison was similar to a study by Ay and Kisi (2014), who used monthly precipitation data in Turkey. In comparison between the two methods of trend analysis, it is found that the ITA method was able to detect the trend at different levels

while MK could not see any trend at the same station. In using other meteorological and hydrological data, this result supports the previous studies conducted by Kisi and Ay (2014) and Kisi (2015). They compared the MK test and ITA method using water quality parameters and pan evaporations data and found that the ITA method gave higher accuracy in trend results.

6.5.3 Developing a Forecasting model

6.5.3.1 Monthly forecast

ARIMA model was carried out for future prediction based on the total monthly precipitation in the area. Differencing was used to remove the linearity in a trend of the data and stabilize the variance. Different ARIMA orders were applied to find out the most suitable model and the one that was the best fit with the observed trend. The moving average (q) and autoregressive (p) two different values were selected based on ACF and PACF observations, where differencing (d) was of 1st and 2nd level. The t-test was carried out to find the best ARIMA model among different models for future prediction.

Table 6.2 shows p-values for different ARIMA orders for projected time series from 1973 to 2016. Based on the p-value, all ARIMA models were significant within a 5% significance level, and AIC/BIC values later supported these results. The ARIMA models having minimum AIC/BIC were selected to predict the future precipitation in the area.

The ARIMA order (3,1,3) was well fitted at all stations during most of the rainy season whereas, in Adasy, Shuna, and EIB-AGR have different ARIMA orders where (4,1,3) was found fit during February based on a minimum of AIC/BIC (Fig. 6.9). The

absolute difference between observed and predicted data called absolute error was 0.05 mm in the IRA station during January and 22.61 mm in the Salt station during December.

Table 6.2 ARIMA Models based on AIC/BIC and *p*-value

Station		AIC/BIC				*p*-value			
		(4,1,4)	(4,1,3)	(3,1,3)	(4,2,4)	(4,1,4)	(4,1,3)	(3,1,3)	(4,2,4)
Salt	Jan	394.93	391.61	**388.04**	391.99	0.02	0.03	0.05	0.00
	Feb	417.15	414.23	**412.37**	413.55	0.04	0.02	0.04	0.36
	Dec	80.82	78.63	**75.81**	90.60	0.00	0.00	0.00	0.00
	Seasonal	-8.76	**-12.24**	-8.81	0.79	0.14	0.05	0.18	0.47
Adasy	Jan	346.06	343.20	**340.30**	345.39	0.00	0.01	0.00	0.00
	Feb	372.64	**369.91**	370.50	370.97	0.02	0.02	0.04	0.47
	Dec	81.43	78.67	**77.60**	89.10	0.00	0.00	0.00	0.00
	Seasonal	-5.44	-7.21	**-8.73**	4.69	0.21	0.10	0.10	0.37
Shuna	Jan	318.41	315.26	**312.80**	318.28	0.01	0.02	0.02	0.00
	Feb	31.85	**30.47**	31.00	40.32	0.03	0.02	0.03	0.10
	Dec	82.76	79.06	**76.30**	89.48	0.00	0.00	0.00	0.00
	Seasonal	362.33	**358.93**	360.79	359.87	0.09	0.09	0.09	0.26
EIB-AGR	Jan	360.10	357.76	**353.03**	359.72	0.00	0.00	0.01	0.00
	Feb	381.98	**379.09**	382.76	379.63	0.00	0.00	0.01	0.22
	Dec	81.32	78.63	**76.14**	89.10	0.00	0.00	0.00	0.00
	Seasonal	-5.35	-5.71	**-9.29**	4.91	0.02	0.00	0.00	0.20
IRA	Jan	345.66	343.88	**339.83**	344.94	0.00	0.00	0.00	0.00
	Feb	371.87	369.85	**368.72**	369.49	0.00	0.02	0.01	0.41
	Dec	80.91	78.28	**75.83**	91.98	0.00	0.00	0.00	0.00
	Seasonal	-6.14	**-8.61**	-6.22	3.95	0.00	0.00	0.01	0.08
Average Value	Jan	337.24	336.93	**334.44**	337.98	0.00	0.00	0.00	0.02
	Feb	360.27	360.57	361.05	**358.1**	0.01	0.02	0.00	0.02
	Dec	364.88	363.11	363.75	**362.63**	0.00	0.00	0.00	0.00
	Seasonal	392.56	390.65	393.47	**389.04**	0.00	0.00	0.00	0.00

Numbers in bold indicate to most fitted ARIMA model

6.5.3.2 Average forecast

The average precipitation value was also examined to evaluate the future forecast of precipitation in the entire area. Two ARIMA models that were found suitable were (3,1,3) during January and (4,2,4) during February, December, and seasonal data (Fig. 6.10). The absolute error ranged between 5.37 mm during January month and 28.03 mm during December month.

(a)

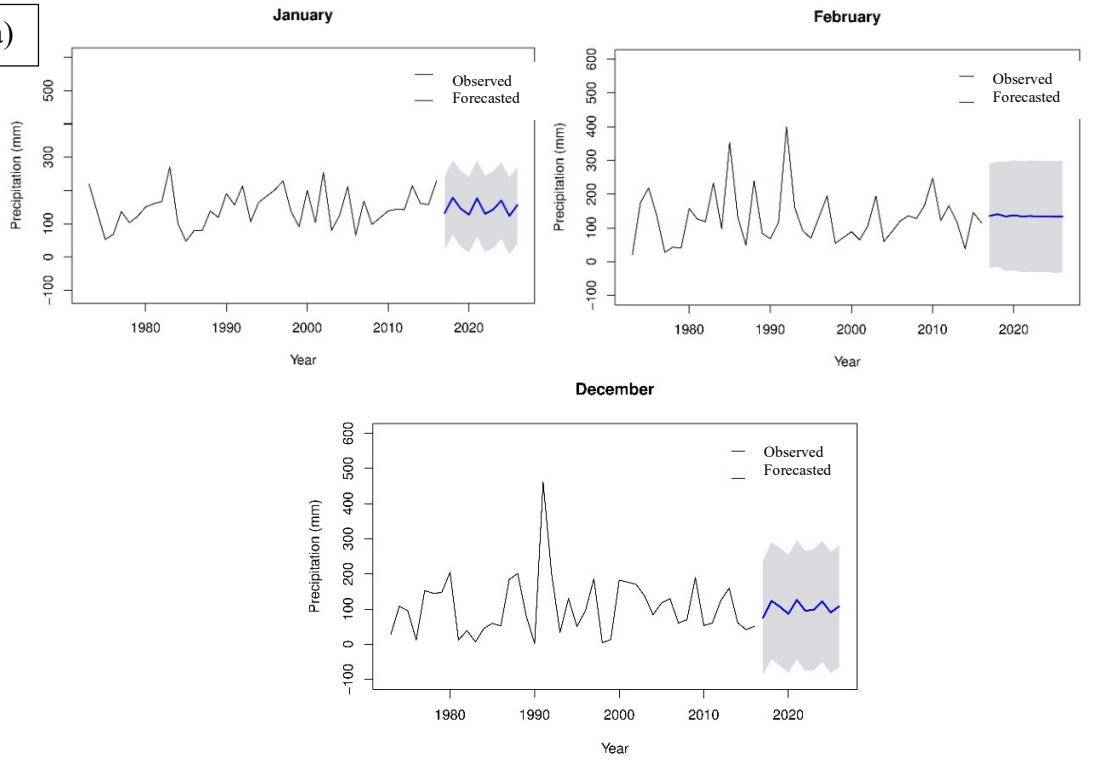
January
February
December
Observed
Forecasted
Precipitation (mm)
Year
1980
1990
2000
2010
2020

(b)

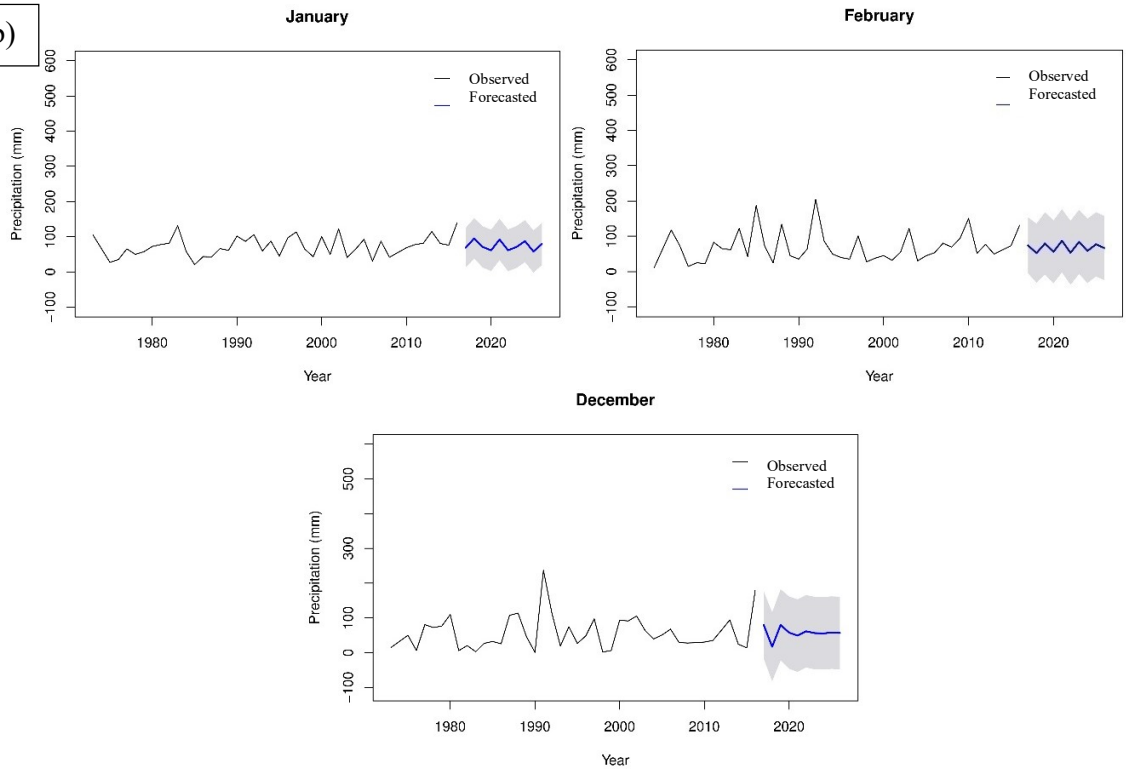
January
February
December
Observed
Forecasted
Precipitation (mm)
Year
1980
1990
2000
2010
2020

(c)

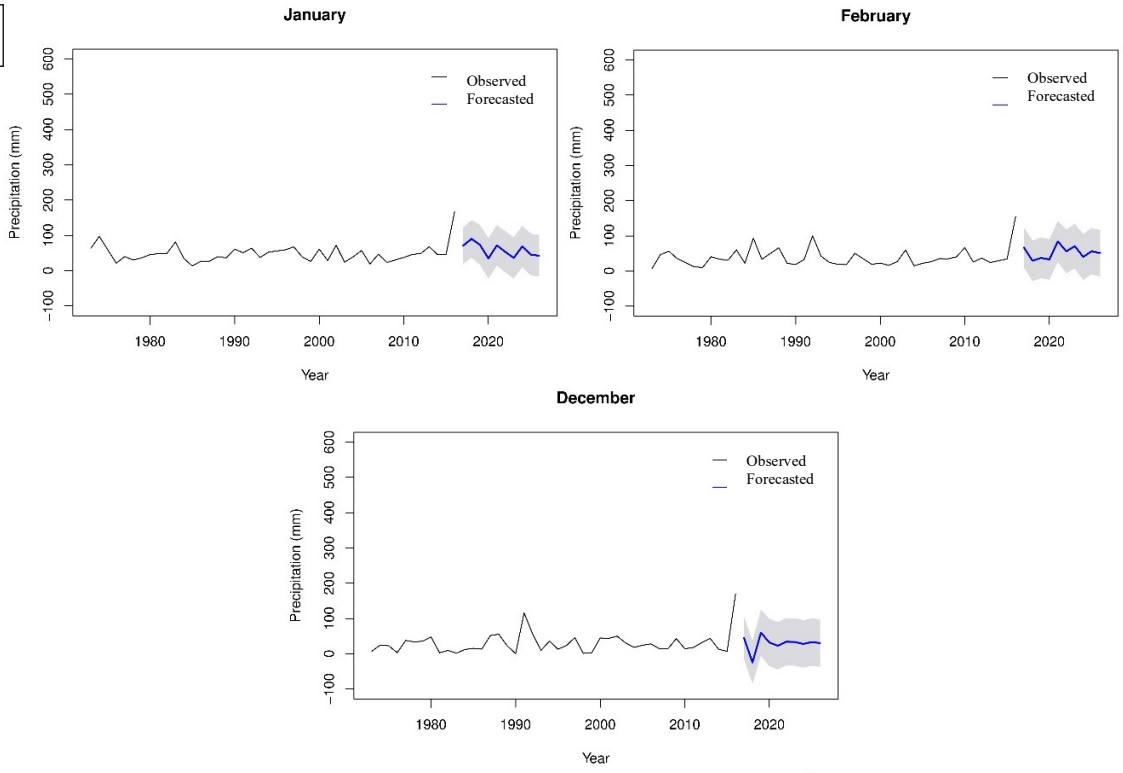
January
February
December
Observed
Forecasted
Precipitation (mm)
Year
−100
0
100
200
300
400
500
600
1980
1990
2000
2010
2020

(d)

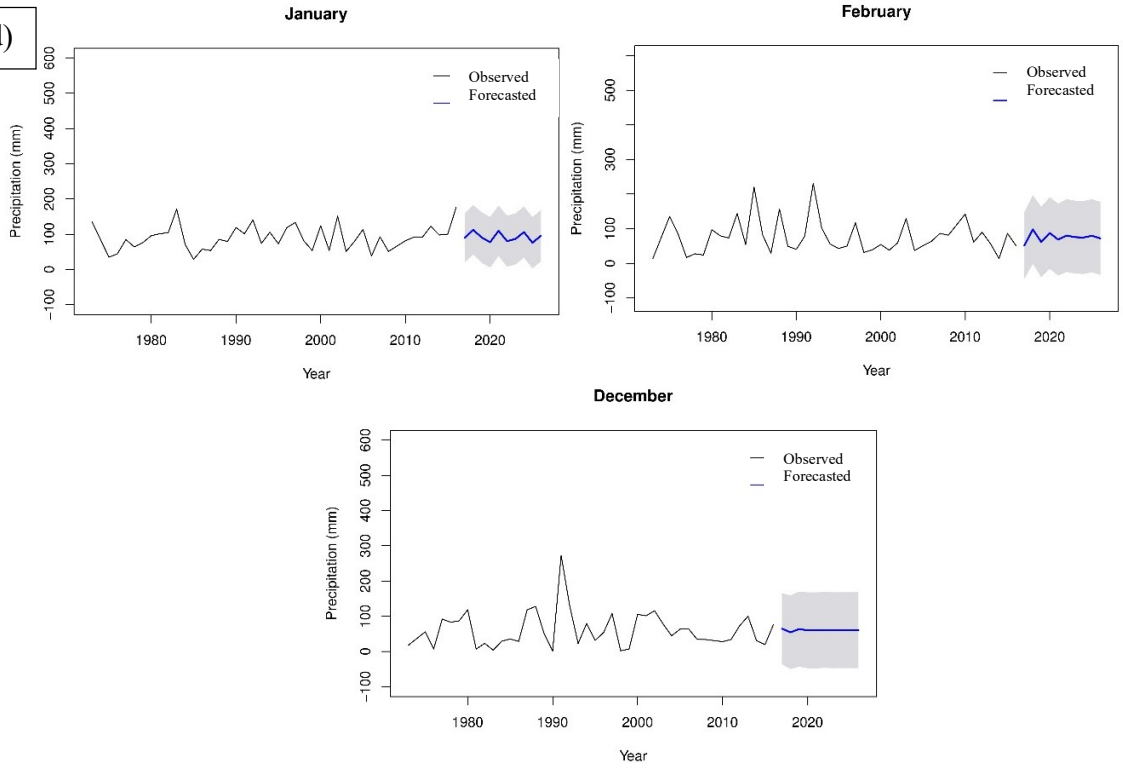
January
February
December
Observed
Forecasted
Precipitation (mm)
Year
−100
0
100
200
300
400
500
600
1980
1990
2000
2010
2020

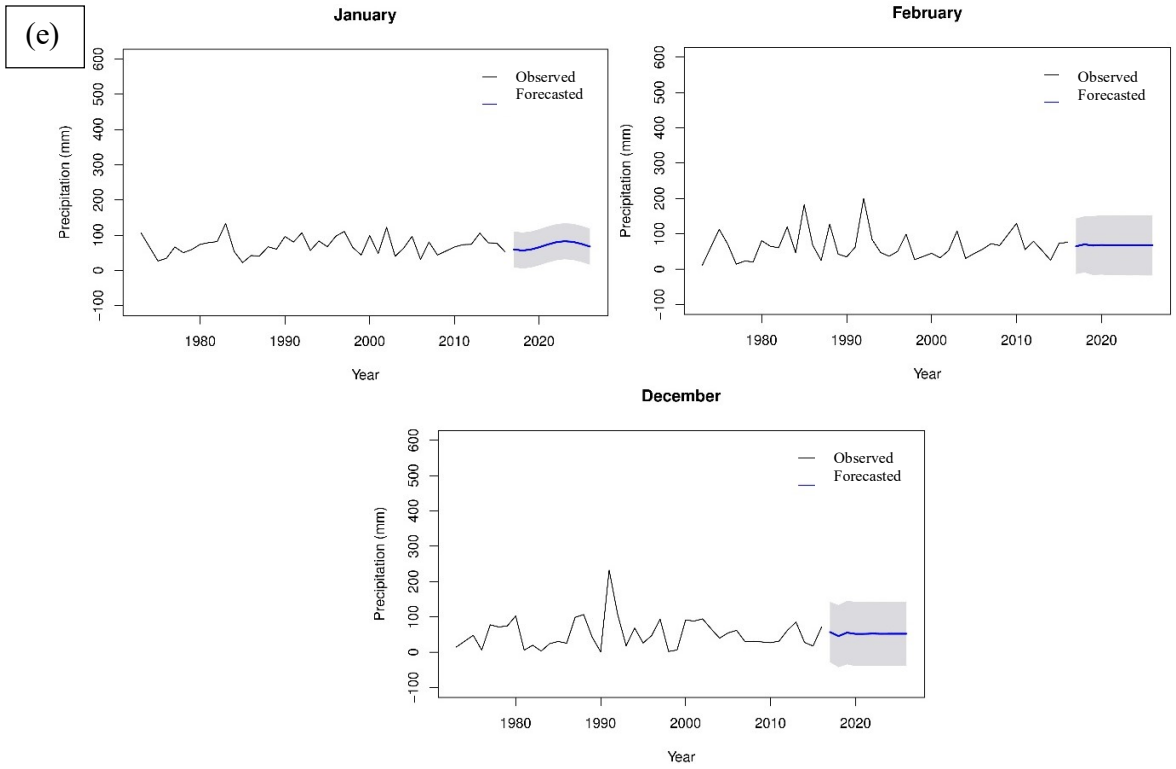

Fig. 6.9 Precipitation prediction through different ARIMA models for (a) Salt station, (b) Adasy station, (c) Shuna station, (d) EIB-AGR station, and (e) IRA station, till 2026 with 80 and 95 bands level

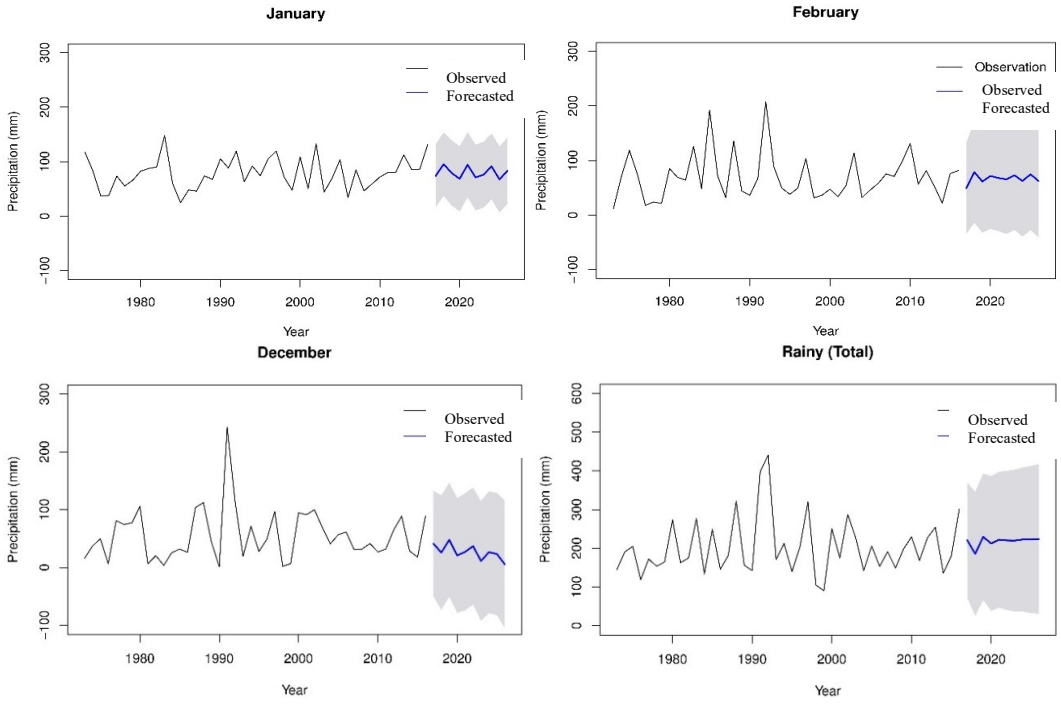

Fig. 6.10 Precipitation prediction using the average value in the catchment

6.5.3.3 Seasonal forecast

Seasonal results show two different ARIMA models. The (4,1,3) order was found well fitted in Salt, Shuna, and IRA stations, whereas the (3,1,3) order fitted well for Adasy and EIB-AGR stations (Fig. 6.11). The absolute error was found between 5.19 mm in Salt station and 51.95 mm in Shuna station.

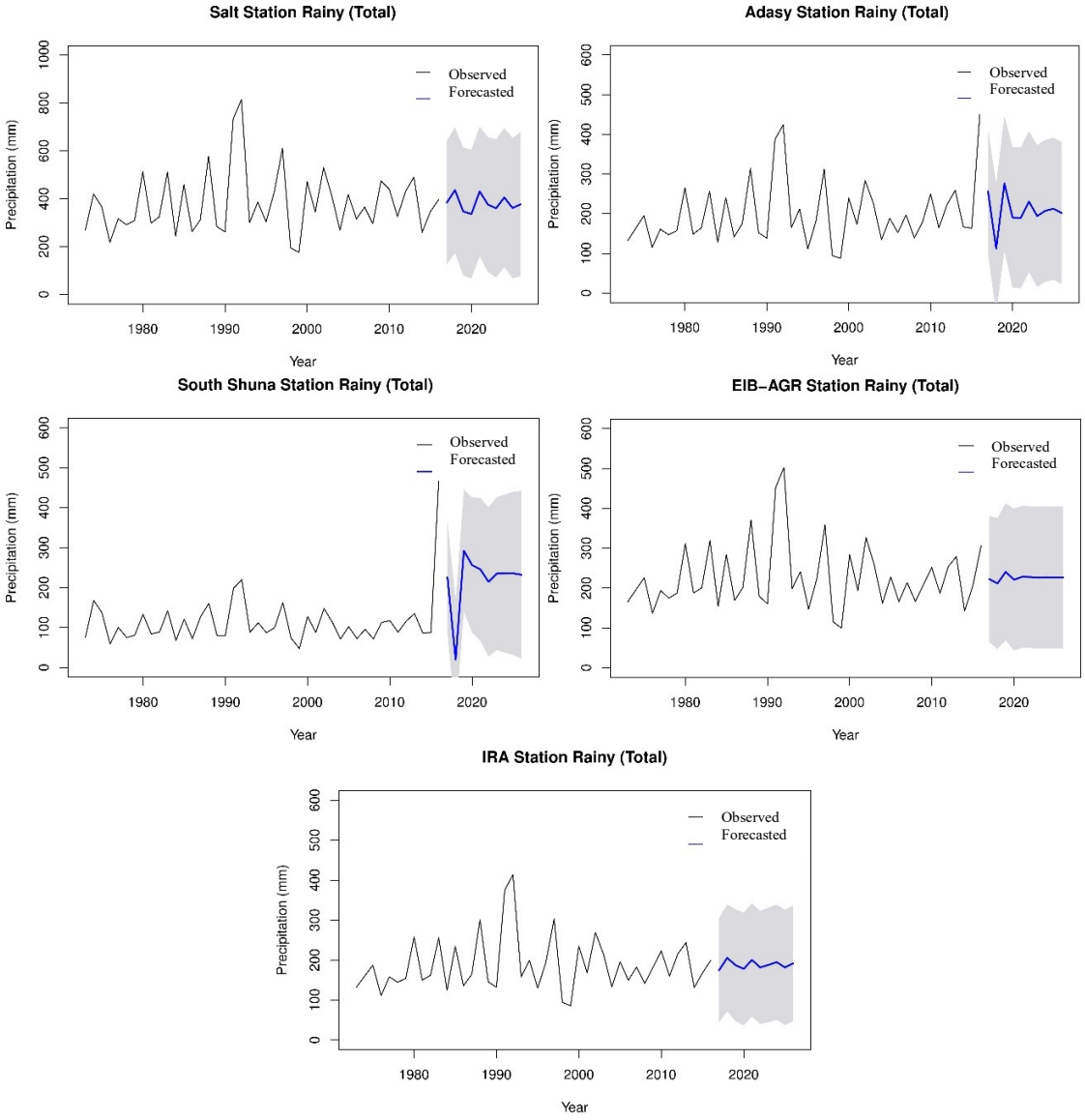

Fig. 6.11 Precipitation prediction during Rainy season using ARIMA models till 2026

The results of the ARIMA model at different levels gave acceptable absolute error while using total monthly based on daily precipitation data. Wang et al. (2014) used monthly precipitation data, and the mean absolute had ranged between 9.41 and 17.82. Narasimha Murthy et al. (2018) conducted a study based on seasonal monthly precipitation data in North-Eastern parts of India. Similarly, the ARIMA model was used in different studies, such as Chattopadhay et al. (2012), and it was concluded that the ARIMA model is practical and functional.

Some cases of the ARIMA model show horizontal or low variation in forecasting and predicted values, where these models are chosen based on AIC/BIC and t-test criteria. Feng et al. (2016) used the ARIMA model to predict the future pattern of annual precipitation based on monthly data. In contrast, the best-fit ARIMA model shows a horizontal line based on minimum statistical measures such as normalized to the mean of observed values.

6.5.4 Future Projection of Trend Analysis

Based on the best-fit models found in the preceding section, the same was used to predict the future precipitation and its trend. The work used two different periods, the first period was the observed data from 2007 to 2016, and the second period used predicted data from the ARIMA model from 2017 to 2026. Fig. **6.12** and **6.13** show three different trend levels viz., low, medium, and high detected for each station at the monthly scale.

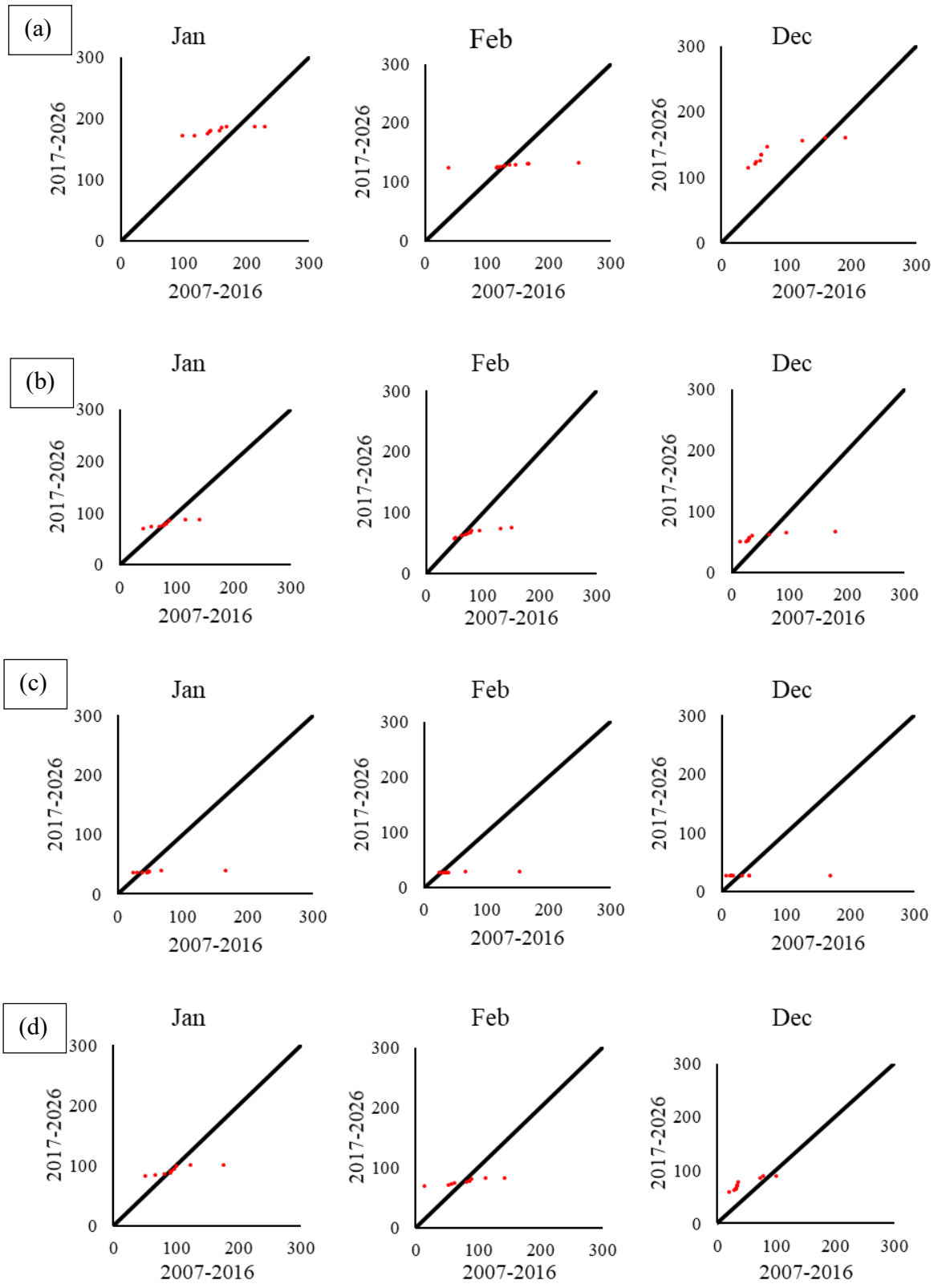
(a)
Jan
Feb
Dec
(b)
Jan
Feb
Dec
(c)
Jan
Feb
Dec
(d)
Jan
Feb
Dec
2017-2026
2007-2016
0
100
200
300

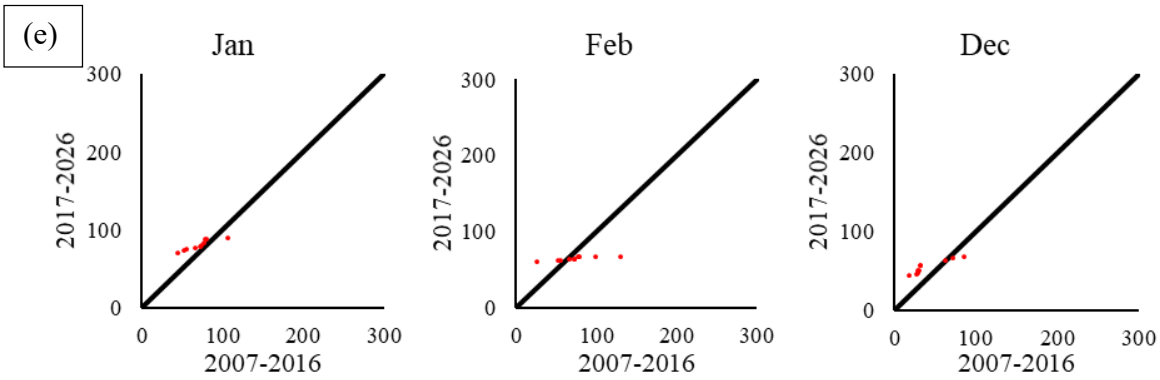

Fig. 6.12 Future monthly precipitation trend at (a) Salt station, (b) Adasy station, (c) Shuna station, (d) EIB-AGR station, and (e) IRA station

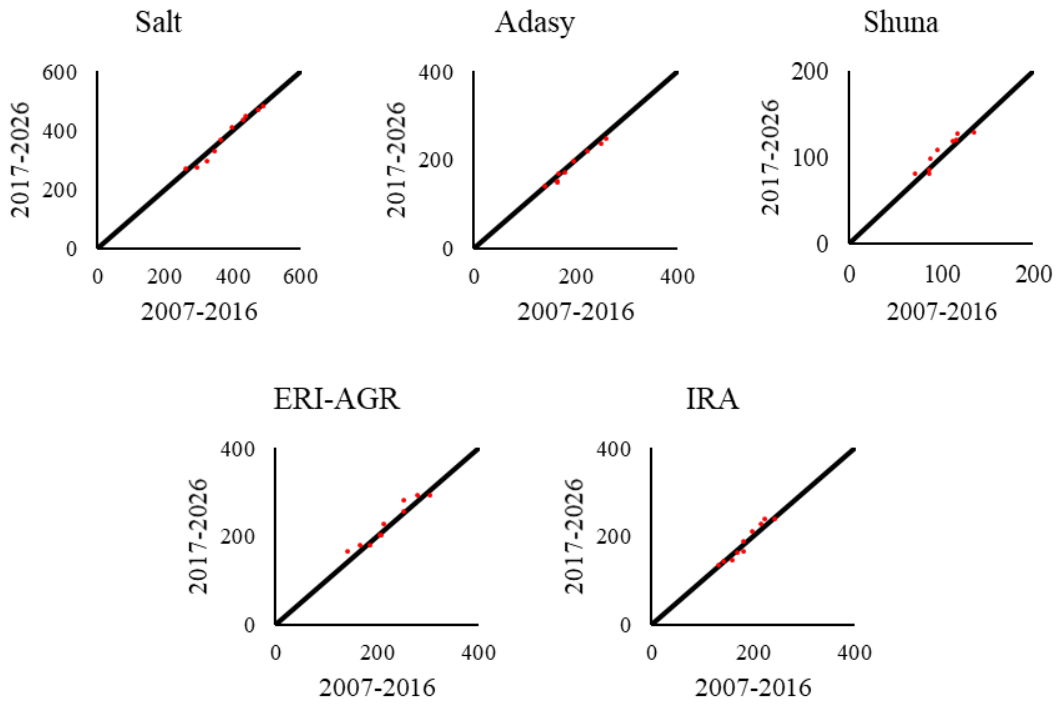

Fig. 6.13 Future monthly precipitation trend in Seasonal data at each station

The results show that the high trend level will decrease for all months at every station, while a low trend level will increase in the same period. The average values during the monthly and rainy scales gave similar results, while different rainfall trends

were detected in seasonal data. Fig. **6.14** shows the trend of the entire catchment on a monthly and seasonal scale.

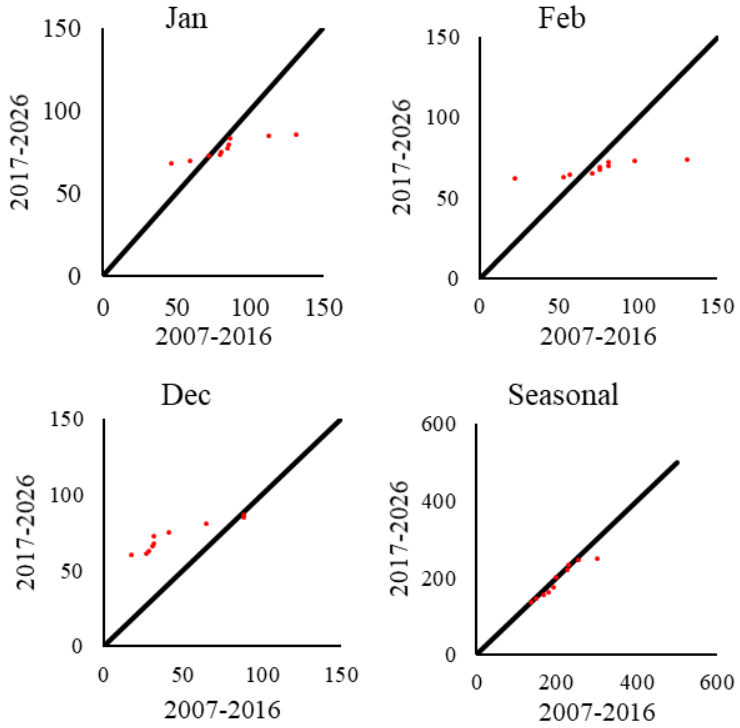

Fig. 6.14 Future monthly precipitation trend in the whole catchment using an average value

The results show a decrease in trend in the next ten years, although a few stations, historical data (1973-2016) show an increasing trend at a high level. The generally high-level trend in the entire area was increased during January month in (1973-2016) and decreasing in the rest of the months. In contrast, future precipitation was increasing in December and decreasing in the rest of the months. The decreasing trend in precipitation corroborates a similar study conducted by Kool (2016) in Jordan valley that showed a decreasing trend during the last decades and in coming decades from more than 600 mm to less than 100 mm.

6.6 Conclusion

In this chapter, the precipitation trend analysis and forecasting in the Wadi Shueib catchment area were studied. This work was divided into two main parts: investigate the trend of precipitation data using MK test and ITA and predict the future precipitation scenario by applying the Box-Jenkins method ARIMA model in the area. The study reveals a decreasing trend in precipitation. This observation can have severe implications for reservoir operation in the catchment, which serves as a significant source of water supply for various uses. The reservoir starts filling during the early rainy season (Dec, Jan, and Feb). Therefore, any decrease in precipitation can affect reservoir water level and storage capacity. In a study by Kool (2016), it was concluded that the Shuna South area, under the Wadi Shueib region, has a water demand of (65.5 Mm^3) while the essential water supply is only 35.0 Mm^3, resulting in a water deficit of 30.5 Mm. Thus, it is concluded that the water deficit will be a serious problem in the area from this study. Hence this framework can give the decision-makers and water managers an early warning to adapt their management practices accordingly.

Chapter 7: SWAT Modeling for Streamflow Prediction

7.1 Introduction

Streamflow data is a must for studying the vulnerability of water availability in an area. However, the availability of streamflow data is always limited, which Predicting the streamflow data using a comprehensive hydrologic model thus becomes a need. This chapter aims The model, once calibrated, and validated will be used to (i) predict continuous streamflow data on a monthly scale and also (ii) perform streamflow prediction for the future period using ARIMA modelling.

7.2 Model Description

The SWAT model is a physically distributed model designed to estimate streamflow, sediment yield, and water quality in agricultural areas based on the interaction of land management practices with climate and soil cover (Arnold et al., 1998). The following water balance equation is the base to compute the hydrologic components:

$$SW_t = SW_0 + \sum_{i=1}^{t}\left(R_{day} - Q_{surf} - E_a - W_{seep} - Q_{gw}\right) \quad 7.1$$

Where SW_t is the soil water content at a time t ; SW_0 is the initial soil water content; t is time (in days); R_{day} is the amount of daily precipitation; Q_{surf} is the amount of surface runoff per day; E_a is the amount of daily evapotranspiration; W_{seep} is the water percolation to the bottom of the soil profile per day; Q_{gw} is the amount of water returning to the groundwater per day.

Further, different variables of land management are recognized based on integrating soil type and land use and land cover data. The soil water content and

infiltration rate can be measured using the curve number method. The curve number method is calculated throughout using equation 7.2 (Neitsch 2011):

$$Q_{surf} = \frac{\left(R_{day} - 0.2S_R\right)^2}{\left(R_{day} - 0.2S_R\right)} \quad 7.2$$

Where Q_{surf} is the equivalent depth of surface runoff (mm); R_{day} is the rainfall depth of the considered day (mm); S_R is the retention parameter (mm).

Where *S* can be calculated by eq. (7.3):

$$S = \frac{1000}{CN} - 10 \quad 7.3$$

where CN is the curve number of the day considered.

7.3 Model Application

7.3.1 Data Requirement

The SWAT model application to an area follows definite steps shown in a flow chart (Fig. 7.1). Watershed delineation, consideration of land use, soil type, and slope of the area and HRU definition are prerequisites to setting the area's SWAT model. Thus intensive data collection and configuring the same for the model form the first step, followed by calibration and validation for the flow data. In the present study, the projected precipitation and temperature data will be taken as inputs to the SWAT model for its calibration. The calibration model will then be used to project streamflow data for the future time period.

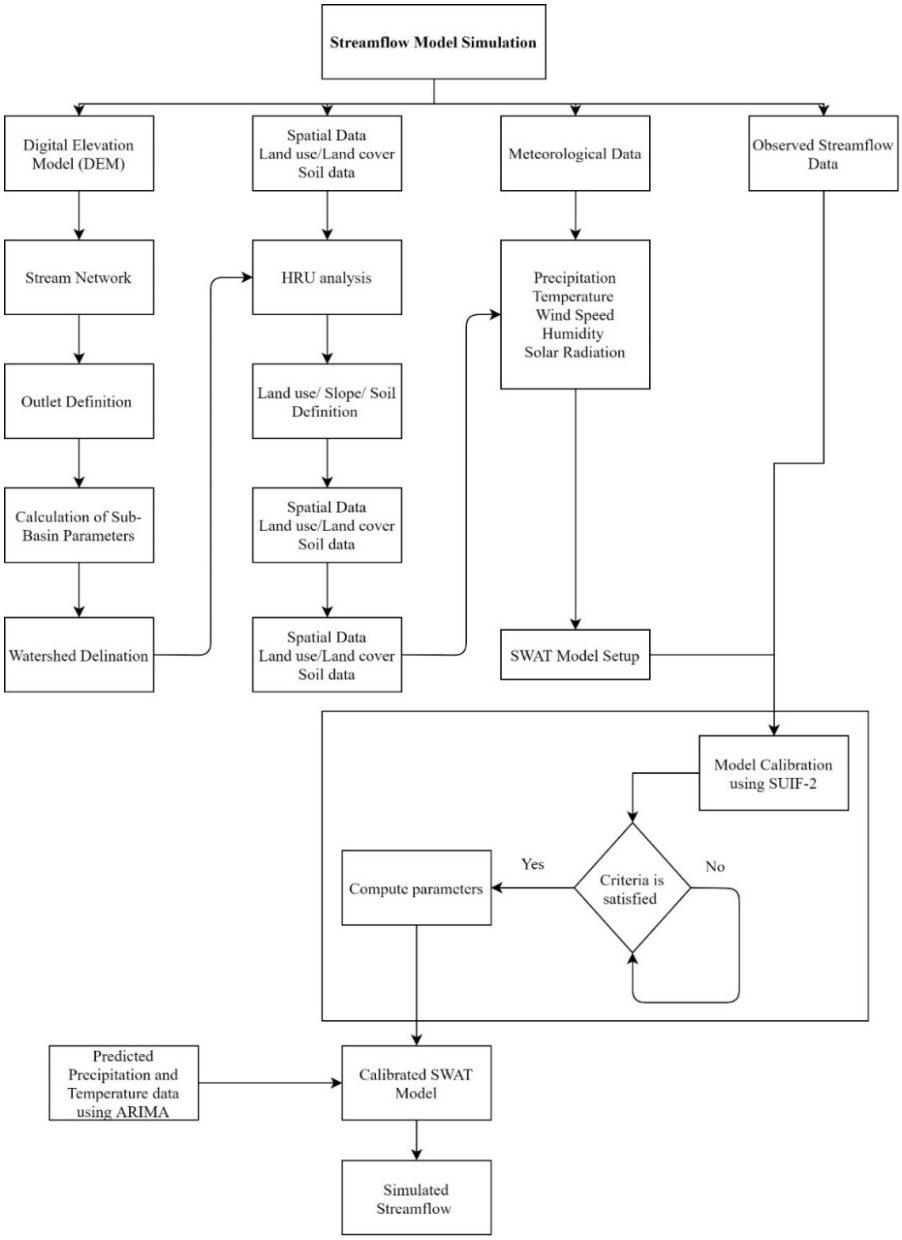

Fig. 7.1 Flowchart depicting SWAT application for the study area

7.3.2 SWAT Model setup

The SWAT model setup is divided into four processes: (i) watershed delineation, (ii) HRU definition, (iii) weather data definition, and (iv) writing input tables.

7.3.2.1 Watershed delineation

The ASTER GDEM (As discussed in chapter 4) was used. A detailed stream network map from Royal Jordanian Geographic Center (RJGC) was used to correct the extracted stream network distortion. With a stream threshold value of 0.5 km^2 and Shueib dam as the watershed outlets, the watershed was delineated with 17 sub-basins, as shown in Fig. 7.2 .

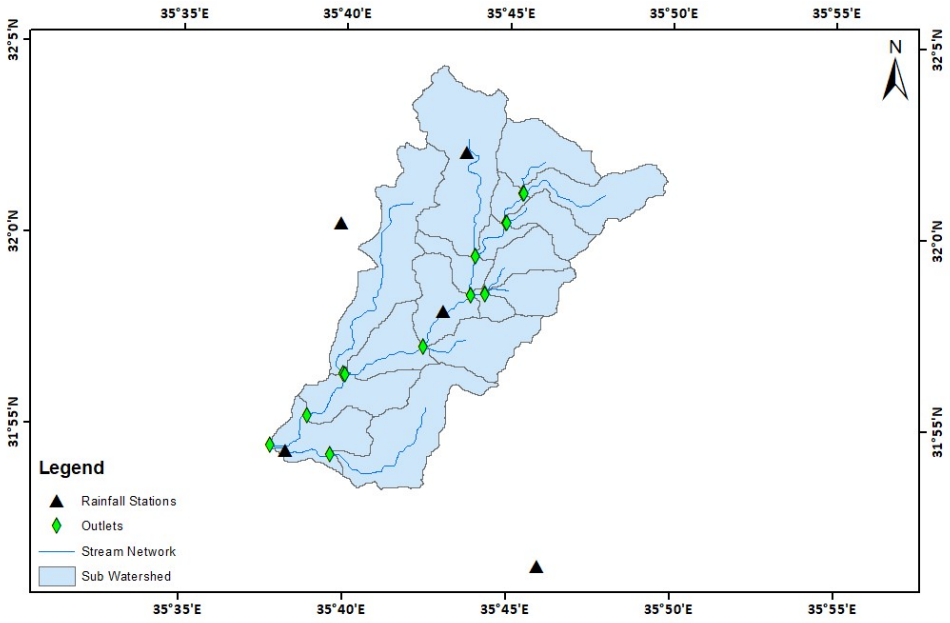

Fig. 7.2 Sub watersheds of Wadi Shueib watershed

7.3.2.2 HRU definition

The HRUs in the catchment were calculated based on the combination of land used land cover, soil, and slope data with various thresholds values. The national land use and land cover of 2011 consisting of urban, vegetation, and water surface (Dam) at the scale of 1:250,000 were used. Land use and land cover details comprise one of the most determinant datasets required in hydrologic models, like SWAT, when creating the HRUs. Table 7.1 shows SWAT land use classification for the area. The land use classes

in the study area are Forest, Irrigated fruit trees, Irrigated non-deciduous trees, Irrigated vegetables, cereal, Natural Vegetation, steppe, Rainfed fruits trees, Rainfed non-deciduous trees, rainfed vegetables, grain, Urban and bare rock, and Waterbodies.

Table 7.1 Land use classification for the SWAT model

Land Use	SWAT Code	% of the total area
Forest	FRSD	2.04
Irrigated fruit trees, Irrigated non-deciduous trees, Irrigated vegetables, cereal, Rainfed Fruit trees, Rainfed non-deciduous trees, and rainfed vegetables	AGRL	31.35
Natural Vegetation, steppe	PAST	30.56
Urban and bare rock	URBN	36.03
Water	WATR	0.013

Source: RJGC, 2010

Soil is another data that have a significant influence on catchment hydrology. The national soil map was surveyed during 1989-1995 and published as 1st edition in 1994. Soil texture, organic matter, available water content, saturated hydraulic conductivity, bulk density, and a hydrologic group of each soil type are the main components of the soil SWAT database. The study area's soil map with exclusive properties and characteristics details were obtained to support the model needs (Refer section 3.2.2 and 3.3.2). These parameters were directly used as input datasets for the model.

The slope in the watershed ranges between 0 and 40 degrees as computed from DEM using ArcGIS software. Given the data layers of land use and soil map and the known information on the slope, the threshold percentage for each layer was decided to be taken as input for the definition of HRUs. In the modeling, multiple HRUs were created as: land cover percentage (%) over sub-basin area = 5%; soil class percentage (%) over land-cover area = 5%; slope class percentage (%) over soil area = 5%. As a result, a total of 526 HRUs were created, divided into 17 sub-basins.

7.3.2.3 Weather data

The daily precipitation data from 1967 to 2016 and obtained from the Ministry of Water and Irrigation, Jordan, was made available for five rain gauge stations (as shown in Fig. 3.1) falling in and around the catchment area. As obtained, the length of daily precipitation data varied from 81, 50, 45, and 44 years at Salt, Adasy, South Shuna, IRA and EIB-AGR stations, respectively. The weather data other than precipitation data such as wind speed, relative humidity, max and min temperature, and solar radiation data was made available for the Shuna weather station located in the study area from 1979-2014. This data was obtained from the Ministry of Water and Irrigation, Jordan (Refer section 3.3.3).

A text file for these data sets was prepared as an input weather data file for the model.

7.3.3 Preliminary Model Run

Four indices, including Nash-Sutcliffe coefficient of efficiency (NSE), correlation coefficient (R^2), Percent Bias (PBIAS), and Relative Error (RE) (Duru et al. 2017; Wang et al. 2019), were evaluated. The NSE compares the relative magnitude of noise variance to data variance, indicating how well the simulated data matches the observed data. The R^2 describes the degree of collinearity between simulated and observed data as it ranges between 1 and 0 based on the degree of linearity relation. In contrast, the PBIAS calculates the slope of simulated data (Gupta et al., 1999). All these statistical metrics are calculated using the Equations (7.4-7.7).

$$NSE = 1 - \frac{\sum_{i=1}^{n}\left(Q_i^{obs} - Q_i^{sim}\right)^2}{\sum_{i=1}^{n}\left(Q_i^{obs} - \overline{Q}_i^{obs}\right)^2} \qquad 7.4$$

$$R^2 = \frac{\left[\sum_{i=1}^{n}\left(Q_i^{obs} - \overline{Q}^{obs}\right)\left(Q_i^{sim} - \overline{Q}^{sim}\right)\right]^2}{\sum_{i=1}^{n}\left(Q_i^{obs} - \overline{Q}^{obs}\right)^2 \sum_{i=1}^{n}\left(Q_i^{sim} - \overline{Q}^{sim}\right)^2} \quad 7.5$$

$$\text{PBIAS} = \frac{\sum_{i=1}^{n}\left(Q_i^{obs} - Q_i^{sim}\right)}{\sum_{i=1}^{n}\left(Q_i^{obs}\right)} \text{x} 100 \quad 7.6$$

$$RE = \frac{\sum_{i=1}^{n}\left(Q_i^{obs} - \overline{Q}^{sim}\right)}{\sum_{i=1}^{n}\left(Q_i^{obs}\right)} \text{x} 100 \quad 7.7$$

Where Q_i^{obs} is observed flow; $\overline{Q}^{obs}$ is average observed flow; Q_i^{sim} is simulated flow; $\overline{Q}^{sim}$ is average of simulated flow. Where all units in m^3/s.

The auto-calibration model results showed a difference in peak values between simulated and observed on a monthly scale. The poor statistical results warranted a calibration procedure to fine-tune the parameters. The predicted streamflow data was close to the observed streamflow data obtained from the Ministry of Water and Irrigation of Jordan for 2003-2016.

7.4 Model Calibration

The model calibration modifies the parameters to predict the streamflow (as in this study). The modifications of these parameters are done to the extent that the observed streamflow data and predicted streamflow data are closely matched. This modification is fulfilled either by manually changing the input parameters or using dedicated software for this purpose. In this study, the SUFI-2 algorithm in SWAT-CUP software was used to

perform the calibration process. This software is freely available from Water Weather Energy Ecosystem. SWAT-CUP is widely used for calibrating and validating SWAT models due to its capabilities of handling many sensitivity analyses like SUFI-2, Particle Swarm Optimization (PSO), GLUE, Parameter Solution (ParaSol), and Markov Chain Monte Carlo (MCMC) algorithms with reasonably straightforward steps. (Abbaspour et al. 2007; Zhang et al. 2019).

The SUFI-2 is a stochastic process that looks at the degree of uncertainties accounted for and generates a range of values for each parameter with fitted value (Abbaspour et al., 2008). The propagation of the uncertainties in the input parameters and the model output variables are expressed as the 95% probability distributions. It is referred to like 95% prediction uncertainty, and it is expected that 95PPU envelops most of the observations (Abbaspour et al., 2018).

Hence, two statistics are defined to quantify the fit between simulation results: *P*- and *R*- factor. *P*-factor represents the enveloped observed data percentage by estimating the result (95PPU), and *R*-factor represents the thickness of the 95 PPU envelope. Good results are achievable if the *P* factor is more significant than 70% (for streamflow) and the *R* factor is around 1.

The SUFI-2 algorithm has four significant steps as follows:

1. The objective function (g_i) is the first part of the algorithm have to be characterized; later, the minimum and maximum ranges (θ_j) of the parameters will be identified.

2. After sensitivity analysis, the initial uncertainty ranges for each parameter at the first round of Latin hypercube testing.
3. After the Latin hypercube and the objective function are assessed, the sensitivity matrix (A_{ij}) and the parameters covariance grid (P) can be calculated by:

$$A_{ij} = \frac{\Delta g_i}{\Delta \theta_j}, i = 1,2,.....,P_m ; j = 1,2,.....,p$$

$$P = S_g^2 (A^T A)^{-1}$$

Where P_m, p, and S_g^2 represent the number of rows in the sensitivity matrix, number of parameters, and the variance of the objective function, respectively.

4. In the last step, the 95PPU is calculated by *P* and *R*- factors.

7.4.1 Sensitivity analysis

The Sensitivity analysis is a method to re-identify the parameters responsiveness and determine the influence on a parameter prediction (Streamflow, in this case). Table-2 shows the parameters which were used in the calibration process. All these parameters determine the occurrence of flow at the watershed outlet.

The SUFI algorithm in SWAT CUP was run six times for all the parameters for 500 simulations in each of the four iterations. **Table 7.2** shows the ranges, fitted values, and global sensitivity for each streamflow parameter. In terms of sensitivity, curve number was the most sensitive parameter, followed by Alpha_BF (base flow alpha-factor). Later, these parameters were used to find the best-simulated streamflow. The streamflow comparison between observed and simulated data was made for 12 years between 2003 and 2014 monthly. The period between 2003 and 2010 was used to

calibrate the model. Fig. 7.4a shows the obtained calibration plot, which was later assessed for statistical metrics given in section 7.6.

Table 7.2 Sensitive analysis and calibration results using SUIF-2, SWATCUP

Parameter	Min_value	Max_value	Fitted_Value	Global Sensitivity	
				t-Stat	P-Value
r__CN2.mgt	-0.25	0.15	-0.24	4.47	0.00
v__ALPHA_BF.gw	0	1	0.2	-4.14	0.00
v__GW_DELAY.gw	0	500	21.14	-2.92	0.00
v__GWQMN.gw	0	500	315.83	-2.40	0.02
v__SURLAG.bsn	0.05	30	10.76	-1.88	0.06
v__ESCO.hru	0	1	0.53	-1.82	0.07
v__EPCO.hru	0	1	0.97	1.74	0.08
v__OV_N.hru	0.1	0.3	0.18	-1.62	0.11
v__SLSUBBSN.hru	-0.5	0.5	0.1	-1.37	0.17
v__DEP_IMP.hru	0	6000	5074.6	-1.31	0.19
v__GW_REVAP.gw	0.2	0.2	0.05	-1.22	0.22
v__REVAPMN.gw	1	100	30.35	-1.14	0.26
v__CH_COV1.rte	0	0.6	0.04	1.13	0.26
v__CH_K2.rte	1	50	13.7	1.00	0.32
v__CH_N2.rte	0.01	0.3	0.08	0.99	0.32
r__SOL_AWC().sol	0.3	1	0.5	0.77	0.44
v__SOL_K().sol	0.25	25	2.22	-0.63	0.53
v__CH_K1.sub	0.05	5	2.24	0.61	0.54
v__CH_N1.sub	1	65	12.99	-0.50	0.61
v__CH_S1.sub	-0.5	1	-0.18	-0.49	0.62
r__SOL_Z().sol	0	0.05	0.03	0.46	0.64
r__GDRAIN.mgt	-0.25	0.25	-0.18	-0.44	0.66
v__SFTMP.bsn	-5	5	-4.46	-0.44	0.66
r__HRU_SLP.hru	0	0.6	0.14	0.43	0.66
r__RCHRG_DP.gw	0	1	0.11	0.37	0.71
r__SOL_CBN().sol	0.5	1	0.57	0.37	0.71
r__SOL_ALB().sol	0	0.25	0.1	-0.36	0.72
v__SMTMP.bsn	-5	5	3.55	0.32	0.75
v__SMFMX.bsn	1.7	6.5	3.79	-0.32	0.75
v__SMFMN.bsn	1.7	6.5	3.2	-0.32	0.75
r__SOL_ZMX.sol	0	0.05	0.05	-0.30	0.76
r__DDRAIN.mgt	-0.1	1	0.16	0.27	0.78
r__TDRAIN.mgt	-0.25	0.25	-0.07	-0.27	0.78
v__SHALLST.gw	0	1000	902.56	0.25	0.80
v__DEEPST.gw	0	6000	923.84	-0.15	0.88
v__CANMX.hru	0	100	83.48	-0.10	0.92
v__EVRCH.bsn	0.5	1	0.68	-0.09	0.92
v__LAT_TTIME.hru	0	180	154.85	-0.06	0.95
v__USLE_K().sol	0	0.65	0.38	0.03	0.98

v_ represents the current parameter value replaced by the given value, and r_ represents the existing parameter multiplied by (1 + given value). CN= Curve number, Alpha_BF= Baseflow alpha-factor, GW_Delay.gw= Groundwater delay, CH_COV1.rte= Channel erodibility factor, CH_K2.rte= Effective hydraulic conductivity in the main channel, CH_N2.rte= Manning's N for the main channel, SOL_AWC.sol= Available water capacity of the soil layer, SURLAG.bsn, SFTMP.bsn ESCO.hru= Soil evaporation compensation factor, OV_N.hru= Manning's N for overland flow, SLSUBBSN.hru= Average slope length, DEP_IMP.hru= Depth to impervious layer, EPCO.hru= Plant uptake compensation factor, REVAPMN.gw= Threshold depth of water in shallow aquifer required for return flow to occur, DDRAIN.hru= Depth to subsurface drain, SOL_K.sol= Saturated hydraulic conductivity, SOL_Z.sol= Depth from the

soil surface to the bottom of the layer, CH_K1.sub= Effective hydraulic conductivity in tributary channel alluvium, CH_N1.sub= Manning's N for tributary channel alluvium, CH_S1.sub= Average Slope of tributary, GW_REVAP.gw= Groundwater revap coefficient

7.5 SWAT Model Validation

The validation is when the observed data (streamflow) is compared with simulated or predicted data without changing the calibration parameters values for a period other than used during the calibration process. This study used the observed streamflow data during the 2011-2013 period for the validation process. The SWAT CUP model and the same set parameter values were configured for the said period and run for one time with 500 iterations. The predicted streamflow values are shown in comparison to the observed values in (Fig. 7.3 b).

7.6 Statistical Evaluation of SWAT Model

The goodness of fit is applied to evaluate the simulation model based on observed data using statistical and graphical interpretations. Total four indices, including Nash-Sutcliffe coefficient of efficiency (NSE), correlation coefficient (R^2), per cent bias (PBIAS), and relative error (RE) (Duru et al. 2017; Wang et al. 2019), were evaluated. The description of these indices has been provided in section (**Section 7.3.3**). The model is generally considered satisfactory or not if R^2 and NSE are more significant than 0.5, PBIAS is less ±25%, and RE is lower than 20% (Zhang et al. 2019).

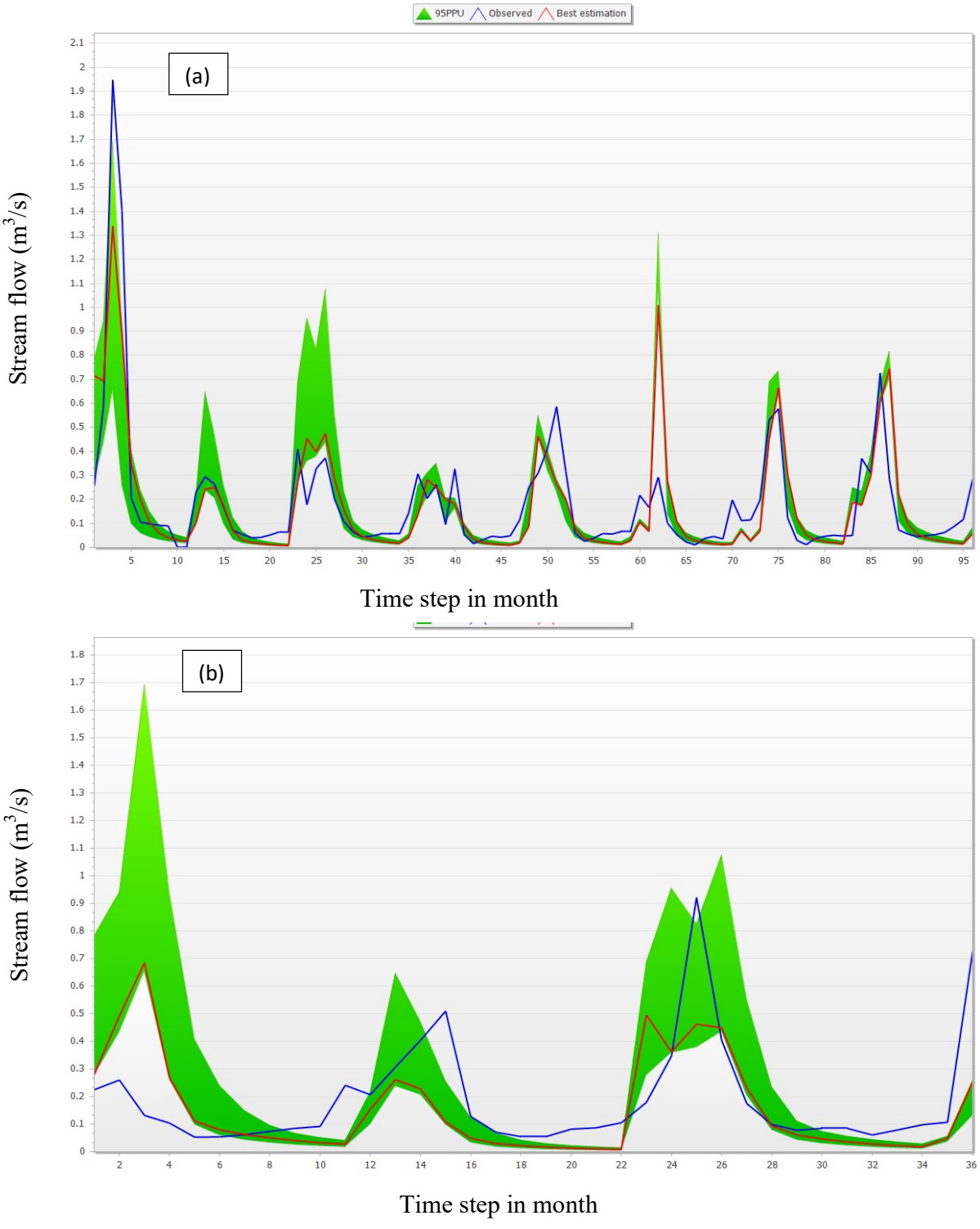

Fig. 7.3 Monthly streamflow (a) during calibration process (2003-2010) (b) during the validation process (2011-2014).

Fig. 7.3 shows the graphical plot of the observed vs predicted streamflow at the catchment outlet. Visually, a good match is observed for the fitted parameters governing the streamflow. However, the best fit was further strengthened by the statistical coefficients obtained, as shown in Table during both the calibration and validation ,7.3 periods. Based on the statistical coefficients, it can be said that the model performance is rated good as the NSE, PBIAS, RE, and R^2 are within the acceptable values. Also, the *P*- and *R*-factors as obtained during calibration and validation periods are shown in Table 7.3.:

Table 7.3 Evaluation of the model performance

Stage	Item	Streamflow
Calibration	NSE	0.65
	RE	0.15
	PBIAS	0.20
	R^2	0.71
	P-factor	0.64
	R-factor	0.43
Validation	NSE	0.58
	RE	0.18
	PBIAS	0.23
	R^2	0.67
	P-factor	0. 57
	R-factor	0.55

7.7 Forecasting the Streamflow data

7.7.1 ARIMA Modeling

In this section, the precipitation and temperature data for the period 2006-2016 and 2004-2014, respectively, were subjected to ARIMA modelling to extend the precipitation and temperature data in the future, and utilize this extended data as forcing variable for SWAT re-run (See chapter 7 section 7.4 regarding Box-Jenkins method ARIMA model).

ARIMA model was carried out for future prediction based on monthly precipitation and temperature data. The ARIMA models having minimum AIC/BIC were selected to predict the future precipitation and temperature in the area during 2014-2030. The ARIMA order (1,0,3) was well fitted for precipitation, whereas for temperature, a different ARIMA order (2,0,4) was found fit (Fig. 7.4). The models were validated with ten years dataset 2006-2016 and 2004-2014, respectively, for both the variables. The difference between observed and predicted data, called absolute error, was found as 0.09 mm in precipitation and 1.3º C in temperature during the work period (2006-2016) and (2004-2014).

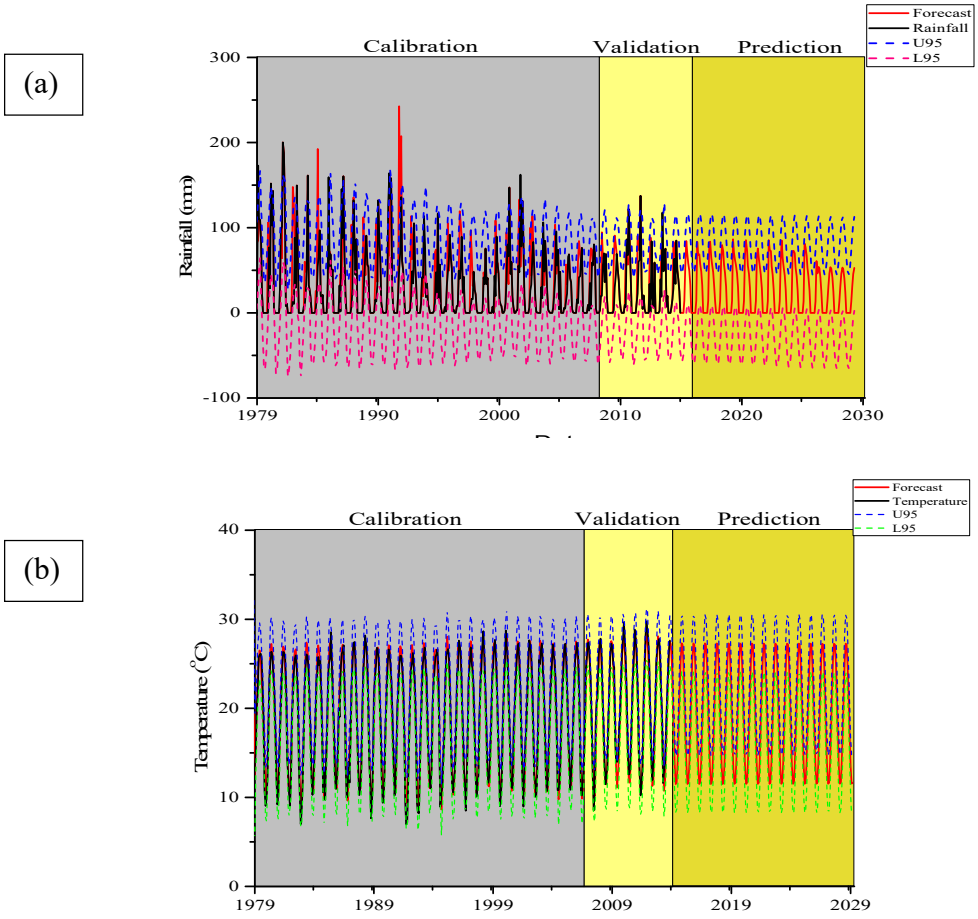

Fig. 7.4 ARIMA model for (a) Precipitation, (b) Temperature during the study period

7.7.2 Future prediction of Streamflow

Later, the monthly forecasted streamflow was estimated based on ARIMA models by running the SWAT model with the projected precipitation and temperature obtained in section 7.7.1. The calibrated parameters for 2003-2013 were utilized in the estimation process, assuming that no significant soil and land use pattern changes will occur in the proposed future period. Fig. 7.5 shows the estimated streamflow from 1979 to 2030, including the calibration and validation period. The absolute error during the calibration period was 0.03 m3/s with R2 being equal to 0.71, while during the validation period, it was found to be 0.08 m^3/s with R^2 equal to 0.63.

It was further interesting to note that the projected streamflow, when subjected to Innovative Trend Analysis, showed a declining trend on a high level, as observed from the observed and predicted streamflow (Fig. 7.5b). As observed, a decreasing trend, especially at a high level, was detected. This falling trend corroborates the falling trend in the precipitation data for the same study area reported in the literature by Al Balasmeh et al. (2019). Since precipitation and streamflow are highly positively correlated, the falling trend in streamflow seems justified for the period up to 2030.

The SWAT calibrated streamflow for the period 2003-2014 and ARIMA- SWAT predicted stream flow up to 2030, where this period is sufficient to show the inflow status for the next decade. The streamflow represents the inflow to the dam reservoir. The dam, the catchment outlet, is also the principal source of water supply for irrigation and other uses such as groundwater recharge. Therefore, with an impeded falling trend in the inflow to the dam as envisaged from this present work, a water deficit in the study area is well anticipated.

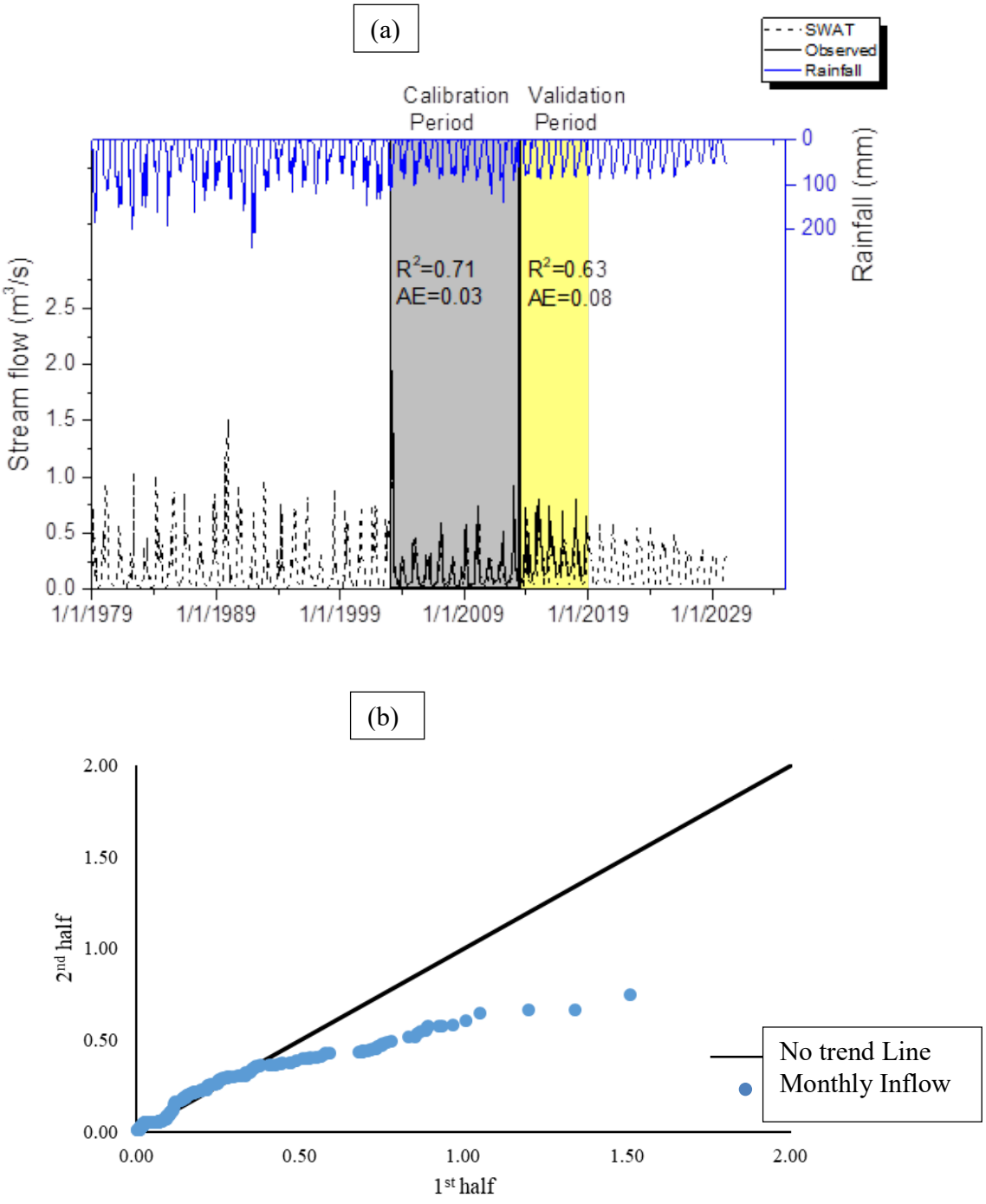

Fig. 7.5 (a) Streamflow prediction using SWAT model and ARIMA model, and **(b)** Innovative trend analysis of streamflow

7.8 Water Deficit in the study area

Water deficit is defined as the difference between inflow and outflow from the reservoir is thus calculated for the present period (2003-2018) and extended up to 2030, assuming a constant average withdrawal of 0.2 m^3/s. A simple time series plot of the water deficit up to 2030, shown in Fig. 7.6, captures an increasing trend in water deficit, warranting an immediate need for water augmentation in the study area. Under no augmentation scenario and at the present withdrawal rate, it is anticipated that by 2020 sufficient water may not be available to meet the reservoir water use.

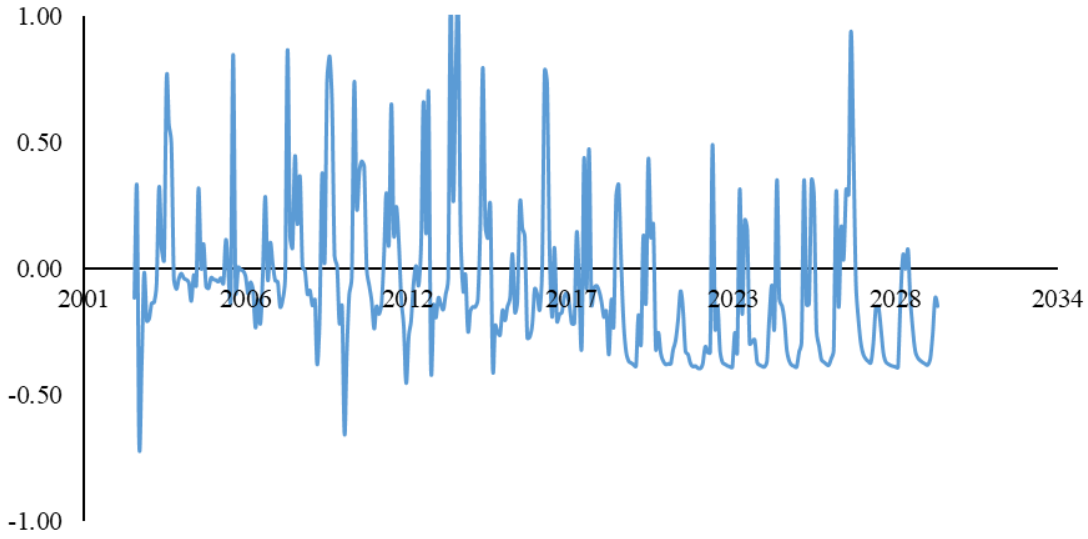

Fig. 7.6 Water deficit based on streamflow and water requirement

7.9 Conclusion

In this chapter, the streamflow data were simulated and predicted. This work was divided into two main parts: simulation and validation of the SWAT model based on historical data up to 2016 and to predict the future availability of streamflow by applying the Box-Jenkins method ARIMA model. The salient observation from this study is that the water deficit in the area is showing an increasing trend in the future. This observation

can have severe implications for reservoir operation in the catchment, which serves as a significant source of water supply for various uses. Thus, it is concluded that the streamflow (inflow into the reservoir) is decreasing, which implies that the water deficit will be a severe problem in the area. This conclusion would suggest different adapts to the natural variability (drought) and reduce unsustainable water resources utilisation (water scarcity) as the central core of chapter 8.

Chapter 8: Estimation of Hybrid Drought Index

8.1 Introduction

A drought is known as a duration of drier-than-normal conditions that results in water-related problems. Considering that drought lessens water availability for intended use, this chapter aims to estimate the hybrid drought index by integrating meteorological, hydrological, and agricultural data. This chapter details the estimation of hybrid drought index using fuzzy set theory and assigning the weight methods using fuzzy-AHP and entropy weight methods. The index has further been validated using the cross wavelet approach.

8.2 Drought and drought index

There are four types of drought: meteorological, hydrological, agricultural and socio-economic drought. The meteorological drought refers to a deficiency in precipitation amount under the normal condition at a specific location and particular time. In contrast, hydrological drought refers to anomalies in surface and sub-surface flow. On the other hand, agricultural drought refers to soil moisture deficit (within the root zone) and crop growth failure. Socio-economic drought refers to a deficit in water resources systems comparing of water demand (Wilhite and Glantz, 1985; Tallaksen and Van Lanen, 2004; Corti et al., 2009; Mishra and Singh, 2010; Sheffield and Wood, 2011; Van der Molen et al., 2011; Seneviratne et al., 2012; Altman, 2013; Svoboda and Fuchs, 2016).

Drought index is a numerical representation of drought conditions assessed using hydrological, meteorological, agricultural, and socioeconomic parameters inputs (Svoboda and Fuchs, 2016). The drought index is one of the most important indicators to

measure and monitor otherwise normal water availability conditions. It can be used for an early warning system. Several drought indices have been developed and reported, e.g. Standardized Precipitation Index (SPI), Standardized Stream Flow Index (SSFI), and Standardized Soil Moisture Index (SSMI). Earlier studies about these indices and their importance have been discussed in Chapter 2.

8.3 Hybrid Drought Index

The estimation of the hybrid drought index for the study area is a systematic procedure. The data related to streamflow, precipitation and soil moisture was required and processed separately to determine SPI, SSFI and SSMI, finally integrated. The following sections describe the procedure for its estimation and also its validation.

8.3.1 Data Analysis

For as long as 44 years, the precipitation data were collected from the Ministry of Water and Irrigation, Jordan, and soil moisture was obtained from the European Space Agency (ESA) Climate Change Initiative soil moisture version 3.3 (See section 4.1.2). The data was further divided into two major seasons, the rainy (October to May) and summer months (June to September). However, streamflow data for the same period was not available. Hence, the SWAT watershed model was calibrated and verified to predict the monthly streamflow data for the same period as the other two variables (Please refer Chapter 7:).

8.3.2 Drought estimation

Taking monthly data of precipitation depth, streamflow, and soil moisture data between 1979 and 2014 as inputs, the drought indices SPI, SSI, and SSMI were calculated. Standardized Precipitation Index (SPI) for each month was computed by estimating the

critical coefficient of gamma distribution (Lin et al. 2014; Winkler et al. 2017) given in Eq. (8.1):

$$g(x_k) = \frac{1}{\beta^{\alpha}\Gamma(\alpha)} x_k^{\alpha-1} e^{-x_k/\beta} \quad \text{for } x_k > 0 \qquad 8.1$$

Thereafter, the precipitation data was transformed to normally distributed SPI and described as in Eq. 8.2:

$$SPI = \frac{P - \overline{P}}{\sigma_P} \qquad 8.2$$

where P is the aggregated precipitation, $\overline{P}$ is the respective mean, and σ_P represents the standard deviation of available data (Keyantash, 2020). Similarly, SSFI and SSMI were also computed in the same method but using streamflow and soil moisture as respective data inputs in estimation.

The magnitude of SPI, SSFI and SSMI, drought index value was found to be varying within -4 to +5. Fig. **8.1** shows the times series plot of the three indices from January 1979 to December 2013. The figure shows that drought has occurred almost every year during non-rainy months and in the wet months (October-May). SPI and SSFI are observed to follow the same pattern. When SPI and SSFI are found to reduce, there is a considerable reduction in SSMI. This severity coincides with the decreasing SPI and SSFI during 1993-2001 (not visible in the figure) and 2003-2013.

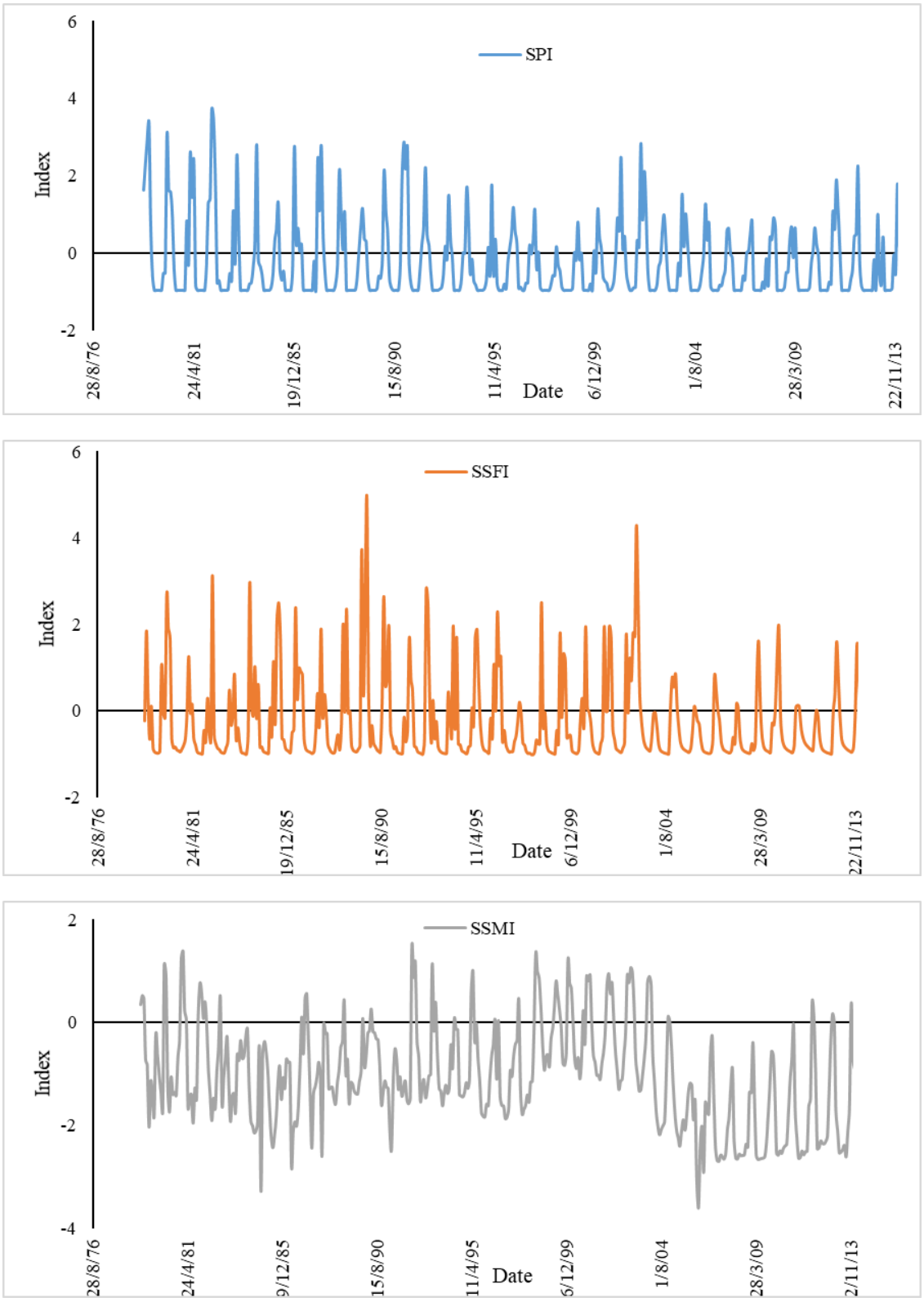

Fig. 8.1 Time series plot of SPI, SSI, and SSMI for Jan 1979 - Dec 2013.

8.3.3 Integrating the drought indices

In real-life cases, the data are shown to be imprecise or vague; for that, the fuzzy set theory is a suitable tool for describing these situations. Where fuzzy handle these situations by referring to a degree to which the specific object belongs to a set. In these situations, though, we might suppose that a certain object x belongs to a certain set Y with a certain degree, but it can be that we are not sure about that. In other words, there might be uncertainty about the membership degree of x in Y, where there is no way to combine that uncertainty into the membership degrees. However, the fuzzy membership function is a suitable mathematical attributive for a Y to make a subjective evaluation of x. Nonetheless, different subjects Y can have different attributions of object x; thus, it is required to use multi membership functions to describe them (Deschrijver and Kerre, 2005; Fan et al., 2019).

Also, assigning weights to the three variables is necessary for aggregating the effects of these variables in the proposed hybrid index. For these, two methods of weight assignment were used and compared. These methods are described in appendix B:

The weights so obtained by the two methods given above are shown in Table 8.1 Based on the values obtained, it can be concluded that the entropy weight method and F-AHP method will assign almost similar weights to three variables used in estimating the drought index. In order of preference, precipitation gets more weightage regarding its importance in describing the drought-like condition while soil moisture has comparatively lesser weightage. Based on the comparison between these methods, it can be seen that the monthly SPI series has the largest weight, whereas the monthly SSMI

series has the smallest weight, which also corroborates with the studies made by Chang et al. 2016 and Zhu et al. 2018.

Table 8.1 Weight assignment based on F-AHP and entropy method

Method	Precipitation	Streamflow	Soil moisture
F-AHP	0.3750	0.3333	0.2917
Entropy weight (monthly)	0.3619	0.3381	0.3000
Entropy weight (3-month)	0.3687	0.3248	0.3065
Entropy weight (6-month)	0.3559	0.3327	0.3114
Entropy weight (12-month)	0.3560	0.3295	0.3145

8.3.4 Estimation of Hybrid Drought Index (HDI)

Based on the analysis in the previous section, the three selected indices were divided into ten classes that ranged from extreme wet to extreme drought (Table 8.2). The EW, SW, MW, LW, AW, AD, LD, MD, SD, and ED represents extreme wet, severe wet, moderate wet, light wet, abnormal wet, abnormal drought, light drought, moderate drought, severe drought, and extreme drought, respectively.

The assumption of hybrid drought index is to build an indicator matrix with *c* classes and *m* indices and expressed in Eq. 8.3 as follows (Zhu et al. 2018):

$$Y = \begin{bmatrix} < a_{12} & [a_{12}, b_{12}] & ..... & [a_{1(c-1)}, b_{1(c-1)}] & > b_{1(c-1)} \\ > a_{22} & [a_{22}, b_{22}] & ..... & [a_{2(c-1)}, b_{2(c-1)}] & < b_{2(c-1)} \\ \vdots & \vdots & \vdots & \vdots & \vdots \\ < a_{m2} & [a_{m2}, b_{m2}] & ..... & [a_{m(c-1)}, b_{m(c-1)}] & < b_{m(c-1)} \end{bmatrix} \quad 8.3$$

To conveniently calculate Eq. (8.4) was used to transform matrix Y:

$$= \begin{cases} y_{i1} = a_{i2} \\ y_{ih} = \dfrac{a_{ih} + b_{ih}}{2}, h = 2, 3, ..., (c-1) \\ y_{ic} = {}_{bi(c-1)} \end{cases} \quad 8.4$$

Table 8.1 HDI system of drought estimation

Drought types	Drought Indices	Drought Classes									
		EW	SW	MW	LW	AW	AD	LD	MD	SD	ED
Metrological drought	SPI	>1.6	[1.3,1.6]	[0.8,1.3]	[0.5,0.8]	[0,0.5]	[-0.5,0]	[-0.8,-0.5]	[-1.3,-0.8]	[-1.3,-1.6]	<-1.6
Hydrological drought	SSFI	>1.6	[1.3,1.6]	[0.8,1.3]	[0.5,0.8]	[0,0.5]	[-0.5,0]	[-0.8,-0.5]	[-1.3,-0.8]	[-1.3,-1.6]	<-1.6
Agriculture drought	SSMI	>1.6	[1.3,1.6]	[0.8,1.3]	[0.5,0.8]	[0,0.5]	[-0.5,0]	[-0.8,-0.5]	[-1.3,-0.8]	[-1.3,-1.6]	<-1.6

where a_{ih} and b_{ih} are the left and right boundary values of the h_{th} index in the i_{th} class, respectively.

$$Y = \begin{bmatrix} y_{11} & y_{12} & \cdots & y_{1c} \\ y_{21} & y_{21} & \cdots & y_{2c} \\ \vdots & \vdots & \vdots & \vdots \\ y_{m1} & y_{m2} & \cdots & y_{mc} \end{bmatrix} = (y_{ih}) \quad 8.5$$

where x_i of the i_{th} index lies in $[y_{ih}, y_{ih+1}]$, the relative membership of x_i to the h_{th} class is calculated in Eq. 8.6 :

$$\mu_{ih}(u) = \frac{y_{ih+1}^{-i(h+1)} x_i}{y_{ih+1}^{-i(h+1)} y_{ih}}, h = 1,2,.....,c-1 \quad 8.6$$

In addition, the relative membership degree to the rest of the classes is zero. Then, the indices matrix of the relative membership degree can be obtained. The relative membership degree of evaluating object to *h* class is computed as in Eq. 8. 7 and Eq. 8.8:

$$\upsilon_h(u) = \sum_{i=1}^{m} \omega_i * \mu_{ih}(u) \quad 8.7$$

$$HDI = \sum_{i=1}^{m} \omega_i B_i \quad 8.8$$

where x_i denotes the weight of the i_{th} index, B_i is the weight of drought class, and $\sum_{i=1}^{m} \omega_i = 1$. The characteristic value of the evaluating object is finally calculated as given in Eq. 8.9 below:

$$H(u) = \sum_{i=1}^{c} \upsilon_h(u) \times h_i \quad 8.9$$

where *H* represents the Hurst index.

8.3.5 Wavelet Analysis for index validation

The wavelet analysis can be useful in studying the periodicity of the component, e.g. rainfall, streamflow, soil moisture, and drought indices. In drought analysis, it can be useful in analyzing drought patterns, drought trends, and drought periodicity from a given index, and Li et al. (2020) have used continuous/cross wavelet transform, wavelet coherence and wavelet cross-correlation to find out the relationship and the links between meteorological drought and hydrological drought.

The XWT of two sequences, x(t) and y(t), can be formed as $W^{XY} = W^X W^{Y*}$ where W^X and W^Y are the transform wavelet of x and y wavelet and * signifies composite conjugation. The cross wavelet power represents as $|W^{XY}|$. The composite debate (W^{xy}) is taken as the indigenous comparative stage among x_n and y_n in the time occurrence period. Along with this, the hypothetical distribution of the cross wavelet power of both time sequences with contextual power spectra P_k^X and P_k^Y is taken in Torrence and Compo (1998) as,

$$D\left(\frac{\left|W_n^X(S)W_n^{Y*}(S)\right|}{\sigma X\,\sigma Y} < p\right) = \frac{U\,\vartheta(p)}{\vartheta}\sqrt{P_k^X P_k^Y} \quad 8.10$$

where, $U\,\vartheta(p)$ is the assurance level connected with the likelihood p for a likelihood density purpose, explained by the square root of the product of two χ^2 distributions.

A bivariate structure termed wavelet coherence must be described to analyse the association among two-time series. In support of the appropriate description of wavelet coherence, it first requires the cross wavelet transform and cross-wavelet power (Afshan et al. 2018; Zhu et al. 2018). The details of these techniques can be found in Afshan et al.

(2018). The following Eq. 8.11 can calculate the XWT for two-time sequence $x(t)$ and $y(t)$:

$$W_{xy}(m,n) = W_x(m,n) W_y^*(m,n) \quad 8.11$$

where $W_x(m,n)$, $W_y(m,n)$ are two continuous wavelet transform of $x(t)$ and $y(t)$, separately, m is location index, n represents the measure, whereas * signifies a composite conjugate. The cross wavelet power can be calculated using cross wavelet transform as $|W_x(m,n)|$. Furthermore, the cross wavelet power spectra disclose regions in the time sequence frequency space. The time sequence displays a massive mutual power that symbolises the confined covariance among the time sequence at every measure (Afshan et al., 2018). The wavelet coherence can identify areas in the time-frequency gap where the observed time series change simultaneously but do not essentially have massive mutual power. According to Torrence and Webster (1999), the equation of adjusted wavelet coherence coefficient is as follows:

$$R^2(m,n) = \frac{\left| N\left(N^{-1} W_{xy}(m,n)\right)\right|^2}{N\left(N^{-1}|W_x(m,n)|\right)^2 N\left(N^{-1}|W_y(m,n)|\right)^2} \quad 8.12$$

Fig. **8.2** displays the continuous wavelet transform between meteorological, hydrological, agriculture, related drought indices and the hybrid drought index. In the figure, the thick curved line represents the cone of influence (CoI); the dashed line is the significance level (5%) for the global wavelet spectrum. Based on the figure, it is found that the periodicity of drought predominately occurs within the band one year, meaning the drought had a frequency of occurrence every year. Studying the relations between drought variations and climatic patterns such as Niño3.4 is helpful to understand the drought mechanism and evaluate the effect of atmospheric circulation on regional

drought characteristics (Guo et al. 2018). Hence, large-scale sunspot activity (Niño3.4 index) was used to validate further the proposed index (Zhu et al. 2018). Fig. 8.2 and 8.3 represent the relations between the proposed index with Niño index also.

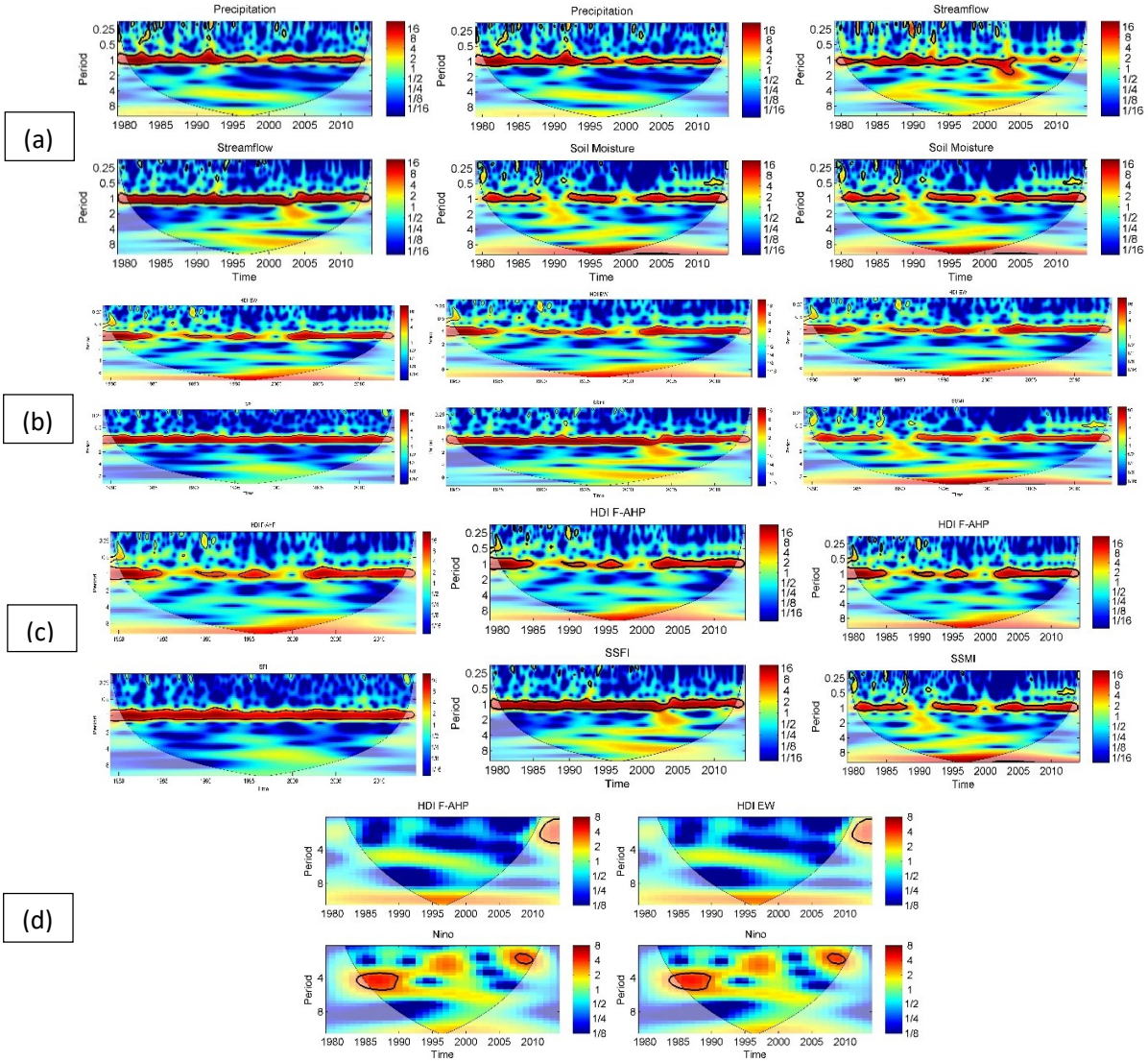

Fig. 8.2 Continuous wavelet power spectra for the time series of the transform relationships of (a) rainfall, streamflow, and soil moisture, (b) HDI using F-AHP with SPI, SSFI, and SSMI, (c) HDI using ET weight with SPI, SSFI, and SSMI, (d) HDI using F-AHP with sunspot number Nino 3.4 index.

The wavelet coherence locates the sections in time-frequency in which the time series co-vary (Fig. 8.4). Fig. **8.3** and Fig. **8.4** provide interesting findings, whereas the

results clearly show a strong relationship between the datasets. In comparison between XWT and WTC results, high power coherence is observed in all regions of the time series.

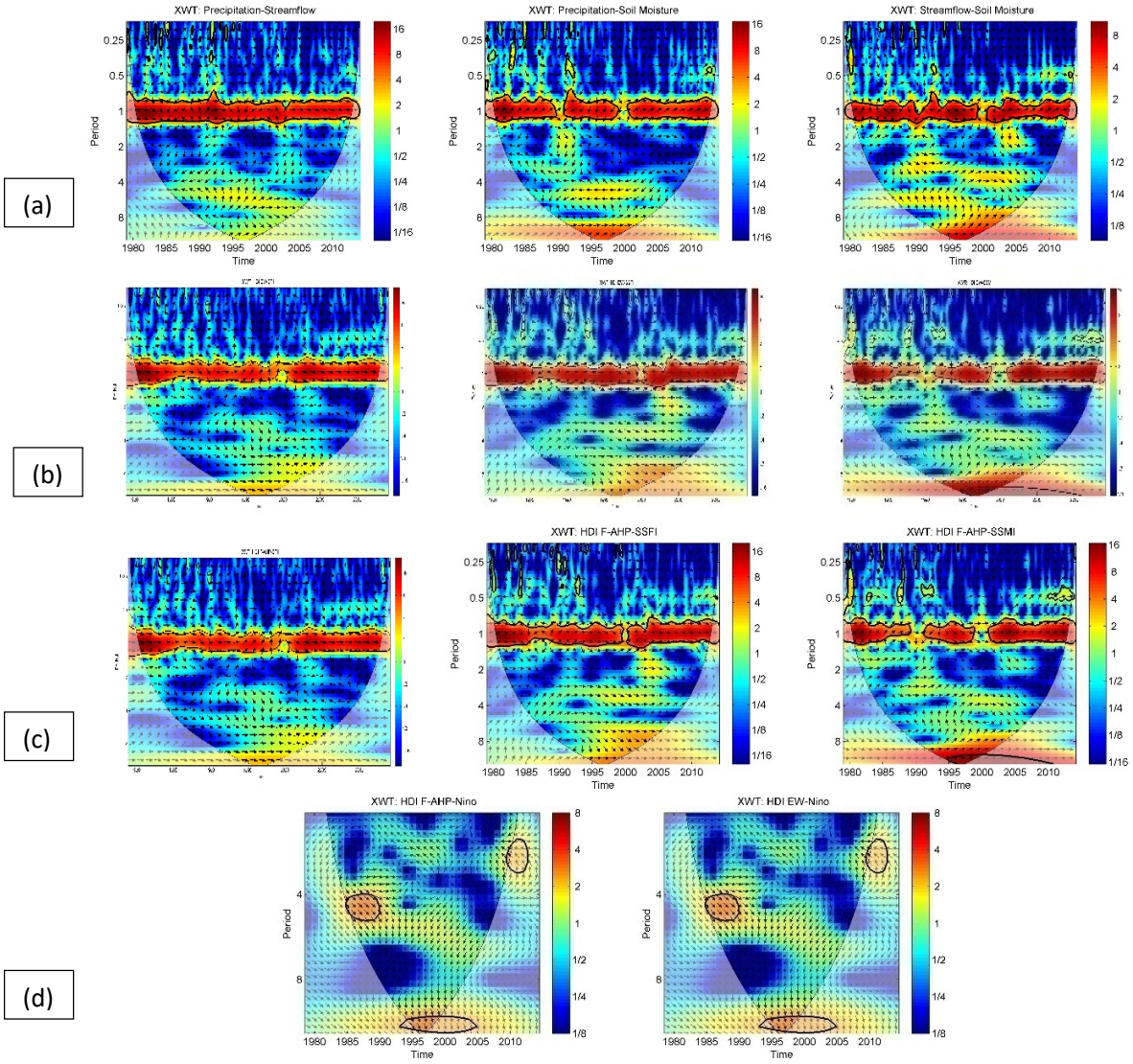

Fig. 8.3 Cross wavelet transform between (a) rainfall, streamflow, and soil moisture, (b) HDI using F-AHP with SPI, SSFI, and SSMI, (c) HDI using ET weight with SPI, SSFI, and SSMI, (d) HDI using F-AHP with sunspot number Nino 3.4 index

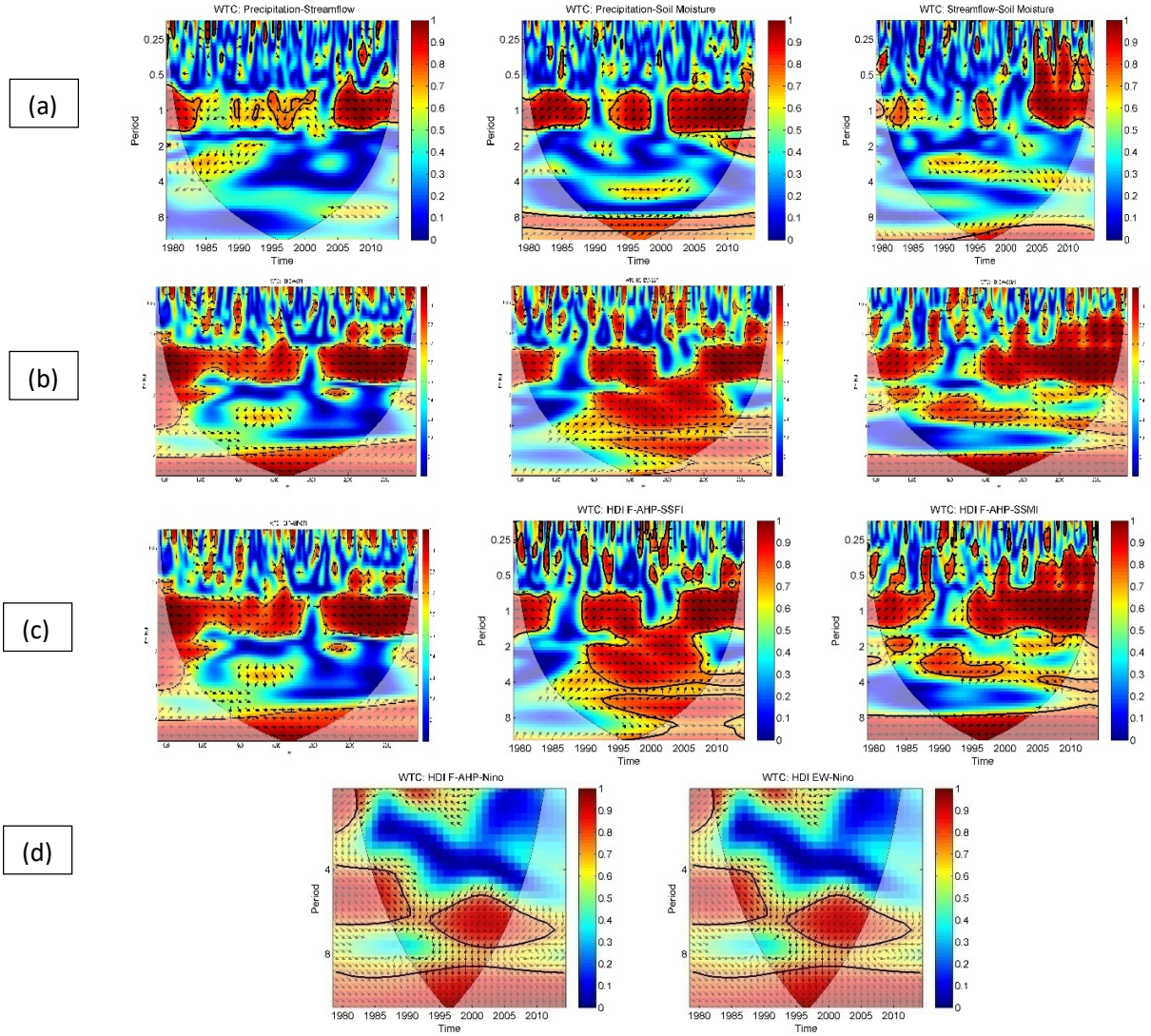

Fig. 8.4 Wavelet Coherence(WCO) between (a) rainfall, streamflow, and soil moisture, (b) HDI using F-AHP with SPI, SSFI, and SSMI, (c) HDI using ET weight with SPI, SSFI, and SSMI, (d) HDI using F-AHP with sunspot number Nino 3.4 index

8.3.6 Understanding Correlations and trend analysis

After working out the drought indices, Pearson Correlation Coefficient (PCC) with 0-, 1-, 3-, and 6-lag was used to analyze the drought delay in the response parameter. The results obtained are given in Table 8.2. A high correlation coefficient between SPI and SSFI/SSMI indicates that precipitation is a significant parameter. In a 1-month accumulation period, it can be observed from the table that the drought condition quickly

changes between months as the PCC coefficient between SPI and SSMI are high (r = 0.53) and SPI and SSFI (r = 0.38). At the same time, soil moisture response to streamflow is weak (r = 0.49) at a different lag time. Also, the 3-months accumulation period shows better performance compared to a shorter timescale for detecting the drought. The 6- and 12-month periods showed similar results for other periods in the soil moisture response to precipitation.

On the other hand, the response of soil moisture to streamflow was clearly shown by PCC values as it increased from r = 0.55 to r = 0.63. The long-term timescale analysis, i.e. 12-month accumulation period, shows that the drought is controlled by streamflow. Based on PCC analysis, it is found that monthly and 3-month cumulative periods were useful in analyzing and detect the short-term behaviour. At the same time, 6- and 12-month were able to capture a long-term behaviour, and hence these periods are more suitable to study the drought conditions in the area.

To further detect the sudden changes in the time series data of precipitation, streamflow, and soil moisture data along with the drought indices computed above, a trend analysis was performed using the Innovative trend analysis method proposed by Şen (2012). Although various methods are available to detect the trend in time series data, the present method was chosen over others for two reasons; first, this method generates seven possible trend conditions compared to trendless, increasing and decreasing trends. Secondly, this method gave better validation when predicting the trend in precipitation data for the same area in a previous study (Al Balasmeh et al., 2019). The analysis of this method on the data set the revealed trend in monthly and seasonal precipitation, streamflow, soil moisture, and their related indices

Table 8.2 PCC analysis for drought indices

Monthly data							
Lag 0	SPI	SSFI	SSMI	Lag 3	SPI	SSFI	SSMI
SPI	1.00			SPI	1.00		
SSFI	0.38	1.00		SSFI	0.36	1.00	
SSMI	0.53	0.49	1.00	SSMI	0.51	0.49	1.00
Lag 1	SPI	SSFI	SSMI	Lag 6	SPI	SSFI	SSMI
SPI	1.00			SPI	1.00		
SSFI	0.38	1.00		SSFI	0.37	1.00	
SSMI	0.53	0.49	1.00	SSMI	0.51	0.49	1.00
3-Months period							
Lag 0	SPI-3	SSFI-3	SSMI-3	Lag 3	SPI-3	SSFI-3	SSMI-3
SPI-3	1.00			SPI-3	1.00		
SSFI-3	0.42	1.00		SSFI-3	0.40	1.00	
SSMI-3	0.57	0.54	1.00	SSMI-3	0.56	0.54	1.00
Lag 1	SPI-3	SSFI-3	SSMI-3	Lag 6	SPI-3	SSFI-3	SSMI-3
SPI-3	1.00			SPI-3	1.00		
SSFI-3	0.41	1.00		SSFI-3	0.40	1.00	
SSMI-3	0.56	0.54	1.00	SSMI-3	0.56	0.54	1.00
6-Months period							
Lag 0	SPI-6	SSFI-6	SSMI-6	Lag 3	SPI-6	SSFI-6	SSMI-6
SPI-6	1.00			SPI-6	1.00		
SSFI-6	0.40	1.00		SSFI-6	0.39	1.00	
SSMI-6	0.55	0.55	1.00	SSMI-6	0.54	0.55	1.00
Lag 1	SPI-6	SSFI-6	SSMI-6	Lag 6	SPI-6	SSFI-6	SSMI-6
SPI-6	1.00			SPI-6	1.00		
SSFI-6	0.39	1.00		SSFI-6	0.39	1.00	
SSMI-6	0.54	0.55	1.00	SSMI-6	0.54	0.55	1.00
12-Months period							
Lag 0	SPI-12	SSFI-12	SSMI-12	Lag 3	SPI-12	SSFI-12	SSMI-12
SPI-12	1.00			SPI-12	1.00		
SSFI-12	0.40	1.00		SSFI-12	0.40	1.00	
SSMI-12	0.48	0.63	1.00	SSMI-12	0.48	0.63	1.00
Lag 1	SPI-12	SSFI-12	SSMI-12	Lag 6	SPI-12	SSFI-12	SSMI-12
SPI-12	1.00			SPI-12	1.00		
SSFI-12	0.40	1.00		SSFI-12	0.40	1.00	
SSMI-12	0.48	0.63	1.00	SSMI-12	0.48	0.63	1.00

.

Table 8.3 Trend identification for various parameters

Monthly data							
Lag 0	SPI	SSFI	SSMI	Lag 3	SPI	SSFI	SSMI
SPI	1.00			SPI	1.00		
SSFI	0.38	1.00		SSFI	0.36	1.00	
SSMI	0.53	0.49	1.00	SSMI	0.51	0.49	1.00
Lag 1	SPI	SSFI	SSMI	Lag 6	SPI	SSFI	SSMI
SPI	1.00			SPI	1.00		
SSFI	0.38	1.00		SSFI	0.37	1.00	
SSMI	0.53	0.49	1.00	SSMI	0.51	0.49	1.00
3-Months period							
Lag 0	SPI-3	SSFI-3	SSMI-3	Lag 3	SPI-3	SSFI-3	SSMI-3
SPI-3	1.00			SPI-3	1.00		
SSFI-3	0.42	1.00		SSFI-3	0.40	1.00	
SSMI-3	0.57	0.54	1.00	SSMI-3	0.56	0.54	1.00
Lag 1	SPI-3	SSFI-3	SSMI-3	Lag 6	SPI-3	SSFI-3	SSMI-3
SPI-3	1.00			SPI-3	1.00		
SSFI-3	0.41	1.00		SSFI-3	0.40	1.00	
SSMI-3	0.56	0.54	1.00	SSMI-3	0.56	0.54	1.00
6-Months period							
Lag 0	SPI-6	SSFI-6	SSMI-6	Lag 3	SPI-6	SSFI-6	SSMI-6
SPI-6	1.00			SPI-6	1.00		
SSFI-6	0.40	1.00		SSFI-6	0.39	1.00	
SSMI-6	0.55	0.55	1.00	SSMI-6	0.54	0.55	1.00
Lag 1	SPI-6	SSFI-6	SSMI-6	Lag 6	SPI-6	SSFI-6	SSMI-6
SPI-6	1.00			SPI-6	1.00		
SSFI-6	0.39	1.00		SSFI-6	0.39	1.00	
SSMI-6	0.54	0.55	1.00	SSMI-6	0.54	0.55	1.00
12-Months period							
Lag 0	SPI-12	SSFI-12	SSMI-12	Lag 3	SPI-12	SSFI-12	SSMI-12
SPI-12	1.00			SPI-12	1.00		
SSFI-12	0.40	1.00		SSFI-12	0.40	1.00	
SSMI-12	0.48	0.63	1.00	SSMI-12	0.48	0.63	1.00
Lag 1	SPI-12	SSFI-12	SSMI-12	Lag 6	SPI-12	SSFI-12	SSMI-12
SPI-12	1.00			SPI-12	1.00		
SSFI-12	0.40	1.00		SSFI-12	0.40	1.00	
SSMI-12	0.48	0.63	1.00	SSMI-12	0.48	0.63	1.00

Y- refers to decrease trend, and N refers to trendless.

The Hurst index was found to be more than 0.5. Other Hurst indices values refer to types of time series, where there are three possible values for Hurst index: i) $H < 0.5$, it refers to the trend of time series in the future will be opposite to the current and past trend. ii) $H = 0.5$, it refers that the time series is independent. iii) $H > 0.5$, it refers that the trend in the future will be similar to the current and past trends (Gammel 1998). Thus, the Hurst index can also be applied to analyse drought persistence in the Wadi Shueib

catchment. It can be easily observed from Fig. **8.5** that the droughts indices are following a trend, which is consistent with the finding of Törnros and Menzel (2014) and Rajsekhar and Gorelick (2017). For verifying the performance of HDI as a multi variables index against single drought indices, the times series plot of SPI, SSFI, and SSMI were compared with HDI shown in Fig. 8.5a.

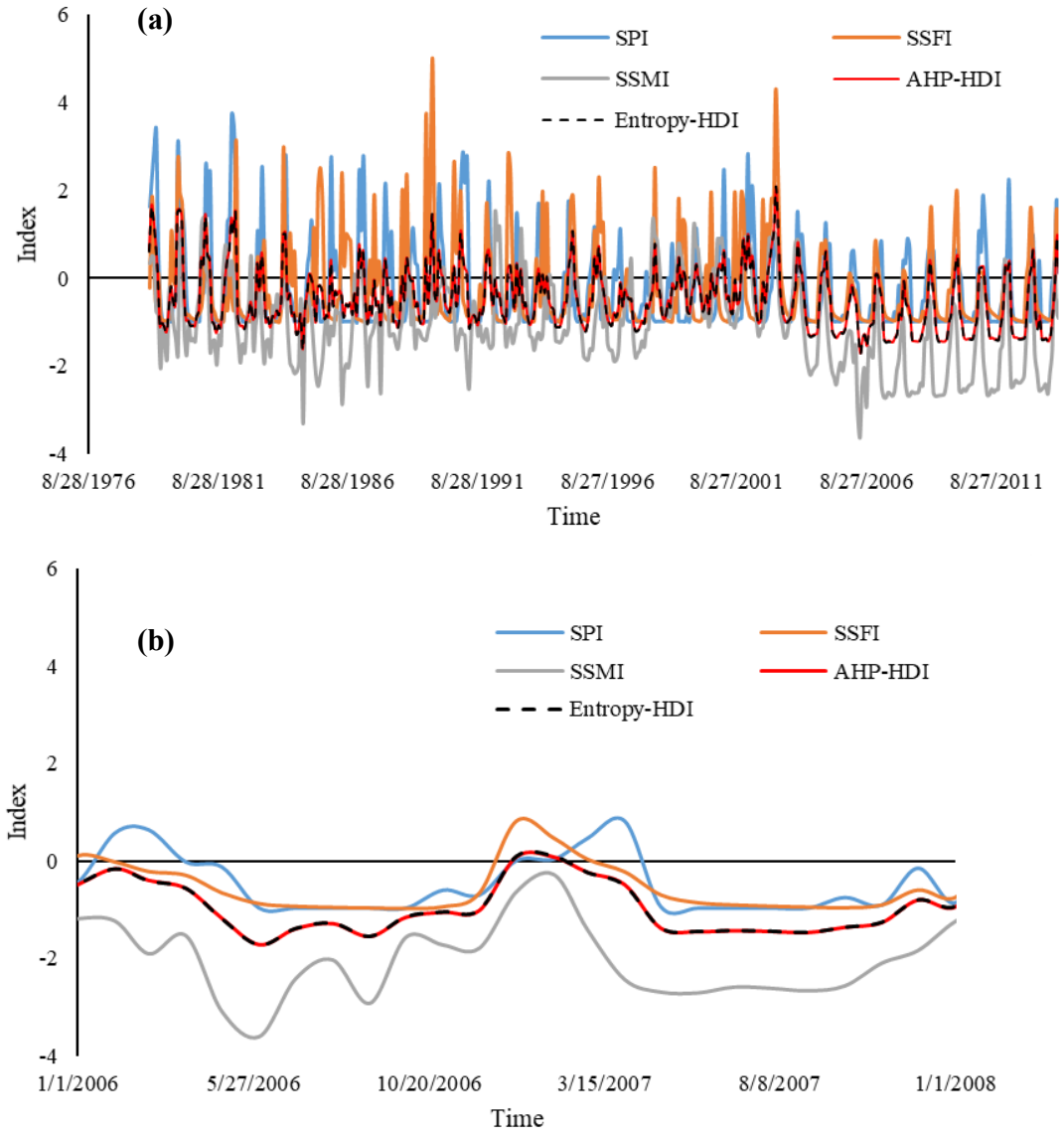

Fig. 8.5 Drought propagation for the basin during a) 1979-2014, b) 2006-2007.

From the figure, it can be observed that HDI follows a similar trend as other indices. For the sake of more clarity, the period between 2006 and 2008 has been highlighted in Fig. 8.5b. From Fig. 8.5b, the trend can be seen between HDI and other drought indices, and the trend is seen to almost relate to other drought indices. The increase and decrease of SPI, SSFI, and SSMI also reflect a similar HDI trend. This trend indicates that HDI can reflect even small changes in the single variable indices, thus allowing for comprehensive characterizations of meteorological, hydrological and agricultural droughts. Based on the PCC test, as given in Table 8.4, a strong correlation between HDI and SPI, SSFI, and SSMI.

Table 8.4 PCC analysis between HDI and other drought indices

Method	SPI	SSFI	SSMI
F-AHP-HDI	0.91	0.84	0.73
Monthly Entropy-HDI	0.91	0.84	0.74
3-month Entropy-HDI	0.95	0.88	0.89
6-month Entropy-HDI	0.94	0.89	0.85
12-month Entropy-HDI	0.67	0.85	0.75

8.4 Conclusions

Thus based on the preliminary analysis, the proposed HDI model's reliability is established, which was further established by performing trend analysis using the wavelet analysis approach given in the Wavelet Analysis for validation section. The wavelet analysis between Hybrid drought indices (HDI) using F-AHP and Entropy weight (EW) and standardized drought indices (SPI, SSFI, and SSMI) was performed. No significant variation was observed in the analysis. A significant positive correlation was found between HDI and other indices in 1-year signal for all dataset series. The wavelet coherence supports this relationship since a strong positive correlation appears in the time series. It is found that HDI shows a statistically significant positive relationship with 1 to

3 years signal in 2008-2012, 4 to 5 years signal in 1985-1990, and 10 to 12 years signal in 1993-2005. Besides that, it has been that the SPI is more sensitive to capture the drought onset. Or in other words, the meteorological drought or deficiency in precipitation is responsible for the onset of various drought types. In contrast, the streamflow drought is more capable of determining the realistic drought persistence.

Chapter 9: Soil Erosion Management Practices

9.1 Introduction

Soil erosion from the watershed and its transportation and deposition in the reservoir is one of the major issues which affect the reservoirs operations. As discussed in previous chapters, Jordan and especially the Wadi Shueib catchment face water deficiency as the water is required mainly for irrigation among other sectors from the Wadi Shueib reservoir. However, it was reported that the reservoir is losing its storage capacity due to the deposited sediment at a higher rate (Ministry of Water and Irrigation of Jordan, 2016). Due to the soil erosion in the catchment, the sediment is carried into the reservoir. So, there is a need for management practices in this catchment for reservoir sustainability and efficient operations for a longer period. However, before implementing any preventive measures at the catchment scale, it must be tested as to which soil erosion management can benefit while keeping the surrounding environment safe. In this chapter, the management practices under laboratory-scale experiments were carried out, and the best organic land cover implemented in the field scale was found. The work deals with the overland flow, infiltration, and soil erosion under different vegetative cover, slopes, and extreme rainfall conditions. The results were verified using mathematical models. This knowledge will help to determine the differences in soil loss and groundwater recharge using different land covers at a larger field scale. The ground slope and rainfall intensity were chosen following the field conditions in extreme cases.

9.2 Experimental Analysis

9.2.1 Experimental Set up

Laboratory-scale experiments were conducted to study the impact of land covers on soil erosion, infiltration, and surface runoff. Using steel plates, an experimental flume was fabricated with dimensions 140 x 100 x 30 cm^3 (Fig. 9.1**).** Six adjustable flow nozzles with 1.6 mm diameter (Spray angle = 40^o - 120^o) were fixed with a pipe network so that water at desired rates could be sprayed uniformly over the surface area of the flume. The experiment was designed for a 175 mm/hr peak rainfall intensity, as measured by a rain gauge. Near the flume outlet, two tapered plates were attached to the body of the flume, one at the top and the other at the bottom, to collect the overland flow and sub-surface flow, respectively (Fig. 9.1). Six holes of 4 cm diameter each were made near the downstream plate to drain the subsurface flow to the tapered plate. The basic requirement of any simulator design must produce near-natural rainfall characteristics (Chouksey et al., 2017; Mhaske et al., 2019). So, similar rainfall characteristics were ensured before experiments were conducted in the laboratory.

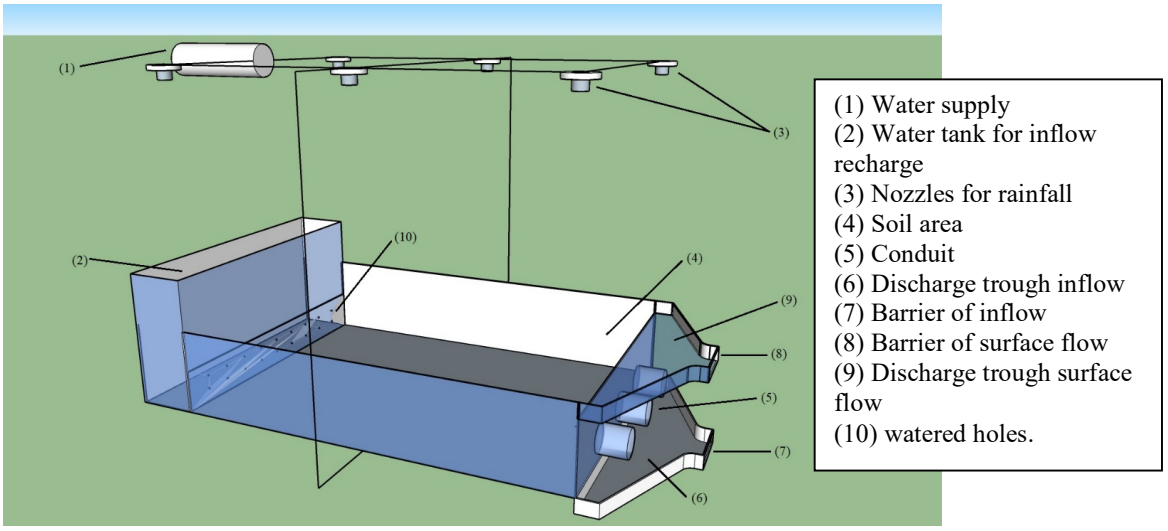

Fig. 9.1 Sprinkler installation diagram

In-situ soil density was measured in the field and the flume using an SDG200 Non-Nuclear Soil Density Gauge (make: Transtech systems). Soil water contents were also measured before each experiment to ensure that soil moisture was similar to the in-situ conditions.

9.2.2 Experimental procedure

A total of 56 experiments (Fig. 9.1) were performed by varying surface slopes, soil types, and organic covers. Almost all the experiments were duplicated to verify consistency in the results. A few initial experiments were conducted to determine the time required for consistent seepage and plan intervals to collect samples (overland and sub-surface flow). Experimental conditions are listed in Table 9.1.

Fig. 9.2 shows the three types of covers used: (i) khus (variety of grass), (ii) dry tree leaves, (iii) and dry wheat straw. Khus resembles dry grass; it is also known as wood wool or excelsior in North America.

Table 9.1 Experiment conditions

Cover	Bare	Dry Leaves	Khus	Wheat Straw	No. of experiments conducted
Soil mark	Slope (%)				
Soil-1	5	5	5	5	16
	10	10	10	10	16
Soil-2	5	5	5	5	8
	7.5	-	-	7.5	4
	10	10	10	10	8
	40	-	-	40	4

Before starting each experiment, the flume was filled with 600 ± 10 kg of natural air-dried soil. This soil was manually spread over the bottom of the flume and compacted such that the layer was not more than 100 mm. Soil density gauge was used to ensure that its density was similar to in-situ soil bulk density (~1900 kg/m^3) up to the top level.

Fig. 9.2 Various covers used in the experiments

Particle size distribution of soil 1 and 2 are given in (Fig. 9.3). Table 9.3 shows soil characteristics and physical properties for each soil type used. The compaction process was carried out in four layers with a top layer of ~30 mm. Soil moisture content was measured 24 hours before starting each experiment using the oven-dry method (at a temperature of about 100 ºC) to ensure a moisture content of ~17.5%. Additional

moisture, if required, was added to the soil in the flume to get similar in-situ soil moisture content. A similar set of experiments was also conducted with bare soil, considered the base case in the present work. The experiments were carried out until the sub-surface flow became steady, with constant precipitation.

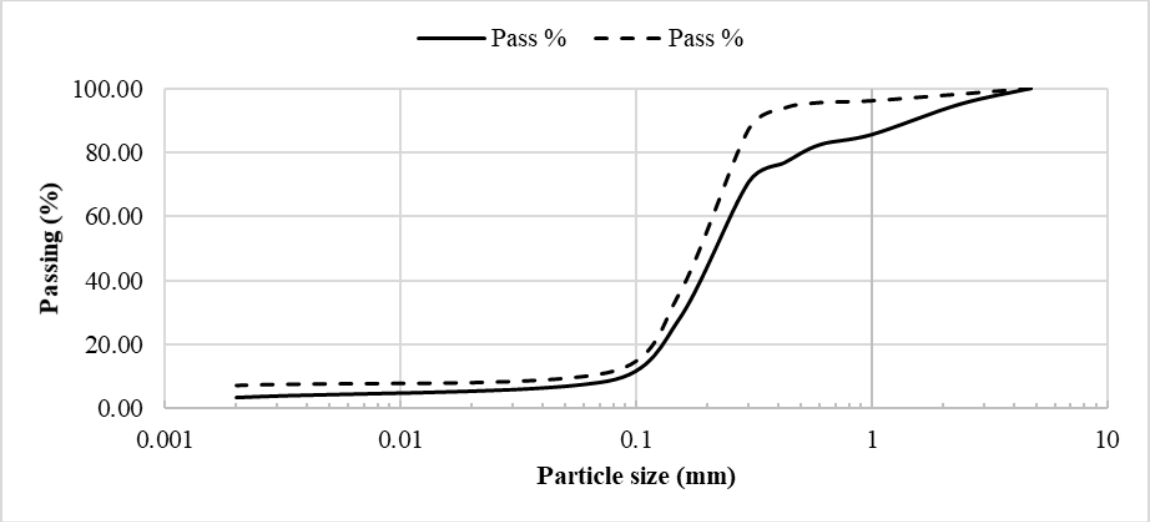

Fig. 9.3 Sieve analysis for Soil-1 (solid line) and Soil-2 (dash line)

9.2.3 Estimation of rainfall parameters

The following section describes the estimation of rainfall parameters such as rainfall intensity, raindrop size, rainfall uniformity, kinetic energy, and rainfall velocity. These parameters directly control soil erosion. Therefore, to obtain consistent results, these parameters need to be set following previous studies conducted by other researchers.

Table 9.2 Detailed results of the experiment

ID	Soil	Cover	Slope (%)	Runoff (ml/s)		Average (ml/s)		Std. Dev.
				Min	Max	Min	Max	
1	1	Bare	5	0	39	0	40.5	3.8
2	1	Bare	5	0	36			
3	1	Bare	5	0	42			
4	1	Bare	5	0	45			
5	1	Dry leaves	5	0	25	0	27.7	4.8
6	1	Dry leaves	5	0	34			
7	1	Dry leaves	5	0	29			
8	1	Dry leaves	5	0	23			
9	1	Khus	5	0	20	0	18.0	2.9
10	1	Khus	5	0	16			
11	1	Khus	5	0	21			
12	1	Khus	5	0	15			
13	1	Wheat Straw	5	0	10	0	12.7	2.5
14	1	Wheat Straw	5	0	13			
15	1	Wheat Straw	5	0	16			
16	1	Wheat Straw	5	0	12			
17	1	Bare	10	0	62	0	58.7	4.6
18	1	Bare	10	0	57			
19	1	Bare	10	0	53			
20	1	Bare	10	0	63			
21	1	Dry leaves	10	0	47	0	45	2.2
22	1	Dry leaves	10	0	46			
23	1	Dry leaves	10	0	42			
24	1	Dry leaves	10	0	45			
25	1	Khus	10	0	44	0	42.2	3.3
26	1	Khus	10	0	39			
27	1	Khus	10	0	40			
28	1	Khus	10	0	46			
29	1	Wheat Straw	10	0	21	0	19.5	2.6
30	1	Wheat Straw	10	0	19			
31	1	Wheat Straw	10	0	22			
32	1	Wheat Straw	10	0	16			
33	2	Bare	5	0	25	0	23.5	2.1
34	2	Bare	5	0	22			
35	2	Dry leaves	5	0	19	0	18.5	0.7
36	2	Dry leaves	5	0	18			
37	2	Khus	5	0	21	0	20.5	0.7
38	2	Khus	5	0	20			
39	2	Wheat Straw	5	0	15	0	13.0	2.8
40	2	Wheat Straw	5	0	11			
41	2	Bare	7.5	0	35	0	33.0	2.8
42	2	Bare	7.5	0	31			
43	2	Wheat Straw	7.5	0	12	0	13.0	1.4
44	2	Wheat Straw	7.5	0	14			
45	2	Bare	10	0	39	0	36.5	3.5
46	2	Bare	10	0	34			
47	2	Dry leaves	10	0	21	0	23.5	3.5
48	2	Dry leaves	10	0	26			
49	2	Khus	10	0	23	0	24.5	2.1
50	2	Khus	10	0	26			
51	2	Wheat Straw	10	0	11	0	13	2.8
52	2	Wheat Straw	10	0	15			
53	2	Bare	40	0	37	0	37.5	0.7
54	2	Bare	40	0	38			
55	2	Wheat Straw	40	0	18	0	16.5	2.1
56	2	Wheat Straw	40	0	15			

Table 9.3 Soil characterization and hydraulic properties

Soil Mark	Soil-1	Soil-2
Sand (%)	85	92
Silt (%)	10	4
Clay (%)	5	4
θ_s (m^3/m^3)	0.36	0.34
θ_f(m^3/m^3)	0.14	0.121
θ_w (m^3/m^3)	0.06	0.051
K_s (mm/s)	0.0188	0.0525

θ_s, θ_f, θ_w, and K_s refer to saturated water content, field moisture capacity, wilting coefficient, and saturated hydraulic conductivity, respectively

9.2.3.1 Rainfall intensity

Rainfall intensity is the main parameter in any experimental study with a rainfall simulator, mostly based on nozzles spray (Parsons and Stone, 2006). Here, full cone spray nozzles were used with a circular spray pattern by Spraying Systems Co., India (www.sprayindia.com). The flow rate and rainfall intensity are affected by water pressure, although the nozzle spray angle remains. The rainfall intensity was measured using Symon's rain gauge (Mhaske et al., 2019).

9.2.3.2 Raindrop size

The drop size of natural rainfall varies from 0.5 to 6 mm, and during heavy rain, it can be still higher. Several methods estimate the raindrop size (e.g. stain, flour pellet, photographic and laser-optical method (Mhaske et al., 2019). The flour pellet method and digital image enhancement techniques were used to measure raindrop size in this work.

Fig. 9.4 shows the impressions of raindrops on the floured surface, where the floured surface was placed on a plate having dimensions (21 x 17 x 5 cm deep) to fill with fine flour to a height of approximately 2.5 cm. The rainfall drops from the nozzle were allowed to fall onto the floured surface for less than 2 seconds (Laws and Parsons, 1943). The flour was kept in an oven for 24 h at 100^{o}C to make the floured surface harder

for further measurements (Kohl, 1974). The image processing enhancement technique was then used to measure the raindrop diameter.

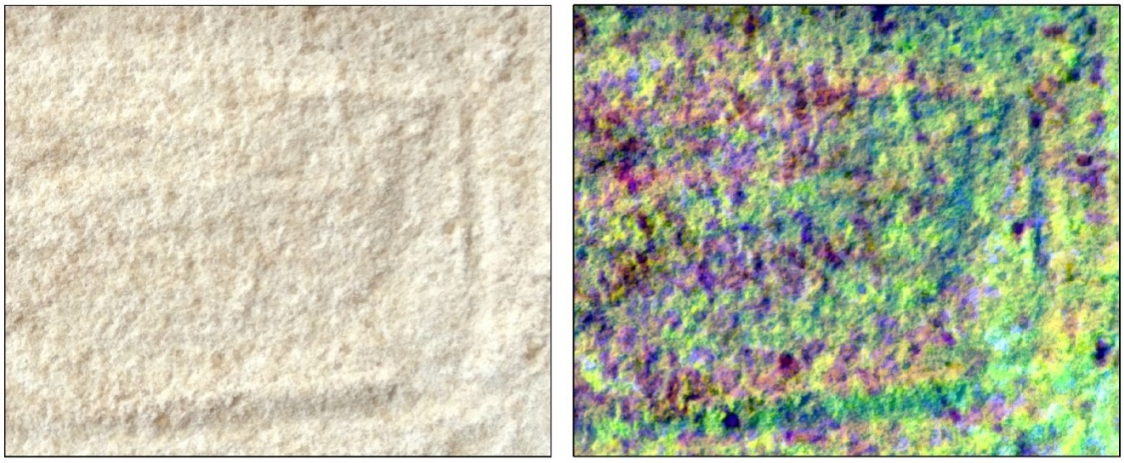

Fig. 9.4 Drop distribution using flour pellet method **(a)** flour exposed and **(b)** digital impressions of raindrops

9.2.3.3 Rainfall uniformity

The spatial distribution of rainfall in the flume provides a measure of rainfall homogeneity. Six adjustable flow nozzles covered a soil surface area of 1.4 m^2. To determine the uniformity coefficient, we used one nozzle at a time. A rectangle of size 0.5 m x 0.5 m was marked on the soil inside the flume. The uniformity of the rainfall distribution was estimated using four dishes kept at equal distances, at corners of the rectangle having a nozzle at the centre. Later, the amount of rainfall collected in these dishes was used to estimate the uniformity using the Christiansen coefficient (C_u) Eq. 9.1 (Mhaske et al., 2019):

$$C_u = 1 - \frac{\sum_{i=1}^{n} |R_i - M|}{nM} \qquad 9.1$$

where R_i represent the amount of rainfall in each petri dish; M is the average rainfall in Petri dishes. The Christiansen coefficient (Cu) varies from 0 to 100% depending on the

uniformity of rainfall, where 100% represents the uniform distribution of rainfall and 0% is the completely non-uniform distribution.

9.2.3.4 Kinetic energy and rainfall velocity

The rainfall *KE* represents the potential ability of rain to disrupt soil aggregates. The *KE,* as proposed by Wischmeier and Smith (1958), is given as Eq. 9.2 and Eq. 9.3:

$$e = 11.897 + 8.73 \log_{10} I \quad 9.2$$

$$KE = \sum_{i=0}^{n} eP \quad 9.3$$

where e is the kinetic energy (J/mm.m^2), I is the rainfall intensity (mm/h), P is the rainfall amount (mm), KE is the kinetic energy (J/m^2), and n is the number of rainfall periods.

The fall velocity of raindrops was estimated based on the comparison between the measured and terminal velocity of raindrops to its diameter (Lows and Parson, 1943) given as:

$$V_R = -0.43d^2 + 3.43d + 0.59 \quad 9.4$$

$$V_T = 3.78d^{0.67} \quad 9.5$$

where V_R represents the raindrop velocity, V_T is the terminal velocity, and d is the diameter of the raindrop (mm). The terminal velocity equation was used by (Fox 2004) and is reasonably accurate across the range of diameter and makes the computation straightforward, comparing with other formulas (Beard, 1976; Rogers and Yau, 1992).

9.2.4 Soil Infiltration Rate

The infiltration rate is considered a vital parameter, affecting the groundwater recharge, and any change of infiltration rate directly influences surface runoff. The soil

infiltration rate was calculated to analyze the dynamic variation of infiltration rate in each case with different land covers by using Eq. (9.6) (Pan and Shangguan, 2006):

$$\phi = \frac{It\cos\gamma - \frac{10R}{S}}{t} \quad 9.6$$

where ϕ refers to the infiltration rate (mm/min), I refers to the rainfall intensity (mm/min), t refers to the time for infiltration (min), γ represents the surface slope in degree, R is the total runoff (ml), and S is the rain-affected area of slope (cm^2).

9.2.5 Mathematical models

From the experimental results, mathematical model coefficients were estimated for overland flow, subsurface flow and infiltration rate. Mu et al. (2015) gave the fitted curves for surface flow and infiltration rate for different land covers based on rainfall intensity and slope. Mu et al. (2015) proposed two equations (Eq. 9.7 and Eq. 9.8) to fit the overland flow and subsurface flow, as i) logarithmic model and ii) polynomial model:

$$f(t) = b\ln(t) + a \quad 9.7$$

$$f(t) = at^2 + bt + c \quad 9.8$$

where f(t) represents model fitting, *a*, *b*, and *c* are the fitting parameters, and *t* is the time.

Mu et al. (2015) also used Horton's and Kostiakov's model to fit the observed infiltration rate.

9.2.5.1 Horton's model

Horton's model is an empirical method of the infiltration equations. Horton gives infiltration capacity as a function of time as in Eq. 9.9 (Horton, 1940):

$$f = f_c + (f_o - f_c)e^{-kt} \quad 9.9$$

where f_o is the initial infiltration capacity (mm/h); f_c is the final or equilibrium infiltration capacity (mm/h); f is the infiltration capacity (mm/h) at time t (h); k is an exponent governing the rate of decline of infiltration capacity (h^{-1}).

Two different cases can happen during the infiltration process: ponding and non-ponding condition cases. These conditions accommodate time-varying rainfall intensities in the ponding condition case, where the rainfall intensity is less than the saturated hydraulic conductivity of the soil during the storm. While in the case of non-ponding, the infiltration capacity of soil is greater than the rainfall intensity.

It shows that if the precipitation exceeds the infiltration capacity, infiltration tends to decrease exponentially. Total infiltrated water depth within a specific period can be represented as an area under the curve at that period.

9.2.5.2 Kostiakov model

Kostiakov (1932) developed a physically-based infiltration model extensively used due to its simplicity and accuracy. Kostiakov models the infiltration capacity to time as in Eq. 9.10 below:

$$f = \beta t^{-\alpha} \qquad 9.10$$

Where, f is the cumulative infiltration rate after time t, β and α are the constants. The parameter β represents the initial water infiltration rate into the soil; α is an index of soil structural stability.

Similarly, observed data were fitted using Eqs. 8.7-8.10 for surface flow, sub-surface flow and infiltration rate. These equations will help understand the dynamics of the infiltration rate (Eqs. 8.9-8.10).

9.2.5.3 USLE model

The Universal Soil Loss Equation (USLE) has provided a model for predicting soil erosion loss that has been used rightly and wrongly throughout the world (Wischmeier and Smith, 1978). USLE was used to calculate the soil loss rate in the runoff plots under different scenarios, as given in Eq. 9.11 below:

$$A = RKLSCP \tag{9.11}$$

where A is the soil loss rate ($t \cdot ha^{-1} \cdot year^{-1}$), R is the average annual rainfall-runoff erosivity factor ($MJ \cdot mm \cdot ha^{-1} \cdot h^{-1} \cdot year^{-1}$), K is the soil erodibility factor ($t \cdot h \cdot MJ^{-1} \cdot mm^{-1}$), L is the slope length factor (dimensionless), S is the slope steepness factor (dimensionless), C is the cover-management factor (dimensionless), and P is the support practice factor (dimensionless).

9.2.5.4 MUSLE model

The Modified Universal Soil Loss Equation (MUSLE) model applies to points where the overland flow enters streams. Then the sediment delivered to these points concentrates on giving the total sediment load delivered to the stream network within a watershed for a given storm event. By including the runoff as an independent factor in predicting erosion, MUSLE improves the accuracy of soil erosion prediction compared to the USLE and Revised USLE models (Sadeghi et al., 2007; Benavidez et al., 2018). MUSLE can be expressed by the following Eq. (9.12):

$$Y = 11.8(Qq)^{0.56} KLSCP \tag{9.12}$$

where Y is the sediment yield in metric tons for a storm event, Q is the runoff volume (m^3), q is the peak flow rate in $m^3 s^{-1}$, K is the soil erodibility factor ($t \cdot h \cdot MJ^{-1} \cdot mm^{-1}$), L is the slope length factor (dimensionless), S is the slope steepness factor (dimensionless), C

is the cover-management factor (dimensionless), and *P* is the support practice factor (dimensionless).

MUSLE equations were used to verify soil loss results from laboratory-scale experiments. It can be worth mentioning that the Universal Soil Loss Equation (USLE) was not used to verify the results due to improved accuracy in the MUSLE model (Williams, 1975a, b; Williams and Berndt, 1977; Neitsch et al., 2005; Sadeghi et al., 2007).

9.2.5.5 Model evaluation

The USLE and MUSLE model predictions were evaluated using the NSE (Nash and Sutcliffe, 1970). NSE was calculated using Eq.7.4.

9.3 Results and Discussion

Before the soil erosion experiments, the rainfall simulator system was calibrated with an average rainfall intensity of 144 mm/h against the natural rainfall occurrence in arid to semi-arid regions. The uniformity of rainfall distribution was ~98% Christiansen coefficient. The raindrop diameters from the nozzles varied between 0.57 and 3.77 mm (Fig. 9.5a). Rainfall velocity, terminal velocity, and kinetic energy of raindrops were estimated to be 2.39 to 7.39 m/s, 2.58 to 9.19 m/s, ~1072.11 J/m^2/h, respectively (Fig. 9.5b). These values are within the range as reported by Laws (1941) under different platforms height and intensities in laboratory conditions, while the rainfall intensity in-situ varied between 30 and 250 mm/h. Fig. 9.6 shows the overland flow directions during the experiment.

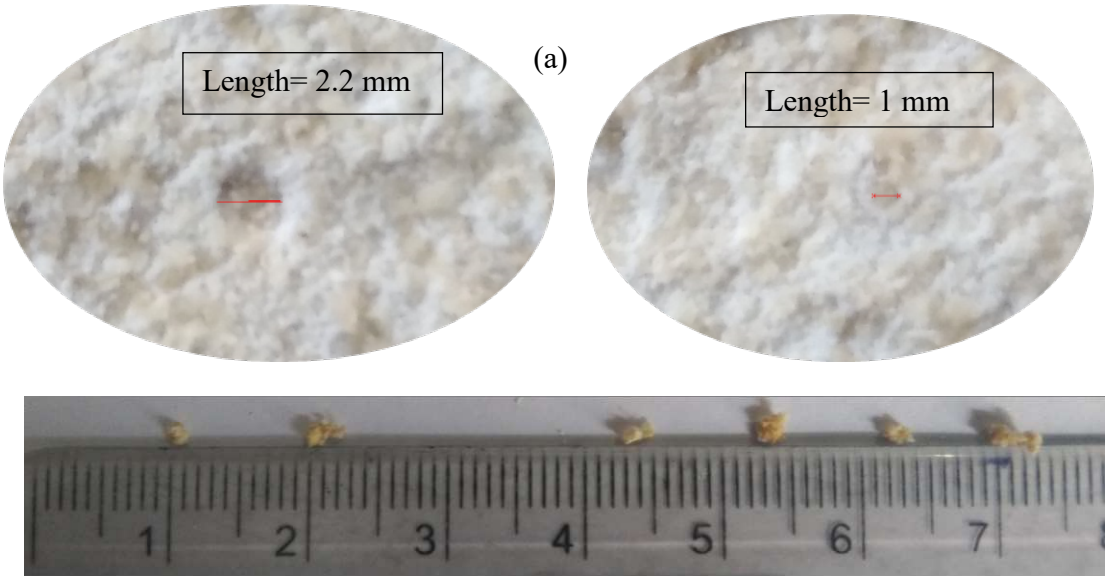

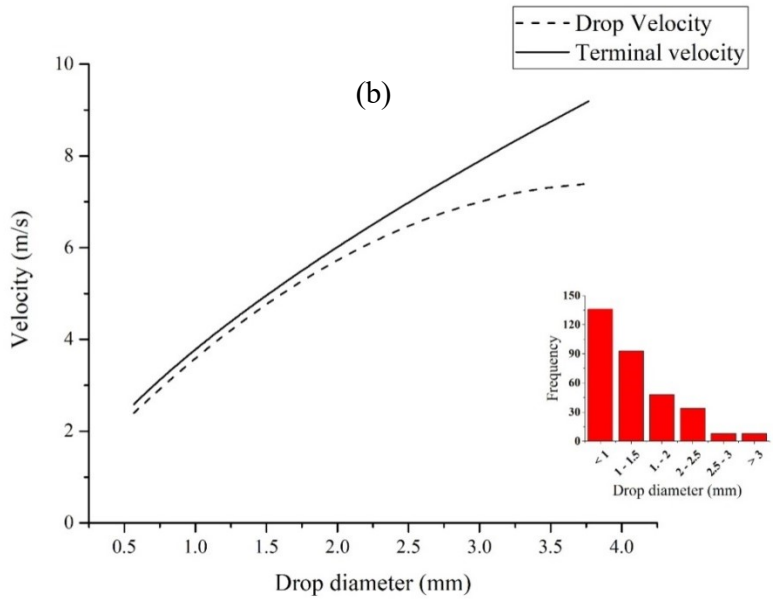

Fig. 9.5 (a) Raindrop diameter calibration using flour pellet method, and (b) Comparison of terminal velocity and measured velocity to raindrop diameters

9.3.1 The Response of Surface Flow

Soil-1 with the bare surface having 5% and 10% slopes exhibited the maximum overland flow rate as ~40 ml/s and ~60 ml/s, respectively (Fig. 9.7a-d). Khus, dry leaves and wheat straw cover, with 10 % slope, reduced the overland flow rate to 40 ml/s, 40

ml/s (33 % reduction) and 25 ml/s (60% reduction), respectively. However, with a 5% slope and wheat straw cover, the overland flow rate was reduced to 15 ml/s. Soil-2 with the bare surface having 5%, 10%, and 40% slope exhibited a maximum overland flow rate of 32, 35, and 55 ml/s, respectively. The flow rate was reduced to 15, 15 and 25 ml/s with wheat straw cover for the respective slopes. Thus a maximum reduction in overland flow rate of ~55% was found using wheat straw in Soil-2. Based on Mu et al. (2015), the surface flow rate was fitted with: (i) 2nd order polynomial and (ii) logarithmic model. The polynomial model fits better than the latter, with R^2 ranging between 0.83- 0.97, as shown in Table 9.4. Fig. 9.8 shows a typical fit of experimental data with the exponential function.

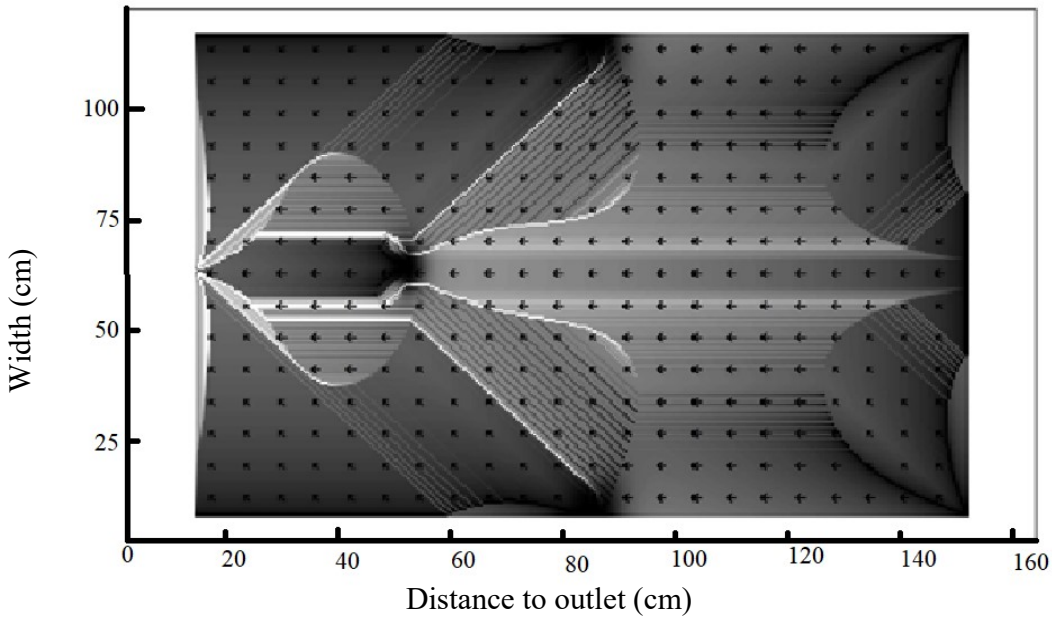

Fig. 9.6 Visualization of flow direction in experiments flume (runoff velocity variation)

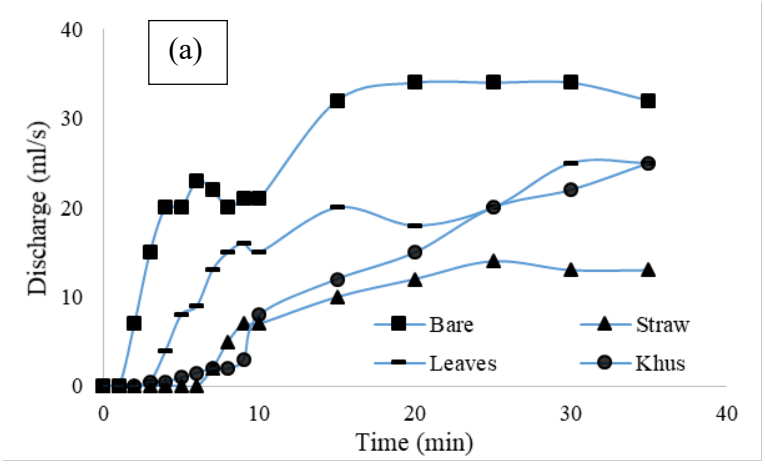
(a)
Discharge (ml/s)
Time (min)
Bare
Straw
Leaves
Khus

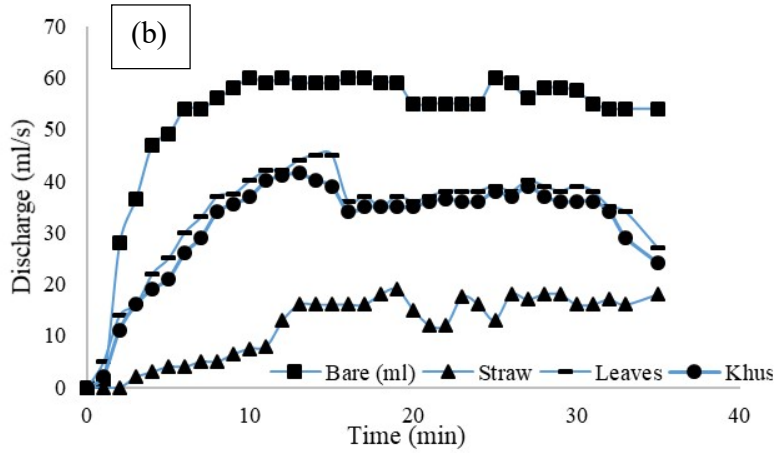
(b)
Discharge (ml/s)
Time (min)
Bare (ml)
Straw
Leaves
Khus

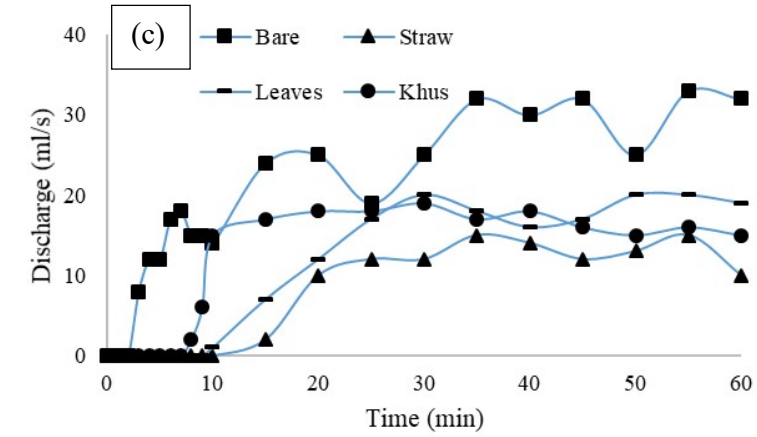
(c)
Bare
Straw
Leaves
Khus
Discharge (ml/s)
Time (min)

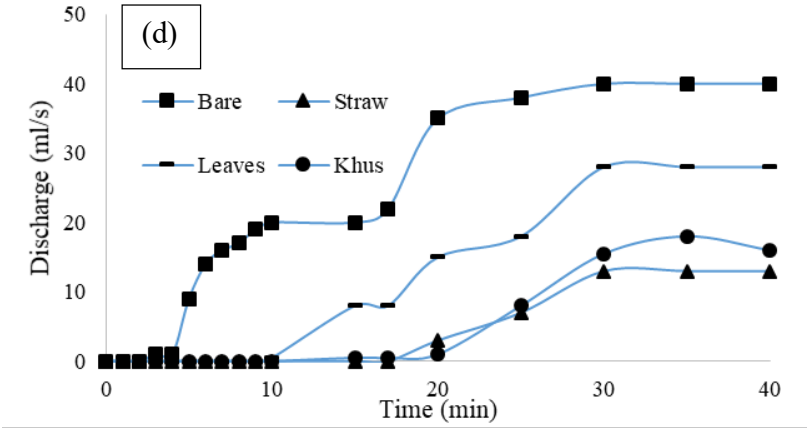

Fig. 9.7 Surface runoff with a) Soil-1and 5% slope, b) Soil-1 and 10% slope, c) Soil-2 and 5% slope, and d) Soil-2 and 10% slope, respectively.

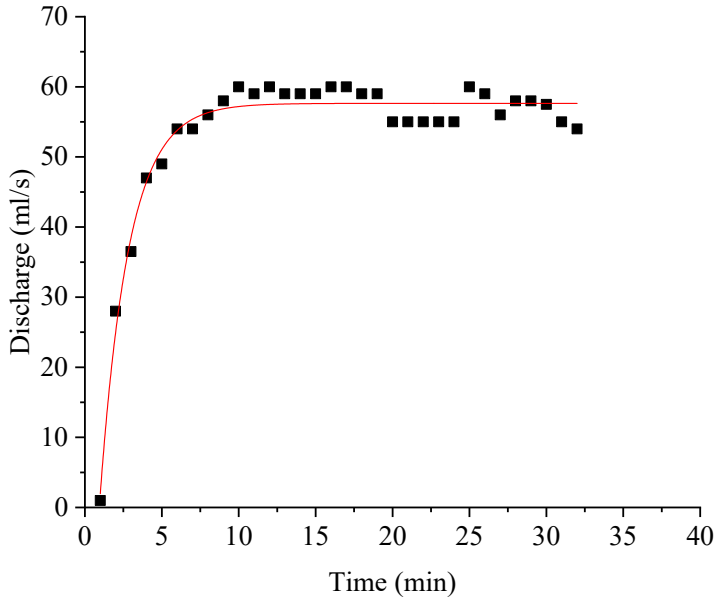

Fig. 9.8 Surface runoff with curve fitting

9.3.2 The Response of Sub-surface Flow

Soil-1 in bare condition with 5% slope only exhibited subsurface flow with a peak flow rate of 8 ml/s. The subsurface flow was increased to ~14 ml/s with wheat straw cover (Fig. 9.9a). Soil-2 with 5% and 10% slopes and the wheat straw cover showed a peak flow rate of 35 ml/s, although there were variations in time response of flow rate (Fig.

9.9b and Fig. 9.9c). The present findings are in agreement with the study conducted by Paul (2006). He reported that vegetation cover increased the groundwater recharge compared to bare soil. In contrast, groundwater recharge with wheat straw was the most efficient cover type among all vegetation covers. Similar to the surface flow rate, the subsurface flow rate also showed a better fit with the polynomial model (Table 9.5).

Table 9.4 Curve fitting of surface flow at different slopes

Surface Flow									
Cover	Slope (%)	Soil mark	$f(t)=b*\ln(t)+a$			$f(t)= at^2+bt+c$			
			a	b	R^2	a	b	c	R^2
Bare	5	1	80.82	-10.03	0.91	-0.32	23.48	-24.06	0.95
	10	1	133.98	-100.29	0.91	-0.26	14.29	-21.16	0.88
	5	2	80.82	-10.03	0.91	-0.13	11.77	44.36	0.84
	7.5	2	92.3	-8.37	0.95	-0.34	20.47	16.69	0.93
	10	2	72.003	63.72	0.82	-0.22	16.12	79.84	0.83
	40	2	159.92	36.97	0.91	-1.02	48	40.18	0.92
Straw	5	1	152.99	-421.02	0.92	0.095	0.11	-4.704	0.89
	10	1	75.92	-74.78	0.81	-0.26	14.29	-21.16	0.88
	5	2	82.91	-173.17	0.9	-0.06	6.18	-26.15	0.91
	7.5	2	41.57	-36.92	0.86	-0.09	7.11	-17	0.96
	10	2	39.63	-32.05	0.78	-0.1	7.71	-13.68	0.88
	40	2	80.61	-18.33	0.88	-0.45	22.07	-4.9	0.89
Leaves	5	1	93.76	-123.9	0.7	0.021	7.91	-39.62	0.95
	10	1	81.023	114.55	0.78	-2.17	60.34	8.6	0.97
	5	2	66.82	-85.19	0.8	-0.09	9.39	-42.26	0.93
	10	2	66.82	-19.46	0.88	-0.17	12.92	12.36	0.9
	5	1	-400.51	153.78	0.82	0.15	-0.85	-2.62	0.9
	10	1	-53.6	59.26	0.74	-0.82	33.48	63.53	0.84
	5	2	59.26	-53.6	0.74	-0.16	12.11	-32.53	0.85
	10	2	76.75	-83.02	0.85	-0.15	12.77	-43.06	0.96

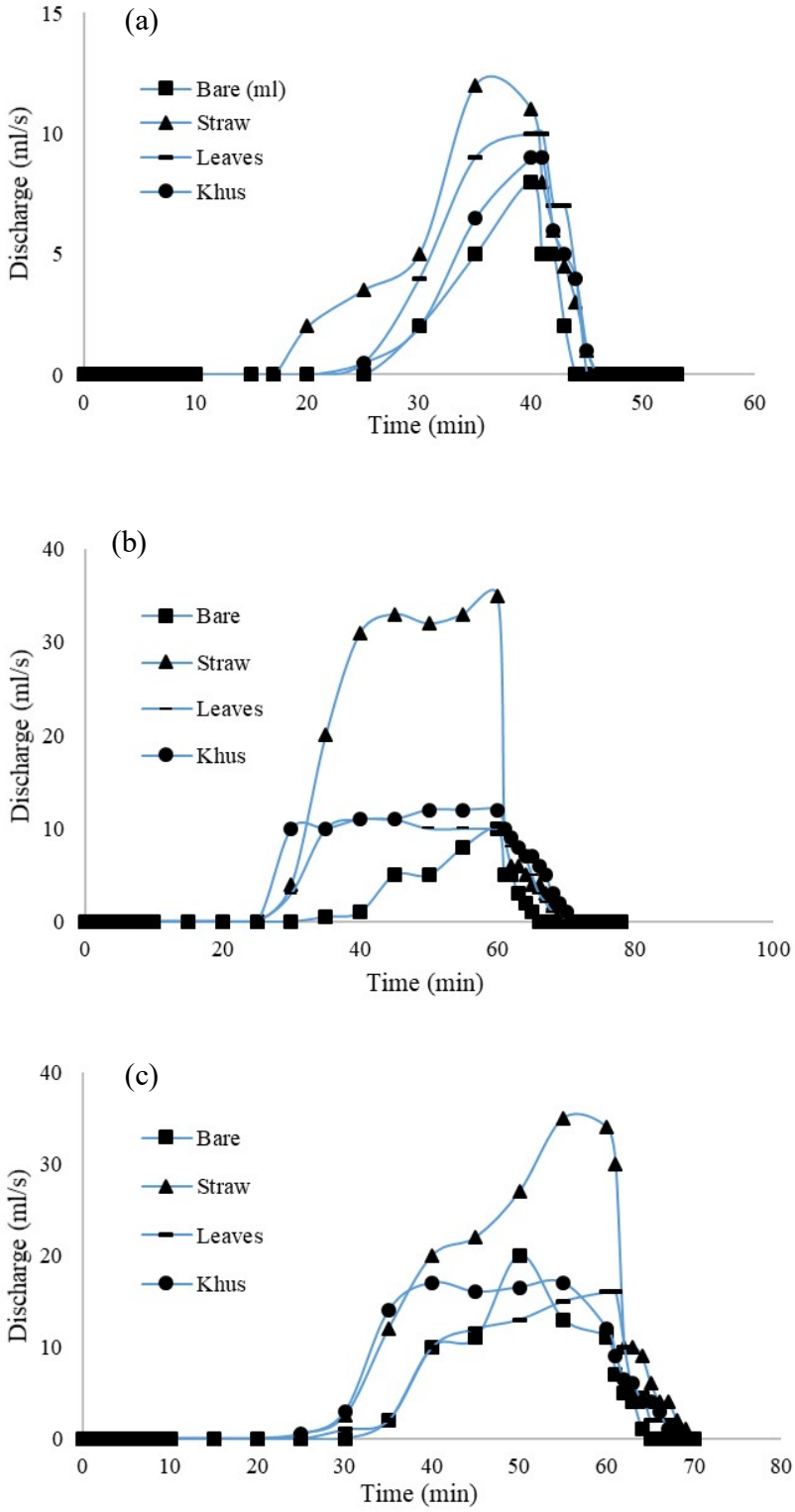

Fig. 9.9 Sub-surface discharge with a) Soil-1 and 5% slope; b) Soil-2 and 10% slope; c) Soil-2 and 5% slope.

Table 9.5 Curve fitting of sub-surface flow at different slopes

Sub-surface Flow									
Cover	Slope (%)	Soil mark	f(t)=b*ln(t)+a			f(t)= at^2+bt+c			
			a	b	R^2	a	b	c	R^2
Bare	5	1	133.98	-100.29	0.91	-0.34	24.39	-31.53	0.95
	10	1	129.57	126.66	0.91	-0.65	33.73	148.61	0.85
	5	2	80.82	-10.03	0.91	-0.143	13.34	22.92	0.94
	7.5	2	92.3	-8.37	0.95	-0.33	19.81	22.56	0.92
	10	2	72.003	63.72	0.82	-0.203	14.73	96.71	0.82
	40	2	159.92	36.97	0.91	-0.97	45.91	55.92	0.9
Straw	5	1	158.92	-438.56	0.94	0.102	-0.018	-4.91	0.91
	10	1	75.92	-74.78	0.81	-0.28	15.02	-27.48	0.87
	5	2	46.58	-60.09	0.75	-0.081	7.46	-35.97	0.9
	7.5	2	41.57	-36.92	0.86	-0.11	7.79	-22.97	0.96
	10	2	39.63	-32.05	0.78	-0.11	7.95	-16.57	0.87
	40	2	80.61	-18.33	0.88	-0.46	22.32	-6.81	0.87
Leavs	5	1	186.92	-404.17	0.94	0.045	7.21	-33.69	0.94
	10	1	80.32	119.12	0.75	-0.57	26.34	87.2	0.93
	5	2	102.29	-200.36	0.92	-0.09	9.39	-42.26	0.93
	10	2	71.12	-26.57	0.91	-0.19	13.53	9.15	0.9
Khus	5	1	105.09	-241.37	0.75	0.15	-0.85	-2.62	0.9
	10	1	81.39	110.46	0.6	-0.59	26.4	88.155	0.86
	5	2	59.26	-53.6	0.74	-0.16	12.12	-32.53	0.85
	10	2	87.48	-115.89	0.89	-0.16	13.33	-50.26	0.97

9.3.3 Time of Initiation of Overland and Sub-surface Flow

The time of initiation is required to understand the effectiveness of a cover to hold the rainwater fallen on the ground for a longer duration and gradually release it to the soil to get sufficient time for infiltration. Fig. 9.7 shows the surface runoff to time under different soil, slope, and cover conditions. The surface runoff initiation time for bare soil with Soil-1 and 5% slope was ~2 minutes, but with khus and leaves surface cover, it increased to ~4 minutes. However, the initiation time was ~7 minutes (~3 times of bare soil) using wheat straw cover. For experiments at10% slope, initiation time increased from 3 minutes for bare soil to 10 minutes for wheat straw (~3 times bare soil). Similar

findings were also observed inflow initiation time with Soil-2, where an increase of approximately five times was observed when using wheat straw compared to bare soil. Whereas, with a 40% slope, no sub-surface flow was recorded up to 30 minutes.

The analysis also showed that soil loss increased with the increase in surface flow (Fig. 9.7), similar to the findings of Kateb et al. (2013). Fox and Bryan (1999) developed a relation among soil erosion rate, runoff rate and slope with their observed data from the laboratory flume. Similarly, following empirical Eqs. (9.13 and 9.14) were obtained from the observed data:

$$\text{Soil Loss}_{\text{Bare}} = 1545.4Q^{1.06}(\tan\alpha)^{1.96} \quad 9.13$$

$$\text{Soil Loss}_{\text{Straw}} = 65Q^{0.02}(\tan\alpha)^{2.69} \quad 9.14$$

where soil loss in g, Q peak surface runoff in ml/s, and α is the slope.

In the above two equations, the soil loss can be computed based on surface runoff and slope. In the case of straw cover, the influence of the surface runoff component is very low compared to the bare soil case. It is because the major precipitation component is stored in the straw mattress and surface runoff becomes very less. Thus, the soil erosion with straw cover depends mainly on the ground slope.

Fig. 9.10 shows a comparison of soil erosion with a slope between bare soil and wheat straw. It can be found that for bare soil, the model fits well (chi square=0.81 against 7.81 with 95% confidence level and degree of freedom 3). However, the model overestimates the erosion rate with straw cover at the higher slope (chi-square = 0.45). A similar study was conducted by Zhang et al. (2004) and Wei et al. (2007). They also reported that vegetation cover is the major parameter affecting surface runoff and soil loss in steep slope areas.

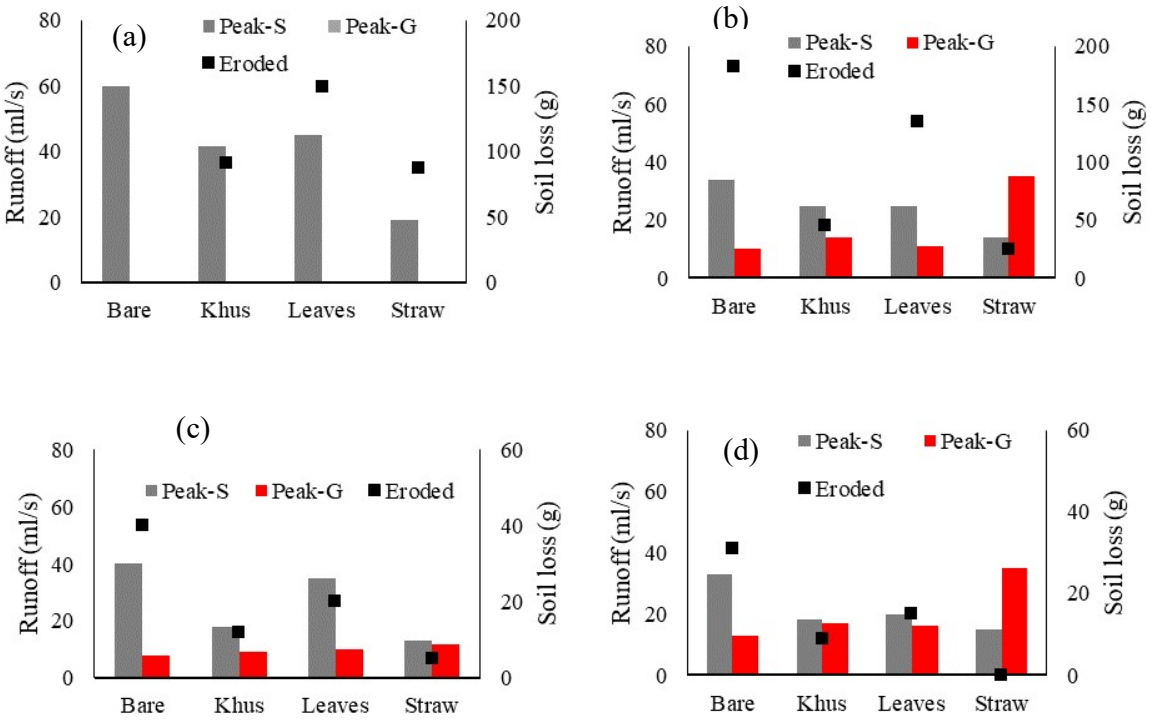

Fig. 9.10 Surface and sub-surface runoff relation with Soil loss among different scenarios using a) Soil-1 and 10% slope, b) Soil-1 and 5% slope, c) Soil-2 and 10% slope, and d) Soil-2 and 5% slope, respectively. ('Peak-S', 'Peak-G', and 'Eroded' represent the peak of surface flow, the peak of sub-surface flow, and mass of soil eroded, respectively)

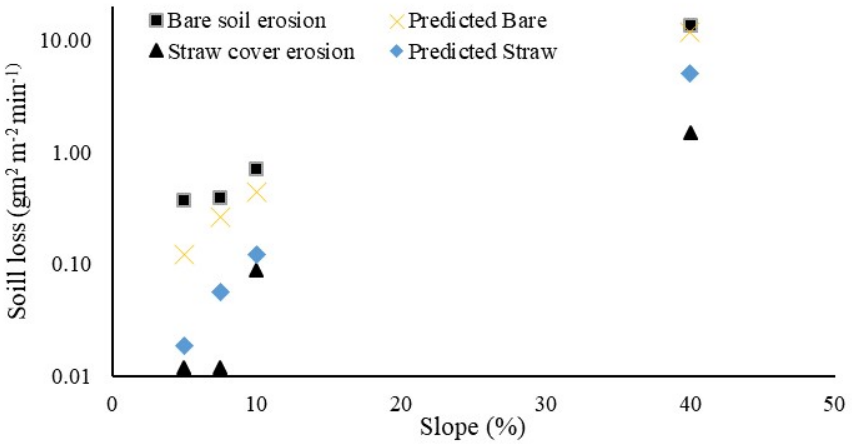

Fig. 9.11 Observed and predicted soil erosion vs slope

9.3.4 Infiltration Rate

In-situ infiltration rate was measured as ~0.3 mm/min with a double-ring infiltrometer test for Soil-1. The infiltration rate in the laboratory was estimated using Eq. 9.6. Fig. 9.12 to Fig. **9.15** shows the infiltration rate for various types of land covers plotted against a slope. Infiltration rate is found maximum for 5% slope and decreases with increase in surface slope. However, the initial infiltration rate was similar to bare soil in all cases (Fig. 9.12). Similar findings were also reported by Mu et al. (2015). Results with straw, khus and dry leaves covers are also shown in Fig. 9.12 - Fig. 9.15. Khus and dry leaves cover showed almost the same infiltration rate in similar conditions. Interestingly, the infiltration rate was almost constant in wheat straw. This result can be due to the tendency of straw to initially retain water from the precipitation and then gradually release it, which leads to a constant infiltration rate.

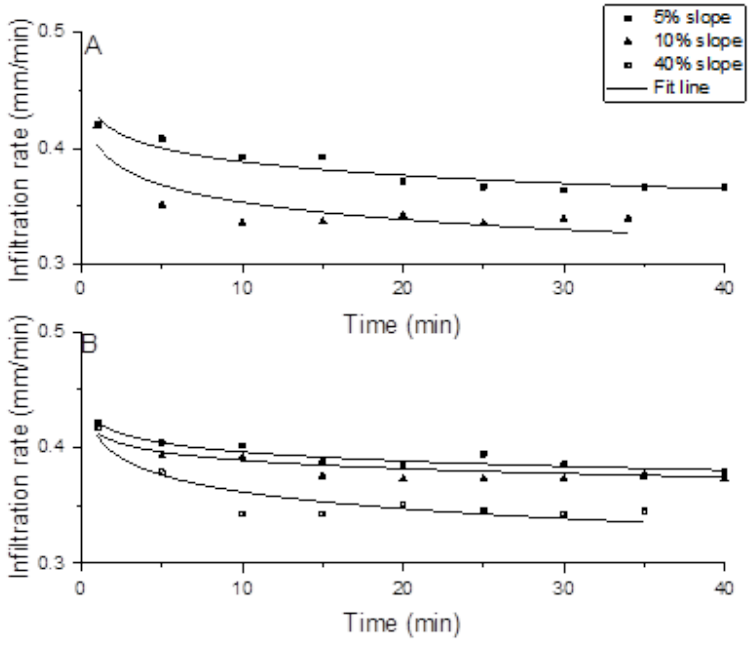

Fig. 9.12 Soil infiltration rate: gradient under bare soil using (A) Soil-1 and (B) Soil-2.

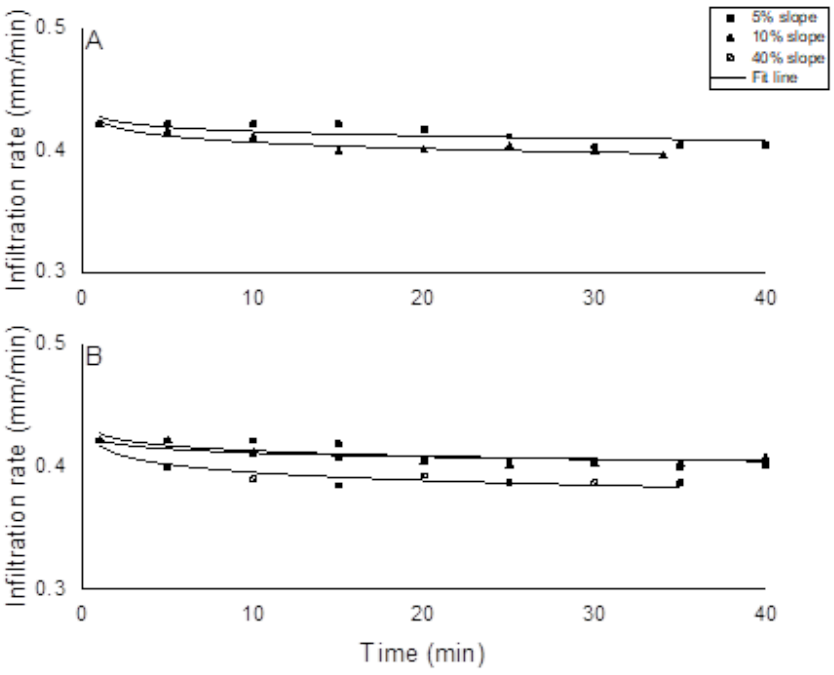

Fig. 9.13 Soil infiltration rate using wheat straw with (A) Soil-1 and (B) Soil-2.

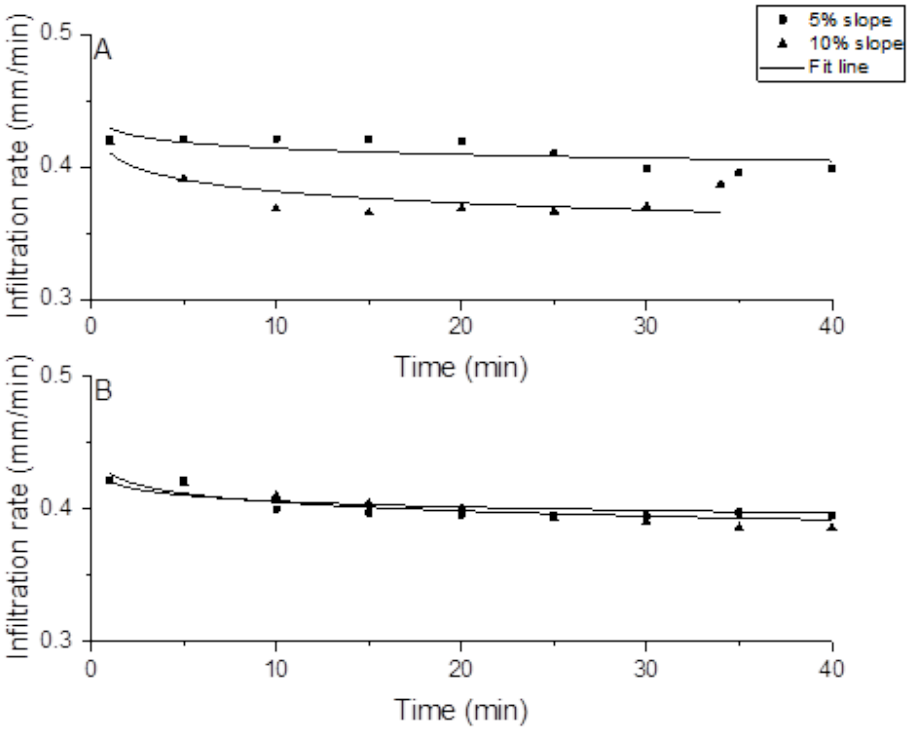

Fig. 9.14 Soil infiltration rate using Khus cover in (A) Soil-1 and (B) Soil-2.

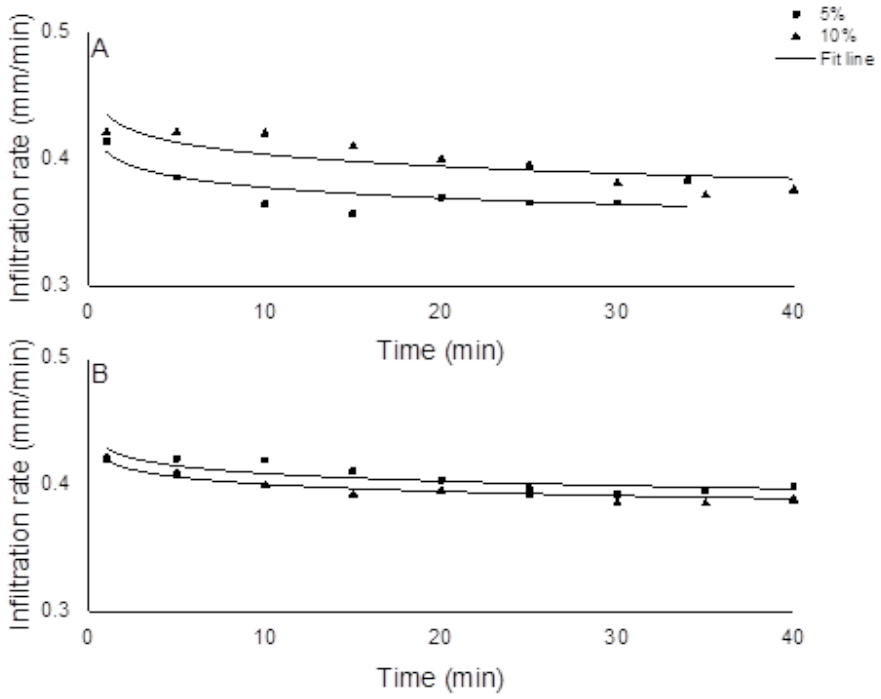

Fig. 9.15 Soil infiltration rate using dry leaves cover in (A) Soil-1 and (B) Soil-2.

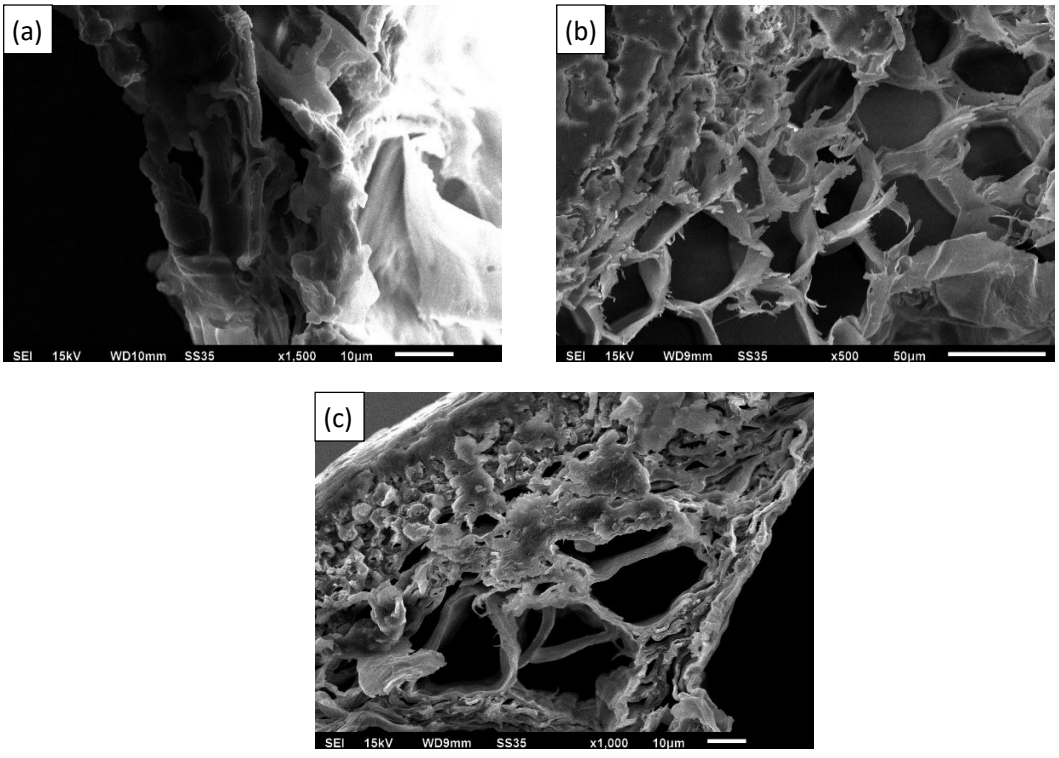

Fig. 9.16 Micro cross-section SEM image of (a) Khus, (b) Wheat Straw, and (c) Rice straw

From the above discussions, it can be concluded that straw cover is the most effective in decreasing overland flow, increasing infiltration, and minimizing soil erosion amongst three alternatives. SEM imaging from the inter-node region of the stem of the wheat straw, rice straw and khus were taken to understand the phenomenon of infiltration in these cases (Fig. 9.16). It was noticed that hollow pith and the scattered placement of the vascular bundles close to the epidermis in wheat and rice straw, while no similar structure was present in khus. These hollow piths act as microtubes and initially store water and then gradually release it, which gets enough time to infiltrate the soil. It may be noted here that there is a chance of sheet flow between the junction of coverings and soil top. However, such flow is negligible compared to the base flow because the effective surface roughness will be high due to the random arrangement of straw on the soil surface. The imaging techniques helped support the findings that wheat straw or rice straw can be effectively used to minimize overland flow and soil erosion. Similar results can be found in the study by Cerdà et al. (2016); they concluded that the wheat straw waste could be effectively used to reduce overland flow and soil loss from agricultural land under simulated rainfall on the field.

Kostiakov's (1932) and Horton's (1940) models were used to fit the infiltration rate through regression analysis for each case (Table 9.6). It was found that Horton's model fits better than the other one in almost all the cases (R^2= 0.80-0.97), similar to Mu et al. (2015), (Fig. 9.12 - Fig. 9.15 with Horton model fit). On the contrary, it is also found that the Kostiakov model performed slightly better at the same slope of 5% slope and different soil type but with Khus as soil cover.

It was found that during continuous precipitation (intensity =144 mm/h, which is nearly the extreme hourly rainfall intensity), only for a short period <~1 min., the infiltration rate was higher than the rainfall intensity, but after that, ponding occurred, the infiltration followed the Horton's equation. Calculations were carried out with revised Horton's equation with ponding conditions (Akan, 1992). The ranges of k value were found within the reported range of the previous studies (e.g., MCcuen, 2005; Terstriep and Stall, 1974).

These observations can be related to underlying theories on which the two models are based. In the Kostiakov model, the parameter β represents the slope found as a function of soil texture (Ma et al., 2016). At milder slopes, irrespective of soil type and soil cover, the performance of the Kostiakov model is poor because studies have found that the model is ideal for expressing horizontal flows but is deficient for vertical flows (Mbagwu, 1994). Compared to the Horton model, the decrease in infiltration rate is primarily related to factors operating at the soil surface rather than the soil's flow process (Xu, 2003). The value of k is found to be a function of surface texture and slope. In the case of straw cover, the value of k is the smallest, and for smoother surfaces such as bare soil, the value of k is large (Nasssif & Wilson, 2009).

Similarly, at low surface slopes, the k value was smaller than the steeper slopes. However, it is worth mentioning that in many cases with straw cover, k almost remains constant even there is a change in experimental conditions. This result could be due to the internal structure of the straw, as discussed earlier.

9.3.5 Erosion prediction through model simulation

Fig. 9.17 compares soil erosion between experimental observations and MUSLE model output. The results were significant (p-value < 0.05) and with acceptable accuracy (NSE~0.93). The effectiveness of straw cover on bare soil is given in Eq. 9.15:

$$Y_{Straw} = \alpha Y_{Bare\ soil} \quad 9.15$$

where α represents the effectiveness of straw cover on soil losses, and average α found to be 0.17 (0.19 – 0.15), while experimental results gave a value of 0.13 (0.14 – 0.12). The result yielded the relation can be given as in Eq. 9.16:

$$Observed_{Straw} = 0.76 \times Modeled_{Straw} \quad 9.16$$

Table 9.6 Curve fitting of infiltration rate at different slopes

Infiltration									
Cover	Slope (%)	Soil Mark	Kostiakov's Model $f(t)=at^b$			Horton's Model $f(t)= a+b*\exp(-t/k)$			
			a	b	R^2	a	b	k	R^2
Bare	5	1	2.18	-0.047	0.89	1.799	0.35	-14.21	0.95
	10	1	1.91	-0.041	0.64	1.694	0.68	-1.89	0.97
	5	2	2.12	-0.029	0.91	1.89	0.22	-10.66	0.89
	7.5	2	2.11	-0.033	0.95	1.89	0.25	-6.97	0.95
	10	2	2.06	-0.026	0.83	1.88	0.25	-5.47	0.9
	40	2	2.09	-0.061	0.91	1.72	0.49	-4.415	0.97
Straw	5	1	2.14	-0.012	0.51	1.898	0.22	9.69	0.86
	10	1	2.14	-0.022	0.82	1.98	0.16	-9.997	0.86
	5	2	2.15	-0.016	0.74	1.99	0.14	24.44	0.87
	7.5	2	2.13	-0.014	0.85	1.99	0.13	-21.2	0.95
	10	2	2.13	-0.014	0.78	8.63	0.12	9.49	0.85
	40	2	2.12	-0.029	0.88	1.94	0.24	-4.79	0.94
Leavs	5	1	2.2	-0.034	0.63	2.02	0.12	9.48	0.85
	10	1	2	-0.029	0.58	1.83	0.35	-3.12	0.83
	5	2	2.17	-0.023	0.79	2.06	-6.77	0.52	0.8
	10	2	2.12	-0.024	0.88	1.94	0.21	-7.18	0.95
Khus	5	1	2.15	-0.015	0.48	1.88	0.54	20.42	0.84
	10	1	2.03	-0.032	0.64	1.84	0.35	-3.47	0.85
	5	2	2.15	-0.0207	0.74	1.98	1.92	2.64	0.92
	10	2	2.17	-0.027	0.84	1.93	0.21	-17.94	0.93

The applicability of the MUSLE model for a spatial scale different from the one it was originally developed is always debatable (Alewell et al., 2019). However, the model overcomes this limitation in its conceptualization. USLE is an empirical model, and like any other empirical method, the model concept is not based on process description and simulation but rather on understanding a process and build a mathematical algorithm out of the relationship (Alewell et al., 2019). Likewise, in the present study, the experiment aims to validate the model with the obtained parameters from experiments, such that sediment erosion risk can be estimated when applied to a coarser scale. While variability is a matter of concern, studies have confirmed that variability did not necessarily increase with increased scale when modelling was performed on a resolution varying from 2m to 250 m (Alewell et al., 2019). So, these results can also be applied from a laboratory scale to a field/watershed scale by adjusting the calibrating parameters.

It is difficult to calibrate individual parameters of the MUSLE model, so a multiplying factor can be used to calibrate the model to match the observed value as given in Eqs. 9.15 and 9.16.

9.4 Model Applied on Jordan

The results were verified with field data from the Wadi Shueib catchment of Jordan. As it was challenging to bring the soil from Jordan and perform the experiments in a remote country, soil with similar hydraulic properties was chosen for the experimental work. These organic covers can be an effective solution for the disposal of agricultural waste and air pollution by burning these materials.

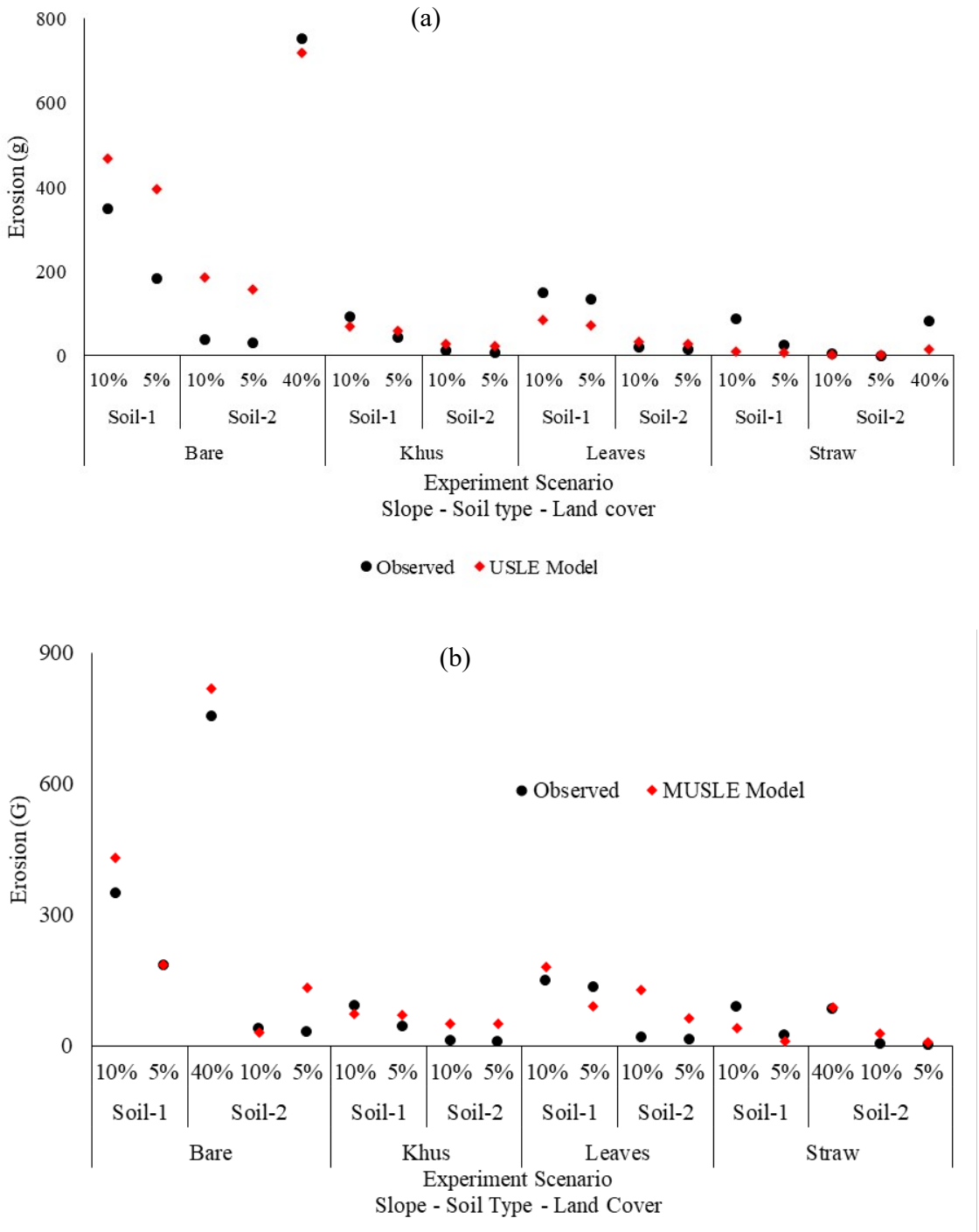

Fig. 9.17 Comparison of observed erosion with **(a)** USLE model and **(b)** MUSLE model under different scenario

9.5 Conclusion

The experimental observations showed significant implications of straw cover on soil erosion and increased infiltration, which helps watershed management and reservoirs sustainability. The experiments were conducted with two soil types and three vegetation covers with different land slopes. In overland flow, the analysis was carried out using two equations proposed by Mu et al. (2015) to calibrate the experimental observations. The Horton's and USLE/MUSLE models were used to validate the infiltration rate and soil erosion.

The wheat straw cover showed maximum effectiveness in controlling soil erosion and increased infiltration rate, which will help improve the groundwater level. At the same time, most countries face problems in handling agricultural waste after harvesting. So this agricultural waste can be effectively used in land cover management. Because the internal structure of these straws acts as micro pipes that can hold water for a longer duration and release gradually later, enhancing the infiltration. The main objective of this work was to minimize soil erosion, which further reduces the sediment deposition at the outlet (reservoir) of the watershed; therefore, the factors of the MUSLE model (such as C and P factors) can be used further in soil erosion estimation in watershed scale.

These results can be further used and applied in the real field, where the watershed is classified depending on the erodibility. On those watershed spots without any natural covers (i.e., bare soil) with high erosions, a straw mattress cover can be applied to protect that land, and in this way, we can reduce the soil loss.

Chapter 10: Conclusions and Recommendations

10.1 Conclusion

This research aimed to perform hydrological modelling to understand the watershed characteristics and meteorological parameters trend and propose a management intervention to augment reservoir capacity in the Wadi Shueib catchment area. Jordan is water-stressed, leading to other problems such as multi-national water issues, water pollution, and sediment deposition. So, to address some of these issues, there is a need to understand better the hydrological phenomenon over one of the watersheds of Jordan. This knowledge can further be considered for other watersheds also.

Initially, it was felt that a reliable topographical database is a bare minimum requirement for any hydrological study. While doing so, the need of selecting a source, which can be cost-effective and at the same time can give maximum accuracy in topography was also envisaged. So, several free and paid DEM/aerial data sources were analysed, and the improved data were analysed to estimate the reservoir sedimentation. The impact of DEM quality on hydrological parameters is important to study as it, in, turn affects the hydrological modelling. Therefore, the DEMs were compared and analyzed based on high-quality DTM from aerial photos. Besides, the reservoir water capacity was monitored through satellite images and synchronized with the reservoir's water level. These methods were validated with reservoirs in different geological settings to ensure that the method applies to all the reservoirs regardless of the environmental conditions in which the reservoir is operating.

The overall key findings of the first objective were:

- The vertical accuracy of TOPO DEM was better (RMSE= 5.40 m), compared of ASTER GDEM (RMSE= 7.10 m) and SRTM DEM (RMSE= 15.07 m).
- The TOPO DEM and ASTER GDEM showed close agreement with DTM for hydrological parameters (Slope, Stream network, and watershed) than SRTM DEM.
- ASTER GDEM showed a close agreement with DTM in Aspect and Flow Direction and found better than TOPO DEM and SRTM DEM.
- The ENN technique efficiently rectified the original DEMs by comparing them with DTM for minimum error.
- Finally, the outcome of this objective proved that the ASTER GeoDEM could be used as a free data source instead of using aerial photography or topographic maps to generate DEM data as a paid source. However, aerial photography or a topographic map of a small area can rectify the open-source DEM data through the ENN technique.

Secondly, trend analysis of precipitation and hydrological modelling was coupled to determine the water stress in the catchment. Then meteorological, hydrological, and agricultural information was coupled to analyze the drought and water availability in the catchment through a hybrid drought index. To lay the basis for this aim, a systematic analysis of watershed management was necessary. The trend analysis and future prediction of precipitation were carried out using Mann-Kendall and innovative trend analysis methods. The prediction was divided into calibration period and validation based on at least ten years of data. It was possible to determine the changing points, variations, and future precipitation predictions in the area through trend analysis and forecasting

models. The semi-distributed, physical- and process-based hydrologic model SWAT in combination with the SUFI-2 were used to build a hydrologic model of the Wadi Shueib catchment. The calibration, validation, sensitivity, and uncertainty analysis were performed to improve the reliability of the model results. The calibration and validation processes were based on known dam inflow data. Both calibration and validation process results were found satisfactory, and the results were presented within a 95% prediction uncertainty band. The drought analysis in the area was analyzed using the calibrated model results. The drought was analyzed by developing a hybrid index using fuzzy set theory based on meteorological, hydrological, and agricultural information.

The overall key findings of the second objective were:

- The MK method and Sen's slope detected a positive trend (0.71-1.52) of precipitation at two stations, Adasy and Salt, within a 10% significance level in monthly and seasonal data.
- On the other hand, the trend of precipitation was detected using ITA in different levels (low, medium, and high) at all stations for monthly, average, and seasonal scales.
- Most of the monthly, average and seasonal precipitation data were fitted well with ARIMA (3,1,3), (4,1,3) and (4,2,4) models, with absolute error ranging between 0.05 and 44.60 mm. The future trend analysis based on ITA results indicated that the catchment's water deficit is expected to increase.
- The ARIMA model used the rainfall and temperature observed data from 1979 to 2004 to build a forecasting model. Given the projected weather data, streamflow was further modelled in SWAT with an absolute error of 0.03 m^3/s and 0.08 m^3/s

during calibration and validation periods, respectively. It was observed that a maximum streamflow deficit is expected to occur with (~ -0.7 m^3/s) starting from 2020 onwards.

- The drought indices based on meteorological, hydrological, and agricultural data was computed, and their trend analysis was performed.
- The hybrid drought index was developed based on fuzzy set theory. HDI confirmed an increasing trend in the drought in the area based on the trend analysis, and the drought variation was dominated by the periodicity of 1 year.

Finally, the outcome of this objective shows that the ITA is the best method to detect the time series trend. In contrast, the SWAT model gave a good simulation for observed streamflow data, which provided a good prediction for the next decades.

In the final step, an experimental investigation was carried out to analyse the soil erosion management system and its effectiveness using different organic covers of the agricultural waste under three different land covers and commonly occurring slopes in the study area. The results were compared with the bare soil case. The experimental results with wheat (or rice) straw cover show an 85% reduction in soil erosion, which is useful information and directs that the proposed cover can be used for field application on a catchment scale (Wadi Shueib Catchment) for a reduction in sedimentation of the reservoir.

The overall key findings of this objective were:

- The use of wheat straw mattresses as soil cover increased infiltration by about 15%. This straw mattress was found as the most efficient amongst other

alternatives. Compared to the bare soil, a decrease by more than 50% in the overland flow and an increase of sub-surface flow by ~50%.

- USLE and MUSLE models were calibrated with the results. It was found that MUSLE was predicting better than the USLE model and hence can be used to predict the actual erosion in the field within an acceptable error ($p < 0.05$).
- In summary, the results obtained from the experiments suggest that wheat/rice straw is very effective irrespective of the land slope and soil type. The following equations of soil erosion were developed based on experimental results:

$$\text{Soil Loss}_{\text{Bare}} = 1350 Q^{0.466} (\tan\alpha)^{2.19} \quad 10.1$$

$$\text{Soil Loss}_{\text{Straw}} = 13.39 Q^{0.02} (\tan\alpha)^{0.26} \quad 10.2$$

- The wheat/rice straw as agricultural waste can be effectively utilized for erosion management. After the harvesting, cultivators normally burn this wheat/rice straw waste in many places. This practice causes severe air pollution. So the use of these straw mattress soil cover can effectively solve air pollution and waste disposal problems.

In Chapter 5, a 3-dimensional model is developed using satellite imagery synchronized with the water level and the reservoir storage. The relationship was established among water surface area, depth and water storage parameters. Due to lack of data from the study reservoir, the model was first validated in Anderson Ranch and Elephant Butte reservoirs of the USA due to the free reservoir data availability. The model worked well for both reservoirs. Then based on the area-water level relationship of the Wadi Shueib dam, respective reservoir capacities were determined. It was found that

the model performed well in this dam through field verification. The calculated annual sediment volume deposition (~0.055Mm^3) in the Wadi Shueib dam was close to the reported value (~0.047 Mm^3) by the Jordan Valley Authority. This sediment deposition quantity was used for the annual average sediment erosion from this catchment in further studies in chapter 9. Moreover, the reservoir status was studied through estimation of the streamflow into the reservoir in chapter 8.

A comprehensive database of the Wadi Shueib catchment was created within the framework of this research, including a complete Meta database.

10.2 Future scope

Due to the importance of modelling and watershed management, it is recommended to increase the number of stations for runoff, precipitation, and soil moisture measurement. Moreover, to improve the model results, the springs discharge can be incorporated to improve the results.

Besides trend and forecasting analyses, many hydrological applications can be developed by incorporating the land use and land cover changes upstream of the catchment. Furthermore, sediment transport modelling, which was ignored in this work due to the non-data availability, is significant in any catchment.

The outputs from this research can support the concerned developers and decision-makers to update the current water resources database of the Wadi Shueib catchment area.

Soil erosion experiments can be extended to a field-scale before actual implementation at the watershed scale. It will help verify the actual soil erosion reduction possible at a watershed scale, and economic study can be carried out.

As arid to semi-arid regions usually have data-scarce in hydrological data (spatially and temporally), it is planned to use the outputs from this research to be generalized to other catchments that have similar characteristics same region or globally.

10.3 Study limitation

Like many other data-scarce regions, this work is also subjected to certain limitations in the context of data quality and quantity. Generally, the available data gives satisfactory results; nevertheless, inclusion of more long-term inflow and sediment deposition along with water quality data, high-resolution satellite images and DEM, and long-term soil moisture data for model calibration, watershed management, and reservoir monitoring could have provided more confidence in the model results.

References

Abbas N. Wassimia S, and Al-Ansari N. (2016). Assessment of Climate Change Impacts on Water Resources of Khabour River in Kurdistan, Iraq using SWAT model. *Journal of Environmental Hydrology*. 24:10.

Abbaspour, K.C. (2008). SWAT-CUP2: SWAT Calibration and Uncertainty Programs- A User Manual. Eawag, Duebendorf, Switzerland.

Abbaspour, K.C., Johnson C.A. and Genuchten M.T. (2004). Estimating uncertain flow and transport parameters using a sequential uncertainty fitting procedure. *Vadose Zone Journal*. 3(4): 1340–1352.

Abbaspour, K.C., Vaghefi S.A., and Srinivasn R. (2018). A guideline for successful calibration and uncertainty analysis for soil and water assessment: A review of papers from the 2016 International SWAT conference. *Water*. 10: 6 DOI: 10.3390/w1001000.

Abbaspour, K.C., Yang, J., Maximov I., Siber, R. Bogner K., Mieleitner J., Zobrist J. and Srinivasan R. (2007). Spatially distributed modelling of hydrology and water quality in the pre-alpine/alpine Thur watershed using SWAT. *Journal of Hydrology*. 333(2-4): 413–430.

Abu-Allaban M., El-Naqa A., Jaber M. and Hammouri N., (2015). Water scarcity impact of climate change in semi-arid regions: a case study in Mujib basin. Jordan. *Arabian Journal Geosciences*. 8: 951–959.

Abushandi E. and Merkel B. (2013). Modeling Rainfall-Runoff Relations Using HEC-HMS and IHACRES for a Single Rain Event in an Arid Region of Jordan. *Water Resources Management*. 27: 2391–2409.

Adam G. Minke, Cherie J. Westbrook, and Garth van der Kamp (2010). Simplified Volume-Area-Depth Method for Estimating Water Storage of Prairie Potholes. *Wetlands*. 30: 541–551.

Afshan S., Sharif A., Loganathan N., and Jammazi R. (2018). Time-frequency causality between stock prices and exchange rates: Further evidences from cointegration and wavelet analysis. *Physica A: Statistical Mechanics and its Applications*. 495: 225-244.

Ajami N.K., Duan Q.Y., and Sorooshian S. (2007). An integrated hydrologic Bayesian multimodal combination framework: confronting input, parameter, and model structural uncertainty in hydrologic prediction. *Water Resources Research*. 43(1): W01403.

Al-Ansari N. (2016). Hydropolitics of the Tigris and Euphrates Basins. *Engineering*. 8: 140–172.

Alexakis D. D., Grillakis M. G., Koutroulis A. G., Agapiou A., Themistocleous K., Tsanis I. K., Michaelides S., Pashiardis S., Demetriou C., Aristeidou K., Retalis A., Tymvios F., and Hadjimitsis D. G., (2014). GIS and remote sensing techniques for the assessment of land use change impact on flood hydrology: the case study of Yialias basin in Cyprus. *Natural Hazards and Earth System Sciences*. 14: 413–426.

Alexander L.V., Zhang X., Peterson T.C., Caesar J., Gleason B., Tank A.M.G.K.,

Haylock M., Collins D., Trewin B., Rahimzadeh F., Tagipour A., Kumar K.R., Revadekar J., Griffiths G., Vincent L., Stephenson D.B., Burn J., Aguilar E., Brunet M., Taylor M., New M., Zhai P., Rusticucci M., and Vazquez-Aguirre J.L. (2006). Global observed changes in daily climate extremes of temperature and precipitation. *Journal of Geophysical Research, Atmosphere*. 38(5): 2423-2434.

Al-Masaeid K. (2010). Community-Based Rangeland Rehabilitation Project in Jordan. Report of the International Workshop on Water Harvesting Techniques and Practices and Their Roles in Enhancing Rural Livelihoods, Held in Beirut, Lebanon on 26th Sep-02nd Oct 2010.

Alsdorf D. E., Rodríguez E., and Lettenmaier D. P. (2007). Measuring surface water from space. *Reviews of Geophysics.* 45, 1:4. https://doi.org/10.1029/2006RG000197

Altman E. N. (2013). Drought Indices In Decision-Making Process of Drought Management. (Master's thesis). The University of South Carolina. Retrieved from https://scholarcommons.sc.edu/etd/2320.

Amirataee B., Montaseri M., & Sanikhani H. (2016). The analysis of trend variations of reference evapotranspiration via eliminating the significance effect of all autocorrelation coefficients. *Theoretical and applied climatology.* 126(1-2): 131-139.

An J, Zheng F., L,Römkens M.J.M., Li G.F, Yang Q.S, Wen L.L., and Wang B. (2013). The role of soil surface water regimes and raindrop impact on hillslope soil erosion and nutrient losses. *Natural Hazards.* 67(2): 411–430.

Ardiansyah P.O.D., Yokoyama R. (2002). DEM generation method from contour lines based on the steepest slope segment chain and a monotone interpolation function. *ISPRS Journal of Photogrammetry and Remote Sensing.* 57: 86–101.

Arnold, J. G., and Williams J. R. (1987). Validation of SWRRB: Simulator for water resources in rural basins. *Journal of Water Resources and Planning Management ASCE.* 113(2): 243-256.

Arnold, J. G., and Allen P. M. (1999). Estimating hydrologic budgets for three Illinois watersheds. *Journal of Hydrology.* 176(1-4): 57-77.

Arnold, J. G., and Allen P. M. (1999). Automated methods for estimating baseflow and groundwater recharge from streamflow records. *Journal American Water Resources Associate.* 35(2): 411-424.

Arnold, J. G., Srinivasan, R., Muttiah, R. S., & Williams, J. R. (1998). Large area hydrologic modeling and assessment: Part I. Model development. *Journal of American Water Resources Association.* 34, 73–89.

Atilgan A., Tanriverdi C., Yucel A., OZ H., and Degirmenci H. (2017). Analysis of long-term temperature data using Mann-Kendall trend test and linear regression methods: the case of the southeastern Anatolia region. Scientific Papers. *Series A. Agronomy.* LX: 455-462.

Avery T. E. and Berlin G. L. (1992). Fundamentals of Remote Sensing and Airphoto Interpretation. 5th Edition. Prentice-Hall Inc.: Upper Saddle River, New Jersey.

Ay M. and Kisi O. (2015). Investigation of trend analysis of monthly total precipitation by an innovative method. *Theoretical and Applied Climatology*. 120 (3–4): 617–

629.

Bàrdossy A. and Duckstein L. (2000). Fuzzy Rule-Based Modeling with Applications to Geophysical, Biological and Engineering Systems, Boca Raton, CRC Press Inc, Florida.

Barnes G.E. (2000). Soil Mechanics – Principles and Practice 2nd Edition, Macmillan Press, London.

Barnes R, Lehman C., and Mulla D. (2014). An efficient assignment of drainage direction over flat surfaces in raster digital elevation models. *Computers & Geosciences.* 62:128–135. doi:10.1016/j.cageo.2013.01.009.

Bates B.C. and Campbell, E.P. (2001). A Markov chain Monte Carlo scheme for parameter estimation and inference in conceptual rainfall-runoff modeling. *Water Resources Research.* 37(4): 937–947.

Bazzaz, F (1993). Global climatic changes and its consequences for water availability in the Arab world. In Water in the Arab World: Perspectives and Prognoses; Roger, R., Lydon, P., Eds.; Harvard University: Cambridge, MA, USA. 243–252.

Beard K.V. (1976). Terminal velocity and shape of cloud and precipitation drops aloft. *Journal of the Atmospheric Sciences.* 33: 851-864.

Behera M. D., Gupta A. K., Barik S. K., Das P., and Panda R. M., (2018). Use of satellite remote sensing as a monitoring tool for land and water resources development activities in an Indian tropical site. *Environmental Monitoring and Assessment.* 190: 401.

Bellu A., Sanches Fernandes L.F., Cortes R.M.V., Pacheco F.A.L. (2016). A framework

model for the dimensioning and allocation of a detention basin system: the case of a flood-prone mountainous watershed. *Journal of Hydrology*. 533: 567-580.

Benavidez R. Jackson B, Maxwell D, and Norton K. (2018). A review of the (Revised) Universal Soil Loss Equation ((R)USLE): with a view to increasing its global applicability and improving soil loss estimates. *Hydrology and Earth System Sciences.* 22: 6059–6086.

Bergström, S. & Brandt, M. (1987). Simulation of runoff and nitrogen leaching from two fields in southern Sweden. *Hydrological Sciences Journal.* 32 (2): 191–205.

Beven, K. and Binley, A. (1992). The future of distributed models – model calibration and uncertainty prediction. *Hydrological Processes.* 6(3): 279–298.

Bingner, R. L. (1996). Runoff simulated from Goodwin Creek watershed using SWAT. *Transactions ASAE*. 39(1): 85-90.

Borges P. A., Franke J., Silva F. D. S., Weiss H., and Bernhofer C. (2014). Differences between two climatological periods (2001–2010 vs 1971–2000) and trend analysis of temperature and precipitation in Central Brazil. *Theoretical and Applied Climatology*. 116: 191–202.

Bowker A. H., and Lieberman G. J. (1972). Engineering Statistics, 2nd Ed. Prentice-Hall, London.

Box G. E. P. and Jenkins G. M. (1976). Time Series Analysis: Forecasting and Control. San Francisco Holden-Day.

Box, G.E.; Jenkins, G. M.; Reinsel, G. C. (1994). Time series analysis: Forecasting and control. 3rd.Edition. New Jersey, Prentice-Hall.

Brockwell P.J. and Davis R.A. (1987). Time Series: Theory and Methods. Springer-Veriag Inc, New York.

Brockwell P. J., and Davis R. A. (1991). Time Series: Theory and Methods 2nd Ed. Springer-Verlag Inc, New York.

Brown R.B. and Saunders M. (2007). Dealing with Statistics: What you need to know. London, McGraw-Hill Education (UK).

Bulygina N., McIntyre N. and Wheater H. (2009). Conditioning rainfall-runoff model parameters for ungauged catchments and land management impacts analysis. *Hydrology and Earth System Sciences.* 13 (6): 893–904.

Cammalleri C., Micale F. and Vogt J., (2016). Recent temporal trend in modelled soil water deficit over Europe driven by meteorological observations. *International Journal of Climatology.* 36: 4903–4912.

Cerdà A, Gonza´lez-Pelayo O´, Gime´nez-Morera A, Jorda´n A, Pereira P, Novara A, Brevik EC, Prosdocimi M, Mahmoodabadi M, Keesstra S, and Orenes FG. (2016). Use of barley straw residues to avoid high erosion and runoff rates on persimmon plantations in Eastern Spain under low frequency—high magnitude simulated rainfall events. *Soil Research.* 54(2): 154–165.

Chang J, Li Y, Wang Y, and Yuan M. (2016). Copula-based drought risk assessment combined with an integrated index in the Wei River Basin, China. *Journal of Hydrology*. 540: 824-834.

Chang M. (2006). Forest Hydrology: An Introduction to Water and Forests, 2nd ed., CRC Press, Bacon Raton, FL.

Chatfield C. (2003). The analysis of time series. An introduction 6th edition. Chapman and Hall/CRC, New York.

Chattopadhyay G., Chakraborthy P., and Chattopadhyay S. (2012). Mann–Kendall trend analysis of tropospheric ozone and its modeling using ARIMA. *Theoretical and Applied Climatology.* 110(3): 321–328.

Chen L. and Lai X. (2011). Comparison between ARIMA and ANN models used in short-term wind speed forecasting. Asia-Pacific Power and Energy Engineering International Conference, APPEEC. 1-4. 10.1109/APPEEC.2011.5748446.

Chowdhury D.R. and Sen D. (2017). Artificial Neural Network Based Trend Analysis and Forecasting Model for Course Selection. *International Journal of Computer Sciences and Engineering (IJCSE)*. 5(2): 20-26.

IPCC, (2007). Climate Change 2007: The Physical Science Basis. Contribution of Working Group I to the Fourth Assessment Report of the Intergovernmental Panel on Climate Change [Solomon, S., D. Qin, M. Manning, Z. Chen, M. Marquis, K.B. Averyt, M. Tignor and H.L. Miller (eds.)]. Cambridge University Press, Cambridge, United Kingdom and New York, NY, USA, 996 pp.

Cromwell J. B., Hannan M. J., Labys W. C., and Terraza M. (1994). Multivariate tests for time series models. Sage Publications, Thousand Oaks, CA.

Cryer J.D., and Chan K.S. Trends. In: Time Series Analysis. Springer Texts in Statistics. New York, NY, Springer, 2008. https://doi.org/10.1007/978-0-387-75959-3_3.

Dahamsheh A. and Aksoy H., (2007). Structural characteristics of annual precipitation data in Jordan. *Theoretical and Applied Climatology.* 88: 201–212.

Davie T. (2008). Fundamentals of hydrology. Taylor & Francis, New York.

Deilami B.R., Al-Saffar M.R.A., Sheikhi1 A., Bala M.I., and Arsal D. (2013). Comparison of Surface Flows Derived from Different Resolution DEM. *International Journal of Engineering & Technology (IJET-IJENS),* 13(1): 82-85.

Demirkesen A.C. (2012). Multi-risk interpretation of natural hazards for settlements of the Hatay province in the east Mediterranean region, Turkey using SRTM DEM. *Environmental Earth Science.* 65: 1895-1907.

Destouni, G., S. M. Asokan, and J. Jarsjo. (2010). Inland Hydro-Climatic Interaction: Effects of Human Water Use on Regional Climate. *Geophysical Research Letters.* 37: L18402. doi:10.1029/2010GL044153.

Ding X., and Li X. (2011). Monitoring of the Water-Area Variations of Lake Dongting in China with ENVISAT ASAR images. *International Journal of Applied Earth Observation and Geoinformation.* 13: 894–901.

Dobos E. and Hengl T. (2009). Soil mapping applications. In: Hengl T., Reuter H. I. (eds), Geomorphometry – concepts, software, applications. *Developments in Soil*

Science. 33: 461–479.

Dracup J. A., Lee K. S., and Paulson Jr E. G. (1980). On the definition of droughts. *Water Resources Research.* 16(2): 297-302.

Duan, Q., Sorooshian, S. and Ibbitt, R. (1988). A maximum likelihood criterion for use with data collected at unequal time intervals. *Water Resources Research.* 24(7), 1163-1173.

Duru U, Arabi M, and Wohl E.E., (2017). Modeling streamflow and sediment yield using the SWAT model: a case study of Ankara River basin, Turkey. *Physical Geography*. 39 (3): 264-289.

El-Beik A. H. A. and Masaad E. M. (1993). Development of a Multi-Application Collinearity Equations Model. *Photogrammetric Record*. 14(82): 635-649.

Eni D. and Adeyeye F. (2015). Seasonal ARIMA Modeling and Forecasting of Rainfall in Warri Town, Nigeria. *Journal of Geoscience and Environment Protection*. 3 (6): 91-98.

Eugene D. Ungar, Zalmem Henkin, Mario Gutman, Amit Dolev, Avrabam Genizi and David Ganskopp. (2005). Inference of Animal Activity from GPS Collar Data on Free-Ranging Cattle. *Rangeland Ecology and Management*. 58(3): 256 - 266.

Fan M., Zhang Z., and Wang C. (2019). Mathematical Models and Algorithms for Power System Optimization: Modeling Technology for Practical Engineering Problems 1st Ed. ISBN: 978-0-12-813231-9. https://doi.org/10.1016/C2014-0-04257-8.

Feng G., Cobb S., Abdo Z., Fisher D.K., Ouyang Y., Adeli A., and Jenkins J.N. (2016).

Trend Analysis and Forecast of Precipitation, Reference Evapotranspiration, and Rainfall Deficit in the Blackland Prairie of Eastern Mississippi. *Journal of Applied Meteorology and Climatology*. 5: 1425-1439.

Ferrari R.L. (1999). Anderson Ranch Reservoir 1998 Sedimentation Survey. U.S. Department of the Interior Bureau of Reclamation. 0MB No. 0704-0188. Technical Service Center, Denver, Colorado.

Fox N.I. (2004). Technical note: The representation of rainfall drop-size distribution and kinetic energy. *Hydrology and Earth System Sciences Discussions, European Geosciences Union*. 8 (5): 1001-1007.

Frey H. and Paul F. (2012). On the suitability of the SRTM DEM and ASTER GDEM for the compilation of topographic parameters in glacier inventories. *International Journal of Applied Earth Observation and Geoinformation*. 18:480–490. doi:10.1016/j.jag.2011.09.020.

Gajbhiye S., Meshram C., Mirabbasi R. and Sharma S. K. (2016). Trend analysis of rainfall time series for Sindh river basin in India. *Theoretical and Applied Climatology*. 125(3–4): 593–608.

Gammel BM. (1998) Hurst's rescaled range statistical analysis for pseudorandom number generators used in physical simulations. *Physical Review E.* 58(2): 2586–2597.

Garbrecht J. and Martz, L. W. (1999). Digital elevation model issues in water resource modeling. Proceedings of the 19th ESRI International User Conference Presentation, San Diego, CA, 1999.

Gaynor PE, and Kirkpatrick RC. (199). Introduction to Time-Series Modeling and Forecasting in Business and Economics, McGraw-Hill, Inc. London.

Gholami A., Panahpour E. and Davami A.H., (2011). Preparing the Curve Number (CN) and Surface Runoff Coefficient (C) Map of the Basin in the Aghche Watershed, Iran. World Academy of Science, Engineering and Technology. *International Journal of Environmental, Chemical, Ecological, Geological and Geophysical Engineering*. 5(9): 476-479.

Gichamo T.Z., Popescu I., Jonoski A., and Solomatine D. (2012). River cross-section extraction from the ASTER global DEM for flood modeling. *Environmental Modelling and Software.* 31: 37–46.

Gilbert S. (2017). Drought and Climate Change in Jordan: An Analysis of the 2008–2009 Drought and Climate Change Impact. Ph.D. Thesis, Pennsylvania State University, State College, PA, USA.

Gioti E., Riga C., Kalogeropoulos K., and Chalkias C., (2013). A GIS-Based Flash Flood Runoff Model Using High Resolution Dem and Meteorological Data. *EARSeL eProceedings*. 12: 33-43.

Gleason, R.A., Tangen B.A., Laubhan M.K., Kermesand K.E., and Euliss J.N.H. (2007). Estimating Water Storage Capacity of Existing and Potentially Restorable Wetland Depressions in a Subbasin of the Red River of the North. U.S. Geological Survey Open File Report 2007–1159. U.S. Geological Survey, Reston, VA.

Gong D.Y. and Wang S.W. (2006). Severe summer rainfall in China associated with

enhanced global warming. *Climate Research.* 16: 51–59.

Gotardo J.J., Rodrigues L.N. and Gomes B.M., (2016). Estimation of climatological water deficit in an experimental watershed in the Brazilian cerrado. *Journal of the Brazilian Association of Agricultural Engineering.* 36(4): 631-645.

Graps A. (1995). Introduction to wavelets. *IEEE Computational Science and Engineering*. 2: 50–61.

Griggs DJ. And Noguer M (2002). Climate change 2001: the scientific basis. Contribution of working group I to the third assessment report of the intergovernmental panel on climate change. *Weather.* 57(8):267–269.

Guo H., Bao A., Liu T., Jiapaer G., Ndayisaba F., Jiang L., Kurban A., and De M.P. (2018). Spatial and temporal characteristics of droughts in Central Asia during 1966-2015. *Science of the Total Environment*. 624: 1523–1538.

Guttman I., Wilks S. S., and Hunter J. S. (1971). Introductory Engineering Statistics. John Wiley & Sons, New York.

Hamed K.H. and Rao A.R. (1998). A modified Mann-Kendall trend test for autocorrelated data. *Journal of Hydrology*. 204(1): 182-196.

Hancock GR., Martinez C., Evans KG., and Moliere DR. (2006). A comparison of SRTM and high-resolution digital elevation models and their use in catchment geomorphology and hydrology: Australian examples. *Earth Surface Processes and Landforms*. 31(11): 1394–1412. doi:10.1002/esp.1335.

Hao Z, Hao F., and Singh V.P. (2016). A general framework for multivariate multi-index

drought prediction based on multivariate ensemble streamflow prediction (MESP). *Journal of Hydrology.* 539: 1-10.

Hao Z., and AghaKouchak A. (2013). Multivariate standardized drought index: a parametric multi-index model Adv. *Water Resources.* 57: 12-18

Hayes M.J, Wilhelmi O.V, Knutson C.L (2004). Reducing drought risk: bridging theory and practice. *Natural Hazards Review.* 5(2): 106–113.

Heim J.RR. (2002). A review of twentieth-century drought indices used in the United States. *Bulletin of the American Meteorological Society.* 83(8): 1149.

Helsel D. R., and Hirsch R. M. (2002). Statistical methods in water resources. Techniques of Water Resources Investigations, chapter A3, Book 4, U.S. Geological Survey, pp 522. [Available online athttp://pubs.usgs.gov/twri/twri4a3/html/toc.html.]

Hielkema J., Prince S., and Astle W. (1986). Rainfall and vegetation monitoring in the savanna zone of the democratic republic of Sudan using the NOAA Advanced Very High Resolution Radiometer. *International Journal of Remote Sensing.* 7(11):1499-1513.

Hodgson M.E., Jensen J.R., Schmidt L., Schill S., and Davis B., (2003). An evaluation of LIDAR- and IFSAR-derived digital elevation models in leaf-on conditions with USGS level 1 and level 2 DEMs. *Remote Sensing of Environment.* 84: 295-308.

Hongmei L., Tianjun Z., and Chao L. (2010). Decreasing Trend in Global Land Monsoon Precipitation over the Past 50 Years Simulated by a Coupled Climate Model. *Advances in atmospheric sciences.* 27(2): 285–292.

Horton R.E. (1940). An approach toward a physical interpretation of infiltration capacity. *Proceedings, Soil Science Society of America.* 5, 399-417.

Hosseini M., Gonzalez Pelayo O., Vasques A.R., Ritsema C., Geissen V., and Keizer J.J. (2017). The short-term effectiveness of surfactant seed coating and mulching treatment in reducing post-fire runoff and erosion. *Geoderma.* 307, 231–237.

Hrissanthou, V., Mylopoulos, N., Tolikas, D. & Mylopoulos, Y. (2003). Simulation modeling of runoff, groundwater flow and sediment transport into Kastoria Lake, Greece. *Water Resources Management*. 17 (3), 223–242.

Hu C., Xu Y., Han L, Yang L. and Xu G. (2016). Long-term trends in daily precipitation over the Yangtze River Delta region during 1960–2012, Eastern China. *Theoretical and Applied Climatology.* 125(1–2): 131–147.

Huang S.Z., Huang Q., Chang J.X., Zhu Y.L., Leng G.Y., and Xing L. (2015). Drought structure based on a nonparametric multivariate standardized drought index across the Yellow River basin, China. *Journal of Hydrology.* 530: 127-136

Huard, D. and Mailhot, A. (2006). A Bayesian perspective on input uncertainty in model calibration: Application to hydrological model _abc. *Water Resources Research.* 42(7), W07416.

Huete A. (2014) Vegetation Indices. In: Njoku, E.G. (eds) Encyclopedia of Remote Sensing. Encyclopedia of Earth Sciences Series. Springer, New York, NY.

Huete, A., Justice C., and Leeuwen W. V. (1999). MODIS vegetation index (MOD 13): Algorithm theoretical basis document.

Huggel C., Schneider D., Miranda PJ., Granados HD., and Kaab A. (2008). Evaluation of ASTER and SRTM DEM data for lahar modeling: a case study on lahars from Popocatepetl Volcano, Mexico. *Journal of Volcanology and Geothermal Research*. 170(1–2):99–110. doi:10.1016/j.jvolgeores.2007.09.005.

Hyndman R.J. and Athanasopoulos G. (2018). Forecasting: Principles and Practice 2nd Ed. OTexts: Melbourne, Australia. http://www.OTexts.com/fpp2. Accessed on 22 Sep 2020.

Izaurralde, R. C., J. R. Williams, W. B. McGill, N. J. Rosenberg, and M. C. Quiroga Jakas. (2006). Simulating soil C dynamics with EPIC: Model description and testing against long-term data. *Ecological Modelling*. 192(3-4): 362-384.

Jarvis A., Rubiano J., Nelson A., Farrow A., and Mulligan M. (2004). Practical use of SRTM data in the tropics: comparisons with digital elevation models generated from cartographic data. International Centre for Tropical, Agriculture (CIAT), Cali, p 32.

Jiang H., Liu C., Sun X., Lu J., Zou C., Hou Y. and Lu X., (2015). Remote Sensing Reversion of Water Depths and Water Management for the Stopover Site of Siberian Cranes at Momoge, China. *Wetlands*. 35(2): 369-379.

Jiang L., Nielsen K., Andersen O. B., Bauer-Gottwein P., (2017). Monitoring recent lake level variations on the Tibetan Plateau using CryoSat-2 SARIn mode data. *Journal of Hydrology*. 544: 109–124.

Kader M.A., Senge M., Mojid M.A., and Ito K. (2017). Recent advances in mulching materials and methods for modifying soil environment. *Soil & Tillage Research.* 168, 155–166.

Kao S.C., and Govindaraju R.S. (2010). A copula-based joint deficit index for droughts. *Journal of Hydrology*. 380 (1–2): 121-134.

Kassambara A. (2017).Machine Learning Essentials: Practical Guide in R 1st Edt. Published by Statistical tools for high-throughput data analysis (http://www.http://www.sthda.com/).

Kateb H.E., Zhang H., Zhang P., and Mosandl R. (2013). Soil erosion and surface runoff on different vegetation covers and slope gradients, A field experiment in Southern Shaanxi Province, China. *Catena*. 105: 1–10.

Kavetski, D., Kuczera, G. and Franks, S.W. (2006a). Bayesian analysis of input uncertainty in hydrological modeling: 1. Theory. *Water Resources Research.* 42(3), W03407.

Keller A., Sakthivadivel R., and Seckler D., 2000. Water scarcity and the role of storage in development. Colombo: International Water Management Institute, IWMI Research Report 39.

Kendall M.G. Rank Correlation Methods, (4th Ed). London: Charles Griffin, 1975.

Kenward T., Lettenmaier D.P., Wood E.F., and Fielding E. (2000). Effects of digital elevation model accuracy on hydrologic predictions. *Remote Sensing of Environment.* 74 (3): 432-444.

Keyantash, J.; National Center for Atmospheric Research Staff. The Climate Data Guide: Standardized Precipitation Index (SPI), (2016). Available online: https://climatedataguide.ucar.edu/climate-data/standardized-precipitation-index-spi (accessed on 22 January 2020).

Kim T. (2000). A Study on the Epipolarity of Linear Pushbroom Images. *Photogrammetric Engineering & Remote Sensing*. (66) 8: 961-966.

Kirkby M. J. (1984). Erosion and environment in Soil Erosion, Ed. by M. J. Kirkby and R. P. C. Morgan (Wiley, Chichester, 1980; Kolos, Moscow), 11–23.

Kisi O. (2015). An innovative method for trend analysis of monthly pan evaporations. *Journal of Hydrology*. 527: 1123-1129.

Kisi O. and Ay M. (2014). Comparison of Mann-Kendall and innovative trend method for water quality parameters of the Kizilirmak River, Turkey. *Journal of Hydrology*. 513: 362–375.

Klement, E.P.; Mesiar, R.; Pap, E. (2005). Triangular norms: Basic notions and properties. In Logical, Algebraic, Analytic and Probabilistic Aspects of Triangular Norms; Klement, E.P., Mesiar, R., Eds.; Elsevier: Amsterdam, Netherlands.

Klir, G. J. and Folger, T. A. (1988) Fuzzy Sets, Uncertainty, and Information, Prentice-Hall, New York.

Knisel, W. G. (1980). CREAMS, a field-scale model for chemicals, runoff, and erosion from agricultural management systems. USDA Conservation Research Report No. 26. Washington, D.C.: USDA.

Kohl R.A. (1974). Drop size distribution from medium-sized agricultural sprinklers. *Transactions ASAE.* 17: 690–693.

Kool J., (2016). Sustainable Development in the Jordan Valley Final Report of the Regional NGO Master Plan. ISBN 978-3-319-30036-8.

Kostiakov A. N. (1932). The dynamics of the coefficients of water percolation in soils and the necessity for studying it from a dynamic point of view for purpose of amelioration. *Society of Soil Sciences.* 14: 17-21.

Kuczera, G. (1983). Improved parameter inference in catchment models. 1. Evaluating parameter uncertainty. *Water Resources Research.* 19(5): 1151–1162.

Kuczera, G., Kavetski, D., Franks, S. and Thyer, M. (2006). Towards a Bayesian total error analysis of conceptual rainfall-runoff models: characterising model error using storm-dependent parameters. *Journal of Hydrology.* 331(1-2): 161–177.

Kumar V., Jain S. K., and Singh Y. (2010). Analysis of long-term rainfall trends in India. *Hydrological Sciences Journal.* 55(4): 484-496.

Kummu M. and Varis O., (2007). Sediment–related impacts due to upstream reservoir trapping, the Lower Mekong River. *Geomorphology*. 85: 275–293.

Kundu P. M. and Olang L. O., (2011). The impact of land use change on runoff and peak flood discharges for the Nyando River in Lake Victoria drainage basin, Kenya. *WIT Transactions on Ecology and the Environment.* 153: 83-94.

Laarhoven MV, Pedrycz W. (1983). A fuzzy extension of Saaty's priority theory. *Fuzzy Sets and Systems.* 11(1–3): 229–241.

Lai L., Fang J., and Zhang Y., (2009). Reservoir Storage Capacity Calculation Using DEM Model. *Jiangxi Surveying and Mapping*. 77: 41–43 (in Chinese).

Laloy, E., Fasbender, D. and Bielders, C.L. (2010). Parameter optimization and uncertainty analysis for plot-scale continuous modeling of runoff using a formal Bayesian approach. *Journal of Hydrology.* 380(1-2): 82-93.

Lan F., Changhe L., Biao Y., and Zhao C. (2012). Long-term trends of precipitation in the North China Plain. *Journal of Geographical Sciences.* 22(6): 989-1001.

Lane, C. R., and D'Amico E. (2010). Calculating the Ecosystem Service of Water Storage in Isolated Wetlands Using LiDAR in North Central Florida, USA. *Wetlands.* 30: 967–977.

Laws J. O. (1941). Measurements of fall-velocity of water droplets and raindrops. *Transaction American Geophysical Union.* 22: 709-721.

Laws J.O. and Parsons D.A. (1943). The relation of raindrop size to intensity. *Transaction American Geophysical Union*. 24: 452–460

Leonard, R. A., W. G. Knisel, and D. A. Still. 1987. GLEAMS: Groundwater loading effects of agricultural management systems. *Transactions ASAE.* 30(5): 1403-1418.

Lin Z., Aifeng L., Jianjum W., Hayes M., Zhenghong T., Bin T., Jiaghui L., and Ming L. (2014). Impact of meteorological drought on streamflow drought in Jinghe river basin of China. Chin. *Geography Sciences*. 24(6): 694-705.

Longobardi A. and Villani P. (2010). Trend analysis of annual and seasonal rainfall time

series in the Mediterranean area. *International journal of climatology.* 30: 1538–1546.

Lu S., Ouyang N., Wu B., Wei Y., and Tesemma Z. (2013). Lake water volume calculation with time series remote-sensing images. *International Journal of Remote Sensing.* 34(22): 7962-7973.

Lu Y. and AbouRizk S.M., (2009). Automated Box–Jenkins forecasting modelling. *Automation in Construction.* 18(5): 547-558.

Lucas R.M., Ellison J.C., Mitchell A., Donnelly B., Finlayson M., and Milne A.K. (2002). Use of stereo aerial photography for quantifying changes in the extent and height of mangroves in tropical Australia. *Wetlands Ecology and Management.* 10: 159. https://doi.org/10.1023/A:1016547214434.

Maillard P., Bercher N., Calmant S., (2015). New processing approaches on the retrieval of water levels in Envisat and SARAL radar altimetry over rivers: A case study of the São Francisco River, Brazil. *Remote Sensing of Environment.* 156: 226–241.

Mann H.B. (1945). Nonparametric tests against trend. *Econometrica*. 13 (3): 245–259.

Manuel P. (2004). Influence of DEM interpolation methods in drainage analysis. GIS Hydro 04. Texas, USA.

Maragatham R. S. (2012). Trend analysis of rainfall data -a comparative study of existing methods. *International Journal of Physics and Mathematical Sciences*. 2(1): 13-18.

Marengo J. A., Tomasella J., Alves L. M., Soares W. R., and Rodriguez D. A. (2011). The drought of 2010 in the context of historical droughts in the Amazon region. *Geophysical Research Letters.* 38:L12703, JUN 22.

Marosi M., Ghomeshi M., and Sarkardeh H., (2015). Sedimentation control in the reservoirs by using an obstacle. *Sadhana*. 40(4): 1373–1383.

Marston R.B. (1952). Ground cover requirements for summer storm runoff control on aspen sites in northern Utah. *Journal of Forestry.* 50, 303-307.

Martinez, W. L. and A. R. Martinez (2004). Exploratory Data Analysis with MATLAB: Computer Science and Data Analysis Series. New York: Chapman and Hall.

Martinez, W. L. and A. R. Martinez (2008). Computational Statistics Handbook with MATLAB, (2nd ed).New York: Chapman and Hall.

Martínez-Murillo JF, Nadal-Romero E., Regüés D., Cerdà A, and Poesen J. (2013). Soil erosion and hydrology of the western Mediterranean badlands throughout rainfall simulation experiments, a review. *Catena.* 106: 101–112.

Masoud AA., and Koike K. (2011). Auto-detection and integration of tectonically significant lineaments from SRTM DEM and remotely-sensed geophysical data. *ISPRS Journal of Photogrammetry and Remote Sensing.* 66(6): 818–832.

McFeeters S. K. (1996). The use of normalized difference water index (NDWI) in the delineation of open water features. *International Journal of Remote Sensing.* 17: 1425–1432.

McKee TB, Doesken NJ, and Kleist J (1993). The relationship of drought frequency and duration to time scales. In Proceedings of the 8th Conference on Applied Climatology. Boston, MA: American Meteorological Society. 17(22): 179–183.

Medina C. E., Gomez-Enri J., Alonso J. J., and Villares P. (2010). Water Volume Variations in Lake Izabal (Guatemala) from In Situ Measurements and ENVISAT Radar Altimeter (RA-2) and Advanced Synthetic Aperture Radar (ASAR) Data Products. *Journal of Hydrology*. 382: 34–48.

Merritt W.S., Letcher R.A., and Jakeman A.J. (2003). A review of erosion and sediment transport models. *Environmental Modelling & Software.* 18(8–9):761–799. doi:10.1016/S1364-8152(03)00078-1.

Meshram S. G., Singh V. P. and Meshram C. (2017). Long-term trend and variability of precipitation in Chhattisgarh State, India. *Theoretical and Applied Climatology.* 129(3–4): 729–744.

Meshram S. G., Singh, S. K., Meshram C., Deo R. C., and Ambade B. (2017). Statistical evaluation of rainfall time series in concurrence with agriculture and water resources of Ken River basin, Central India (1901-2010). *Theoretical and Applied Climatology.* 134(3-4): 1231–1243.

Mhaske S.N., Pathak K., and Basak A. (2019). A comprehensive design of a rainfall simulator for the assessment of soil erosion in the laboratory. Catena. 172, 408-420.

Miliaresis GC and Paraschou CVE. (2005). Vertical accuracy of the SRTM DTED level 1 of Crete. *International Journal of Applied Earth Observation and Geoinformation.* 7: 49–59.

Minke A. G. and Westbrook C. J., (2010). Simplified Volume-Area-Depth Method for Estimating Water Storage of Prairie Potholes. *Wetlands*. 30: 541–551.

Mishra AK, Singh VP (2010). A review of drought concepts. *J. of Hydrology*. 391(1): 202–216.

Mitasova H., and Hofierka J. (1993). Interpolation by regularized spline with tension: II application to terrain modeling and surface geometry analysis. *Mathematical Geosciences.* 25(6): 657–669. doi:10.1007/BF00893172

Mohammad, A.H., Jung, H.C., Odeh, T., Bhuiyan C., and Hussein H. (2018). Understanding the impact of droughts in the Yarmouk Basin, Jordan: monitoring droughts through meteorological and hydrological drought indices. *Arabian J. of Geosciences*. 11: 103.

Mohammadi K., Eslami H. R. and Dayyani Dardashti Sh. (2005). Comparison of Regression, ARIMA and ANN Models for Reservoir Inflow Forecasting using Snowmelt Equivalent (a Case study of Karaj). *Journal of Agricultural Science and Technology.* 7: 17-30.

Mohan S. and Vedula S. (1995). Multiplicative seasonal Arima model for long-term forecasting of inflows. *Water Resources Management.* 9: 115-126.

Mokarram M. and Hojati M., (2016). Landform classification using a sub-pixel spatial attraction model to increase spatial resolution of digital elevation model (DEM). The Egyptian Journal of Remote Sensing and Space Science. 21(1): 111-120.

Montgomery, D.C., Cheryl, L.J. and Kulahci, M. Introduction to Time Series Analysis and Forecasting, John Wiley & Sons, New York, 2008.

Moradkhani, H., Hsu, K.L., Gupta, H. and Sorooshian, S. (2005). Uncertainty assessment of hydrologic model states and parameters: sequential data assimilation using the particle filter. *Water Resources Research.* 41(5): W05012.

Mu W, Yu F, Li C., Xie Y., Tian J., Liu J., and Zhao N. (2015). Effects of Rainfall Intensity and Slope Gradient on Runoff and Soil Moisture Content on Different Growing Stages of Spring Maize. *Water*. 7: 2990-3008.

Mukherjee S., Joshi PK., Mukherjee S., Ghosh A., Garg RD., and Mukhopadhyay A. (2013). Evaluation of vertical accuracy of open source digital elevation model (DEM). *Intl.J.of Applied Earth Observation and Geoinformation.* 21:205–217.

Mushtaq F. and Lala M.G.N. (2017). Assessment of climatic variability in the catchments of Himalayan Lake, Jammu & Kashmir. *Geocarto International.* 32(10): 1090-1104.

Narasimha Murthy K.V., Saravana R. and Vijaya Kumar K. (2018). Modeling and forecasting rainfall patterns of southwest monsoons in North–East India as a SARIMA process. *Meteorology and Atmospheric Physics.* 130(1): 99-106.

Narasimha Murthy, K.V., Saravana, R. & Vijaya Kumar, K., (2018). Stochastic modelling of the monthly average maximum and minimum temperature patterns in India 1981–2015. *Meteorology and Atmospheric Physics.* 1-13.

NASA LP DAAC (2013). MODIS Land Products Quality Assurance Tutorial: Part 2, How to interpret and use MODIS QA information in the Vegetation Indices product suite, https://lpdaac.usgs.gov/sites/default/files/public/modis/docs/MODIS_LP_QA_Tutorial-2.pdf.

Neitsch, S. L., Arnold, J. G., Kiniry, J. R., Srinivasan, R., & Williams, J. R. (2005). Soil and water assessment tool, theoretical documentation: Version 2005. Temple, TX: USDA Agricultural Research Service and Blackland Research Center.

Neitsch, S.L.; Arnold, J.G.; Kiniry, J.R.; Williams, J.R. (2011). Soil and Water Assessment Tool; Theoretical Documentation Version 2009; Texas Water Resources Institute: College Station, TX, USA.

Nguyen C, Starek M.J., Tissot P.E., Cai X., and Gibeaut J. (2019). Ensemble Neural Networks for Modeling DEM Error. *ISPRS International Journal of Geo-Information. ISPRS International Journal of Geo-Information.* 8: 444.

Niemeyer, S. (2008). New drought indices, options méditerranéennes. *Sér. A: Sémin. Méditerr.*80: 267–274.

Nikolakopoulos KG.., Kamaratakis EK., and Chrysoulakis N. (2006) SRTMvs ASTER elevation products: comparison for two regions in Crete. *Greece. International Journal of Remote Sensing.* 27(21):4819–4838. doi:10.1080/01431160600835853

Oguchi T., Aoki T., and Matsuta N. (2003). Identification of an active fault in the Japanese Alps from DEM-based hill shading. *Computers & Geosciences*. 29(7): 885–891. doi:10.1016/S0098-3004(03)00083-9.

Orun A. B., and Natarajan K. (1994). A Modified Bundle Adjustment Software for SPOT Imagery and Photography: Tradeoff. *Photogrammetric Engineering and Remote Sensing.* 60(12): 1431-1437.

Osborn, H. B. & Hickok, R. B. (1968). Variability of rainfall affecting runoff from a semi-arid rangeland watershed. *Water Resources Research*. 4 (1): 199–203.

Ouma, Y. O., and Tateishi, R. (2006). A water index for rapid mapping of shoreline changes of five East African Rift Valley lakes: An empirical analysis using Landsat TM and ETM+ data. *International Journal of Remote Sensing.* 27(15): 3153–3181.

Ozdemir A. and Leloglu UM. (2018). A fast and automated hydrologic calibration tool for SWAT. *Water and Environment Journal*. https://doi.org/10.1111/wej.12419.

Pakoksung K. and Takagi M. (2016). Digital elevation models on accuracy validation and bias correction in vertical. *Modelling Earth System Environment*. 2:11. DOI 10.1007/s40808-015-0069-3

Palizdan N., Falamarzi Y., Huang Y.F., Lee T.S., and Ghazali A.H. (2014). Regional precipitation trend analysis at the Langat River Basin, Selangor, Malaysia. *Theoretical and Applied Climatology*. 117: 589–606.

Pan C.Z., and Shangguan Z.P. (2006). Runoff hydraulic characteristics and sediment generation in sloped grassplots under simulated rainfall conditions. *Journal Hydrology.* 331: 178–185.

Pandey A., Chaube U.C., Mishra S.K., and Kumar D. (2016). Assessment of reservoir sedimentation using remote sensing and recommendations for desilting Patratu Reservoir, India. *Hydrological Sciences Journal.* 61:4: 711-718.

Park S, Oh C, Jeon S, Jung H., and Choi C. (2011). Soil erosion risk in Korean watersheds, assessed using the revised universal soil loss equation. *Journal Hydrology.* 399(3–4): 263–273. doi:10.1016/j.jhydrol.2011.01.004.

Patel A., Katiyar S.K., and Prasad V. (2016). Performances evaluation of different open source DEM using Differential Global Positioning System (DGPS). *The Egyptian Journal of Remote Sensing and Space Sciences.* 19(1): 7–16.

Paul M.J. (2006). Impact of land-use patterns on distributed groundwater recharge and discharge. *Chinese Geographical Science.* 16: 229–235.

Peña D., Tiao G. C., and Tsay R. S. (2001). A Course in Time Series Analysis, (1st Ed). New York: John Wiley and Sons.

Peña D., Tiao G.C., Tsay R.S. (2001). A Course in Time Series Analysis. A Wiley-Interscience Publication. John Wiley & Sons, Inc.

Pereira P, Gimeı`nez-Morera A, Novara A, Keesstra S, Jorda´n A, Masto RE, Brevik E, Azorin-Molina C, and Cerda` A. (2015). The impact of road and railway

embankments on runoff and soil erosion in eastern Spain. *Hydrology and Earth System Sciences.* 12: 12947–12985.

Pike R.J., (2000). Nano-metrology and terrain modelling-Convergent practice in surface characterisation. *Tribology International*. 33(9): 593-600.

Pilgrim, D. H., Chapman, T. G. & Doran, D. G. (1988). Problems of rainfall-runoff modeling in arid and semi-arid regions. *Hydrological Sciences Journal.* 33 (4): 379–400.

Plessis W. P. D. (1999). Linear regression relationships between NDVI, vegetation and rainfall in Etosha National Park, Namibia. *Journal of Arid Environments.* 42: 235–260.

Pockrandt, B. R. (2014). A multi-year comparison of vegetation phenology between military training lands and native tallgrass prairie using TIMESAT and moderate-resolution satellite imagery. Thesis. Master of Arts. Kansas State University.

Prosdocimi M, Jorda´n A, Tarolli P, Keesstra S, Novara A, Cerda` A. (2016). The immediate effectiveness of barley straw mulch in reducing soil erodibility and surface runoff generation in Mediterranean vineyards. *Science of the Total Environment.* 547: 323–330.

Pulighe G. and Fava F., (2013). DEM extraction from archive aerial photos: accuracy assessment in areas of complex topography. *European Journal of Remote Sensing.* 46: 363-378.

Rajsekhar D. and Gorelick S. M. (2017). Increasing drought in Jordan: Climate change and cascading Syrian land-use impacts on reducing transboundary flow. *Science Advances*. 3(8).

Rajsekhar D.P., Singh V.K., and Mishra A. (2015). Multivariate drought index: an information theory based approach for integrated drought assessment *Journal of Hydrology*. 526: 164-182.

Ranhao S., Baiping Z., and Jing T. (2008). A Multivariate Regression Model for Predicting Precipitation in the Daqing Mountains. *Mountain Research and Development.* 28(3-4): 318–325.

Reichert, P. and Mieleitner, J. (2009). Analyzing input and structural uncertainty of nonlinear dynamic models with stochastic, time-dependent parameters. *Water Resources Research.* 45(10): W10402.

Renschler CS., and Harbor J. (2002). Soil erosion assessment tools from point to regional scales: the role of geomorphologists in land management research and implementation. *Geomorphology.* 47(2–4): 189–209.

Riepl D. (2013). Knowledge-Based Decision Support for Integrated Water Resources Management with an Application for Wadi Shueib, Jordan. *KIT Scientific Publishing*. ISBN: 3731500116, 9783731500117.

Rizeei H.M., Pradhan B., and Saharkhiz M.A., (2018). Surface runoff prediction regarding LULC and climate dynamics using coupled LTM, optimized ARIMA, and GIS-based SCS-CN models in tropical region. *Arabian Journal of*

Geosciences. 11: 53.

Rogers RR. and Yau MK. A short course in cloud physics. Pergamon Press, Oxford, UK, 1992.

Romstad B., and Etzelmuller B. (2012). Mean-curvature watersheds: a simple method for segmentation of a digital elevation model into terrain units. *Geomorphology*. 139–140: 293–302. doi:10.1016/j. geomorph.2011.10.031.

Roodposhti, S.M.; Aryal, J.; Shahabi, H.; Safarrad, T. (2016). Fuzzy Shannon Entropy: A Hybrid GIS-Based Landslide Susceptibility Mapping Method. *Entropy.* 18: 343. doi:10.3390/e18100343.

Rouse J.W., Haas R.H., Jr. Schell J.A., and Deering, D. W. (1974). Monitoring vegetation systems in the Great Plains with ERTS. Third ERTS-1 Symposium (pp. 309–317). Washington, DC: NASA.

Saaty TL. 1990. How to make a decision: The analytic hierarchy process. *European Journal of Operational Research.* 48(1): 9–26.

Saaty TL. 2013. The analytic network process. http://iors.ir/journal/article-1-27-en.pdf

Sada A.A., Abu-Allaban M. and Al-Malabeh A., 2015. Temporal and Spatial Analysis of Climate Change at Northern Jordanian Badia. *Jordan Journal of Earth and Environmental Sciences*. 7: 87 – 93.

Sadeghi SHR, Mizuyama T, Miyata S, Gomi T, Kosugi K, Mizugaki S, and Onda Y. (2007). Is MUSLE apt to small steeply reforested watershed? *Journal of Forest Resources.* 12: 270-277..

Saleh, A., J. G. Arnold, P. W. Gassman, L. W. Hauck, W. D. Rosenthal, J. R. Williams, and A. M. S. McFarland. 2000. Application of SWAT for the upper North Bosque River watershed. *Transactions ASAE*. 43(5): 1077-1087.

Samet R., Askerzade Askerbeyli I.N., and Varol C., (2010). An implementation of automatic contour line extraction from scanned digital topographic maps. *Applied Mathematics and Computation*. 9(1): 116-127.

Sameta R. and Hancer H., (2012). A new approach to the reconstruction of contour lines extracted from topographic maps. *Journal of Visual Communication and Image Representation.* 23(4): 642-647.

Sanikhani H., Kisi O. Mirabbasi R., and Meshram S.G., (2018). Trend analysis of rainfall pattern over the Central India during 1901–2010. *Arabian Journal of Geosciences*. 11:437.

Santhi, C., J. G. Arnold, J. R. Williams, W. A. Dugas, R. Srinivasan, and L. M. Hauck. 2001. Validation of the SWAT model on a large river basin with point and nonpoint sources. *American Water Resources Association.* 37(5): 1169-1188.

Santillan J. R., Makinano M. M. and Paringit E. C., (2010), Detection of 25-year land-cover change in a critical watershed in southern Philippines using Landsat MSS and ETM+ images: importance in watershed Rehabilitation. *International Society of Photogrammetry and Remote Sensing*. XXXVIII: 221-226.

Santos R.M.B., Sanches Fernandes L.F., Moura J.P., Pereira M.G., and Pacheco F.A.L. (2014). The impact of climate change, human interference, scale and modeling

uncertainties on the estimation of aquifer properties and river flow components. *Journal of Hydrology*. 519: 1297-1314.

Scanlon B.R.., Reedy R.C., Stonestrom D.A., Prudic D.E., and Dennehy K.F. (2005). Impact of land use and land cover change on groundwater recharge and quality in the southwestern US. *Global Change Biology.* 11, 1577–1593.

Schaefli, B., Talamba, D.B. and Musy, A. (2007). Quantifying hydrological modeling errors through a mixture of normal distributions. *Journal of Hydrology.* 332(3-4): 303–315.

Schenk T. (2005). Introduction to Photogrammetry. Department of Civil and Environmental Engineering and Geodetic Science. The Ohio State University. 2070 Neil Ave., Columbus, OH 43210.

Schindewolf M. and Schmidt J. (2012). Parameterization of the EROSION 2D/ 3D soil erosion model using a small-scale rainfall simulator and upstream runoff simulation. *Catena.* 91: 47–55.

Schoups, G. and Vrugt, J. (2010). A formal likelihood function for parameter and predictive inference of hydrologic models with correlated, heteroscedastic, and non-Gaussian errors. *Water Resources Research.* 46(10): W10531.

Schwanghart W, Groom G, Kuhn NJ, and Heckrath G. (2013). Flow network derivation from a high resolution DEM in a low relief, agrarian landscape. *Earth Surface Processes and Landforms*. 38(13):1576–1586. doi:10.1002/esp.3452.

Sen P.K. (1968). Estimates of the regression coefficient based on Kendall's tau. *Journal*

of the American Statistical Association. 63 (324): 1379–1389.

Şen Z. (2012). Innovative Trend Analysis Methodology. *Journal of Hydrologic Engineering.* 17(9): 1042-1046.

Şen Z., (2013). Trend identification simulation and application. *Journal of Hydrologic Engineering.* 10.1061/(ASCE)HE.1943-5584.0000811.

Shafique M., van der Meijde M., Kerle N., van der Meer F. (2011). Impact of DEM source and resolution on topographic seismic amplification. *International Journal Applied Earth Observation and Geoinformatics.* 13: 420–427.

Shakhatreh Y. (2010). Trend Analysis for rainfall and Temperatures in three Locations in Jordan. Food Security and Climate Change in Dry Areas, 1-4 February 2010. Amman Jordan.

Shamoot S. and Hussini H., 1969. Soil and land resources in Jordan. Paper presented at the Near East and Water use Meeting, Amman.

Shanlong Lu, Ninglei Ouyang, Bingfang Wu, Yongping Wei & Zelalem Tesemma (2013) Lake water volume calculation with time series remote-sensing images, *International Journal of Remote Sensing.* 34(22): 7962-7973.

Sheffield, J., E. F. Wood, and M. L. Roderick (2012). Little change in global drought over the past 60 years, *Nature*. 491(7424): 435–438.

Smets T., Poesen J., Bhattacharyya R., Fullen M. A., Subedi M., Booth C. A., Kertész A., Szalai Z., Toth A., Jankauskas B., Jankauskiene G., Guerra A., Bezerra J. F. R., Yi Z., Panomtaranichagul M., Bühmann C. and Paterson D. G., (2011).

Evaluation of biological geotextiles for reducing runoff and soil loss under various environmental conditions using laboratory and field plot data. *Land Degradation and Development.* 22(5): 480-494.

Sorooshian, S. and Dracup, J.A. (1980). Stochastic parameter estimation procedures for hydrologic rainfall-runoff models – correlated and heteroscedastic error cases. *Water Resources Research.* 16(2): 430–442.

Srinivasan, R., T. S. Ramanarayanan, J. G. Arnold, and S. T. Bednarz. 1998. Large-area hydrologic modeling and assessment: Part II. Model application. *J. American Water Resour. Assoc*. 34(1): 91-101.

Strahler, A. N. Quantitative geomorphology of drainage basins and channel networks. Handbook of Applied Hydrology, New York, Mc. Graw Hill Book Company, 1964.

Sun M, Li X., and Kim G. (2018). Precipitation analysis and forecasting using singular spectrum analysis with artificial neural networks. *Cluster Computing*. 1-8. https://doi.org/10.1007/s10586-018-1713-2.

Sun M. and Kim G. (2016). Quantitative monthly precipitation forecasting using cyclostationary empirical orthogonal function and canonical correlation analysis. *Journal of Hydrologic Engineering.* 21(1): 1-13.

Tarawneh QY., and Chowdhury S. (2018). Trends of Climate Change in Saudi Arabia: Implications on Water Resources. *Climate*. 6(8): 1-19. doi:10.3390/cli6010008

Tarawneh Z.S. (2011). Water supply in Jordan under drought conditions. *Water Policy.* 13: 863-876.

Tarboton DG., Bras RL., and Rodrigues-Iturbe I. (1992). On the extraction of channel networks from digital elevation data. In: Beven KJ, Moore ID (eds) Terrain analysis and distributed modelling in hydrology. Wiley, New York, pp 85–104.

Taud, H., Parrot, J.F., Alvarez, R. (1999). DEM generation by contour line dilation. *Computers & Geosciences.* 25: 775–783.

Taylor, J.W.; Buizza, R. (2002). Neural network load forecasting with weather ensemble predictions. *IEEE Transactions on Power Systems*. 17: 626–632.

Terêncio D.P.S., Sanches Fernandes L.F., Cortes R.M.V., and Pacheco F.A. L. (2017). Improved framework model to allocate optimal rainwater harvesting sites in small watersheds for agro-forestry uses. *Journal of Hydrology.* 550: 318-330.

Terêncio D.P.S., Sanches Fernandes L.F., Cortes R.M.V., Moura J.P., and Pacheco F.A. L., 2018. Rainwater harvesting in catchments for agroforestry uses: A study focused on the balance between sustainability values and storage capacity. *Science of Total Environment*. 613-614: 1079-1092.

Thomas J., and Prasannakumar V. (2016). Temporal analysis of rainfall (1871–2012) and drought characteristics over a tropical monsoon-dominated State (Kerala) of India. *Journal of Hydrology.* 534: 266–280.

Thomas, Prasannakumar and Vineetha (2015). Suitability of spaceborne digital elevation models of different scales in topographic analysis: an example from Kerala, India. *Environmental Earth Science.* 73:1245–1263.

Thomson, et al. v. Thompson, et al. (2001). Embryo Project Encyclopedia (2010-09-29). ISSN: 1940-5030 http://embryo.asu.edu/handle/10776/2059.

Törnros, T. and Menzel, L. (2014). Addressing drought conditions under current and future climates in the Jordan River region. *Hydrology and Earth System Sciences.* 18: 305–318, https://doi.org/10.5194/hess-18-305-2014.

Torrence C, Compo GP (1998). A practical guide to wavelet analysis. *Bulletin of the American Meteorological Society.* 79(1):61–78.

Touma D., Ashfaq M., Nayak M.A., Kao S.C., and Diffenbaugh N.S. (2015). A multi-model and multi-index evaluation of drought characteristics in the 21st century. *Journal Hydrology.*526: 196-207

Tourian M.J., Elmi O., Chen Q., Devaraju B., Roohi Sh. and Sneeuw N., (2015). A spaceborne multisensor approach to monitor the desiccation of Lake Urmia in Iran. *Remote Sensing of Environment*. 156: 349–360.

Toutin, Th. (1995). Multi-source data fusion with an integrated and unified geometric modeling. *EARSeL Advances in Remote Sensing.* 4(2):118–129.

USDA, Soil Conservation Service. (1986). Urban hydrology for small watersheds. SCS Technical Release 55, U.S. Government Printing Office, Washington, D.C.

USGS (1998). Standards for digital elevation models. Part 3, quality control, National Mapping Program Technical Instructions. United States Geological Survey, p 10. Retrieved from http://nationalmap.gov/standards/demstds.html.

USGS (2017). https://nationalmap.gov/small_scale/printable/climatemap.html. (Accessed on 1st Jan 2020).

Valderrama-Landeros L., Flores-de-Santiago F., KovacsJ. M. and Flores-Verdugo F., (2018). An assessment of commonly employed satellite-based remote sensors for mapping mangrove species in Mexico using an NDVI-based classification scheme. *Environmental Monitoring Assessment*. 190: 23.

Valeriano MM, Kuplich TM, Storino M, Amaral BD, Mendes JN Jr, Lima DJ. (2006) Modelling small watersheds in Brazilian Amazonia with shuttle radar topographic mission-90 m data. *Computers & Geosciences.* 32(8): 1169–1181. doi:10.1016/j.cageo.2005.10.019.

Vaze J, Teng J, and Spencer G. (2010). Impact of DEM accuracy and resolution on topographic indices. *Environmental Modelling & Software.* 25(10):1086–1098.

Vrugt, J.A., Diks, C.G.H., Bouten, W., Gupta, H.V. and Verstraten, J.M. (2005). Towards a complete treatment of uncertainty in hydrologic modelling: combining the strengths of global optimization and data assimilation. *Water Resources Research.* 41(1): W01017.

Waiser M (2006). Relationship between hydrological characteristics and dissolved organic carbon concentrations and mass in northern prairie wetlands using a

conservative tracer approach. *Journal of Geophysical Research.*doi:10.1029/2005JG000088

Walling D.E., (2006). Human impact on land-ocean sediment transfer by the world's rivers. *Geomorphology.* 79: 192–216.

Wang H., Gao J., Li X., Wang H., and Zhang Y. (2014). Effects of Soil and Water Conservation Measures on Groundwater Levels and Recharge. *Water.* 6: 3783-3806.

Wang HR, Wang C., Lin X., and Kang J. (2014). An improved ARIMA model for precipitation simulations. *Nonlinear Processes in Geophysics.* 21: 1159–1168.

Wang W, Yang X, and Yao T. (2012) Evaluation of ASTER GDEM and SRTM and their suitability in hydraulic modelling of a glacial lake outburst flood in southeast Tibet. *Hydrological Process.* 26(2): 213–225. doi:10.1002/hyp.8127.

Wang W. C., Chau K. W., Xu D. M., and Chen X. Y. (2015). Improving Forecasting Accuracy of Annual Runoff Time Series Using ARIMA Based on EEMD Decomposition. *Water Resources Management.* 29(8): 2655–2675.

Wang W-C, Chau K-W, Cheng C-T, Qiu L. (2009) A comparison of performance of several artificial intelligence methods for forecasting monthly discharge time series. *Journal of Hydrology.* 374(3–4): 294–306.

Wang Z, Li J, Lai C., Zeng Z., Zhong R., Chen X., Zhou X., Wang M. (2017). Does drought in China show a significant decreasing trend from 1961 to 2009?. *Science of the Total Environment.* 579: 314-324.

Wang, X., Zhang, P., Liu, L., Li, D., and Wang, Y. (2019). Effects of Human Activities on Hydrological Components in the Yiluo River Basin in Middle Yellow River. *Water.* 11, 689.

Wei W., Chen L.D., Fu B.J., Huang Z.L., Wu D.P., and Gui L.D. (2007). The effect of land uses and rainfall regimes on runoff and soil erosion in the semi-arid loess hilly area, China. *Journal of Hydrology.* 335: 247–258.

Werz H. (2006). The use of remote sensing imagery for groundwater risk intensity mapping in the Wadi Shueib, Jordan. PhD thesis, Department of Applied Geology, University of Karlsruhe, Germany.

Wheater, H. S., Sorooshian, S. & Sharma, K. D. (2008). Hydrological Modeling in Arid and Semi-arid Areas, Cambridge University Press, Cambridge, 206 pp.

White, K. L., and I. Chaubey. 2005. Sensitivity analysis, calibration, and validations for a multisite and multivariable SWAT model. *Journal American Water Resources. Assoc*. 41(5): 1077-1089.

Williams, J. R. (1995). The EPIC Model. In V. P. Singh (Ed.), Computer Models of Watershed Hydrology. Highland Ranch, CO: Water Resources Publications.

Wilson JP. and Gallant JC. (2000). Terrain analysis: principles and applications. New York, Wiley, 2000.

Wilson, J. P. (2012). Digital terrain modeling. *Geomorphology*. 137(1): 107–121.

Winkler K., Gessner U., and Hochschild V. (2017). Identifying Droughts Affecting Agriculture in Africa Based on Remote Sensing Time Series between 2000–2016:

Rainfall Anomalies and Vegetation Condition in the Context of ENSO. *Remote Sensing.* 9(8): 831; https://doi.org/10.3390/rs9080831.

Wischmeier W.H. and Smith D.D. (1958). Rainfall energy and its relation to soil loss. *Transaction American Geophysical Union*. 39: 285–291.

Wischmeier W.H. and Smith D.D. (1978). Predicting rainfall erosion losses - a guide to conservation planning. In, United States Department of Agriculture Agricultural Handbook. vol. 537 U.S. Government Printing Office, Washington D.C., USA.

Wise S.M. (2007). Effect of differing DEM creation methods on the results from a hydrological model. *Computers & Geosciences.* 33: 1351–1365.

Wissenschaftlicher Beirat Globale Umweltveränderung (WBGU) (2007), World in Transition: Climate Change as Security Risk, German edition published in 2007 entitled Welt im Wandel: Sicherheitsrisiko Klimawandel, Springer-Verlag Berlin, Heidelberg, New York, 2008. ISBN 978-3-540-73247-1.

World Meteorological Organization (WMO) and Global Water Partnership (GWP), 2016: Handbook of Drought Indicators and Indices (M. Svoboda and B.A. Fuchs). Integrated Drought Management Programme (IDMP), Integrated Drought Management Tools and Guidelines Series 2. Geneva.

Wu Q. and Lane C. R., (2017). Delineating wetland catchments and modeling hydrologic connectivity using lidar data and aerial imagery. *Hydrology and Earth System Science.* 21: 3579–3595.

Wu S, Li J., and Huang GH. (2008). A study on DEM-derived primary topographic attributes for hydrologic applications: sensitivity to elevation data resolution. *Applied Geography.* 28(3): 210–223. doi:10.1016/j.apgeog.2008.02.006.

Xie K., Wu Y., Ma X., Liu Y., Liu B., and Hessel R. (2003). Using contour lines to generate digital elevation models for steep slope areas: a case study of the Loess Plateau in North China. *Catena*. 54: 161–171.

Barnes R, Lehman C, Mulla D (2014). An efficient assignment of drainage direction over flat surfaces in raster digital elevation models. *Computers & Geosciences.* 62: 128–135. doi:10.1016/j.cageo.2013.01.009.

Xin D., Zhou X., and Zheng H., (2006). Contour Line Extraction from Paper-based Topographic Maps. *Journal of Information and Computing Science.* 1(5): 275-283.

Yang, J., Reicher, P., Abbaspour, K.C., Xia, J. and Yang, H. (2008). Comparing uncertainty analysis techniques for a SWAT application to the Chaohe Basin in China. *Journal of Hydrology.* 358: 1–23.

Yang, J., Reichert, P. and Abbaspour, K.C. (2007b). Bayesian uncertainty analysis in distributed hydrologic modeling: a case study in the Thur River basin (Switzerland). *Water Resources Research.* 43(10): W10401.

Yang, J., Reichert, P., Abbaspour, K.C. and Yang, H. (2007a). Hydrological modelling of the Chaohe Basin in China: statistical model formulation and Bayesian inference. *Journal of Hydrology.* 340(3-4): 167–182.

Yang, J., Reichert, P., Abbaspour, K.C., Xia, J. and Yang, H. (2008). Comparing uncertainty analysis techniques for a SWAT application to the Chaohe Basin in China. *Journal of Hydrology.* 358(1-2): 1– 23.

Yu J., Yang C., Liu C., Song X., Hu S., Li F., and Tang C. (2009). Slope runoff study in situ using rainfall simulator in mountainous area of North China. *Journal of Geographical Sciences.* 19: 461–470.

Zadeh LA. (1965). Fuzzy sets inform. *Control*. 8: 338-353.

Zhang B., Yang Y.S., and Zepp H. (2004). Effect of vegetation restoration on soil and water erosion and nutrient losses of a severely eroded clayey plinthudult in southeastern China. *Catena.* 57: 77–90.

Zhang Q, Wang B-D, He B, Peng Y, Ren M-L. (2011) Singular spectrum analysis and ARIMA hybrid model for annual runoff forecasting. *Water Resources Management*. 25(11): 2683–2703.

Zhang S., Li Z., Hou X., and Yi Y. (2019). Impacts on watershed-scale runoff and sediment yield resulting from synergetic changes in climate and vegetation. *Catena*. 179: 129-138.

Zhu, J., Zhou, L. & Huang, S. (2018). A hybrid drought index combining meteorological, hydrological, and agricultural information based on the entropy weight theory. *Arabian Journal of Geosciences*. 11: 91.

List of Publications

SCI Journals (Published):

Al Balasmeh, O.I., Babbar, R. and Karmaker, T. (2020). Hybrid Drought Index for Addressing Drought in Wadi Shueib Catchment Area in Jordan. *Journal of Hydroinformatics*. 22 (4): 937–956.

Al Balasmeh, O.I., Babbar, R. and Karmaker, T. (2019). Trend analysis and ARIMA modeling for forecasting precipitation pattern in Wadi Shueib catchment area in Jordan. *Arabian Journal of Geosciences*. 12(27). Doi:10.1007/s12517-018-4205-z.

Book Chapter:

Al Balasmeh O.I., and Karmaker T. (2020). Accuracy Assessment of the Digital Elevation Model, Digital Terrain Model (DTM) from Aerial Stereo Pairs and Contour Maps for Hydrological Parameters. In: Ghosh J., da Silva I. (eds) Applications of Geomatics in Civil Engineering. *Lecture Notes in Civil Engineering*, vol 33. Springer, Singapore. https://doi.org/10.1007/978-981-13-7067-0_35.

Conference:

Al Balasmeh O., Karmaker T. & Babbar R. (2020). 'Estimation of Reservoir Capacity and Sediment Deposition Using Remote Sensing Data'. World Environmental & Water Resources Congress **2020**. Henderson, NV, USA. DOI: 10.1061/9780784482957.016.

Al Balasmeh, O.I., Karmaker, T. and Babbar, R. (2019). Designing alternate method to minimize Overland Flow and increase groundwater recharge in Smart Cities: An Experimental approach. World Environmental & Water Resources Congress.

Al Balasmeh, O.I., Babbar, R. and Karmaker, T. (2019). Investigation of Rainfall-Runoff Modelling Using Remote Sensing and GIS in Wadi Araba Sub-basin, North River Side Basin, Jordan. World Environmental & Water Resources Congress.

Journal Papers in Preparation:

Al Balasmeh, O.I., Karmaker, T. and Babbar, R. Experimental Investigation and Modelling of Rainfall Induced Erosion of Arid to Semi-Arid Region Soil under Various Vegetative Land Covers. (Under Review).

Al Balasmeh, O.I., Babbar, R. and Karmaker, T. Streamflow prediction in water stress area of Wadi Shueib Catchment in Jordan. (Under Review).

Al Balasmeh, O.I., Karmaker, T. and Babbar, R. Ensemble Neural Network for Minimizing Digital Elevation Model Error for Hydrologic Study. (Under Review).

Al Balasmeh, O.I., Karmaker, T. and Babbar, R. Estimating Capacity and Sediment Deposition of Dam Using Multi-date Satellite Imagery in data-scarce Region. (Under Review).

Appendix A. Precipitation and temperature in Wadi Shueib Catchment

Precipitation as rainfall generally occurs from October to March in this catchment. The maximum annual rainfall exceeds 500 mm (44 % of the recorded years) at the northern high altitude lands. At the same time, it decreases towards the Jordan valley, where annual precipitation is below 450 mm (67 % of the recorded years). This analysis is carried out based on spatial interpolation of long term annual average precipitation (Fig. A.1).

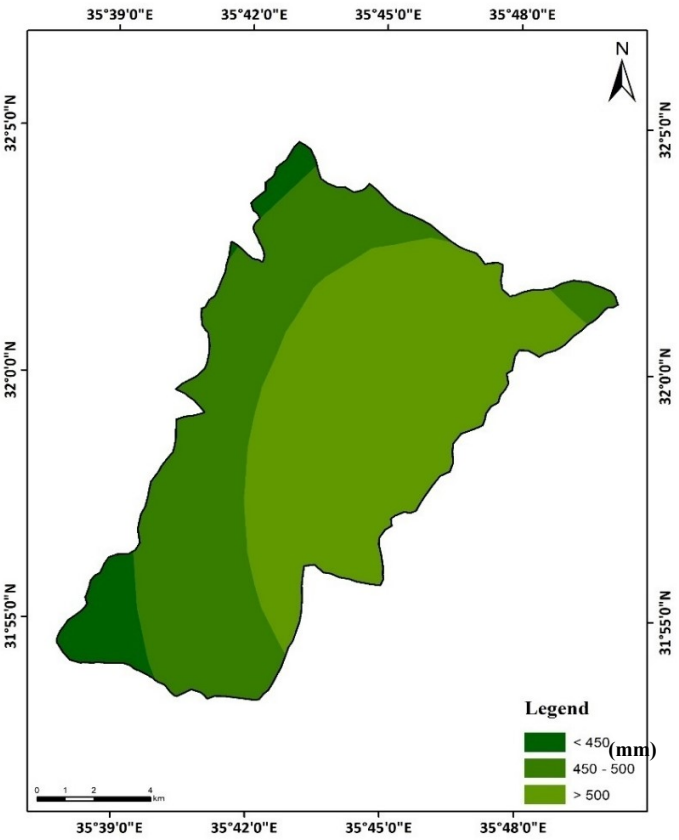

Fig. A.1 Long-term Average annual precipitation in the Wadi Shueib catchment area

The average temperature in the catchment shows an increasing trend of approximately 2-3 °C month, as the average temperature is ~12 °C in January and ~30 °C in July and August (Fig. 3.3). The variations were observed in average monthly precipitation and temperature using long-term datasets from two high altitude gauging stations situated at Jordan valley of Wadi Shueib (Fig. A.2). Besides that, Black (2010) reported that the catchment faces inter-annual precipitation variability with a standard deviation of ~35%, which lies 30% above the average of the stations near the upper Jordan valley at the Lower Jordan Valley.

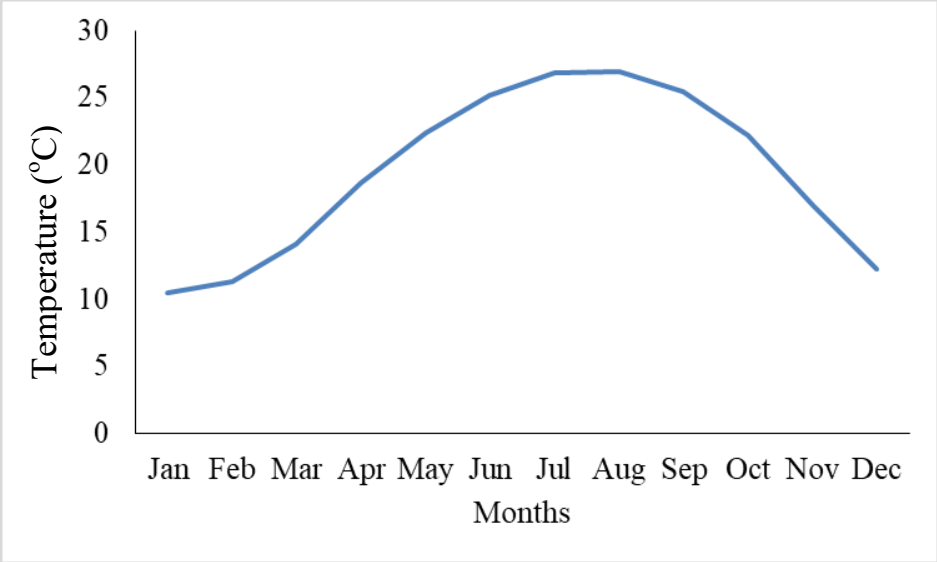

Fig. A.2 Variation of average temperature in Wadi Shueib catchment

According to the Ministry of Water and Irrigation of Jordan, potential evaporation rates were measured using Class-A Pan evaporimeter at two stations in the catchment (Shunet Nimrin Evap. St and Ain Al-Basha). Figure 3.4 shows the monthly variation of the evaporation rates and the maximum evaporation rate observed at the catchment. The

figure shows that the evaporation rate downstream is higher compared to the upper stream station.

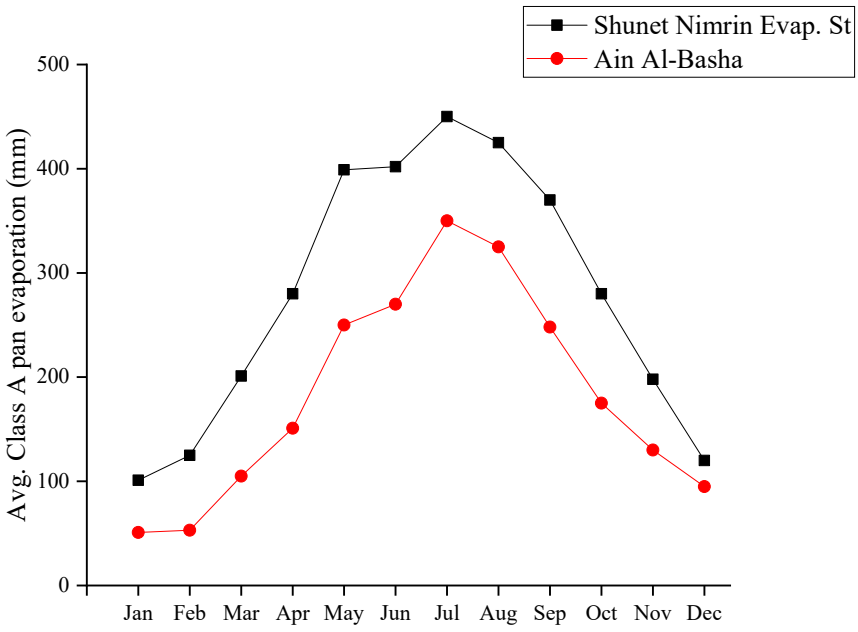

Fig. A.3 Monthly average Class A-Pan evaporation rates

Appendix B. Fuzzy AHP and weight estimation method

Entropy weight method

The Entropy approach has been widely applied to measure the disorder degree of information in information theory (Chng et al. 2016; Zhu et al. 2018). The method is adopted to reflect the difference of the index in different schemes. The high weight represents high differences with small entropies in the time series (Chng et al. 2016; Zhu et al. 2018). It takes objective information measurement for weight estimation (Chng et al. 2016; Zhu et al. 2018). The Entropy Weight method (EW) is expressed as in Eq.B.1 and Eq. B.2:

$$P_i = -k \sum_{j=1}^{n} f_{ij} \ln f_{ij}, i = 1, 2, ..., m \quad \text{B.1}$$

$$W_i = \frac{1 - P_i}{m - \sum_{i=1}^{m} P_i} \quad \text{B.2}$$

where f_{ij} is the frequency of j^{th} evaluating object in an i^{th} index.

To better comprehend the data into seasonal and annual considerations, entropy weights were found for each variable's monthly, 3-month, 6-month and 12-month data.

Fuzzy-AHP method

Lotfi Zadeh (1965) has proposed Fuzzy logic approach to compute the degree of truth instead of using true or false Boolean logic (0 or 1). The principle of fuzzy is to recognize its membership as fuzzy membership, which can be defined as any real number

between [0,1]. Each member indicates the degree of membership. A fuzzy number can be defined as in Eq. 8.5.:

$$F=\left\{\left(x,\mu_F(x)\right),x\in\mathbb{R}\right\} \quad \text{B.3}$$

Where x is a real number and has a value between $-\infty < x < \infty$, $\mathbb{R}$ is a universal set of the real number, and $\mu_F(x)$ is a membership function. The $\mu_F(x)$ represents a degree of membership between 0 and 1. The value zero means that it is not a set member, and the value 1 means that it is fully a member of a set.

The Fuzzy-AHP (F-AHP) was also carried out to determine the weight for each drought index (SPI, SSFI, and SSMI). These indices were evaluated based on previous studies and expert opinions using Pairwise Comparison (PWC). Laarhoven and Pedrycz (1983) carried out the F-AHP method for the first time based on the logarithmic least squares method. The F-AHP has been involved in different fields due to its reasonable logic (Laarhoven and Pedrycz, 1983). In this chapter, Analytical Hierarchy Processes (AHP) assign appropriate weights to individual indices (Saaty 1990). The general form of the PWC matrix model (Saaty 2013) is as in Eq. 8.6. The fuzzy number levels used to build the PWC matrix are given in Table B.1.

Table B.1 Fuzzy number levels

Fuzzy number	Linguistic variable
1	Equally importance
3	Moderately importance
5	Strongly importance
7	Very strongly importance
9	Extremely importance
2, 4, 6, 8	Intermediate values between adjacent scale values

$$A = a_{ij} = \begin{bmatrix} 1 & y_{12} & .... & y_{1n} \\ y_{21} & 1 & .... & y_{2n} \\ \vdots & \vdots & \vdots & \vdots \\ y_{m1} & y_{m2} & .... & 1 \end{bmatrix} = \begin{bmatrix} 1 & y_{12} & .... & y_{1n} \\ 1/y_{12} & 1 & .... & y_{2n} \\ \vdots & \vdots & \vdots & \vdots \\ 1/y_{1n} & 1/y_{21} & .... & 1 \end{bmatrix} \quad \text{B.4}$$

The element a_{ij} is a measure of the preference of the element of the row '*i*' relative to the element of column '*j*'. AHP assigns 1 to all elements of the diagonal of the pairwise comparison matrix. The weights matrix, W = (w_1, w_2, …w_n) were calculated based on eigenvector method in Eq. B.5 (Saaty, 1990) as:

$$\alpha_{ij} = \frac{a_{ij}}{\sum_{i=1}^{n} a_{ij}} \quad \text{B.5}$$

$$w_i = \frac{\sum_{i=1}^{n} \alpha_{ij}}{n} \quad \text{B.6}$$

The degree of coherence was applied to determine the consistency of weight between the judgments in pairs provided by the decision-maker (where *CR*<0.1 indicates consistent judgments).

$$\begin{bmatrix} 1 & y_{12} & .... & y_{1n} \\ y_{21} & 1 & .... & y_{2n} \\ \vdots & \vdots & \vdots & \vdots \\ y_{m1} & y_{m2} & .... & 1 \end{bmatrix} \times \begin{bmatrix} w_1 \\ w_2 \\ \vdots \\ w_n \end{bmatrix} = \begin{bmatrix} w'_1 \\ w'_2 \\ \vdots \\ w'_n \end{bmatrix} \quad \text{B.7}$$

$$\lambda_{\max} = \frac{1}{m} \times \left(\frac{w'_1}{w_1} + \frac{w'_2}{w_2} + \cdots + \frac{w'_n}{w_n} \right) \quad \text{B.8}$$

Following this, the Consistency Index (*CI*) and the Consistency Ratio (*CR*) as given in Eqs. B.9-B.10 were calculated. In general, *CI*< 0.1 is taken as a tolerable error range (Saaty 1990).

$$CI = \frac{\lambda_{\max} - n}{n - 1} \quad \text{B.9}$$

$$CR = \frac{CI}{RI} \quad \text{B.10}$$

The possible values of the random Index corresponding to a number of variables are given in Table B.2.

Table B.2 Random Index (RI) for number of variables

N	1	2	3	4	5	6	7	8	9	10
RI	0.00	0.00	0.58	0.90	1.12	1.24	1.32	1.41	1.45	1.49

Where *N* refers to the number of variables